Electronic states in externally modulated dilute magnetic semiconductor/superconductor hybrids

Amthong, Attapon

Award date:
2012

Awarding institution:
University of Bath

Electronic states in externally modulated dilute magnetic semiconductor/superconductor hybrids

submitted by

Attapon Amthong

for the degree of Doctor of Philosophy

of the

University of Bath

Department of Physics

September 2012

Abstract

Dilute magnetic semiconductors (DMSs) are attractive. They are candidate materials for applications in novel spintronic devices. Because of the giant Zeeman effect in the paramagnetic state, a magnetic field can be used to manipulate the spin and charge of carriers in DMSs. One possibility is to exploit the nonhomogeneous magnetic fields due to superconductors. In this thesis, the heterostructures of the planar DMS and superconductors in different geometries and superconducting states are investigated to understand the electronic structure of electrons in the DMS.

The combination of a superconducting disk in the Meissner state and the planar DMS is studied using both simple and realistic models of the magnetic field associated with the disk. The giant Zeeman interaction is found to substantially influence the energies of magnetically confined states in the adjacent DMS. In the simple model field, the giant Zeeman energy acts as an extra confining potential and results in spin dependent electron states exhibiting different spatial distributions, while the more realistic model field results in confined states exhibiting a variety of mixed spin characters.

The hybrid of a superconducting film in a superconducting vortex state and the DMS is then explored. The concentrated magnetic field due to an isolated vortex is shown to trap strongly spin polarised electron states. In the case of an Abrikosov lattice of vortices, interactions between vortex-bound states result in a band structure which can be controlled by the magnitude of an external uniform magnetic field. It is found that the numerical band structures obtained using a basis of Landau states differ from those previously reported, leading to the development of a tight-binding theory to confirm their corrections. Another hybrid investigated is a square superconductor above the DMS. In this case, the arrangement of vortices is distorted by the boundary of the sample, leading to the possibility of multivortex state and/or giant vortex states. It is discovered that the magnetic field due to the former state induces "molecular" electron states in the DMS, while that due to the latter state induces electron states with increased spatial distribution. Tight-binding theory is again used to describe the observed energy levels and the interactions between electron states induced by the magnetic fields due to separated vortices in the multivortex state.

Acknowledgements

I would like to express my gratitude to my supervisor, Dr Simon Crampin, who provided me the chance to undertake this work and offered tremendous assistance, support and guidance. I would also like to thank the staff and students in the Department of Physics for comfortable research environment.

Further thanks go to the Royal Thai Government and the Office of Educational Affairs (OEA) for all their financial support.

Finally, I would like to thank my beloved family and friends for all their encouragement over the years.

Contents

Chapter 1

Introduction

Dilute magnetic semiconductors (DMSs) [1, 2, 3] are unique materials which possess both semiconducting and magnetic properties. They are formed by the dilute doping of magnetic ions into conventional semiconductors. The concepts from two branches in condensed matter physics, semiconductor physics and magnetism, are used to understand their physics. At sufficiently high temperatures and sufficiently low concentration of magnetic ions, they are in a paramagnetic state, exhibiting an extraordinary behaviour in a magnetic field. The energy splitting due to the Zeeman effect is extremely large and can dramatically influence electronic structure of charge carriers in the sample. For this reason, there has been much interest in DMSs in nonhomogeneous magnetic fields [4, 5, 6, 7, 8, 9]. Of particular interest is the prediction by Berciu and Jankó [5] that the inhomogeneous magnetic field created by nanoscale permalloy disks can trap spin polarised carriers in DMSs. They showed that the giant Zeeman splitting could play an important role not only in confining charge carriers, but also in manipulating their spin degrees of freedom, with applications in spintronics [10, 36].

This thesis concerns the exploitation of the inhomogeneous field associated with superconductors. We study the hybrid superconductors/DMS systems in an external magnetic field and focus on the electronic structure of electrons in the DMS. Inhomogeneous magnetic fields can be generated by superconductors in many situations, depending upon the magnitude of an external field, and the size and geometry of the superconductor. The first option is using a superconductor in a Meissner state, where it expels a sufficiently low external field from the interior, resulting in an inhomogeneous field in the immediate vicinity, into

which can be placed a DMS.

Another possibility is to use the field associated with a superconducting vortex state which is found in a type-II superconductor. If the size of a superconductor is sufficiently large, Abrikosov vortices where a magnetic field passes through will exist in the superconductor. These are arranged in triangular lattice [12], resulting in a periodic magnetic field in a nearby DMS. One benefit of using this field is that the periodicity can be varied by varying the external magnetic field; as the applied field increases, the distance between vortices will decrease. When the size of a superconductor is comparable to the coherence length or the penetration depth, the boundary of a superconductor strongly affects the vortex arrangement and the resulting magnetic field profile due to the vortices [81, 82, 83]. Varying the external magnetic field can alter the number of vortices, and their configuration in the superconductor. Many possible magnetic field profiles produced by superconductors increase the opportunity to exploit the giant Zeeman energy to control spin and charge transport properties in hybrid systems, potentially enabling novel electronic devices.

The thesis is structured in the following way. In the rest of this Chapter, some background details of superconductivity and DMSs are presented. We concentrate on the behaviour of superconductors and DMSs in magnetic fields, which are of particular relevance to the work in this thesis. After that, the hybrid superconductors/DMS systems are discussed in the following Chapters.

In Chapter 2, the hybrid of a superconducting disk and a thin DMS is considered. The system is known as a magnetic quantum dot [43]. In the Meissner state, an inhomogeneous magnetic field in the DMS plane can be approximated by a model magnetic field. The effect of giant Zeeman interaction on the energy spectrum and magnetically confined states of electrons in the plane is discussed.

In Chapter 3, the study of the magnetic quantum dot in Chapter 2 is extended. We use a more realistic magnetic field profile consisting of normal and radial components. The effect of these two components is explored separately to understand the energy spectrum and confined states due to the realistic field. The results of this Chapter are compared with those in Chapter 2.

In Chapter 4, the hybrid of a superconducting film in the Abrikosov vortex phase and a DMS plane is considered. We repeat and extend the work of Rappoport *et al.* [6]. Spin polarised bound states in a DMS, confined by an isolated

vortex are confirmed. However, the energy band structure of electrons in a presence of a periodic lattice of vortices is different from those previously reported. To verify our results, a tight-binding model is developed and used to reproduce the energy bands.

In Chapter 5, the hybrid of a square superconductor in a vortex state and a planar DMS is considered. The similarities and differences of the energy spectrum and the magnetically confined states in the DMS due to a single vortex state (one vortex in a nanoscale superconductor) and an isolated vortex state (one vortex in an extended superconductor) are discussed. We then extend the study to the case of the electronic states in the DMS when the neighbouring nanoscale superconductor contains a small numbers of vortices, identifying a new kind of Zeeman-bound molecular state. To achieve further insight, a tight-binding model is again applied to describe the system.

The final Chapter contains a conclusion of the whole thesis, and some suggestions for experiments related to the hybrid systems studied here.

1.1 Superconductors in a magnetic field

In 1911, superconductivity was discovered by Kamerlingh Onnes [13]. He found that the dc resistivity of mercury dropped abruptly to zero when the temperature was less than a very low critical temperature T_c. This extraordinary behaviour is similar to that of an ordinary metal with perfect conductivity. However, the magnetic properties of a superconductor are completely different from those of a perfect conductor. In 1933, Walter Meissner and Robert Ochsenfeld discovered that a superconductor was able to expel an external field B_a. This phenomenon, called "the Meissner effect", is caused by an induced current flowing at the surface of the superconductor, which generates a magnetic field opposing the external field.

If the external field is increased sufficiently, it can penetrate into the sample which results in the sample returning to the normal state. How this happens allows superconductors to be classified into two types, as illustrated in figure 1-1. The magnetisation $\vec{M}$ of a type-I superconductor, satisfying $-\vec{M} = \vec{B}_a/\mu_0$ [14], initially increases in proportion to the external field B_a. However, when the field is greater than the critical field, B_c, the magnetisation suddenly drops

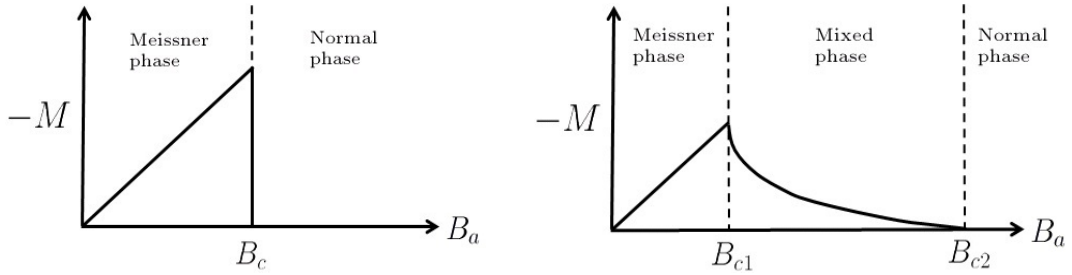

(a) (b)

Figure 1-1: Magnetisation as a functions of an external field B_a for (a) type-I and (b) type-II superconductors.

to zero and the superconductivity is destroyed. This is shown in figure 1-1 (a). In a type-II superconductor, there are two critical fields known as the lower and upper critical fields B_{c1} and B_{c2} respectively. When $B_a < B_{c1}$, the Meissner state appears like in a type-I superconductor. However, if $B_{c1} < B_a < B_{c2}$, a new quantum state called "a mixed state" occurs, in which there is the mixing of the normal and the superconducting state (see figure 1-1 (b)). Several theories have been developed to describe the behaviour of superconductors. Here, we will focus on the Ginzburg-Landau theory [15] which is widely used to study superconducting states in a magnetic field.

1.1.1 Ginzburg-Landau Theory

The Ginzburg-Landau theory [15] is based on the idea that a phase transition in a superconductor can be characterised by a parameter ψ called an "order parameter". It is assumed to be a function of temperature T with [16]

$$\psi = \begin{cases} 0 & T > T_c \\ \psi(T) & T < T_c. \end{cases} \tag{1.1}$$

One can interpret the order parameter as the wavefunction of the superconducting electrons or Cooper pairs [17]. From now on, ψ_a will denote the order parameter at a certain temperature T_a. The basic assumption of the theory is that the Helmholtz free energy per unit volume f is determined by ψ and can be expanded

in a Taylor series about ψ_a:

$$f(\psi) = f(\psi_a) + \frac{df(\psi_a)}{d\psi}(\psi - \psi_a) + \frac{1}{2}\frac{d^2 f(\psi_a)}{d\psi^2}(\psi - \psi_a)^2 + ... \tag{1.2}$$

Note that in the above expansion, we also assume that f is a differentiable function of ψ. Then, we take the limit as $T_a \rightarrow T_c^+$ on both sides of the equation to obtain

$$f(\psi) = f_n + \frac{df(0)}{d\psi}\psi + \frac{1}{2}\frac{d^2 f(0)}{d\psi^2}\psi^2 + ..., \tag{1.3}$$

where f_n is the free energy density of a normal phase. Because $f(\psi)$ is always real, but ψ may be complex, equation (1.3) is expressed as

$$f(\psi) = f_n + \frac{df(0)}{d|\psi|}|\psi| + \frac{1}{2}\frac{d^2 f(0)}{d|\psi|^2}|\psi|^2 + ... \tag{1.4}$$

However, the free energy density in this form is not generally a differentiable function of ψ because of the odd powers of $|\psi|$. Therefore, we only consider terms with even powers [18], and truncate the series with,

$$f_s = f_n + \alpha\,|\psi|^2 + \frac{1}{2}\beta\,|\psi|^4\,, \tag{1.5}$$

where f_s is the free energy density of a superconducting phase and

$$\alpha = \frac{1}{2}\frac{d^2 f(0)}{d|\psi|^2}, \quad \beta = \frac{1}{12}\frac{d^4 f(0)}{d|\psi|^4}. \tag{1.6}$$

The expression in (1.5) applies when the order parameter does not vary with position so that the free energy F_s is $f_s V_s$, where V_s is the volume of the specimen. More generally, ψ will have a spatial variation and the free energy then has the form

$$F_s = \int f_s(\psi(\vec{r}, T))d^3\vec{r}, \tag{1.7}$$

where the integral is carried out over the volume of the sample, and in this case, it is also necessary to include the kinetic energy associated with the Cooper pairs of charge $-2e$ and mass m^* that are described by the order parameter,

$$F_s = F_n + \int \alpha\,|\psi(\vec{r})|^2 + \frac{1}{2}\beta\,|\psi(\vec{r})|^4\,d^3\vec{r} + \frac{\langle p^2\rangle}{2m^*}, \tag{1.8}$$

where $\langle p^2 \rangle = \int (-i\hbar\vec{\nabla}\psi)^* \cdot (-i\hbar\vec{\nabla}\psi) d^3\vec{r} = \hbar^2 \int \left|\vec{\nabla}\psi\right|^2 d^3\vec{r}$. In a magnetic field, the quantum mechanical momentum $-i\hbar\vec{\nabla}$ is replaced by $-i\hbar\vec{\nabla} + 2e\vec{A}$. Therefore, the free energy of a superconductor in a magnetic field becomes [16]

$$\begin{aligned} F_s &= F_n + \int \left\{ \alpha \left|\psi(\vec{r})\right|^2 + \frac{1}{2}\beta \left|\psi(\vec{r})\right|^4 + \frac{1}{2m^*} \left|(-i\hbar\vec{\nabla} + 2e\vec{A})\psi(\vec{r})\right|^2 \right\} d^3\vec{r} \\ &\quad + \frac{1}{2\mu_0} \int |\vec{B}(\vec{r})|^2 d^3\vec{r}, \end{aligned} \tag{1.9}$$

where the final field term describes the magnetic energy of the total magnetic field $\vec{B}$, which contains contribution from the external field and the field induced by the supercurrent. $\vec{A}$ is the corresponding vector potential, with $\vec{B} = \vec{\nabla} \times \vec{A}$. The first integral extends over the volume of the sample, while the second one extends over all space.

In order to obtain the Ginzburg-Landau equations, we minimise the free energy in (1.9) with respect to ψ and $\vec{A}$. Minimising the energy for variations of the order parameter yields

$$\delta F_s = \int \left\{ \alpha\psi\delta\psi^* + \beta \left|\psi\right|^2 \psi\delta\psi^* + \frac{1}{2m^*}(\Pi\delta\psi)^* \cdot \Pi\psi + c.c \right\} d^3\vec{r}, \tag{1.10}$$

where $\Pi = -i\hbar\vec{\nabla} + 2e\vec{A}$ and *c.c.* stands for complex conjugate. We then use the divergence theorem and the identity, $\vec{\nabla} \cdot (\delta\psi^*\vec{F}) = (\vec{\nabla}\delta\psi^*) \cdot \vec{F} + \delta\psi^*(\vec{\nabla} \cdot \vec{F})$, to reexpress the last term as

$$\begin{aligned} \int (\Pi\delta\psi)^* \cdot \Pi\psi d^3\vec{r} &= i\hbar \int (\vec{\nabla}\delta\psi^*) \cdot \Pi\psi d^3\vec{r} + 2e \int \vec{A}\delta\psi^* \cdot \Pi\psi d^3\vec{r} \\ &= i\hbar \int \delta\psi^* \Pi\psi \cdot d\vec{S} - i\hbar \int \delta\psi^* \vec{\nabla} \cdot \Pi\psi d^3\vec{r} \\ &\quad + 2e \int \vec{A}\delta\psi^* \cdot \Pi\psi d^3\vec{r} \\ &= i\hbar \int \delta\psi^* \Pi\psi \cdot d\vec{S} + \int \delta\psi^* (-i\hbar\vec{\nabla} + 2e\vec{A}) \cdot \Pi\psi d^3\vec{r} \\ &= i\hbar \int \delta\psi^* \Pi\psi \cdot d\vec{S} + \int \delta\psi^* (\Pi^2\psi) d^3\vec{r}, \end{aligned}$$

where the surface integral is over the boundary of the superconductor. Now δF_s can be written as

$$\begin{aligned}\delta F_s &= \int \delta\psi^* \left\{ \alpha\psi + \beta \left|\psi\right|^2 \psi + \frac{1}{2m^*}\Pi^2\psi \right\} d^3\vec{r} + c.c. \\ &\quad + \int \frac{i\hbar}{2m^*}\delta\psi^*(\Pi\psi)\cdot d\vec{S} + c.c. \end{aligned} \tag{1.11}$$

F_s will be a minimum free energy when $\delta F_s = 0$. That means the order parameter has to satisfy

$$\alpha\psi + \beta \left|\psi\right|^2 \psi + \frac{1}{2m^*}\Pi^2\psi = 0 \tag{1.12}$$

within the volume of the superconductor and

$$\hat{n}_s \cdot \Pi\psi = 0, \tag{1.13}$$

where $\Pi = -i\hbar\vec{\nabla} + 2e\vec{A}$, and $\hat{n}_s$ is a unit normal vector to the surface of a superconductor. (1.12) is the first Ginzburg-Landau equation, and (1.13) identifies the boundary condition satisfied by the order parameter.

Next, we consider the variation in the free energy due to the vector potential. After some algebra, we find

$$\delta F_s = \int \left\{ \frac{e}{m^*}\delta\vec{A}\psi^* \cdot \Pi\psi + c.c \right\} d^3\vec{r} + \frac{1}{\mu_0}\int \vec{B}\cdot(\vec{\nabla}\times\delta\vec{A}) d^3\vec{r}. \tag{1.14}$$

Using the identity $\vec{\nabla}\cdot(\vec{F}\times\vec{G}) = -\vec{F}\cdot(\vec{\nabla}\times\vec{G}) + \vec{G}\cdot(\vec{\nabla}\times\vec{F})$, the second integral can be expressed as

$$\frac{1}{\mu_0}\int \vec{B}\cdot(\vec{\nabla}\times\delta\vec{A}) d^3\vec{r} = \frac{1}{\mu_0}\int \delta\vec{A}\cdot(\vec{\nabla}\times\vec{B}) d^3\vec{r}. \tag{1.15}$$

In deriving (1.15), $\int \vec{\nabla}\cdot(\vec{B}\times\delta\vec{A}) d^3\vec{r} = \int (\vec{B}\times\delta\vec{A})\cdot d\vec{S} = 0$ because $\delta\vec{A} = 0$ at infinity. After substituting (1.15) into (1.14), we obtain

$$\delta F_s = \int \delta\vec{A}\cdot\left\{ \frac{1}{\mu_0}(\vec{\nabla}\times\vec{B}) + \frac{e}{m^*}\left[\psi^*\Pi\psi + c.c.\right] \right\} d^3\vec{r}. \tag{1.16}$$

Again, F_s will be minimised when $\delta F_s = 0$. Due to the Maxwell equation $\vec{\nabla} \times \vec{B} = \mu_0 \vec{j}$, we identify the current density due to the supercurrent as

$$\begin{aligned} \vec{j_s} &= -\frac{e}{m^*} \left[\psi^* \Pi \psi + c.c.\right] \\ &= \frac{i\hbar e}{m^*}(\psi^* \vec{\nabla}\psi - \psi \vec{\nabla}\psi^*) - \frac{4e^2}{m^*} |\psi|^2 \vec{A}. \end{aligned} \tag{1.17}$$

This is the second Ginzburg-Landau equation. It must be emphasised that $\vec{A}$ is the vector potential due to both supercurrents and external currents that produce the external applied field. In the following, both Ginzburg-Landau equations are used to derive some important parameters in a superconductor.

Characteristic length scales

There are two characteristic length scales which can be derived from the two Ginzburg Landau equations (1.12) and (1.17). Let us first consider equation (1.12) when the vector potential $\vec{A}$ is zero:

$$\frac{-\hbar^2}{2m^*}\nabla^2\psi + \alpha\psi + \beta |\psi|^2 \psi = 0. \tag{1.18}$$

The obvious solution is a constant $\psi_0 = \sqrt{-\alpha/\beta}$ which can be used to describe the order parameter in a superconductor in the ideal Meissner state (when the superconductor expels the magnetic field completely). If ψ is real, we can express ψ in units of ψ_0 and obtain

$$\frac{-\hbar^2}{2m^*}\nabla^2 f_0 + \alpha f_0 - \alpha f_0^3 = 0, \tag{1.19}$$

where $f_0 = \psi/\psi_0$. Because the coefficient α has the units of energy, a natural length scale ξ is defined as

$$\xi = \sqrt{\frac{\hbar^2}{2m^*|\alpha|}}. \tag{1.20}$$

This is the well known coherence length, which is used to characterise the spatial variation of the order parameter.

Another length scale can be derived from the second Ginzburg-Landau equation. If the external magnetic field is small, we can assume that the order parameter distributes uniformly inside a superconductor as $\psi = \psi_0$. Therefore, the

supercurrent density (1.17) becomes

$$\vec{j_s} = -\frac{4e^2}{m^*} |\psi_0|^2 \vec{A}. \tag{1.21}$$

Taking the curl of the above equation and using the Maxwell equation $\vec{\nabla} \times \vec{B} = \mu_0 \vec{j}$, we obtain

$$\vec{\nabla} \times \vec{\nabla} \times \vec{B} = -\frac{\mu_0}{m^*} 4e^2 |\psi_0|^2 \vec{B}. \tag{1.22}$$

Finally, applying the vector cross product $\nabla \times \left(\nabla \times \vec{A}\right) = \nabla(\nabla \cdot \vec{A}) - \nabla^2 \vec{A}$ in the Coulomb gauge allows us to to reexpress (1.22) as

$$\nabla^2 \vec{B} = \vec{B}/\lambda^2. \tag{1.23}$$

Here λ, known as the penetration depth, determines the spatial variation of the magnetic field, and is given by [19]

$$\lambda = \sqrt{\frac{m^* \beta}{4e^2 \mu_0 |\alpha|}}. \tag{1.24}$$

The upper critical magnetic field

When a type-II superconductor is placed in an external magnetic field B_a which exceeds the upper critical magnetic field B_{c2}, the order parameter ψ describing the superconducting state is exactly zero, and the external field B_a passes through the sample. If B_a is just below B_{c2}, ψ will be small. In this case, the field inside the superconductor can be approximated by the external field $\vec{B}_a$ [16], for which the corresponding vector potential $\vec{A}$ in the Landau gauge is given by $\vec{A} = (0, xB_a, 0)$. Then, the Ginzburg-Landau equation (1.12) reads as

$$\alpha\psi + \beta |\psi|^2 \psi + \frac{1}{2m^*} \left(-i\hbar\vec{\nabla} + 2exB_a\hat{j}\right)^2 \psi = 0. \tag{1.25}$$

The second term can also be neglected since ψ is assumed to be small, leading to

$$\left(-\frac{\hbar^2\nabla^2}{2m^*} - \hbar\omega i x \frac{\partial}{\partial y} + \frac{m^*\omega^2 x^2}{2}\right) \psi = -\alpha\psi, \tag{1.26}$$

where $\omega = 2eB_a/m^*$. We recognise this as the Schrödinger equation describing

a particle of charge $-2e$ moving with the cyclotron frequency ω in a uniform magnetic field. Landau [49] suggested that the solution of this equation should be

$$\psi\left(\vec{r}\right) = e^{i(k_y y + k_z z)} f\left(x\right), \tag{1.27}$$

where substitution shows that the function f satisfies

$$-\frac{\hbar^2}{2m^*}\frac{d^2}{dx^2}f + \frac{m^*\omega^2}{2}\left(x - x_0\right)^2 f = \left(-\alpha - \frac{\hbar^2 k_z^2}{2m^*}\right) f, \tag{1.28}$$

where $x_0 = -\hbar k_y / m^*\omega$. This is equivalent to the Schrödinger equation describing a one dimensional harmonic oscillator of a particle with mass m^*, centred at $x = x_0$, with the energy of the oscillator replaced by $-\alpha - \hbar^2 k_z^2/2m^*$. Therefore, we immediately get the quantisation

$$\left(n + \frac{1}{2}\right)\hbar\omega = -\alpha_n - \frac{\hbar k_z^2}{2m^*}. \tag{1.29}$$

The sample begins exhibiting superconductivity when $n = 0$ and $k_z = 0$, corresponding to the lowest possible energy $\hbar\omega = -2\alpha$. As a result, we get the maximum value of the magnetic field that can cause superconductivity,

$$B_{c2} \;=\; -\frac{\alpha m^*}{e\hbar} = \frac{\hbar}{2e\xi^2}. \tag{1.30}$$

In 1957, Abrikosov [12] contributed to the main development of type-II superconductors. He predicted a structure of the two dimensional periodic lattice of vortices by considering a superconductor in a magnetic field that is slightly below B_{c2}. Many experiments [20, 21, 22, 23] have confirmed his prediction (see figure 1-2). Abrikosov was awarded the Nobel Prize in Physics in 2003.

1.2 The Zeeman effect in a dilute magnetic semiconductor

We now switch attention to the properties of electrons in a dilute magnetic semiconductor. In a magnetic field, the energy levels of each quantum state will be

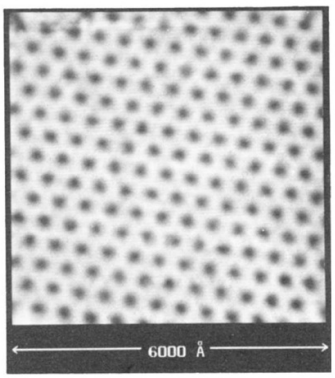

Figure 1-2: Abrikosov flux lattice produced by a magnetic field of 1 T in $NbSe_2$ at 1.8 K [22], observed by scanning tunnel microscopy.

disturbed differently, depending on a magnetic moment associated with it. One consequence is that the field can split degenerate energy levels. This phenomenon is called "The Zeeman effect". For simplicity, let us consider an electron (charge $-e$) moving freely in space. In a magnetic field $\vec{B}$, the interaction between the magnetic moment of the particle, $\vec{\mu}$, and the field will result in the potential energy: $U = -\vec{\mu} \cdot \vec{B}$. Due to spin, an electron possesses the intrinsic magnetic moment [24]:

$$\vec{\mu} = -g_s \frac{e}{2m_e} \vec{s} = -\frac{1}{2} g_s \mu_B \vec{\sigma}, \tag{1.31}$$

where g_s is the electron spin g-factor, m_e is the electron rest mass, $\vec{s}$ is the spin operator $\vec{s} = \hbar\vec{\sigma}/2$, and $\mu_B = e\hbar/2m_e$ is the Bohr magneton. Now, the Hamiltonian of the particle is the combination of the kinetic energy and the potential energy U, usually called the Zeeman energy,

$$\widehat{H} = \frac{(\hat{p} + e\vec{A})^2}{2m_e} + \frac{1}{2} g_s \mu_B \vec{\sigma} \cdot \vec{B}, \tag{1.32}$$

where $\hat{p}$ is the momentum operator and $\vec{A}$ is the vector potential ($\vec{B} = \vec{\nabla} \times \vec{A}$). In free space or in a nonmagnetic semiconductor, the Zeeman term is normally very small and often neglected, compared with the kinetic term. However, the influence of the magnetic field can be increased by doping magnetic ions into a semiconductor.

A dilute magnetic semiconductor (DMS) [25, 26, 27] is just such a semicon-

ductor, which has been doped to contain some magnetic atoms. It was first recognised in 1977 when Komarov [28] found the giant enhancement of magnetic-optical effects in Mn-doped CdTe. In the early study of DMSs, II-VI compounds containing Mn ions were intensively investigated; for instance, CdMnSe, ZnMnSe ZnMnTe [29, 30, 31]. Subsequently, the study was extended to III-V compounds with other magnetic ions; Co, Cr, V, Fe, Eu [32, 33, 34]. All DMSs are able to exhibit both semiconducting and magnetic properties. The magnetic phase of a DMS can be paramagnetic, antiferromagnetic, or spin-glass, depending upon temperature and magnetic concentration. Figure 1-3 shows a magnetic phase diagram for CdMnTe, which is typical of all DMSs [2]. At sufficiently low Mn fraction x, and sufficiently high temperature T, the DMS is in a paramagnetic phase. However, when x is large, and at low T, the interaction between magnetic ions can cause the DMS to be in a spin-glass or antiferromagnetic state.

A DMS in a paramagnetic state is useful in manipulating the spin of charge carriers and can be applied in spintronic devices. In this state, there is an exchange interaction between band electrons and electrons associated with magnetic ions. If the magnetic field is applied in the z direction $\vec{B} = B\hat{z}$, the Hamiltonian

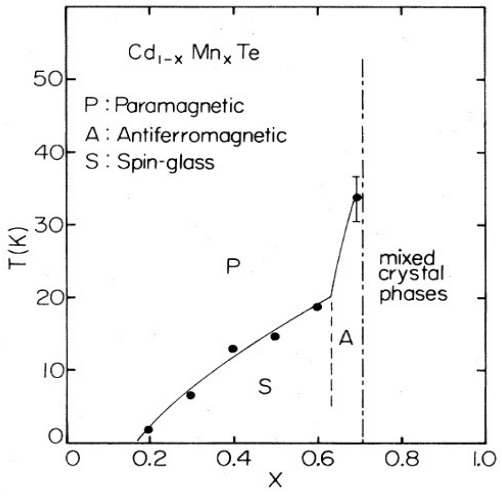

Figure 1-3: Phase diagram for $Cd_{1-x}Mn_xTe$, where x is a fraction of Cd which has been substituted by Mn. From Ref. [2].

describing electrons in the DMS, including the exchange energy, is given by [1, 2]

$$\widehat{H} = \frac{(\hat{p} + e\vec{A})^2}{2m^*} + \frac{1}{2} g^* \mu_B \sigma_z B - \frac{1}{2} N_0 \alpha x \langle S_z \rangle \sigma_z, \tag{1.33}$$

where m^* and g^* are the effective mass and g-factor of band electrons. The material dependent exchange constant $N_0\alpha$ can be obtained experimentally, and $\langle S_z \rangle$ is the average spin per magnetic site. Similar to the conventional Zeeman term, the exchange term disappears when there is no external magnetic field (since the spins are random and hence $\langle S_z \rangle = 0$), and appears when the field is non-vanishing. Therefore, Furdyna [1, 2] proposed the introduction of the effective g-factor g_{eff}, which consists of the standard g-factor and the exchange contribution:

$$g_{\text{eff}} = -g^* + \frac{N_0 \alpha x \langle S_z \rangle}{\mu_B B}. \tag{1.34}$$

Now, the Hamiltonian (1.33) becomes

$$\widehat{H} = \frac{(\hat{p} + e\vec{A})^2}{2m^*} - \frac{1}{2} g_{\text{eff}} \mu_B \sigma_z B. \tag{1.35}$$

In experiments on DMSs [3, 35], a very large energy splitting due to Zeeman interaction is found, indicating an enhanced effective g-factor which originates from the strong interaction between band electrons and those localised on the partially filled shell of magnetic ions. In a sufficiently low magnetic field, the splitting energy $\Delta E = g_{\text{eff}} \mu_B B$ decreases linearly with increasing B (see figure 1-4). That is, in this limit g_{eff} can be assumed to be a constant. In a sufficiently high field, ΔE is converged because of the saturation magnetisation due to the magnetic ions. To date, the largest value of g_{eff} measured is 600 [35] in CdMnSe, while the electron spin g-factor is just about 2. This giant effective g-factor can enormously change the transport and magnetic properties of the semiconductor, allowing the magnetic field to manipulate the spin degree of freedom of the charge carriers.

There has been much interest in the potential application of DMSs in spintronics [36, 37], which aims to control and manipulate the spin and charge of carriers to enhance the ability to store, transmit, and process quantum infor-

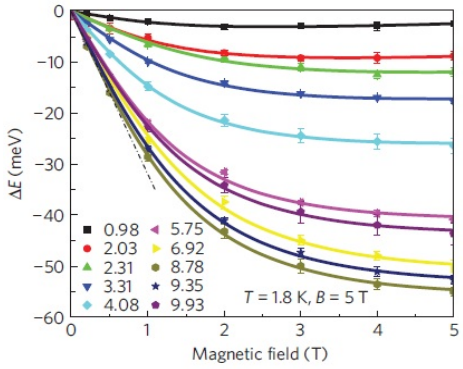

Figure 1-4: The Zeeman splitting of CdMnSe as a function of a magnetic field for various Mn concentrations, when the temperature is 1.8 K. From Ref. [35].

mation in electronic devices. In order to use spin in new and improved devices, one has to find effective ways to generate spin polarised currents, detect spin polarisation, and inject and manipulate spin polarised carriers [26, 38]. DMSs are promising candidate materials for spintronic applications. According to the fact that spin up and spin down electrons feel different Zeeman potentials in a DMS, theoretical works [39, 40, 41] have predicted that hybrid systems consisting of nonmagnetic semiconductors and DMSs could produce spin polarised currents. These have been recently confirmed in the experimental work of Olbrich [42]. In this thesis, the presented work aims to use a DMS to manipulate the spin degree of freedom of charge carriers by an external magnetic field, which is part of the study of spintronics.

Having discussed the fundamental concepts of a superconductor and a DMS in a magnetic field, we now study the heterostructure of a superconductor and a planar DMS in the following Chapters.

Chapter 2

Magnetic quantum dots in a dilute magnetic semiconductor

A magnetic quantum dot was first proposed by L. Solimany and B. Kramer [43]. It can be realised by depositing a superconducting disk with radius R underneath the plane of two dimensional electron gas (2DEG) (see figure 2-1 (a)). The difference between the usual quantum dot system and a magnetic quantum dot is that electrons are confined magnetically in an inhomogeneous magnetic field. Due to the Meissner effect of the superconductor, an applied magnetic field is expelled resulting in a magnetic field in the plane that can be approximated as zero in the dot region ($r < R$) and constant outside ($r \geq R$). Consequently, the classical motion of electrons in such a system is characterised by cyclotron orbits outside the dot and straight line trajectories inside, as sketched in figure 2-1 (b) [44]. The advantage of a magnetic quantum dot is that the energy spectrum and behaviour of electrons in the 2DEG can be controlled by an applied field [44, 45, 46]. The eigenstates of the dot distribute both inside and outside the dot region, exhibiting intermediate behaviour between Landau level states and circular quantum dot states. When an applied field is sufficiently small, the eigenstates will extend mostly outside the dot region where the field is uniform and behave like Landau states. On the other hand, when an applied field is sufficiently large, the eigenstates will be confined inside the dot where the field vanishes and behave like the eigenstates of a circular quantum dot with an infinite barrier. A close relation between the quantum eigenstates and the classical trajectories is also reported [44, 46, 47].

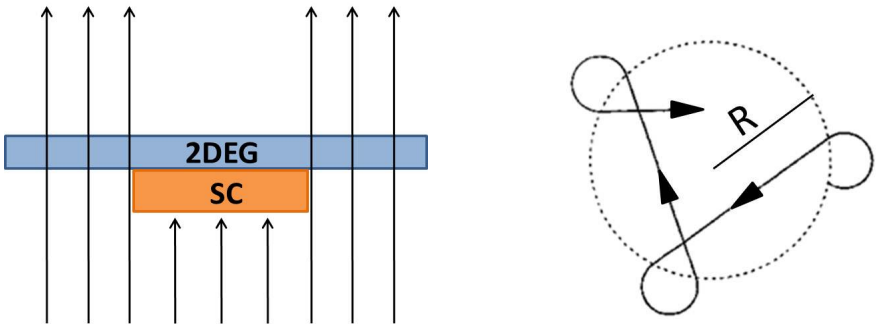

(a) (b)

Figure 2-1: (a) The hybrid system of a DMS and a superconducting disk in an applied magnetic field. (b) A classical electron orbit in a magnetic quantum dot [44].

In this Chapter, we study the electronic structure and dynamics of electrons in a magnetic quantum dot in a DMS; the 2DEG previously studied is replaced by a DMS. We find that the electron eigenstates, eigenenergies, and trajectories are different from those of the previous studies. The exchange interaction between the charged carriers and the doped magnetic ions results in an extremely large modified g factor, g_{eff}. This allows us to consider the Zeeman energy to be a spin-dependent potential. It can either attract or scatter charged carriers, depending upon their spin, and lead to a spin-dependent spatial distribution of Zeeman localised states. The semiclassical interpretation is used to explain the quantum results. A clear correspondence between probability currents and electrons' trajectories will be presented. In order to understand the effect of the inhomogeneous magnetic field due to the superconducting disk, we begin by considering the classic problem of a DMS in a uniform magnetic field, which results in the well-known Landau levels.

2.1 Landau quantisation in a DMS

Classically, a particle with charge q moving with a velocity $\vec{v}$ in a uniform magnetic field $\vec{B}$ experiences the Lorentz force $\vec{F} = q(\vec{v} \times \vec{B})$. In quantum mechanics, this problem was first studied by L.D. Landau who found the energy levels of the

particle are discrete. These are now called "Landau levels" [49]. In the following, we will consider the charged particle constrained to the $x-y$ plane of a DMS in the constant uniform magnetic field $\vec{B} = B\hat{z}$, including in the Hamiltonian the Zeeman term which is dominant. The Hamiltonian of a free charged particle ($q = -e$) with spin can therefore be written as

$$\widehat{H} = \frac{(\hat{p} + e\vec{A})^2}{2m^*} - \frac{1}{2} g_{\text{eff}} \mu_B \vec{\sigma} \cdot \vec{B}, \tag{2.1}$$

where m^* is the effective mass of the particle in the DMS, $\hat{p}$ is the momentum operator, $\vec{A}$ is the vector potential, $\vec{B} = \vec{\nabla} \times \vec{A}$, and the second term on the right hand side is the Zeeman energy. In cylindrical coordinates (r, ϕ, z), it is convenient to choose the symmetric gauge $\vec{A} = Br/2\hat{\phi}$ so that we can then rewrite the Hamiltonian as

$$\widehat{H} = -\frac{\hbar^2 \nabla^2}{2m^*} - \frac{i\hbar}{2}\omega_c \frac{\partial}{\partial \phi} + \frac{1}{8} m^* \omega_c^2 r^2 - \frac{1}{2} g_{\text{eff}} \mu_B \sigma_z B, \tag{2.2}$$

where $\omega_c = eB/m^*$ is the cyclotron frequency. Because the Hamiltonian commutes with the angular momentum operator $\hat{L}_z$ and the Pauli matrix σ_z, the eigenfunctions can be expressed as

$$\Psi^{\sigma}_{nm}(r, \phi) = e^{im\phi} \psi^{\sigma}_{nm}(r)\, \chi_{\sigma}, \tag{2.3}$$

where a radial quantum number n, an angular momentum m and spin σ are good quantum numbers. χ_σ is $\binom{1}{0}$ and $\binom{0}{1}$ for spin up and spin down respectively. Substituting Ψ^{σ}_{nm} into the Schrödinger equation equation $\widehat{H}\Psi = E\Psi$, we obtain the radial equation:

$$\frac{\hbar^2}{2m^*}\left(\psi'' + \frac{\psi'}{r} - \frac{m^2}{r^2}\psi\right) + \left(E - \frac{1}{8} m^* \omega_c^2 r^2 - \frac{\hbar \omega_c}{2} m + \sigma g_{\text{eff}} \mu_B B\right)\psi = 0, \tag{2.4}$$

where σ is $1/2$ and $-1/2$ for spin up and spin down respectively. In equation 2.4, for simplicity, the radial wavefunction $\psi^{\sigma}_{nm}(r)$ is written as ψ and ψ' represents the derivative of $\psi^{\sigma}_{nm}(r)$ with respect to r. We then define the dimensionless parameter

$$\rho = \frac{m^* \omega_c r^2}{2\hbar} = cr^2, \tag{2.5}$$

to express the Schrödinger equation equation (2.4) in terms of ρ as

$$\rho\psi'' + \psi' + \left(-\frac{\rho}{4} + \beta - \frac{m^2}{4\rho}\right)\psi = 0, \tag{2.6}$$

where $\beta = E/\hbar\omega_c - m/2 + \sigma g_{\text{eff}}\mu_B B/\hbar\omega_c$, and now ψ' represents the derivative of $\psi^{\sigma}_{nm}(\rho)$ with respect to ρ. The solution of (2.6) is described in Appendix A. The normalised eigenstates are obtained in terms of Kummer-M functions [93].

$$\psi^{\sigma}_{nm}(r) = \frac{1}{\ell_B\,|m|!}\left[\frac{(|m|+n)!}{2^{|m|}n!}\right]^{\frac{1}{2}} \exp\left(\frac{-r^2}{4\ell_B^2}\right)\left(\frac{r}{\ell_B}\right)^{|m|} M(-n, |m|+1, r^2/2\ell_B^2), \tag{2.7}$$

where $\ell_B = \sqrt{\hbar/eB} = \sqrt{\hbar/m^*\omega_c}$ is the magnetic length and $n = \beta - |m|\,/2 - 1/2$. The eigenvalues can be obtained by considering the behaviour of the Kummer-M functions which are finite polynomials when n is 0 or positive. The restriction leads to the energy quantisation,

$$E^{\sigma}_{nm} \;=\; \hbar\omega_c\left(n + \frac{m}{2} + \frac{|m|}{2} + \frac{1}{2}\right) - \sigma g_{\text{eff}}\mu_B B, \tag{2.8}$$

where n is 0,1,2,3..., m is $0, \pm1, \pm2, \pm3$..., and $\sigma = \pm 1/2$, corresponding to the Landau levels obtained in [49] for the case $g_{\text{eff}} = 0$. Clearly, the state with $m = 0$ has the same energy as the states with negative m, and indeed each Landau level is infinite-fold degenerate as seen in figure 2-2. The corresponding eigenstates exhibit unusual behaviour: their radial dependence is a function of $|m|$ so that the states with $+m$ and $-m$ have the same distribution, but their energies are different as seen in figure 2-3 (a). Figure 2-3 (b) shows that as usual the number of nodes is related to the radial quantum number n. Finally, note that the Zeeman term does not affect the wavefunctions, but it does split the degenerate energy levels of the spin up and spin down states.

2.2 Theoretical models of magnetic quantum dots in a DMS

A magnetic quantum dot and an example of classical electron confinement are shown schematically in figure 2-1. In this section, we explore how electrons are

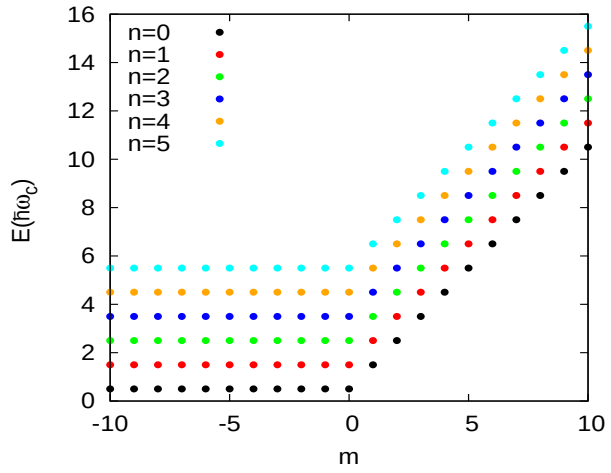

Figure 2-2: Dependence of the lowest six eigenenergies on the angular momentum m and the radial quantum number n when g_{eff} is zero. When $g_{\text{eff}} \neq 0$, the spectrum is rigidly displaced vertically by an amount $-\sigma g_{\text{eff}} \mu_B B/\hbar\omega_c$.

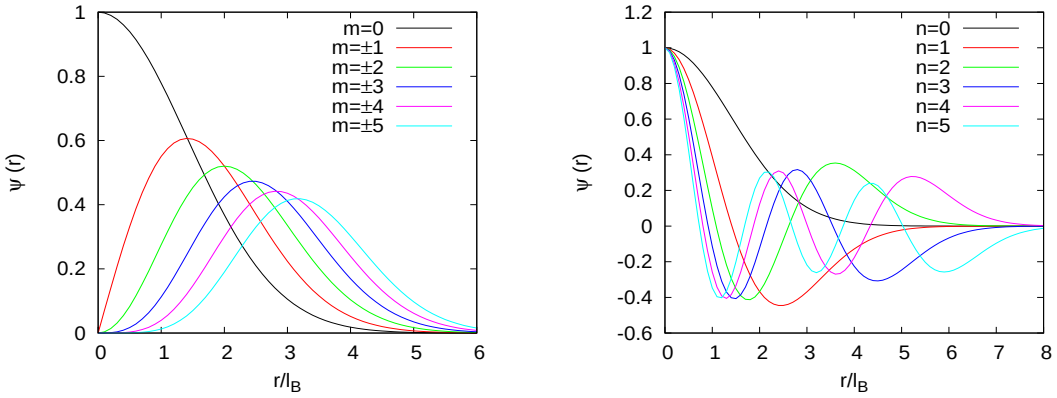

(a) (b)

Figure 2-3: Radial wavefunctions with quantum numbers (a) $n = 0$, various m and (b) $m = 0$, various n.

trapped quantum-mechanically when moving within a DMS. In order to find an analytical solution to the problem, the magnetic field profile and vector potential in the DMS are approximated. We assume that an adjacent superconducting disk expels an applied field perfectly, so that there is no magnetic field passing through the superconductor even at the edge. Therefore, the inhomogeneous magnetic field and corresponding vector potential in a DMS plane are taken to be

$$\vec{B} = \begin{cases} 0 & r < R \\ B\hat{z} & r \geq R \end{cases} \tag{2.9}$$

and

$$\vec{A} = \begin{cases} 0 & r < R \\ B(r^2 - R^2)/2r\hat{\phi} & r \geq R. \end{cases} \tag{2.10}$$

These model fields are used widely in previous related studied [44, 46, 47] since they contain the important physical characteristic of actual fields. Using the effective mass approximation, one can consider a single electron with effective mass m^* moving freely inside the dot region and experiencing the applied field when it is outside. Therefore, the Schrödinger equation equation is given by $\widehat{H}\Psi = E\Psi$, where

$$\widehat{H} = \begin{cases} p^2/2m^* & r < R \\ (\hat{p} + e\vec{A})^2/2m^* - \frac{1}{2}g_{\text{eff}}\mu_B\vec{\sigma}\cdot\vec{B} & r \geq R \end{cases} \tag{2.11}$$

Considering the symmetry of the system, we can again use an angular momentum m and spin σ as good quantum numbers. This is the main reason why we study the Landau levels in the symmetric gauge; it is easy to compare the results of this problem with the Landau levels, whereas using the Landau gauge $(0, Bx, 0)$ gives different good quantum numbers. Similar to the Landau states, the general eigenstates here can be written as

$$\Psi^{\sigma}_{nm}(r, \phi) = e^{im\phi}\psi^{\sigma}_{nm}(r)\chi_{\sigma}. \tag{2.12}$$

Because the magnetic field is a step function, we can consider the solution inside and outside the dot region separately and then match the wavefunctions at the boundary to obtain the eigenenergies. For $r < R$, we use $\nabla^2 = \frac{\partial^2}{\partial r^2} + \frac{1}{r}\frac{\partial}{\partial r} + \frac{1}{r^2}\frac{\partial^2}{\partial \phi^2}$

and find the radial equation:

$$-\frac{\hbar^2}{2m^*}\left[\frac{\partial^2}{\partial r^2}+\frac{1}{r}\frac{\partial}{\partial r}-\frac{m^2}{r^2}\right]\psi^\sigma_{nm}(r)=E\psi^\sigma_{nm}(r)\quad r<R. \tag{2.13}$$

All of the quantities are expressed in the following dimensionless units: $r=\rho\ell_L$, $E=\epsilon\hbar\omega_L$, and $R=\sqrt{s}\ell_L$, where $\omega_L=eB/2m^*$ is the Larmor frequency, half the cyclotron frequency ω_c, and $\ell_L=\sqrt{\hbar/(m^*\omega_L)}$. Then, one can rewrite the radial equation (2.13) as

$$\left[\frac{\partial^2}{\partial\rho^2}+\frac{1}{\rho}\frac{\partial}{\partial\rho}-\frac{m^2}{\rho^2}+2\epsilon\right]\psi^\sigma_{nm}(\rho)=0\quad\rho<\sqrt{s}, \tag{2.14}$$

which has as solutions Bessel functions of order m: $\psi^\sigma_{nm}(\rho)=J_m(\sqrt{2\epsilon}\rho)$ if $\rho<\sqrt{s}$. It is obvious that the inside solutions are independent of spin and only concerned with the kinetic energy of system. For $r\geq R$, after deriving straightforwardly, we find that the Zeeman term can be visualised as a spin-dependent potential as evident in the radial equation:

$$\begin{aligned}\frac{1}{2m^*}\left[-\hbar^2\left(\frac{\partial^2}{\partial r^2}+\frac{1}{r}\frac{\partial}{\partial r}-\frac{m^2}{r^2}\right)+2e\hbar mB\frac{(r^2-R^2)}{2r^2}+(e\vec{A})^2\right]\psi^\sigma_{nm}(r)&\\ -\sigma g_{\rm eff}\mu_B B\psi^\sigma_{nm}(r)\;=\;E\psi^\sigma_{nm}\quad r\geq R\;.&\end{aligned} \tag{2.15}$$

In deriving this, we have used $\sigma_z\chi_\sigma=2\sigma\chi_\sigma$ where σ is $1/2$ and $-1/2$ for spin up and spin down respectively. Then, transforming to dimensionless variables as before, we get

$$\left[\frac{\partial^2}{\partial\rho^2}+\frac{1}{\rho}\frac{\partial}{\partial\rho}-\frac{m_{\rm eff}^2}{\rho^2}-\rho^2+2(\epsilon-m_{\rm eff}+\zeta)\right]\psi^\sigma_{nm}(\rho)=0\quad\rho\geq\sqrt{s}, \tag{2.16}$$

where

$$m_{\rm eff}=m-s, \tag{2.17}$$

and ζ is the Zeeman energy in the unit of $\hbar\omega_L$:

$$\zeta=\sigma g_{\rm eff}\mu_B B/(\hbar\omega_L)=\sigma g_{\rm eff}m^*/m_e. \tag{2.18}$$

To solve (2.16), we introduce $\tilde{\rho}=\rho^2$ so that

$$\left[\tilde{\rho}\frac{\partial^2}{\partial\tilde{\rho}^2}+\frac{\partial}{\partial\tilde{\rho}}+\left(-\frac{\tilde{\rho}}{4}+\beta-\frac{m_{\rm eff}^2}{4\tilde{\rho}}\right)\right]\psi_{nm}^{\sigma}(\tilde{\rho})=0. \tag{2.19}$$

Here, $\beta=(\epsilon-m_{\rm eff}+\zeta)/2$. (2.19) is similar to (2.6) except for the effective angular momentum $m_{\rm eff}$ so that the solution may similarly be expressed by the linear combination of the Kummer-M and Kummer-U functions as discussed in Appendix A. In this case, the Kummer-M function is dropped as it makes the wavefunction infinite as $\tilde{\rho}\to\infty$. Therefore, we obtain the solution:

$$\psi_{nm}^{\sigma}(\rho)=e^{-\rho^2/2}\rho^{|m_{\rm eff}|}U\left(-\beta+\frac{|m_{\rm eff}|}{2}+\frac{1}{2},|m_{\rm eff}|+1,\rho^2\right)\quad\rho\geq\sqrt{s}. \tag{2.20}$$

Actually, (2.20) corresponds to a Landau eigenstate (2.7) in which the angular momentum m is replaced by $m_{\rm eff}$ (note also that these two expressions are presented in different length scales). This is sensible since outside to the magnetic dot electrons travel in a uniform magnetic field. If the superconducting disk disappears (equivalent to setting $s=0$), $m_{\rm eff}$ will become m and the outside solutions will become exactly the Landau eigenstates. Therefore, s is a dimensionless parameter which can be used to describe the system considered. In this calculation, we use it to identify the size of the disk and the magnitude of the external field by

$$s=\left(\frac{R}{\ell_L}\right)^2=\frac{eBR^2}{2\hbar}=\frac{\Phi}{\Phi_0}, \tag{2.21}$$

where Φ is defined by $\Phi=B\pi R^2$ and $\Phi_0=h/e$ is the magnetic flux quantum. In other words, the physical meaning of s is the magnetic flux missing from the dot region in units of Φ_0. Having found the inside and outside solutions, we take into account the boundary condition where the wavefunctions and their first derivatives must be continuous at $\rho=\sqrt{s}$

$$\begin{aligned}\psi_{in}(\epsilon,\rho=\sqrt{s}) &= \psi_{out}(\epsilon,\rho=\sqrt{s})\\ \psi'_{in}(\epsilon,\rho=\sqrt{s}) &= \psi'_{out}(\epsilon,\rho=\sqrt{s})\end{aligned}$$

or

$$\big(\ln\psi_{in}(\epsilon,\rho=\sqrt{s})\big)'=\big(\ln\psi_{out}(\epsilon,\rho=\sqrt{s})\big)'. \tag{2.22}$$

Before using (2.22) to calculate the eigenenergies and eigenfunctions, we can explore their nature roughly by looking at equations (2.14) and (2.16), which describe a one-dimensional radial system with the effective potential $V_{\text{eff}}^{\sigma}(\rho)$ given by

$$V_{\text{eff}}^{\sigma}(\rho) = \begin{cases} \dfrac{m^2}{2\rho^2} & \rho < \sqrt{s} \\ \dfrac{m_{\text{eff}}^2}{2\rho^2} + \dfrac{\rho^2}{2} + m_{\text{eff}} - \zeta & \rho \geq \sqrt{s}. \end{cases} \tag{2.23}$$

Considering $V_{\text{eff}}^{\sigma}(\rho)$ gives us insight into the solutions. Figure 2-4 shows how g_{eff} affects the potential. In the figure, $m^* = 0.5m_e$ and $s = 5$, corresponding to a system with radius $R = 500$ nm and magnetic field $B = 0.026$ T. If g_{eff} is zero, spin up and down electrons are confined in the same potential. As g_{eff} increases, there will be the splitting of the potential outside, leading to a spin-dependent distribution of the eigenfunctions. Let us concentrate on the low energy states of each spin. Figure 2-4 suggests us that spin down eigenstates tend to exist inside the dot region since the Zeeman splitting acts as a barrier to trap them, while spin up eigenstates tend to distribute outside. The dependence of the effective potential on a negative m is shown in figures 2-5 . It shows that when $|m|$ increases, both spin up and spin down states tend to distribute increasing away from the origin (one gets the same behaviour for positive m). This behaviour is also found in Landau eigenstates (see figure 2-3 (a)).

Finally, according to figure 2-4, when g_{eff} is very large (as shown in the Introduction, this can have values up to 600), we expect that the Zeeman energy is the most dominant term. In this limit, it can be approximated as a hard wall potential which can completely trap spin down electrons inside the dot region and completely exclude spin up electrons to outside. In what follows, we will consider spin-dependent confinement in the ideal case where the Zeeman term is extremely large.

(i) The ideal case for spin down

In this case, we have that a spin down electron with effective mass m^* moves freely in the circular billiard consisting of a boundary with a circular hard wall. Thus, we can take for the Hamiltonian

$$\widehat{H}_{\downarrow} = \begin{cases} p^2/2m^* & r < R \\ \infty & r \geq R. \end{cases} \tag{2.24}$$

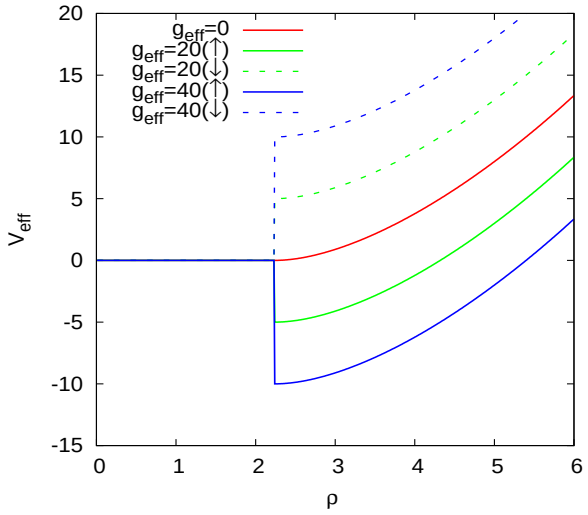

Figure 2-4: The spin dependent effective potential plotted as a function of the dimensionless length $\rho = r\ell_L$ for $m = 0$, $m^* = 0.5m_e$, $s = 5$, and various values of g_{eff}. Solid lines represent the spin up potentials, while dashed lines represent the spin down potentials.

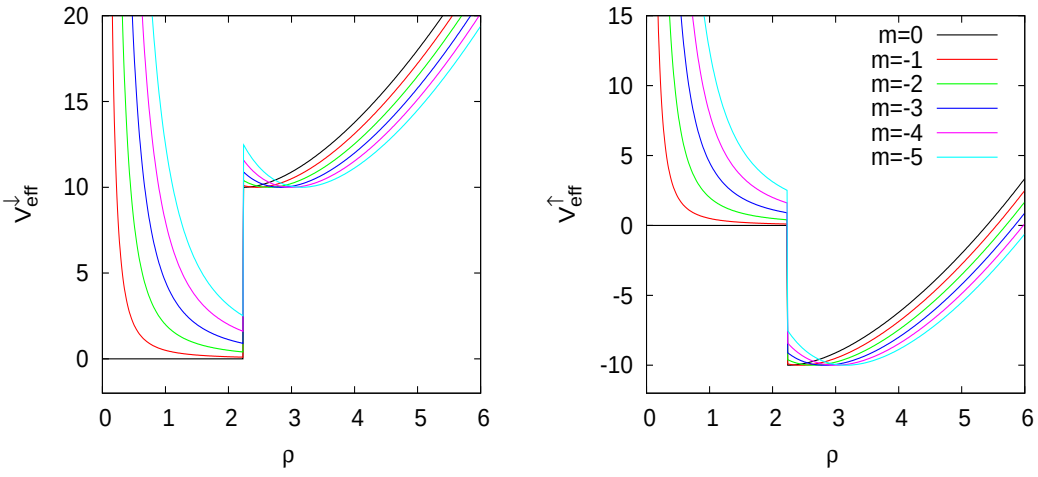

(a) (b)

Figure 2-5: (a) The spin down and (b) spin up effective potential plotted as a function of the dimensionless length $\rho = r\ell_L$ for $m^* = 0.5m_e$, $s = 5$, $g_{\text{eff}} = 40$, and various values of m.

Expressing all of the parameters in the same units as before and using the boundary condition $\psi(r = R) = 0$, we obtain the eigenvalues and eigenfunctions as

$$\epsilon^{\downarrow}_{nm} = \alpha^2_{nm}/(2s) \tag{2.25}$$

and

$$\psi^{\downarrow}_{nm}(\rho) = J_m(\rho\sqrt{2\epsilon^{\downarrow}_{nm}}), \tag{2.26}$$

where α_{nm} is the n^{th} zero of Bessel functions J_m. Due to the property $J_{-m}(x) = (-1)^m J_m(x)$, it is clear that the zeroes of $J_{-m}(x)$ are similar to those of $J_m(x)$ and results in the ideal spin down energies being two-fold degenerate ($\epsilon^{\downarrow}_m = \epsilon^{\downarrow}_{-m}$).

(ii) The ideal case for spin up

For the spin up case, although an electron is perfectly scattered by the Zeeman hard wall, they will still occupy bound states which are confined by the magnetic field and corresponding vector potential outside the dot. The Hamiltonian is given by

$$\widehat{H}_{\uparrow} = \begin{cases} \infty & r < R \\ (\hat{p} + e\vec{A})^2/2m^* - \dfrac{1}{2} g_{\text{eff}} \mu_B \sigma_z B & r \geq R. \end{cases} \tag{2.27}$$

Expressing all of the parameters in the same units as before and using the boundary condition $\psi(r = R) = 0$, we obtain the eigenvalues and eigenfunctions

$$\epsilon^{\uparrow}_{nm} = -2\eta_n + |m_{\text{eff}}| + m_{\text{eff}} + 1 - \zeta \tag{2.28}$$

and

$$\psi^{\uparrow}_{nm}(\rho) = e^{-\rho^2/2} \rho^{|m_{\text{eff}}|} U\left(-\beta + \frac{|m_{\text{eff}}|}{2} + \frac{1}{2}, |m_{\text{eff}}| + 1, \rho^2\right), \tag{2.29}$$

where, $\beta = (\epsilon^{\uparrow}_{nm} - m_{\text{eff}} + \zeta)/2$ and η_n is the n^{th} zero of the Kummer-U function, satisfying $U(\eta_n, |m_{\text{eff}}| + 1, s) = 0$. If the Landau levels (2.8) are expressed in units of $\hbar\omega_L$, one has the Landau quantisation: $E^{\sigma}_{nm}/(\hbar\omega_L) = 2n + |m| + m + 1 - \zeta$ which resembles the expression (2.28). This is the result of the circular Zeeman hard wall perturbing the system of an electron in a uniform field.

2.3 Spin dependent localisation

Having considered the general nature and limiting character of electron states in a magnetic quantum dot in a DMS, we now present numerical results for the eigenenergies and eigenstates. First, we consider the case where g_{eff} is extremely large and compare them with the solutions in the ideal cases. Matching the wavefunctions by using the boundary conditions (2.22), we obtain the spin-dependent spectrum shown in figure 2-6 and 2-7, where $g_{\text{eff}} = 500$, $s = 5$, and $m^* = 0.5m_e$. The corresponding spin-polarised eigenstates are shown in figure 2-8 (a) and (b).

We see that the two ideal models considered above provide a good approximation to the energy spectrum in this case especially when $|m|$ is small for spin down and $|m|$ is big for spin up. As expected, the giant Zeeman potential traps spin down eigenstates inside the dot region (see figure 2-8 (b)) and results in nearly two-fold degeneracy of spin down energies, $\epsilon_m^{\downarrow} \approx \epsilon_{-m}^{\downarrow}$ seen in figure 2-7. The spin up eigenstates exhibit a very different spatial distribution, seen in figure 2-8 (a). They distribute mostly outside the dot region. From now on, we will describe states which distribute mostly inside the dot region as "quantum dot states" and states which distribute mostly outside as "quantum antidot states". Of course, the spin up antidot states will experience mostly the constant field so that their eigenenergies would be expected to be close to Landau levels: $E_{nm}^{\sigma}/(\hbar\omega_L) = 2n + |m| + m + 1 - \zeta$, especially the states with large $|m|$ which are localised far from the origin. However, we find that as $|m|$ increases, the eigenenergies approach the Landau levels with m replaced by m_{eff}: $E_{nm_{\text{eff}}}^{\sigma}/(\hbar\omega_L) = 2n + |m_{\text{eff}}| + m_{\text{eff}} + 1 - \zeta$. In other words, the existence of the superconducting disk shifts the normal Landau levels to be the Landau levels with m_{eff}. This is surprising because the electrons that occur far from the dot region cannot feel the magnetic flux missing due to the disk and their energies might therefore be expected to be the normal Landau levels. However, the Schrödinger equation which governs the energies also contain the vector potential, and this is modified by the presence of the disk even at large distances.

We now consider smaller values of g_{eff}, which lead to Zeeman interactions that are insufficient to completely confine charge carriers. Figure 2-9 shows the spectrum obtained for different g_{eff}. When g_{eff} is zero (figure 2-9 (c)), every confined state is independent of the Zeeman term, resulting in two-fold degeneracy

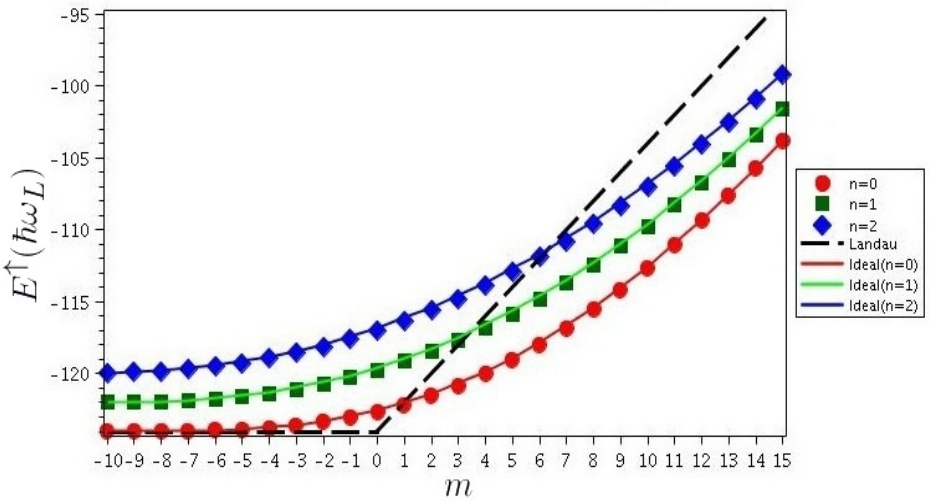

Figure 2-6: Comparison of the lowest three spin up eigenenergies (points) and the ideal spin up energies (lines) with angular momentum m when g_{eff} is 500, $s = 5$, and $m^* = 0.5m_e$. The black dashed line represents the spin up ground states of the Landau levels ($E^{\uparrow}_{n=0}$).

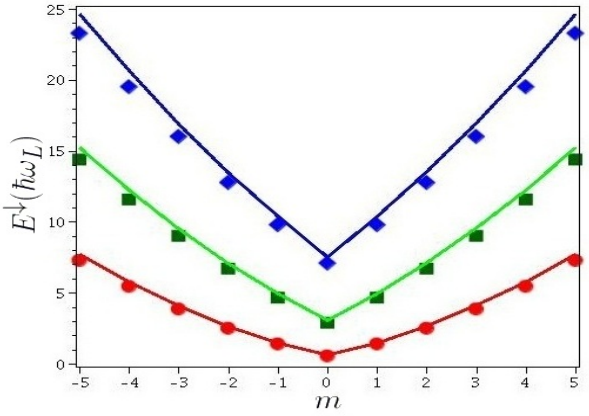

Figure 2-7: Comparison of the lowest three spin down eigenenergies (points) and the ideal spin down energies (lines) with angular momentum m when g_{eff} is 500, $s = 5$, and $m^* = 0.5m_e$.

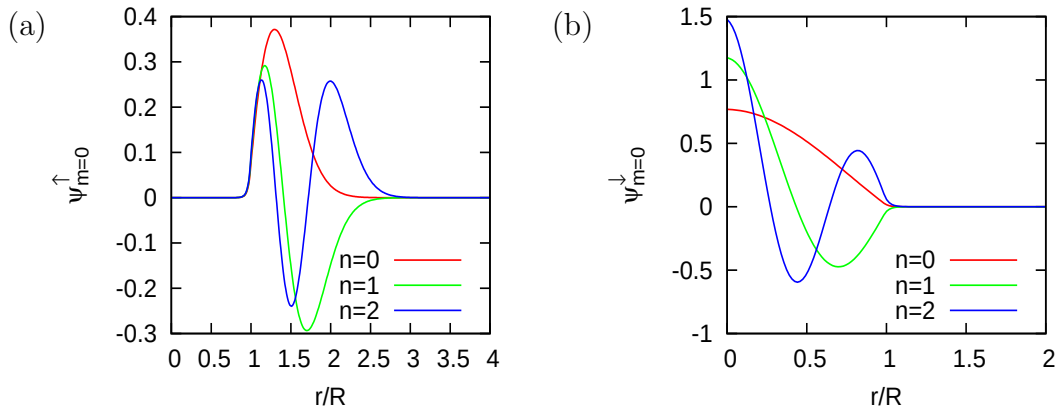

Figure 2-8: Radial wavefunctions corresponding to the lowest three eigenstates with $m = 0$ for (a) spin up and (b) spin down, calculated by g_{eff}=500, $s = 5$, and $m^* = 0.5m_e$.

($E^{\uparrow}_{nm} = E^{\downarrow}_{nm}$). The spectrum in this case can coincide with that of electrons in a magnetic dot in a conventional semiconductor as studied by [44, 46, 47, 48]. A non-vanishing g_{eff} makes spin up and spin down eigenenergies different. For large $|m|$, it clearly lowers the energy levels of the spin up states, but raises the levels of spin down states. We see each spectrum consists of many energy patterns. These reflect the spatial distribution of the bound states, and are discussed in the following.

Spin down eigenstates can be divided into three kinds: quantum dot, intermediate, and Landau-like states. Examples of quantum dot states are shown in figure 2-10 (a). They are normally found when $|m|$ and n are sufficiently small, attracted to the quantum dot area by the Zeeman potential. Looking at the effective potential $V^{\downarrow}_{\text{eff}}$ with $g_{\text{eff}} = 40$ in figure 2-4, we expect that the bound states whose energies are less than 10 $\hbar\omega_L$ are quantum dot states distributing mostly inside the dot region and decay outside. This is the reason why the spin down eigenenergies which are less than 10 $\hbar\omega_L$ in the figure 2-9 (e) are nearly two-fold degenerate ($\epsilon^{\downarrow}_{m} \approx \epsilon^{\downarrow}_{-m}$) like the spin down eigenenergies in figure 2-7. Examples of Landau-like states are shown in figure 2-10 (c). They are found when $|m|$ is large enough and occur overwhelmingly outside the dot, where the magnetic field is uniform. Their energy levels are close to the Landau levels with m_{eff}. As seen in figure 2-9 (d) and (e), the energy levels that become nearly constant with increasingly negative m present an energy spectrum reminiscent of Landau-like

states. Finally, looking at the effective potential $V_{\text{eff}}^{\downarrow}$ with $g_{\text{eff}} = 40$ in figure 2-4, we expect that states whose energy is greater than 10 $\hbar\omega_L$ will extend over the region both inside and outside the dot. This is the distribution of intermediate states, which are normally found when n is sufficiently large and $|m|$ is sufficiently small, as shown in figure 2-10 (b). It is difficult to predict the energy spectrum of this kind of states because of their spatial distribution.

Spin up eigenstates can also be divided into three kinds: quantum antidot, intermediate, and Landau-like states. Intermediate and Landau-like states are shown in figure 2-11 (b) and (c). They behave like those previously discussed and give energy spectra similar to those in the spin down eigenenergies. Quantum antidot states are found when $|m|$ and n are sufficiently small. Looking at the effective potential $V_{\text{eff}}^{\uparrow}$ with $g_{\text{eff}} = 40$ in figure 2-5 (b), we expect that bound states whose energies are negative will distribute outside and decay when they extend into the Zeeman barrier. Examples of these are shown in figure 2-11 (a). They distribute mostly outside like Landau-like states, but are strongly perturbed by the Zeeman potential. In the absence of the superconductor, the Landau states with $m = 0$ do not vanish at the origin, while the states with large $|m|$ will extend far from the origin as shown in figure 2-3. With the superconductor present, states with $m = 0$ are strongly perturbed and pushed by the Zeeman potential to the region outside, resulting in quantum antidot states, while states with large $|m|$ are also perturbed, but the perturbation is weak and these result in Landau-like states. We notice that the energy spectrum of the quantum antidot states in figure 2-9 (a) and (b) is not linear in m like that in figure 2-6.

In this section, we have studied electron states in a magnetic quantum dot in a DMS. The Zeeman energy plays a key role in spin dependant confinement. It leads to spin dependent states which exhibit different spatial distribution. For very large g_{eff}, the ideal models, where the Zeeman term acts as a hard wall potential, are good approximation to the spin up and spin down solutions. The spin up eigenstates are confined by the magnetic field, and extend mostly outside the dot. On the other hand, the spin down eigenstates are confined inside the dot region by the Zeeman hard wall like a quantum billiard system. For smaller g_{eff}, we find that the energy spectrum consists of many energy patterns concerning the distribution of the eigenfunctions. Considering the effective potential, we can classify the spin up and spin down eigenstates by their distribution.

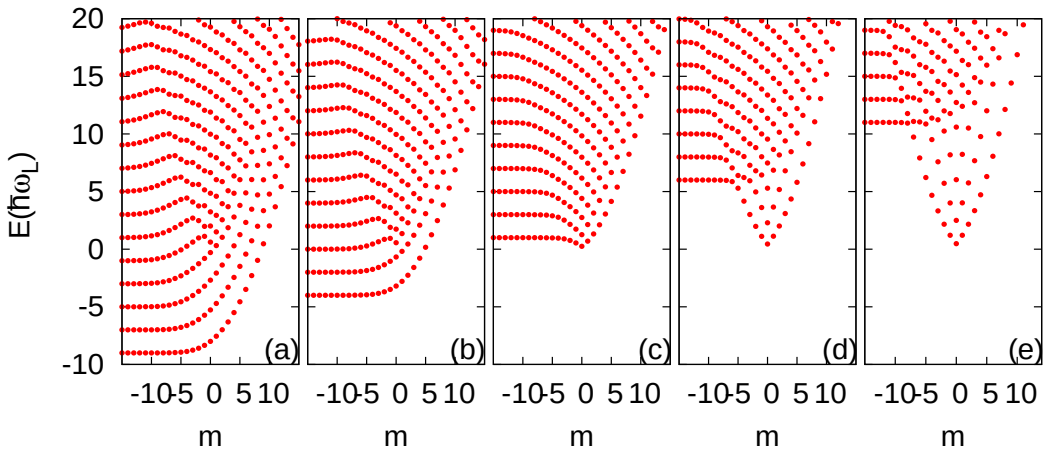

Figure 2-9: The spin dependent energy spectrum for $s = 5$, $m^* = 0.5m_e$, and several values of g_{eff}. (a) $E^{\uparrow}$ with $g_{\text{eff}} = 40$, (b) $E^{\uparrow}$ with $g_{\text{eff}} = 20$, (c) $E^{\uparrow}$ and $E^{\downarrow}$ with $g_{\text{eff}} = 0$, (d) $E^{\downarrow}$ with $g_{\text{eff}} = 20$, and (e) $E^{\downarrow}$ with $g_{\text{eff}} = 40$.

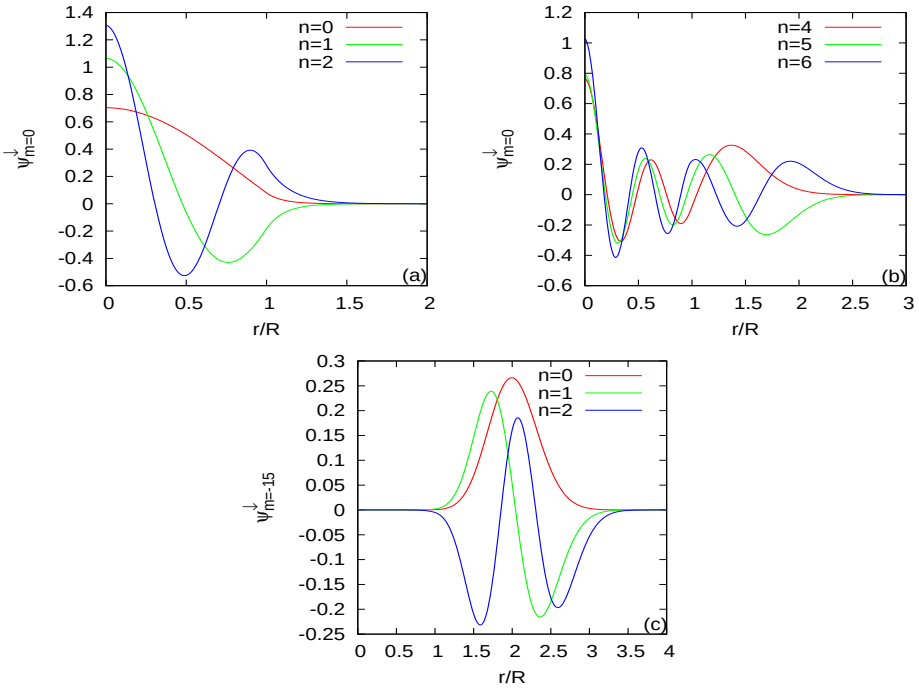

Figure 2-10: The distribution of spin down radial wavefunctions: (a) quantum dot, (b) intermediate, and (c) Landau-like states, when g_{eff} is 40, $s = 5$, and $m^* = 0.5m_e$.

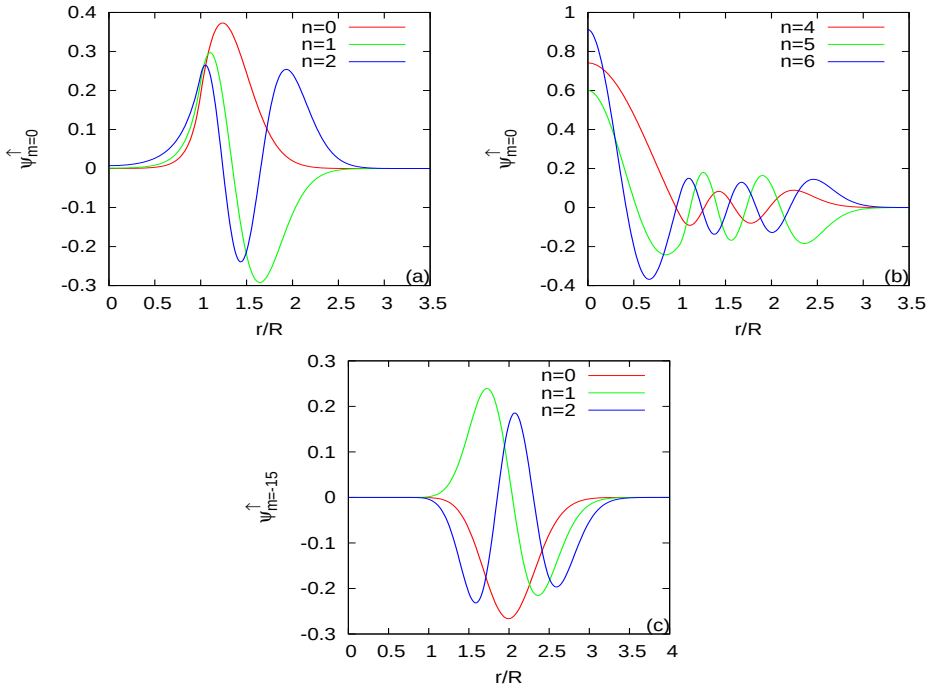

Figure 2-11: The distribution of spin up radial wavefunctions: (a) quantum antidot, (b) intermediate, and (c) Landau-like states, when g_{eff} is 40, $s = 5$, and $m^* = 0.5m_e$.

2.4 Semiclassical interpretation

In order to describe the magnetically confined quantum states in a DMS intuitively, we now turn to a semiclassical approach. In a DMS where g_{eff} is very large, the motion of electrons cannot be characterised by straight paths and classical orbits as shown in figure 2-1 (b). The giant Zeeman interaction acts as a hard wall potential. As a result, spin down confinement can be considered as the problem of a circular billiard, which has been studied by many authors [50, 51, 52]. They have found that the classical trajectories of the electron in the billiard consist of straight line segments visualised in figure 2-12. However, a spin up electron will feel a different Zeeman potential, and be confined outside. Possible trajectories in this case are sketched in figure 2-13 (a); the electron may travel as a classical orbit far from the dot, move around the dot, or form a skipping orbit (in which it repeatedly hits the dot and is reflected). In this section, the relation between

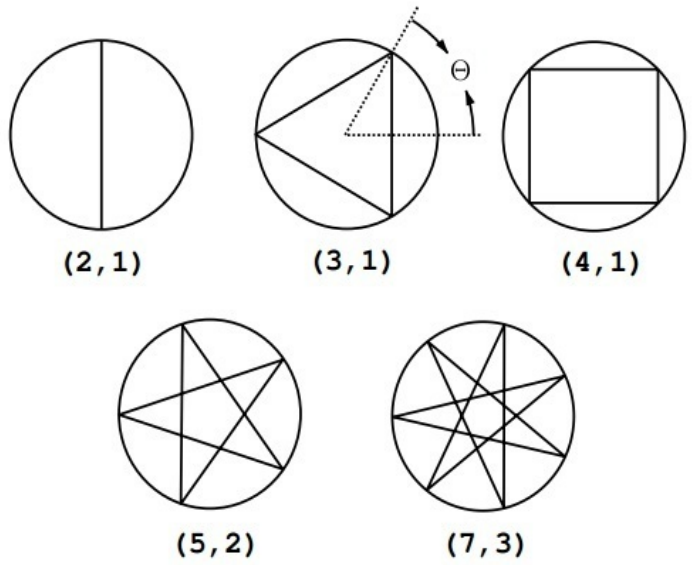

Figure 2-12: Classical periodic trajectories of a particle in the circle billiard consisting of a boundary with a circular hard wall. Each trajectory is described by (m_r, m_φ) where m_r is the number of sides of the polygons and m_φ is the number of turns around the centre. Θ is given by $\Theta = \pi m_\varphi / m_r$. From Ref. [50]

spin up trajectories and quantum eigenstates is presented semiclassically.

The classical motion of a spin-up electron can be described by 2 parameters, γ and σ, corresponding to the distance from the origin to the centre of a cyclotron orbit (the radius of the guide centre), and the radius of the orbit respectively (see figure 2-13 (b)). Here, the semiclassical approach of C. S. Lent [53] is modified to describe our quantum results. The key idea is to define two new quantum operators whose eigenvalues represent γ and σ. First, we recall the equations of the circular motion describing an electron in a uniform magnetic field [54]:

$$x = x_0 - R_c \sin(\omega_c t), \tag{2.30}$$

$$y = y_0 + R_c \cos(\omega_c t), \tag{2.31}$$

where (x_0, y_0) represents the centre of a cyclotron orbit, R_c is the orbital radius, and ω_c is the cyclotron frequency. The x and y components of the velocity can be obtained by differentiating equation (2.30) and (2.31) with respect to time.

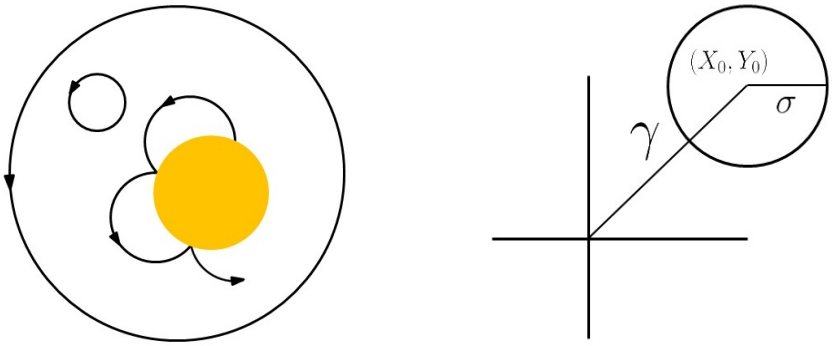

(a) (b)

Figure 2-13: (a) Possible classical trajectories of spin up electrons. The yellow circle represents the superconducting disk. (b) A cyclotron orbit described by 2 physical quantities; the guide centre of the classical orbit γ, and cyclotron radius σ.

We then can define quantum operators straightforwardly,

$$\hat{x}_0 = x - \frac{\hat{v}_y}{\omega_c}, \tag{2.32}$$

$$\hat{y}_0 = y + \frac{\hat{v}_x}{\omega_c}, \tag{2.33}$$

where $\hat{v}_x$ and $\hat{v}_y$ are velocity operators, and the position operators are just coordinates in position space, $\hat{x} = x$ and $\hat{y} = y$. Unfortunately, the Hamiltonian (2.11) does not commute with these operators, $\hat{x}_0$ and $\hat{y}_0$, so the positions of the orbital centres and the energies cannot be known simultaneously. Therefore, we define a further operator:

$$\widehat{\Gamma}^2 = \hat{x}_0^2 + \hat{y}_0^2 = r^2 + \left(\frac{\hat{v}}{\omega_c}\right)^2 + \frac{1}{\omega_c}(y\hat{v}_x + \hat{v}_x y - x\hat{v}_y - \hat{v}_y x), \tag{2.34}$$

whose eigenvalues are γ^2. Using the canonical momentum, $\vec{p} = m^*\vec{v} - e\vec{A}$, and the vector potential of the magnetic quantum dot, $\vec{A} = B(r^2 - R^2)/2r\hat{\phi}$, for $r > R$, we obtain the velocity operators

$$\hat{v}_x = \frac{1}{m^*}\left[\hat{p}_x - \frac{e}{2}B_y\left(1 - \frac{R^2}{r^2}\right)\right], \tag{2.35}$$

$$\hat{v}_y = \frac{1}{m^*}\left[\hat{p}_y + \frac{e}{2}B_x\left(1 - \frac{R^2}{r^2}\right)\right]. \tag{2.36}$$

Now, one can see easily that $[\hat{v}_x, y] = 0$ and $[\hat{v}_y, x] = 0$. Then, we use the commutation relation, (2.35), and (2.36) to rewrite the operator $\widehat{\Gamma}^2$ as

$$\begin{aligned}
\widehat{\Gamma}^2 &= r^2 + \left(\frac{\hat{v}}{\omega_c}\right)^2 + \frac{2}{\omega_c}(y\hat{v}_x - x\hat{v}_y) \\
&= \left(\frac{\hat{v}}{\omega_c}\right)^2 + \left(\frac{-2\widehat{L}_z}{eB} + R^2\right) \\
&= \frac{2m^*}{(eB)^2}\frac{(\hat{p} + e\vec{A})^2}{2m^*} + R^2 - \frac{2\widehat{L}_z}{eB},
\end{aligned} \tag{2.37}$$

where $\widehat{L}_z = x\hat{p}_y - y\hat{p}_x$ is the z component of an angular momentum operator. Because the operator $\widehat{\Gamma}^2$ commutes with the ideal spin up Hamiltonian (2.27), for large g_{eff} we can use the spin up eigenstates of the Hamiltonian (2.11) to approximate the value of γ^2 as

$$\begin{aligned}
\gamma^2 \approx \left\langle \Psi^{\uparrow}_{nm} \middle| \widehat{\Gamma}^2 \middle| \Psi^{\uparrow}_{nm} \right\rangle &= \left(\epsilon^{KE}_{nm}\hbar\omega_L\right)\frac{2m^*}{(eB)^2} + R^2 - \frac{2m\hbar}{eB} \\
&= \left(\frac{\epsilon^{KE}_{nm}}{2} + s - m\right)\ell_L^2,
\end{aligned} \tag{2.38}$$

where $\Psi^{\uparrow}_{nm}$ are the eigenstates of the Hamiltonian (2.11), s is the magnetic flux missing, defined in (2.21), and ϵ^{KE}_{nm} are the expectation values of kinetic energies in the unit of $\hbar\omega_L$, given by

$$\begin{aligned}
\epsilon^{KE}_{nm} &= \frac{1}{\hbar\omega_L}\left\langle \Psi^{\uparrow}_{nm} \middle| \frac{(\hat{p} + e\vec{A})^2}{2m^*} \middle| \Psi^{\uparrow}_{nm} \right\rangle \\
&= \frac{1}{\hbar\omega_L}\left\langle \Psi^{\uparrow}_{nm} \middle| \widehat{H} + \frac{1}{2}g_{\text{eff}}\mu_B\vec{\sigma}\cdot\vec{B} \middle| \Psi^{\uparrow}_{nm} \right\rangle \\
&\approx \epsilon^{\uparrow}_{nm} + \frac{1}{\hbar\omega_L}\left(\frac{1}{2}g_{\text{eff}}\mu_B B\right) = \epsilon^{\uparrow}_{nm} + \zeta,
\end{aligned} \tag{2.39}$$

where, $\epsilon^{\uparrow}_{nm}$ are the eigenenergies of the Hamiltonian (2.11). In deriving this, we assume that the normalised $\Psi^{\uparrow}_{nm}$ distribute mostly outside the dot region where $B(r)$ is constant; therefore, $\int \left|\Psi^{\uparrow}_{nm}\right|^2 B(r) d^2\vec{r} \approx B$. In the same way, we can find

the semiclassical cyclotron radius by constructing the operator:

$$\widehat{\Sigma}^2 = (x - \hat{x}_0)^2 + (y - \hat{y}_0)^2 . \tag{2.40}$$

Its eigenvalues, σ^2, can be approximated as

$$\sigma^2 = \left(\epsilon_{nm}^{KE}/2\right) \ell_L^2. \tag{2.41}$$

In the limit of large $|m|$, where the eigenenergies $\epsilon_{nm}^{\uparrow}$ approach the Landau levels with m_{eff}, $E_{n,m_{\text{eff}}}^{\uparrow}/\left(\hbar\omega_L\right) = 2n + |m_{\text{eff}}| + m_{\text{eff}} + 1 - \zeta$, the kinetic energies will be independent of the Zeeman term ζ, $\epsilon_{nm}^{KE} \approx 2n + |m_{\text{eff}}| + m_{\text{eff}} + 1$. As a result, we have

$$\gamma = \ell_L \sqrt{n + \frac{1}{2}} \quad \text{and} \quad \sigma = \ell_L \sqrt{n + \frac{1}{2} + m_{\text{eff}}} \tag{2.42}$$

for large positive m, while

$$\gamma = \ell_L \sqrt{n + \frac{1}{2} - m_{\text{eff}}} \quad \text{and} \quad \sigma = \ell_L \sqrt{n + \frac{1}{2}} \tag{2.43}$$

for large negative m. Notice that γ for positive m and σ for negative m are not functions of m_{eff}. In the quantum mechanical calculations, we saw wavefunctions that extended further from the origin with increasing values of $|m|$. The two above equations (2.42) and (2.43) can also describe this behaviour by using the guide center γ and cyclotron radius σ as sketched in figure 2-13 (b). For a certain value of n, equation (2.42) shows that a classical electron with increasingly positive m will move further from the origin by increasing values of σ, while equation (2.43) shows that the electron with increasingly negative m will move further by increasing values of γ. The difference between the behaviour of positive and negative $|m|$ states can be seen by classical orbits, but quantum wavefunctions cannot illustrate this difference. This is an example of using the parameters γ and σ to describe magnetically confined quantum states. Next, the probability current density will be discussed. We then study the relation between the probability current density and a classical orbit described by γ and σ.

The probability current density.

A continuity equation is an equation concerning the transport of a conserved quantity, such as mass, energy, and, electric charge. In electrodynamics, it is

used to describe the flow of electric charge (electric current) through surfaces from one region of space to another. In quantum mechanics, in non-dissipative single particle systems the probability to find a particle is conserved, so we can also use it to calculate the probability (particle) current density of each eigenstate [55], with

$$\begin{aligned}\vec{j}_{nm} &= \frac{i\hbar}{2m^*}(\Psi_{nm}\vec{\nabla}\Psi^*_{nm} - \Psi^*_{nm}\vec{\nabla}\Psi_{nm}) + \frac{1}{m^*}e\vec{A}|\Psi_{nm}|^2 \\ &= \frac{\hbar}{m^*\ell_L}\left[\frac{m}{\rho} + \Theta(\rho - \sqrt{s})\left(\rho - \frac{s}{\rho}\right)\right]|\psi_{nm}(\rho)|^2\hat{\phi}, \end{aligned} \tag{2.44}$$

where Θ is the Heaviside step function. In deriving this, we have used the eigenfunctions (2.12) and the vector potential (2.10). Notice that only a ϕ component of the current exists; the particle current density is simply clockwise or counterclockwise circulation around the origin.

A clear correspondence that exists between the current densities of the spin up eigenstates of the Hamiltonian (2.11) and classical orbits determined by the guiding centre (2.38) and cyclotron radius (2.41) is illustrated in figures 2-14, and 2-15. When m is large and negative, the particle current density flows both counterclockwise and clockwise directions as shown in figure 2-14 (a) and (b), while the corresponding classical electron moves as a cyclotron orbit. We notice that the parameter γ is a good approximation to the border separating these two directions of the current density. In figure 2-14 (c) and (d), as m becomes less negative, we find the cyclotron orbit moves closer to the dot. Because a classical electron cannot tunnel into the dot, it cannot complete the circular orbit. Instead, the electron will be repeatedly reflected at the edge of the dot. This trajectory is normally called a skipping orbit [56, 57], resulting in a reduced amount of clockwise current density.

The current density with non-negative m only flows in counterclockwise direction as illustrated in figure 2-15. Figure 2-15 (a)-(c), depicts the corresponding orbits which are skipping orbits. We notice that there is no intersection between the circles of the orbits outside the dot region. This leads to the one-way current density. As m increases, the radius of the cyclotron orbit is large enough to fully enclose the dot to form the counterclockwise current density as illustrated in figure 2-15 (d).

To summarise, cyclotron and skipping orbits have been used to describe the probability current densities of the eigenstates. For sufficiently large $|m|$, cyclotron orbits are found. Depending on the the values of γ and σ, the orbits can depict two-way current density when m is negative, and one-way current density when m is positive. For sufficiently small $|m|$, skipping orbits are found. Depending on the the values of γ and σ, the orbits can depict two-way current density when m is negative, and one-way current density when m is non-negative.

2.5 Summary

To conclude, in this Chapter we have considered a model used to describe electrons in a magnetic quantum dot in a DMS. The giant g-factor can enhance the Zeeman energy and results in spin dependent states which exhibit different spatial distribution. For very large g_{eff}, spin up and spin down solutions can be approximated as those of ideal models for which analytical solutions exist. Spin up eigenstates extend mostly outside the dot, while spin down eigenstates are strongly confined inside. For smaller g_{eff}, we find that the energy spectrum consists of many energy patterns. We classify the spin dependent eigenstates by considering the effective potential and find that the distribution of the eigenstates is related to the energy spectrum. The magnetically confined states in a DMS are described intuitively by using a semiclassical approach. Cyclotron and skipping orbits are used to describe the probability current densities of the eigenstates. They can depict how a classical electron forms one-way and two-way current densities.

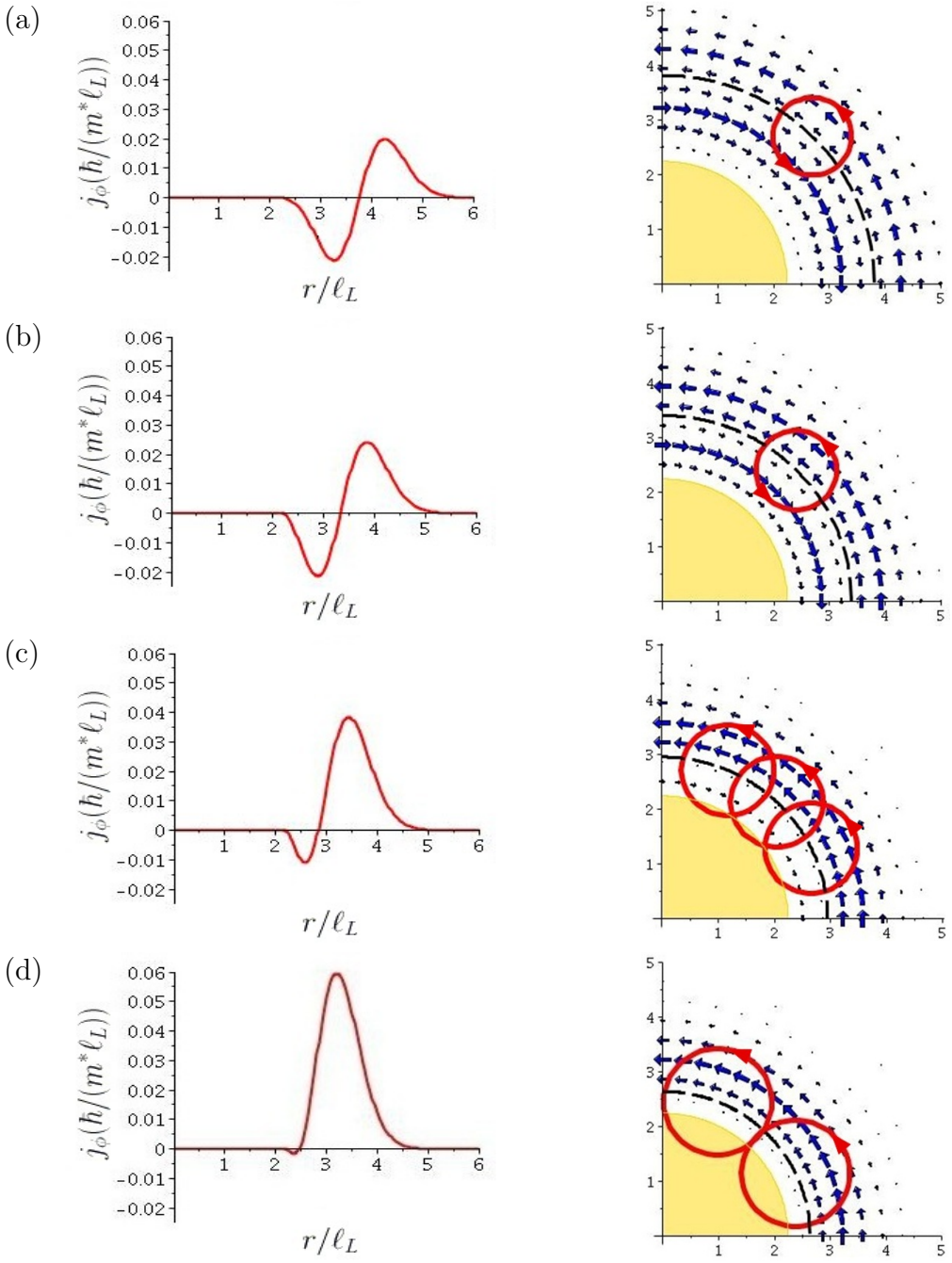

Figure 2-14: On the left, the particle current densities of the eigenstate $\Psi^{\uparrow}_{n=0,m}$ with m= −9 (a), −6 (b), −3 (c), and −1 (d). On the right, corresponding classical trajectories (red circles) are superimposed upon the particle current density illustrated as a vector field (blue arrows). The quadrant of yellow circles show the area from which the magnetic field is excluded. The dashed lines show guide-centre radii γ. Here, the magnetic flux missing s is 5, g_{eff}=500, and the length scale is measured in units of ℓ_L.

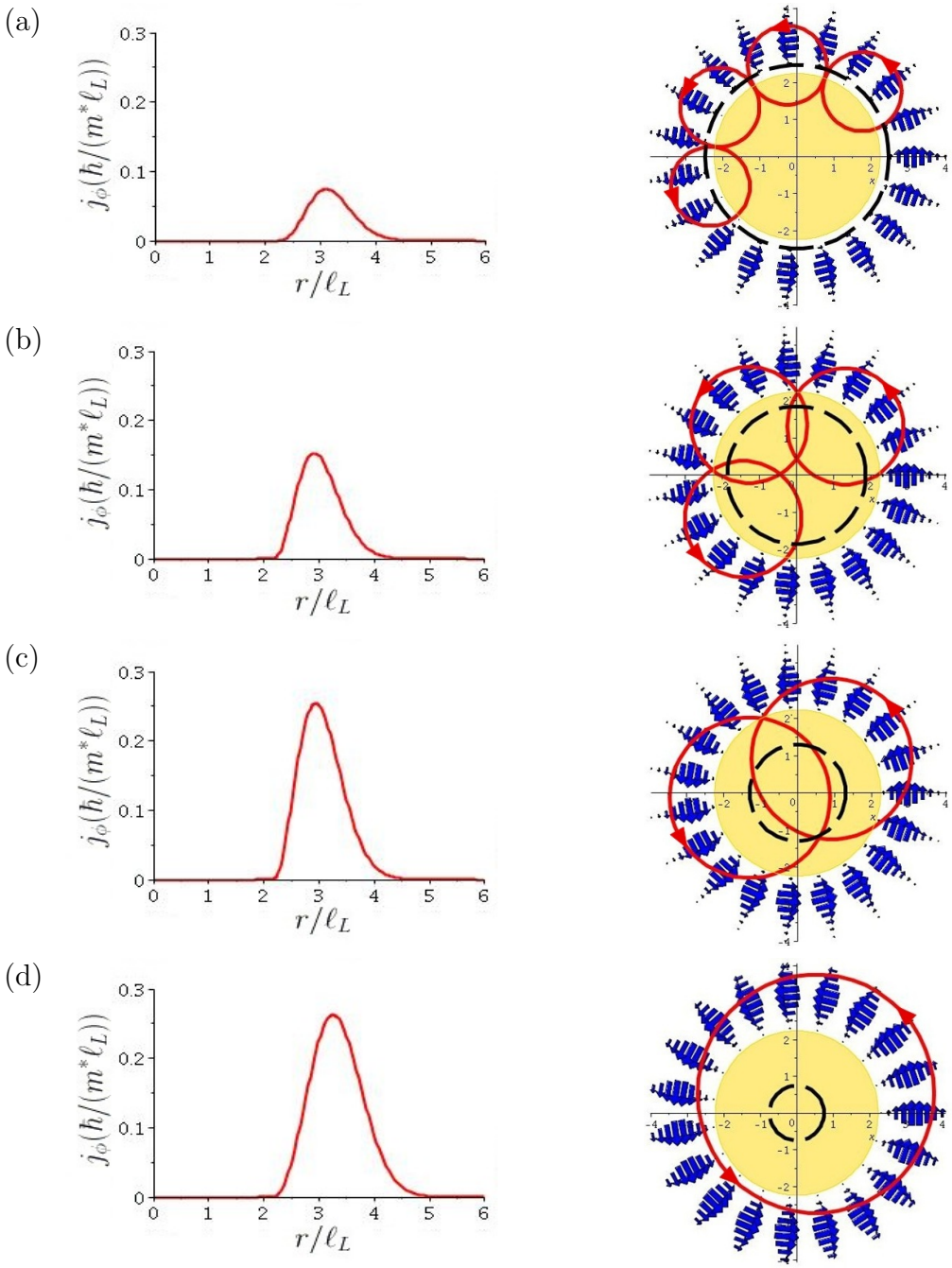

Figure 2-15: On the left, the particle current densities of the eigenstate $\Psi^{\uparrow}_{n=0,m}$ with m= 0 (a), 4 (b), 10 (c), and 15 (d). On the right, corresponding classical trajectories (red circles) are superimposed upon the particle current density illustrated as a vector field (blue arrows). The yellow circles show the area from which the magnetic field is excluded. The dashed lines show guide-centre radii γ. Here, the magnetic flux missing s is 5, g_{eff}=500, and the length scale is measured in units of ℓ_L.

Chapter 3

Magnetic templating by a superconducting disk

In the previous Chapter, a model describing the heterostructure of a DMS and a superconductor in a magnetic field was explored. The simplicity of the magnetic field model used allowed analytical solutions. Moreover, the beauty of this model is that the particle current density in quantum mechanics can be envisioned by a trajectory of a classical particle. Although a similar description of the magnetic field has been widely used [43, 44, 46, 47, 48], in reality it is not such a good approximation to the actual field. As discussed before, one consequence is that the eigenenergies with large angular momentum tend towards the Landau levels with effective quantum number m_{eff} instead of approaching the normal Landau levels. That means using the model may give rise to a large error when m is significantly different from m_{eff}, such as when the superconducting disk is large.

In this Chapter, we will seek to use a more realistic magnetic field profile to improve a description the eigenstates far from the disk. In this regard, it must be noted that the magnetic field cannot be simplified as in the previous calculation because it does not satisfy conservation of the magnetic flux. Another important point is the direction of the field. Not only the normal component but also the radial component of the field is expected to influence the system. The Zeeman energy due to the normal component can be considered as a spin dependent potential, while the radial component will change the symmetry of the system. The new symmetry means one cannot study spin dependent eigenstates; each state will consist of spin up and spin down components. The effect of the Zeeman

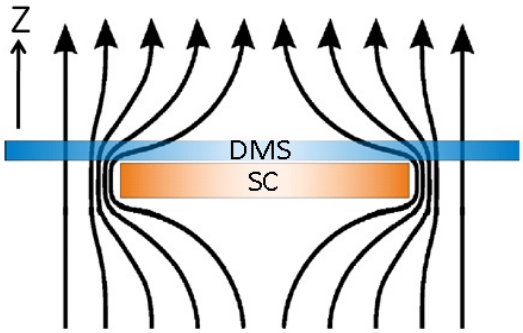

Figure 3-1: A sketch of the magnetic field around a superconductor.

energy is now complicated. In order to get further insight, we need to study the problem systematically.

3.1 Magnetic field profile

The expulsion of a magnetic field is a phenomenon which is found in a Meissner state of a superconductor. Because the magnetic flux is a conserved quantity, if the magnetic field distributing inside a superconductor is expelled, it will enhance the field distributing outside. For an ideal superconductor where the external field is expelled perfectly, one could expect the magnetic field to concentrate at the superconducting edge as sketched in figure 3-1.

In this calculation, we will find the vector potential $\vec{A}$ and the corresponding magnetic field, $\vec{B} = \vec{\nabla} \times \vec{A}$, outside the superconducting disk by solving the Maxwell equations

$$\begin{aligned} \vec{\nabla} \cdot \vec{B} &= 0, \\ \vec{\nabla} \times \vec{B} &= 0. \end{aligned} \tag{3.1}$$

The sample is assumed to be very thin and act as a perfect diamagnetic material. Choosing the cylindrical coordinate (r, ϕ, z), and placing the disk with radius R on $z = 0$ plane in the applied magnetic field $B_a\hat{z}$, we have the conditions: $B_z(r < R, z = 0) = 0$ and $B_\phi = 0$ everywhere. Both the Maxwell equations above can be expressed by a single equation $\nabla^2\phi = 0$, where ϕ is the magnetic

scalar potential ($\vec{B} = -\vec{\nabla}\phi$). The solution of this equation with the present boundary conditions was considered by Morse and Feshbach [58]. From their result, we can find the magnetic field through $B_z = -\frac{\partial \phi}{\partial z}$ and $B_r = -\frac{\partial \phi}{\partial r}$ to obtain [45]

$$\frac{B_z}{B_a} = 1 + \frac{2}{\pi}\left[\frac{\xi}{\xi^2+\eta^2} - \arctan\left(\frac{1}{\xi}\right)\right], \tag{3.2}$$

$$\frac{B_r}{B_a} = -\frac{2}{\pi}\left[\frac{\eta\rho}{(1+\xi^2)(\xi^2+\eta^2)}\right], \tag{3.3}$$

and the corresponding vector potential,

$$\frac{A_\phi}{B_a R} = \frac{\rho}{2}\left(1 + \frac{2}{\pi}\left[\frac{\xi}{\xi^2+1} - \arctan\left(\frac{1}{\xi}\right)\right]\right). \tag{3.4}$$

Here

$$\xi^2 = \frac{1}{2}\left(\sqrt{\left[\rho^2+\zeta^2-1\right]^2 + 4\zeta^2} + \left[\rho^2+\zeta^2-1\right]\right) \tag{3.5}$$

and

$$\eta^2 = \frac{1}{2}\left(\sqrt{\left[\rho^2+\zeta^2-1\right]^2 + 4\zeta^2} - \left[\rho^2+\zeta^2-1\right]\right); \tag{3.6}$$

are coordinates in the oblate spheroidal coordinate system. $r = \rho R$, and $z = \zeta R$. The non-vanishing components of the magnetic field and the vector potential are shown in figure 3-2, where the Meissner effect is seen to lead to small values of B_z and large values of B_r when $r < R$. As sketched in figure 3-1, the magnetic fields concentrate at the edge in order to preserve the field. Far from the disk, B_z approaches the applied field B_a, while B_r disappears. Clearly, small values of z result in highly inhomogeneous fields. For the vector potential, we note that far away from the dot region, A_ϕ becomes linear in r and approaches $B_a r/2$, the vector potential due to the uniform field B_a. When $r < R$, the absence of A_ϕ is caused by expulsion of a magnetic field. In this Chapter, we will discuss many magnetic field models. In order to avoid confusion, form now on the fields above satisfying the Maxwell equations will be referred to as "the actual magnetic field".

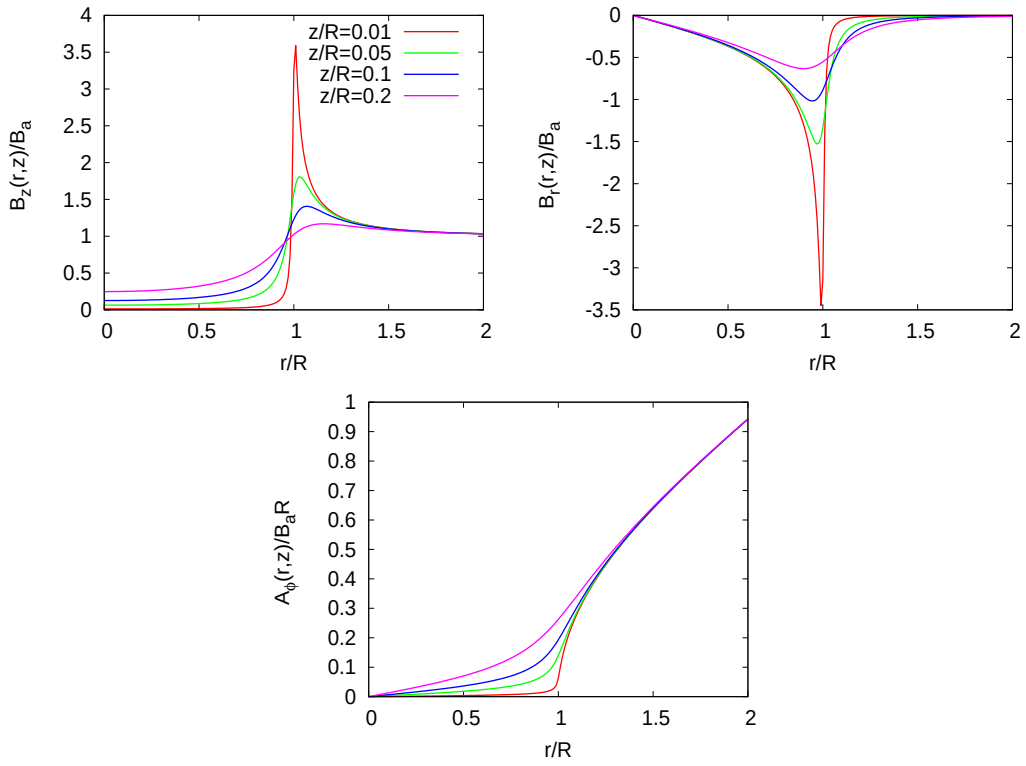

Figure 3-2: Non-vanishing components of the magnetic field (B_z and B_r) and the vector potential A_ϕ due to an ideal superconducting disk plotted as a function of the radial distance r for various values of z.

3.2 The solutions due to the actual magnetic field

After finding the actual magnetic field in the previous section, we will use it to calculate the electronic structure of electrons in the plane of a DMS on top of an isolated superconducting disk. We still use the single-particle Schrödinger equation to describe an electron in the plane as we did in Chapter 2. Here, the magnetic field is more realistic with both radial and normal components of the field included, as well as the concentration of the field at the edge of the disk. The Hamiltonian is again given by

$$\widehat{H} = (\hat{p} + e\vec{A})^2/2m^* - \frac{1}{2} g_{\text{eff}} \mu_B \vec{\sigma} \cdot \vec{B}, \tag{3.7}$$

where $\vec{B}$ and $\vec{A}$ are the actual magnetic field and the corresponding vector potential. An important difference between this calculation and the previous one is the symmetry of the system. The Hamiltonian (3.7) and the z component of the angular momentum have simultaneous eigenfunctions. In contrast, due to the presence of the radial component of $\vec{B}$, the Hamiltonian does not commute with the z component of the spin operator $\hat{s}_z$. As a result, spin is no longer a good quantum number here. In contrast to the model presented in Chapter 2, the eigenfunctions of the Hamiltonian are now a combination of spin up and spin down wavefunctions,

$$\Psi(r,\phi) = \begin{pmatrix} \exp(im\phi)\psi_m^{\uparrow}(r) \\ \exp(ip\phi)\psi_p^{\downarrow}(r) \end{pmatrix}, \tag{3.8}$$

where p and m are angular momentum. Because of the symmetry of the Hamiltonian, it is found that $\psi_m^{\uparrow}e^{im\phi}$ is only coupled to $\psi_{m+1}^{\downarrow}e^{i(m+1)\phi}$, so that the general form of eigenfunctions is given by [5, 6] (see Appendix B)

$$\Psi_m(r,\phi) = \exp(im\phi)\begin{pmatrix} \psi_m^{\uparrow}(r) \\ \psi_{m+1}^{\downarrow}(r)\exp(i\phi) \end{pmatrix}. \tag{3.9}$$

Although the actual field can be expressed in analytical form (equations (3.2)-(3.4)), the solution of the Schrödinger equation cannot be found analytically. In the following section, numerical methods called "basis set or superposition methods" will be introduced to find the eigenenergies and the eigenfunctions.

3.2.1 Basis set or superposition methods

The symmetry of the system including the radial field B_r indicates that the eigenfunctions are a combination of spin up and spin down components. Here, the eigenenergies and eigenfunctions will be calculated by basis set or superposition methods. The general idea of these numerical methods is to turn a differential equation problem into a generalised eigenvalue problem by expanding the dependent variable in the differential equation in a complete set of functions. Firstly, we make each term in the Hamiltonian (3.7) dimensionless to obtain $\widetilde{H}\Psi_m = \epsilon\Psi_m$, where

$$\widetilde{H} = -\widetilde{\nabla}^2 - 8\frac{B_a}{B_0}i\frac{a_\phi}{\rho}\frac{\partial}{\partial\phi} + 16\left(\frac{B_a}{B_0}\right)^2 a_\phi^2 - 2g_{\text{eff}}\frac{m^*}{m_e}\vec{\sigma}\cdot\frac{\vec{B}}{B_0}. \tag{3.10}$$

Here, $m^* = 0.5m_e$, $r = \rho R$, $E = \epsilon E_0$, $E_0 = \hbar^2/(2m^*R^2)$, $B_0 = 2\Phi_0/(\pi R^2)$, $\Phi_0 = h/e$, $A_\phi = a_\phi B_a R$, and $\widetilde{\nabla}^2 = \frac{1}{\rho}\frac{\partial}{\partial\rho}\left(\rho\frac{\partial}{\partial\rho}\right) + \frac{1}{\rho^2}\frac{\partial^2}{\partial\phi^2}$. Note that the unit of energy is different from that used in Chapter 2. If we want to explore the spectrum by varying the applied field B_a, it is more sensible to measure the energy in a unit of the constant parameter E_0 rather than $\hbar\omega_L$, which itself varies with B_a. In this calculation, B_a/B_0 is the ratio that can be used to identify the size of the disk and the magnitude of the external field in the same way as the missing magnetic flux s describes the system in the previous calculation. The relation between them is $B_a/B_0 = s/2$.

The eigenfunctions in (3.9) can be rewritten as

$$\Psi_m(\rho,\phi) = \Psi^\mu(\rho,\phi) = \sum_{\sigma=\pm\frac{1}{2}} \psi^\sigma_{\mu-\sigma}(\rho) e^{i(\mu-\sigma)\phi}\chi_\sigma, \tag{3.11}$$

where $m = \mu - \frac{1}{2}$; $\mu = \pm\frac{1}{2}, \pm\frac{3}{2}, \pm\frac{5}{2}$, etc., and $\chi_\sigma = \binom{1}{0}$ and $\binom{0}{1}$ for $\sigma = \frac{1}{2}$ and $-\frac{1}{2}$ respectively. Next, we will search for a basis set to describe the radial functions $\psi^\sigma_{\mu-\sigma}(\rho)$. Because a set of polynomials can be used to approximate arbitrary curves, $\psi^\sigma_{\mu-\sigma}(\rho)$ may be expanded in a complete set of B-spline functions (see Appendix C) as

$$\psi^\sigma_{\mu-\sigma}(\rho) = \sum_j a_j^{\mu\sigma} B_j(\rho), \tag{3.12}$$

where $B_j(\rho)$ is the j^{th} B-spline function. The main reason of choosing B-spline functions is that we will exploit the flexibility of the B-spline basis to concentrate functions near the radius of the superconducting disk, where the enhanced magnetic field causes the eigenfunctions to vary rapidly. Substituting (3.12) into (3.11), we get

$$\Psi^\mu(\rho,\phi) = \sum_j \sum_\sigma a_j^{\mu\sigma} B_j(\rho) e^{i(\mu-\sigma)\phi}\chi_\sigma. \tag{3.13}$$

In principle, the number of j is infinite, and the radial functions $\psi^\sigma_{\mu-\sigma}(\rho)$ extend from 0 to ∞. However, computationally, we can choose a finite j and determine ψ over a finite distance d. $\psi(\rho)$ decays exponentially at a large distance, so we can expect the wavefunction to be negligible beyond a finite distance d. Moreover, the accuracy of curve interpolation can be increased by increasing the number of B-spline functions. Therefore, we also expect the wavefunction to be accurately described by the finite number of j. It is always true that the wavefunction with

less energy oscillates less than that with more energy. As a result, the greater the energy of the wavefunction is, the greater number of j that will be likely needed. After substituting (3.13) into the Schrödinger equation, multiplying from the left by $\rho B_{j'}(\rho)e^{-i(\mu-\sigma')\phi}\chi^{\dagger}_{\sigma'}$, and integrating from $\rho = 0$ to $\rho = d$ and from $\phi = 0$ to $\phi = 2\pi$, for each j' and σ', we obtain

$$\sum_{j}\sum_{\sigma}\widetilde{H}_{j'\sigma',j\sigma}a_{j}^{\mu\sigma} = \epsilon\sum_{j}\sum_{\sigma}O_{j'\sigma',j\sigma}a_{j}^{\mu\sigma}, \tag{3.14}$$

where

$$O_{j'\sigma',j\sigma} = \delta_{\sigma\sigma'}2\pi\int_{0}^{d}B_{j'}B_{j}\rho d\rho \tag{3.15}$$

and

$$\begin{aligned}
\widetilde{H}_{j'\sigma',j\sigma} &= \delta_{\sigma\sigma'}2\pi\left[(\mu-\sigma)^{2}\int_{0}^{d}B_{j'}\left(\frac{1}{\rho}\right)B_{j}d\rho - \int_{0}^{d}B_{j'}\left(\frac{\partial}{\partial\rho}\rho\frac{\partial}{\partial\rho}\right)B_{j}d\rho\right] \\
&\quad +\delta_{\sigma\sigma'}16\pi\left(\frac{B_{a}}{B_{0}}\right)(\mu-\sigma)\int_{0}^{d}B_{j'}a_{\phi}B_{j}d\rho \\
&\quad +\delta_{\sigma\sigma'}32\pi\left(\frac{B_{a}}{B_{0}}\right)^{2}\int_{0}^{d}\rho B_{j'}a_{\phi}^{2}B_{j}d\rho \\
&\quad -8g_{\text{eff}}\frac{m^{*}}{m_{e}}\delta_{\sigma\sigma'}\sigma\pi\int_{0}^{d}\rho B_{j'}\left(\frac{B_{z}}{B_{0}}\right)B_{j}d\rho \\
&\quad -4g_{\text{eff}}\frac{m^{*}}{m_{e}}\left(1-\delta_{\sigma\sigma'}\right)\pi\int_{0}^{d}\rho B_{j'}\left(\frac{B_{r}}{B_{0}}\right)B_{j}d\rho.
\end{aligned} \tag{3.16}$$

Equation (3.14) has the form of the generalised eigenvalue problem $\widetilde{H}a = \epsilon Oa$, where $\widetilde{H}$ and O are $2\times j_{\max}$ dimensional matrices, ϵ is the eigenvalue, and a, a vector of coefficients $a_{j}^{\mu\sigma}$, is the eigenvector.

3.2.2 The energy spectrum

The basis set methods give us the generalised eigenvalue problem (3.14). We now solve the problem and present numerical solutions of the Schrödinger equation describing an electron in a DMS plane in the actual field. In figure 3-3 and 3-4, we have typically used 500 B-spline functions to converge the eigenvalues to at least 2 significant figures. Firstly, we investigate the dependence of the eigenenergies on the angular momentum m for several values of the applied field B_a, as shown in figure 3-3, where $g_{\text{eff}} = 40$ and $z = 0.004R$ have been assumed. Although spin cannot be used to specify the eigenstates, it is possible to explore the spin expectation value defined by

$$\langle \sigma_z \rangle = \langle \Psi_m | \sigma_z | \Psi_m \rangle = 2\pi \int_0^\infty \left(\left| \psi_m^{\uparrow} \right|^2 - \left| \psi_{m+1}^{\downarrow} \right|^2 \right) r dr, \tag{3.17}$$

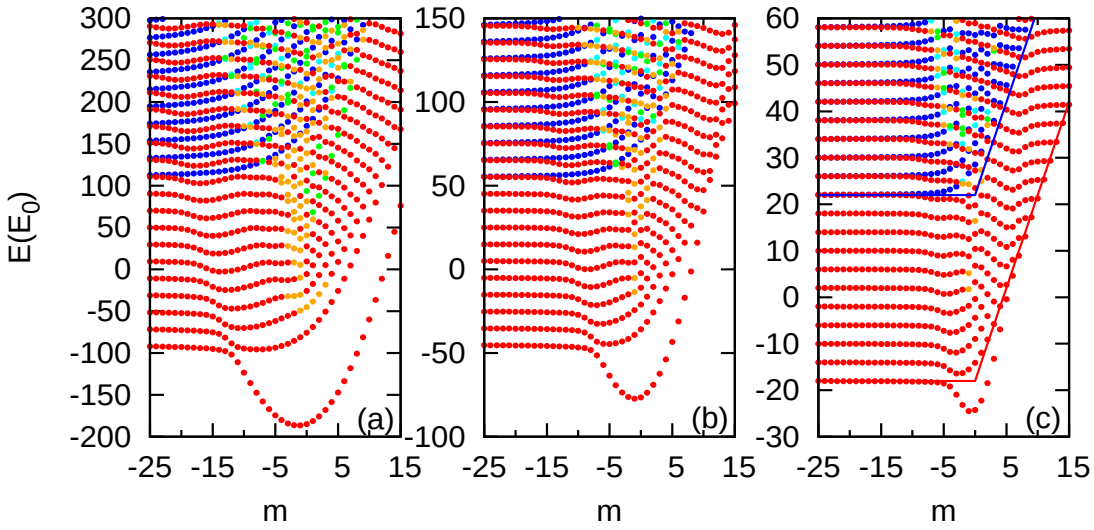

Figure 3-3: The energy spectrum as a function of m for $B_a/B_0 = 2.50$ (a), 1.25 (b), 0.50 (c). The colour of each dot represents the spin expectation value of each state; red, orange, green, cyan, and blue mean the spin expectation value is in the range of $[1.0, 0.6)$, $[0.6, 0.2)$, $[0.2, -0.2)$, $[-0.2, -0.6)$, and $[-0.6, -1.0]$ respectively. Here, $g_{\text{eff}} = 40$, $z/R = 0.004$, and $m^* = 0.5m_e$. The solid red and blue lines in (c) represent the energies of the spin up and spin down Landau states with $n = 0$. Note the different vertical ranges for the three panels.

where σ_z is the z component of Pauli matrices. Obviously, if the state is normalised and purely a spin up state, $\langle\sigma_z\rangle$ will be 1, and it will be -1 for a purely spin down state. The value of $\langle\sigma_z\rangle$ is used to determine the colour chosen to display the eigenvalues in figure 3-3. Considering these, we notice that the spin mixed states, represented by orange, green, and cyan dots, occur when $|m|$ is small, while the spin polarised states, represented by red and blue dots, are found when $|m|$ is large. With increasing value of the applied field, the spin mixed states are found for larger $|m|$. We can also check whether the actual magnetic field gives correct energy levels for the states that exist far away from the dot. In this case, it is found that the energies approach those of the Landau levels, as they should, since most of the amplitude of the wavefunctions of the states with large $|m|$ arises for $r > R$, where the field is uniform. This suggests that the actual field which satisfies the Maxwell equation is reliable. In order to compare the spectrum with the results obtained in the previous Chapter, in figure 2-9, we plot the spectrum obtained with the actual field for several values of $g_{\rm eff}$ in figure 3-4, where the energy unit is changed to $\hbar\omega_L$ and B_a/B_0 is given by 2.5, corresponding to the magnetic flux missing $s = 5$. Comparison is not easy because spin is not a good quantum number. If $g_{\rm eff}$ is zero, the Zeeman term

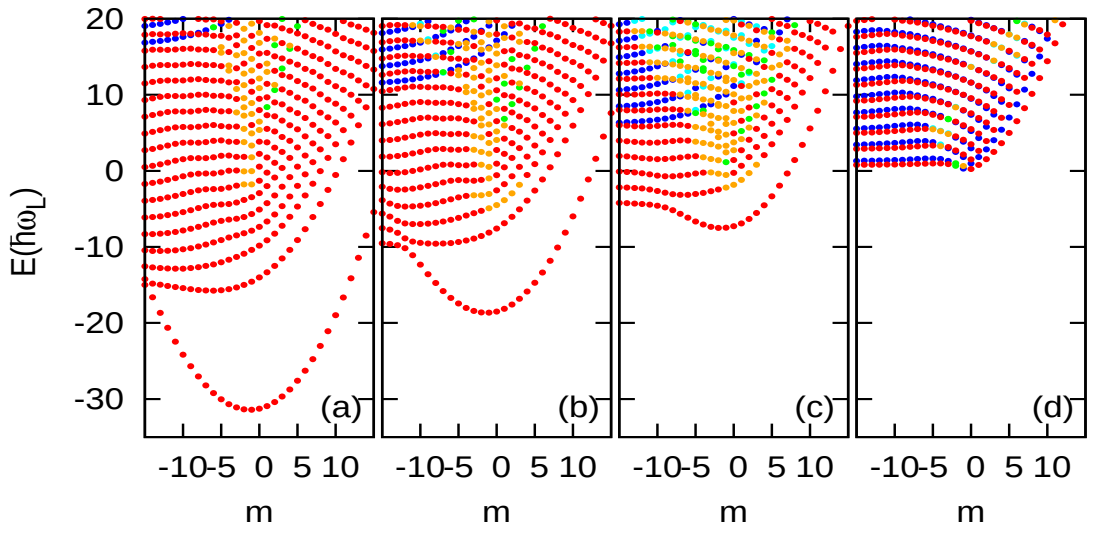

Figure 3-4: The energy spectrum as a function of m for $g_{\rm eff}$=60 (a), 40 (b), 20 (c), 1.0 (d). As figure 3-3, the colour of each state represents the spin expectation value. Here, $B_a/B_0 = 2.5$ ($s = 5$), $z/R = 0.04$, and $m^* = 0.5m_e$.

disappears. Consequently, the spin up and spin down eigenenergies are identical. As g_{eff} increases, the splitting of the spin up and spin down energies occurs, clearly seen for large value of $|m|$. The mixing of spin appears when $|m|$ is small. We also find that for each m the lowest energy tends to separate from the others with increasing of Zeeman potential. This behaviour is not at all present in the results obtained with the approximate field in Chapter 2.

Clearly, the existence of the superconducting disk significantly disturbs the Landau quantisation, and results in a complex spectrum, especially the states trapped near the dot region. So far, we have presented the results without any explanation. To get further insight, we will approximate the actual magnetic field, and study the effects of each component and aspect of the field.

3.3 Approximation of the actual magnetic field

The aim of this section is to find an approximated magnetic field which still contain essential physics of the actual field. We expect that using the approximated field will help us to find analytical solutions and to understand the complex spectrum due to the actual field. Considering figure 3-2, the field B_z might be approximated as a step function shown in (2.9), when z/R is 0.1 or 0.2. For smaller values of z, this model is clearly insufficient, as the magnetic concentration at the superconducting edge becomes larger with decreasing values of z, and definitely cannot be neglected. This concentration will likely play a key role in electron confinement, especially when electron wavefunctions distribute near the edge of the dot. Reijniers [45] suggests that the concentration can be compensated by a delta function δ; hence, the field B_z could be approximated as

$$B_z(r) = B_a\Theta(r - R) + C\delta(r - R), \tag{3.18}$$

where Θ is the Heaviside step function. In this model field, the magnetic field outside the dot region is not perturbed by the superconductor. It must be emphasised that δ has the unit of 1/length, so C must have the unit of magnetic flux density·length. The next important point is the strength of the delta function. In the problem of a particle moving in a one dimensional delta potential [55], the eigenenergies depend upon the strength of the delta potential. We therefore

expect C to influence the eigenenergies of our problem, and so we need to find a suitable value of C that can describe the actual field well. In the absence of the superconductor, the magnetic flux passing through the superconducting disk area is $\Phi_1 = B_a \pi R^2$. When the superconductor is placed in the system, all of flux Φ_1 is assumed to be perfectly expelled and then only penetrate into the edge of the superconducting disk; thus, we can approximate the magnetic field in the dot region to be $C\delta(r-R)\hat{z}$. Now, one could calculate the magnetic flux through this area,

$$\Phi_2 = \int \vec{B} \cdot d\vec{A} = \int_0^{2\pi} \int_0^R C\delta\left(r-R\right) r dr d\phi = 2\pi CR. \tag{3.19}$$

According to the conservation of magnetic flux, it needs to satisfy $\Phi_1 = \Phi_2$. Thus, we obtain the strength of the delta function as $C = B_a R/2$. We reexpress the field in (3.18) and obtain the corresponding vector potential straightforwardly:

$$B_z(r) = B_a \Theta(r-R) + B_a \frac{r}{2} \delta(r-R), \tag{3.20}$$

$$A_\phi(r) = B_a r \Theta(r-R)/2. \tag{3.21}$$

Notice that outside the dot region, the vector potential is exactly that due to the uniform field B_a.

When a DMS is close to the superconductor, there is also the magnetic concentration in the case of the field B_r. Although the impact of this field has not been fully understood yet, we estimate that it is necessary to include the field in the calculation. In the condition where z is extremely small, we can neglect z^2 in (3.5) to get $2\xi^2 \approx \sqrt{(\rho^2-1)^2} + \rho^2 - 1$. Depending on the value of ρ, this equation can be expressed as

$$\xi^2 = (\rho^2 - 1)\Theta\left(\rho - 1\right), \tag{3.22}$$

where $\rho = r/R$. Similarly, (3.6) can be approximated by $2\eta^2 \approx \sqrt{(\rho^2-1)^2} - \rho^2 + 1$ so that we can write

$$\eta^2 = (1-\rho^2)\Theta\left(1-\rho\right). \tag{3.23}$$

Substituting (3.22) and (3.23) into (3.3) yields

$$\frac{B_r}{B_a} = -\frac{2}{\pi}\frac{\rho}{\sqrt{1-\rho^2}}\Theta\left(1-\rho\right). \tag{3.24}$$

This form of B_r describes a radial component of the field which exists inside the dot region, increases linearly for small ρ, and goes to infinity at the disk radius. Therefore, we propose a possible model of B_r,

$$\frac{B_r}{B_a} = -\frac{2}{\pi}\rho\Theta\left(1-\rho\right) + C'\delta\left(\rho-1\right), \tag{3.25}$$

which has these characteristics. To determine C', we require the integral $\int_0^\infty B_r r dr$ using B_r in (3.24) and (3.25) to be the same and obtain $C' = \frac{2}{3\pi} - \frac{1}{2}$.

The approximated field B_z will be used to calculate the energy spectrum in section 3.4, while the approximated field B_r will be used in section 3.5. Both of them are useful to understand the complex energy spectrum seen in figures 3-3 and 3-4.

3.4 The effects of the normal component of the magnetic field

According to the complex energy spectrum in figures 3-3 and 3-4, we expect that considering the effect of each component of the magnetic field individually will lead to a greater understanding of the electronic properties of the hybrid system. In this section, we focus on the effect of the B_z field by using the approximated field defined in (3.20). This model field was first used by Reijniers [45] who considered numerically the problem of a magnetic quantum dot in a conventional semiconductor (they prefer to call the system a magnetic antidot, but it is exactly the same system that we call a magnetic quantum dot). Here, we develop an analytical solution to find the energy spectrum of electrons in a magnetic quantum dot in a DMS, including the Zeeman energy in the calculation. Ignoring the radial component of the field means we can keep spin as a good quantum number, as was the case in the calculations presented in Chapter 2. The difference between the two models defined by (2.9) and (3.20) is just the delta function due to the magnetic concentration. We therefore begin by studying the effect of a delta function potential to understand the nature of the confined states

associated with the potential.

3.4.1 Spectrum of a delta potential

The problem of a particle confined in a one dimensional delta potential well $\alpha\delta(x)$ has been discussed widely in quantum mechanics books [55]. It has been shown that this quantum well has precisely a single bound state whose energy is proportional to the square of the strength of the potential α^2. The problem we will consider is slightly different. We assume that a particle with effective mass m^* is captured in a ring trap by a delta function potential which is zero everywhere except when $r = R$. The Schrödinger equation of our problem is given by $\widehat{H}\Psi_m = E\Psi_m$, where the Hamiltonian is

$$\widehat{H} = \frac{p^2}{2m^*} - \alpha r\delta\left(r - R\right). \tag{3.26}$$

Here, α is a positive constant with units of energy, characterising the strength of the delta potential. Substituting the eigenfunction $\Psi_m\left(r,\phi\right) = e^{im\phi}\psi_m\left(r\right)$ into the Schrödinger equation, we can rewrite the Schrödinger equation as

$$\left[-\left\{\frac{\partial^2}{\partial\rho^2} + \frac{1}{\rho}\frac{\partial}{\partial\rho} - \frac{m^2}{\rho^2}\right\} - \frac{\alpha}{E_0}\rho\delta\left(\rho - 1\right)\right]\psi_m\left(\rho\right) = \epsilon\psi_m\left(\rho\right). \tag{3.27}$$

In (3.27), ρ and ϵ are dimensionless variables, where $\rho = r/R$ and $\epsilon = E/E_0$ with $E_0 = \hbar^2/(2m^*R^2)$. For a bound state, ϵ will be negative. As a result, the solutions can be expressed in terms of the modified Bessel functions of the first kind I_m and the second kind K_m:

$$\psi_m\left(\rho\right) = \begin{cases} I_m\left(\sqrt{|\epsilon|}\rho\right) & \rho < 1 \\ K_m\left(\sqrt{|\epsilon|}\rho\right) & \rho > 1. \end{cases} \tag{3.28}$$

In order to find the eigenvalues, the inside and outside wavefunctions need to satisfy the boundary conditions:

$$\psi_{in}\left(\rho = 1\right) = \psi_{out}\left(\rho = 1\right), \tag{3.29}$$

$$\psi'_{out}(\rho = 1) - \psi'_{in}(\rho = 1) = -\frac{\alpha}{E_0}\psi_{out}\left(\rho = 1\right). \tag{3.30}$$

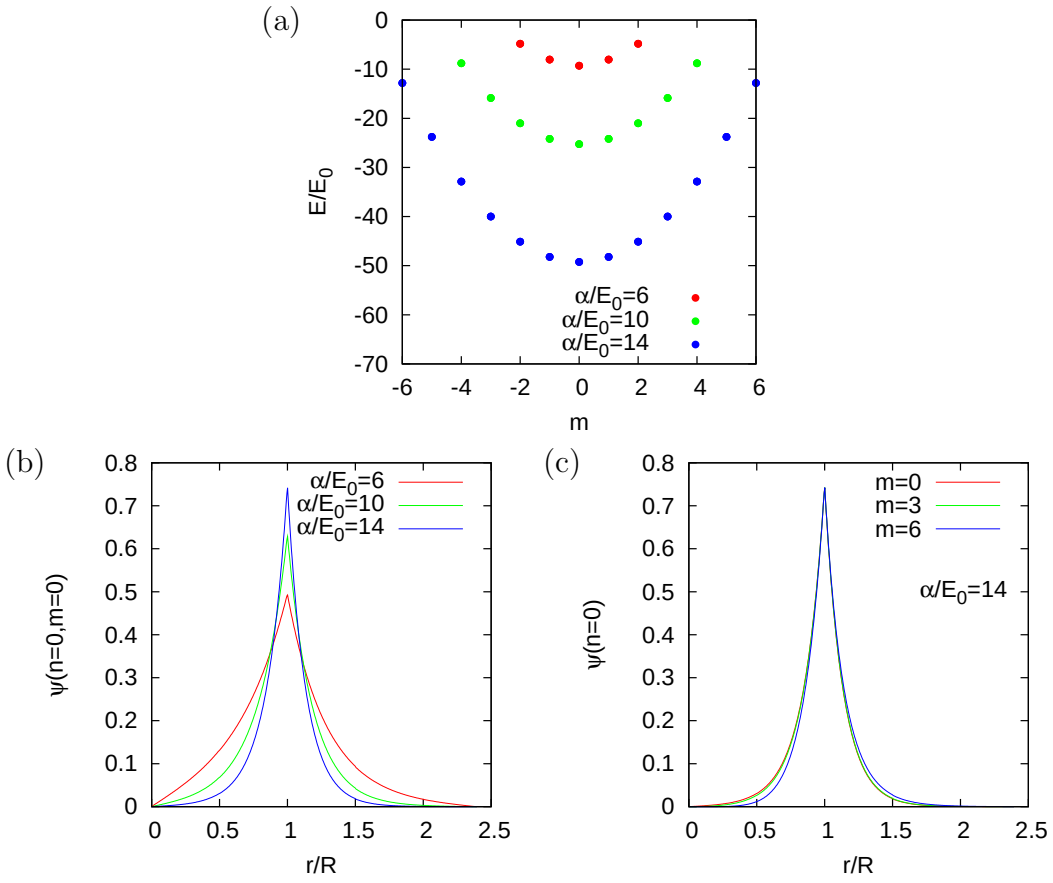

Figure 3-5: (a) The eigenenergies of the ring delta function potential plotted as a function of m for various values of α/E_0. (b) The normalised radial wavefunctions with the quantum numbers $(n = 0, m = 0)$ for various values of α/E_0. (c) The normalised radial wavefunctions with the quantum numbers $(n = 0)$ for various values of m, when $\alpha = 14$.

In deriving the second condition (3.30), we multiply (3.27) by ρ, integrate from from $1 - \eta$ to $1 + \eta$, and take the limit as $\eta \to 0$ on both sides of the equation.

The energy spectrum found numerically from the transcendental equations (3.29,3.30) is shown in figure 3-5 (a). We find that there is at most only one bound state for each value of m irrespective of the magnitude of α. The eigenenergies are two-fold degenerate with $E_m = E_{-m}$. This quantum degeneracy can be understood by considering the solutions (3.28), and recalling $I_m(x) = I_{-m}(x)$ and $K_m(x) = K_{-m}(x)$, where m is an integer. As a result, positive and negative m give identical energies. Physically, the degeneracy is a result of the system being identical under $\phi \to -\phi$. As expected, the energies do depend upon the

strength of the potential α, becoming increasingly negative with increasing α. We find the potential can trap a finite number of bound states with sufficiently small $|m|$. Figure 3-5 (b) shows the wavefunctions with $m = 0$ are strongly localised at the radius of the delta potential, where they peak, decaying exponentially to either sides. As the potential strength increases, they decay more rapidly. This behaviour is also found in case of a one dimensional delta function potential [55]. With increasing $|m|$, the eigenfunctions slightly extend further from the radius of the potential as shown in figure 3-5 (c). This is because of the strong confinement due to the delta function potential.

3.4.2 Spectrum of the approximated normal field

Having considered the energies and bound states of the delta potential, we now present the calculation of electron confinement due to the approximated field B_z. The Hamiltonian of an electron with the effective mass m^*, travelling in a DMS plane in the presence of such a field is

$$\widehat{H} = \frac{(\hat{p} + eA_\phi\hat{\phi})^2}{2m^*} - \frac{1}{2}g_{\text{eff}}\mu_B\sigma_z B_z, \tag{3.31}$$

where B_z and A_ϕ are the approximated magnetic field (3.20) and the corresponding vector potential (3.21). The symmetry of the system is similar to that in Chapter 2, allowing us to write the eigenfunctions in separable form as $\Psi^\sigma_{nm}(r,\phi) = e^{im\phi}\psi^\sigma_{nm}(r)\chi_\sigma$. Because the field is not continuous at the radius of the superconducting disk, we find solutions valid inside and outside separately before matching. We measure all of the variables in the same units as employed in section 2.2. For $r < R$, the absence of the magnetic field results in solutions: $\psi^\sigma_{nm}(\rho) = J_m(\sqrt{2\epsilon}\rho)$, which are exactly the same as the inside solutions of section 2.2. However, for $r \geq R$ the outside solutions are different. The vector potential outside is now exactly the potential due to a uniform magnetic field and the model field (3.20) is infinity at $r = R$. We do the same calculation straightforwardly as we did before in section 2.2 and find the radial equation:

$$\left[\frac{\partial^2}{\partial\rho^2} + \frac{1}{\rho}\frac{\partial}{\partial\rho} - \frac{m^2}{\rho^2} - \rho^2 + 2\left(\epsilon - m + \zeta + \zeta\frac{\rho}{2}\delta(\rho - \sqrt{s})\right)\right]\psi^\sigma_{nm}(\rho) = 0 \quad \rho \geq \sqrt{s}, \tag{3.32}$$

where $\sqrt{s}$ is the superconductor radius R in the unit of ℓ_L and ζ is the Zeeman energy in the unit of $\hbar\omega_L$; $\zeta = \sigma g_{\text{eff}} m^*/m_e$. For $\rho > \sqrt{s}$, the delta function does not contribute and the above expression becomes the same as the equation (2.16) with m_{eff} is replaced by m. As a result, the outside solutions can be obtained immediately as

$$\psi^{\sigma}_{nm}(\rho) = e^{-\rho^2/2}\rho^{|m|}U\left(-\beta + \frac{|m|}{2} + \frac{1}{2}, |m| + 1, \rho^2\right) \quad \rho > \sqrt{s}. \tag{3.33}$$

The effective potential can be obtained by considering equation (3.32),

$$V^{\sigma}_{\text{eff}}(\rho) = \begin{cases} \dfrac{m^2}{2\rho^2} & \rho < \sqrt{s} \\ \dfrac{m^2}{2\rho^2} + \dfrac{\rho^2}{2} + m - \zeta(1 + \dfrac{\rho}{2}\delta(\rho - \sqrt{s})) & \rho \geq \sqrt{s}. \end{cases} \tag{3.34}$$

In side and outside solutions are matched at $\rho = \sqrt{s}$, according to conditions established by integrating across the delta function at $\rho = \sqrt{s}$. As in the previous section, we multiply equation (3.32) by r and integrate from $\sqrt{s} - \eta$ to $\sqrt{s} + \eta$, before taking the limit as $\eta \to 0$, yielding

$$\psi_{in}\left(\rho = \sqrt{s}\right) = \psi_{out}\left(\rho = \sqrt{s}\right), \tag{3.35}$$

$$\psi'_{out}(\rho = \sqrt{s}) - \psi'_{in}(\rho = \sqrt{s}) = -\zeta\sqrt{s}\psi_{out}\left(\rho = \sqrt{s}\right). \tag{3.36}$$

Solving (3.35) and (3.36), we obtain the energy spectrum displayed in figure 3-6. In order to compare with the spectrum in the figure 2-9, both plots are on the same scale range. We find the eigenenergies of each spectrum approach the Landau levels for large values of $|m|$. This result suggests that the magnetic field model (3.20) describe well the states far away from the dot. When $g_{\text{eff}} = 0$, the eigenenergies are doubly degenerate ($E^{\uparrow} = E^{\downarrow}$). We see that the spectrum in figure 3-6 (c) is similar to that in figure 2-9 (c). However, figure 3-6 (c) is more reliable for energies with large $|m|$. When $g_{\text{eff}} > 0$, the Zeeman potential destroys the spin degeneracy. The spin dependent energies are shown in 3-6 (a), (b), (d), and (e). Each spectrum consists of many energy patterns, depending on the distribution of the bound states. Similar to the spectrum in figure 2-9, spin down eigenstates can be divided into three kinds: quantum dot, interme-

diate, and Landau-like states, while there are four kinds of spin up eigenstates: quantum antidot, intermediate, Landau-like, and edge states. All kinds of spin down eigenstates and the first three kinds of spin up eigenstates are found in the spectrum of both figures. They are already discussed in section 2.3. The spin dependent localisation of these kinds of states can be concluded into three cases.

(i) For sufficiently large $|m|$, both spin up and spin down eigenstates are called Landau-like states as they behave like Landau states.

(ii) For sufficiently small $|m|$ and n, spin up eigenstates become quantum antidot states whose energies are negative. They are strongly perturbed by the Zeeman barrier and extend mostly outside the dot region. Spin down eigenstates become quantum dot states whose energies are positive. They are confined by the Zeeman well and distribute mostly inside.

(iii) For sufficiently small $|m|$ but large n, quantum antidot states whose energies are greater than the Zeeman barrier will become intermediate states which are able to extend both inside and outside the dot. Quantum dot states whose energies are greater than the Zeeman well will become intermediate states which are also able to distribute both inside and outside the dot.

The additional states found here are edge states. They are defined to be the

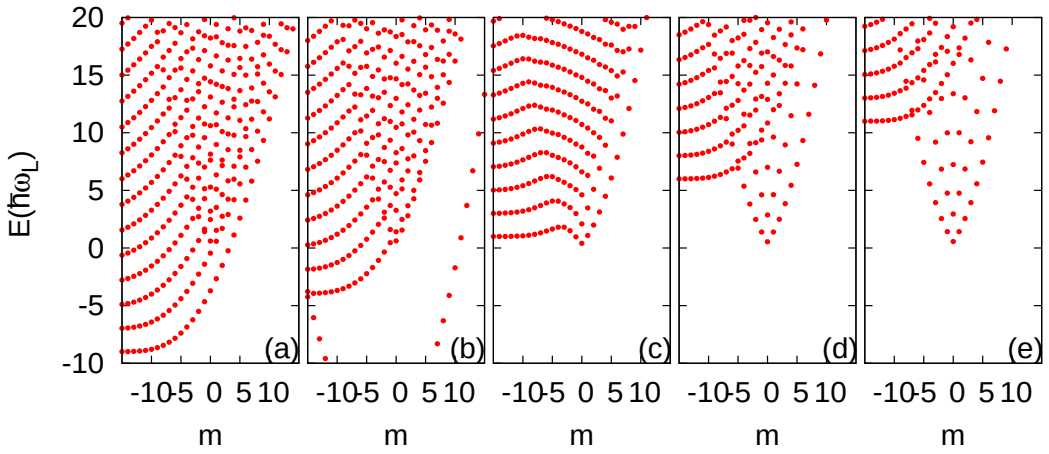

Figure 3-6: The spin dependent energy spectrum for $s = 5$, $m^* = 0.5m_e$, and several values of g_{eff}. (a) $E^{\uparrow}$ with $g_{\text{eff}} = 40$, (b) $E^{\uparrow}$ with $g_{\text{eff}} = 20$, (c) $E^{\uparrow}$ and $E^{\downarrow}$ with $g_{\text{eff}} = 0$, (d) $E^{\downarrow}$ with $g_{\text{eff}} = 20$, and (e) $E^{\downarrow}$ with $g_{\text{eff}} = 40$.

states that are strongly localised by the concentration of the magnetic field at the edge of the dot. Considering the effective potential (3.34), one can see that at $\rho = \sqrt{s}$ the spin dependant Zeeman term $\zeta\frac{\rho}{2}\delta(\rho - \sqrt{s})$ representing the magnetic concentration will be a confining potential for spin up solutions, but becomes a scattering potential for spin down solutions. Therefore, we expect that edge states will be spin up states and behave like the bound states studied in section 3.4.1. As partly seen in figure 3-6 (b), where $g_{\text{eff}} = 20$, the lowest energy state for each m is separated from the rest and is an edge state. Because the Zeeman energy ζ can be considered as the strength the delta potential $\zeta\frac{\rho}{2}\delta(\rho - \sqrt{s})$, the energy levels of edge states are sensitive to ζ. We find the energies of edge states for $g_{\text{eff}} = 40$ are very low, so we plot them separately in figure 3-7 (a). Unlike the spectrum due to a delta potential, they are not two-fold degenerate ($E_m \neq E_{-m}$). Edge states are found when $|m|$ is sufficiently small and become Landau-like states when $|m|$ is sufficiently large.

Figures 3-7 (b) and (c) show some wavefunctions corresponding to the spectrum in figure 3-7 (a). Clearly, when m is between 0 and -26, the bound states are strongly localised at the edge as edge states. They slightly extend far from the origin as $|m|$ increases because of the strong confinement due to the delta function potential (this behaviour is also visible in figure 3-5 (c)). When m is less than -26, the states suddenly become Landau-like states and their energies are also very close to the Landau levels. This behaviour is also found for positive m.

To summarise, comparing the energy spectrum due to the two model fields, (2.9) studied in Chapter 2 and (3.20) including the concentrated magnetic field at the edge of of the superconductor, we find that their spectra consist of similar energy patterns. The bound states in each spectrum are classified by their spatial distribution as already discussed in section 2.3. However, the obvious difference is the existence of edge states, which are only found in the latter model. They arise due to the concentration of the magnetic field which is not included in the former model. We also find that the field (3.20) satisfying conservation of magnetic flux describes more correctly quantum states far from the dot. Although these model fields have been considered by Reijniers [45] who investigated their effect on electrons in a conventional 2DEG, that study only focused on electron states with small values of m and did not report on the validity of the fields for describing

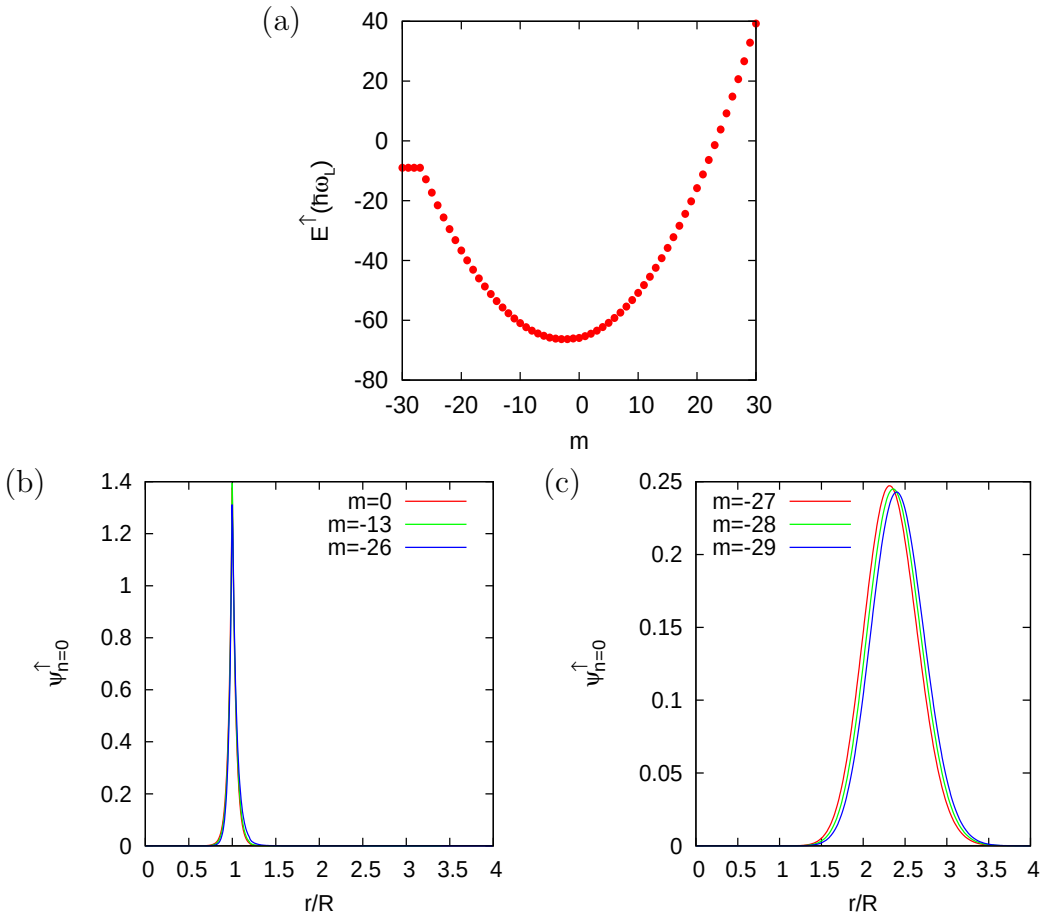

Figure 3-7: (a) The spin up energy spectrum of the state with $n = 0$ for $s = 5$, $m^* = 0.5m_e$, and g_{eff}=40. (b) Some corresponding radial wavefunctions with $n = 0$, which are edge states. (c) Some corresponding radial wavefunctions with $n = 0$, which are Landau-like states. The wavefunctions are plotted in the same length scale in order to compare their spatial distribution.

large $|m|$ states. By studying the hybrid system in the approximated B_z field (3.20), we have been able to see how the normal component of the magnetic field influences energies and bound states. The giant g-factor enhances the Zeeman energy due to B_z, which acts as a spin dependent potential. However, there are aspects of the hybrid system in the actual field still to be understood. The symmetries of these two systems are different and do not allow us to compare their energy spectra easily. In the next section, the radial component of the magnetic field is included, resulting in a system whose symmetry is similar to that in the actual field. We therefore expect to get further insight.

3.5 The effects of the radial component of the magnetic field

Ignoring the radial component of the magnetic fields allows spin to be used to index the quantum states and enables the nature of spin dependent states to be studied. In the previous section, the spin dependent spectrum was investigated by using the approximated B_z field (3.20) including magnetic concentration. It was found that the giant Zeeman potential due to B_z acts as a spin dependent potential. The spectrum can be understood, but it fails in part to describe the spectrum due to the actual magnetic field, shown in figure 3-3. In order to further understand the effect of the actual field, the radial component of the field is now included. In this section, we will use the approximated B_r field (3.25) and focus on how the giant Zeeman potential due to B_r affects the energy spectrum.

Once again we start with the Hamiltonian of an electron with the effective mass m^*, travelling in a DMS plane on top of a superconducting disk, given by

$$\widehat{H} = (\hat{p} + e\vec{A})^2/2m^* - \frac{1}{2} g_{\text{eff}} \mu_B \vec{\sigma} \cdot \vec{B}, \tag{3.37}$$

where $\vec{B} = B_z\hat{z} + B_r\hat{r}$ with B_z and B_r the approximated field components given in (3.20) and (3.25) respectively. We use the vector potential $\vec{A}$ (3.21) corresponding to the B_z field. The symmetry of the Hamiltonian is similar to that in equation (3.7). Spin is not a good quantum number. Therefore, eigenfunctions are a combination of spin up and spin down wavefunctions and can be expressed as

$$\Psi_m(r,\phi) = \exp(im\phi) \begin{pmatrix} \psi_m^{\uparrow}(r) \\ \psi_{m+1}^{\downarrow}(r)\exp(i\phi) \end{pmatrix}. \tag{3.38}$$

Although the B_r field has been approximated to be a simple function, analytical solutions of the Hamiltonian (3.37) cannot be found. Then, we use the basis set methods discussed in section 3.2.1 to solve the Schrödinger equation numerically.

Before considering the results, we can use perturbation theory to investigate the solutions. The Hamiltonian (3.37) can be rewritten as

$$\widehat{H} = \widehat{H}_0 + \widehat{H}_1, \tag{3.39}$$

where $\widehat{H}_0$ is the Hamiltonian without the Zeeman energy and $\widehat{H}_1 = -\frac{1}{2} g_{\text{eff}} \mu_B \vec{\sigma} \cdot \vec{B}$ is the Zeeman energy. The solution of $\widehat{H}_0$ was considered in section 3.4.2 (the case $g_{\text{eff}} = 0$). Its eigenfunctions have the form $\Psi^{\sigma}_{nm} = e^{im\phi} \psi^{\sigma}_{nm}(r) \chi_{\sigma}$ and are two-fold degenerate as shown in figure 3-6 (c) ($E^{\uparrow}_{nm} = E^{\downarrow}_{nm}$). When g_{eff} is sufficiently small, we can consider $\widehat{H}_1$ as a perturbation. First order degenerate perturbation theory with the subspace of degenerate states [59] gives the secular equation:

$$\begin{vmatrix} H^1_{\uparrow\uparrow} - E^1_{nm} & H^1_{\uparrow\downarrow} \\ H^1_{\downarrow\uparrow} & H^1_{\downarrow\downarrow} - E^1_{nm} \end{vmatrix} = 0, \tag{3.40}$$

where $H^1_{\sigma\sigma'} = \int_0^{2\pi} \int_0^{\infty} (\Psi^{\sigma}_{nm})^{\dagger} \widehat{H}^1 \Psi^{\sigma}_{nm} r dr d\phi$, $\sigma = \uparrow$ or $\downarrow$, and E^1_{nm} are the correction to unperturbed energies E_{nm}. We will consider the effects of B_z and B_r separately by dividing $\widehat{H}^1$ into $\widehat{H}^1_z$ and $\widehat{H}^1_r$, where $\widehat{H}^1_z = -\frac{1}{2} g_{\text{eff}} \mu_B \sigma_z B_z$ and $\widehat{H}^1_r = -\frac{1}{2} g_{\text{eff}} \mu_B \sigma_r B_r$. σ_z and σ_r are the z and r components of the Pauli matrices,

$$\sigma_z = \begin{pmatrix} 1 & 0 \\ 0 & 1 \end{pmatrix} \quad \text{and} \quad \sigma_r = \begin{pmatrix} 0 & e^{-i\phi} \\ e^{i\phi} & 0 \end{pmatrix}. \tag{3.41}$$

Using the z component of the Zeeman energy $\widehat{H}^1_z$ to calculate $H^1_{\sigma\sigma'}$, we obtain the secular equation:

$$\begin{vmatrix} H^1_{\uparrow\uparrow} - E^1_{nm} & 0 \\ 0 & H^1_{\downarrow\downarrow} - E^1_{nm} \end{vmatrix} = 0, \tag{3.42}$$

where

$$H^1_{\uparrow\uparrow} = -g_{\text{eff}} \mu_B \pi \int_0^{\alpha} B_z \left| \psi^{\uparrow}_{nm} \right|^2 r dr, \tag{3.43}$$

$$H^1_{\downarrow\downarrow} = +g_{\text{eff}} \mu_B \pi \int_0^{\alpha} B_z \left| \psi^{\downarrow}_{nm} \right|^2 r dr. \tag{3.44}$$

The roots of the equation are obviously $E^1_{nm} = H^1_{\uparrow\uparrow}$ or $E^1_{nm} = H^1_{\downarrow\downarrow}$. Therefore, B_z perturbs the degenerate energy levels E_{nm}, splitting them into two levels given by $E_{nm} + H^1_{\uparrow\uparrow}$ and $E_{nm} + H^1_{\downarrow\downarrow}$. Because B_z in our calculation is always positive, the former levels are lower than the unperturbed levels, while the latter are higher. Using the r component of the Zeeman energy $\widehat{H}^1_r$ to calculate $H^1_{\sigma\sigma'}$,

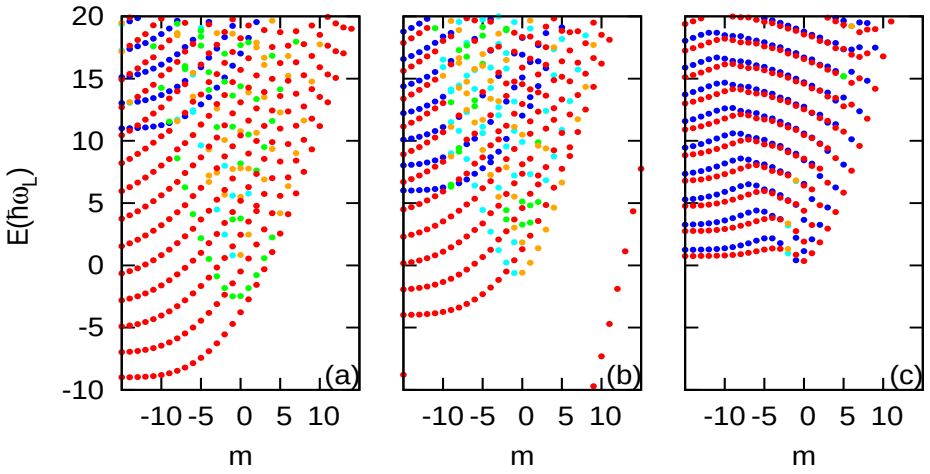

Figure 3-8: The energy spectrum as a function of m for g_{eff}=40 (a), 20 (b), and 1 (c). As figure 3-3, the colour of each state represents the spin expectation value. Here, $s = 5$ and $m^* = 0.5m_e$.

we get $H^1_{\uparrow\uparrow} = H^1_{\downarrow\downarrow} = H^1_{\uparrow\downarrow} = H^1_{\downarrow\uparrow} = 0$. This indicates that B_r will not perturb the energy levels of the unperturbed Hamiltonian $\widehat{H}_0$ to first order. This result, of course, is restricted to the situation when the perturbation is small, compared to $\widehat{H}_0$.

Now, we turn to the numerical results. The energy spectrum of the Hamiltonian (3.37) is shown in figure 3-8. First, we consider the spectrum with $g_{\text{eff}} = 1.0$. Comparing the spectrum in figure 3-8 (c) with that in figure 3-4 (d), we find that they consist of similar energy patterns, and that most of the confined states are spin up or spin down dominant states. In this case, we expect that the Zeeman term is small enough to be described by the perturbation theory, which shows that B_z will cause the splitting of the doubly degenerate levels ($E^{\uparrow}_{nm} = E^{\downarrow}_{nm}$). The results in figure 3-8 (c) agree with the theory. For the states with large $|m|$, we see that there is an energy splitting of predominantly spin up and spin down states. This is because the states distribute outside the dot region, where B_z is non-vanishing. This splitting can be described by the integrals (3.43) and (3.44). As $|m|$ decreases, the probability of finding the states inside the dot increases, resulting in a smaller energy splitting because of the absence of B_z inside. We have seen that B_r, which is non-vanishing inside the dot, does not perturb energy levels to leading order.

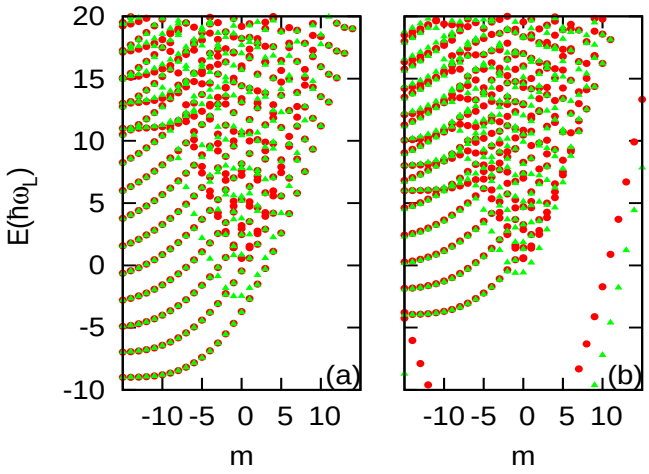

Figure 3-9: The energy spectrum as a function of m for g_{eff}=40 (a), 20 (b). The spin up and spin down spectrum in figure 3-6 are plotted in one figure and represented by red dots. The spin mixed spectrum in figure 3-8 is represented by green triangles. Here, $s = 5$ and $m^* = 0.5m_e$.

For bigger values of g_{eff} in figure 3-8 (a) and (b), we do see the effects of B_r. It couples together the spin up and spin down wavefunctions, and results in the spin mixed states, evident when $|m|$ is small. For large $|m|$, we only see spin polarised states (up and down) because of the absence of B_r outside the dot. Figure 3-9 (a) and (b) shows how B_r affects the eigenenergies. Each plot consists of the spin up and spin down spectrum for figure 3-6, calculated in the absence of B_r and represented by red dots, and the spin mixed spectrum for figure 3-8, obtained when B_r is included and represented by green triangles. We see B_r affects the energies of spin polarised states differently, depending upon their spatial distribution. Because states that exist mostly outside the dot will be only slightly perturbed by B_r, the energy levels of spin up and spin down Landau-like states, and spin up antidot states do not change significantly. When B_r is included, their eigenenergies represented by red dots are superimposed by green triangles. However, the energies of edge states are significantly lowered by B_r as they are localised at the superconductor radius, where B_r is significant. Clearly, first-order perturbation theory fails to describe this strong perturbation by B_r. The other states are spin up and spin down intermediate states, and spin down quantum dot states. They are partly found inside the dot, so we expect B_r to

affect their energy levels. The energies of these three kinds of states overlay one another in the same region of the spectrum, so it is difficult to see the effect of B_r. However, one can see some red dots which are not covered by green triangles, along with some red dots that are covered. This indicates that B_r perturbs some spin dependent energies in this region.

To summarise this section, the effect of the Zeeman energy due to B_r has been investigated. It changes the symmetry of the Hamiltonian from that when only the z component of the Zeeman interaction is included, coupling spin up and spin down wavefunctions together into the eigenstates. Perturbation theory shows that B_r does not perturb the eigenenergies to leading order. Our numerical results confirm this prediction. However, for sufficiently large g_{eff}, it obviously leads to spin coupling and has an effect on the energies of states that distribute inside the dot, especially the edge states that are strongly localised at the radius of the superconductor.

3.6 Interpretation of the solutions due to the actual magnetic field

In section 3.2.2, we presented results for the electronic structure of electrons in the plane of a DMS on top of an isolated superconducting disk by using the actual magnetic field that satisfies the Maxwell equations. This field gives more reliable results than the model field (2.9) previously considered in Chapter 2, as it gives correct eigenenergies for large $|m|$. However, the energy spectrum is found to be very complex. Approximating the actual field to study the effect of the transverse and radial components of the magnetic field has been considered in section 3.4 and 3.5. We now return to the solutions due to the actual magnetic field, drawing on our new found understanding to interpret and explain the solutions.

Considering the spectrum in figure 3-3, we find that it consists of many energy patterns. The radial component of the actual field B_r couples spin up and spin down components and results in all bound states being spin mixed states. We will consider the behaviour of these states and describe them in terms of the three kinds of spin down eigenstates and four kinds of spin up eigenstates discussed in section 3.4.2. In the following, we focus on the eigenstates in figure 3-3 (b) in

various conditions.

When $|m|$ is sufficiently small and $n = 0$, the lowest energy state for each m separates from others. The corresponding wavefunctions are shown in figure 3-10. These states are strongly localised at the radius of the superconductor as edge states discussed previously. The predominantly spin-up character is due to the normal magnetic field B_z at the radius of the superconductor, acting as an attractive Zeeman potential for spin up states and as a Zeeman barrier for spin down states. The small spin-down character is due to spin mixing by B_r. Obviously, these states are a direct consequence of the concentration of the field at the edge of the superconducting disk.

When $|m|$ is sufficiently large, the eigenenergies resemble Landau levels and approach the Landau levels with increasing values of $|m|$. Examples of the wavefunctions corresponding to these eigenstates are shown in figure 3-11. They mostly distribute outside the dot region. Although they are far from the dot, B_r is still able to induce very small spin down components into the wavefunctions, but the spin expectation values are close to purely spin up. The magnitudes of the spin down components at the radius of the superconductor increase rapidly with decreasing values of $|m|$, and evolve into strongly localised spin down components as shown in figure 3-10 when $|m|$ is small enough. Figure 3-12 illustrates the second-lowest energy eigenstates ($n = 1$) for different m. These have an additional node compared to the $n = 0$ states. Indeed, number of nodes is determined by the radial quantum number n. With decreasing values of $|m|$, it is more difficult to see nodes of the spin down component because of the strong localisation at the superconductor radius.

When $|m|$ is sufficiently small and n is a small nonzero number, the eigenstates are not confined by the concentration of the magnetic field. Examples of these states are shown in figure 3-13, where $n = 1$ states are displayed. The number of nodes of the spin up and spin down wavefunctions is 1, but this is not obvious for the spin down components because of their small magnitude outside the dot. This spin down behaviour is also visible in figure 3-12. Like spin up quantum antidot states, the spin up components distribute mostly outside the dot and decay when they enter into the dot. Figure 3-14 supports the interpretation that the spin up components in figure 3-13 behave like quantum antidot states. According to section 3.4.2, the energies of quantum antidot states must be negative.

Figure 3-14 shows that spin up wavefunctions with negative energies distribute like quantum antidot states, while spin up wavefunctions with positive energies extend both inside and outside the dot like spin up intermediate states. The spin down components in figure 3-13 and 3-14 are confined inside the dot like spin down quantum dot states. Because they only extend over a small region (inside the dot), the spin expectation values are mainly spin up, represented by red and orange dots in figure 3-3 (b). In this case, we can conclude that B_r combines spin up antidot states/intermediate states with spin down quantum dot states to form the eigenstates.

When $|m|$ is sufficiently small but n is a big number, the spin down components will change their distribution, resulting in unpredictable spin expectation. Figure 3-15 shows how we can distinguish the eigenstates in this case from those in the previous one. When $n = 9, 11$, and 13, the spin down components behave like quantum dot states. These values of n are not large enough to be classified into this case. When $n \geq 15$ spin down components are able to extend outside the dot like spin down intermediate states. The spin up components also distribute as spin up intermediate states. Matching the eigenstates in figure 3-15 to the energy levels in figure 3-3 (b), we see that the combination of spin up and spin down intermediate states results in unpredictable spin expectation values. As one can see in figure 3-3 (b), variation in the spin expectation is found when $|m|$ is sufficiently small and n is sufficiently big.

Finally, looking at figure 3-3, we see that the area where there is variation in the spin expectation values becomes larger with increasing value of B_a/B_0. This is because Landau states tend to distribute near the dot more as B_a increases. That is, Landau states have a greater possibility of being perturbed by the inhomogeneous magnetic field due to the superconductor when B_a increases. Looking at figure 3-4, we see that the lowest energy for each m tends to separate from the rest of the spectrum as g_{eff} increases. This is because the g-factor enhances the Zeeman potentials due to B_z. As shown and discussed in section 3.4.2, the energy levels of edge states are sensitive to g_{eff}.

3.7 Summary

In this Chapter, we have extended the study of a magnetic quantum dot in a DMS by considering the actual magnetic field, which is more realistic than the model field used in Chapter 2. We find that the actual field consisting of both normal and radial components, B_z and B_r, is more reliable as it can describe correctly the energies of an electron far from the dot. There are two important differences with the model field in Chapter 2. The first is the concentration of the magnetic field at the edge of the superconductor. This can lead to states that are strongly localised at the edge of the superconductor. The second is B_r. It changes the symmetry of the Hamiltonian and results in spin mixed eigenstates. Studying the effects of the normal and radial components separately has allowed us to understand the complicated spectrum and the behaviour of the spin mixed eigenstates that exist in the presence of the actual field.

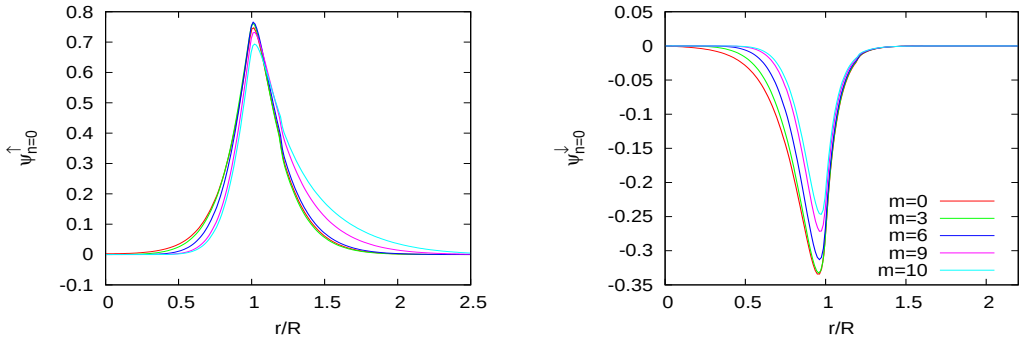

Figure 3-10: The spin up and spin down components of the eigenstates with $n = 0$ for various small $|m|$, when $g_{\text{eff}} = 40$, $z/R = 0.004$, $m^* = 0.5m_e$, and $B_a/B_0 = 1.25$.

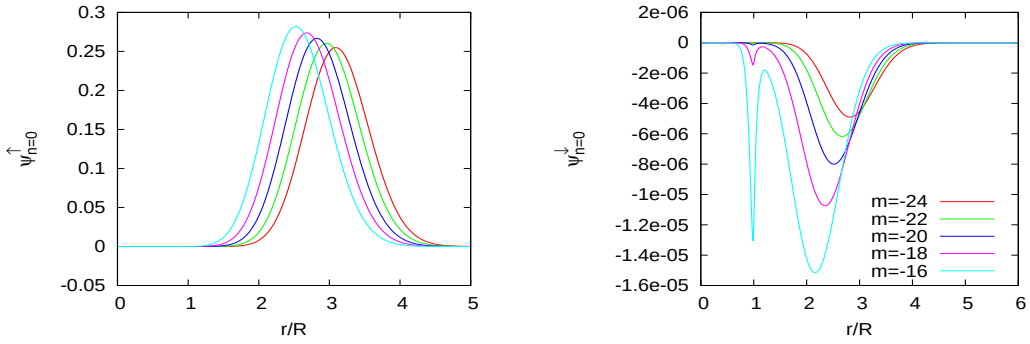

Figure 3-11: The spin up and spin down components of the eigenstates with $n = 0$ for various large $|m|$, when $g_{\text{eff}} = 40$, $z/R = 0.004$, $m^* = 0.5m_e$, and $B_a/B_0 = 1.25$.

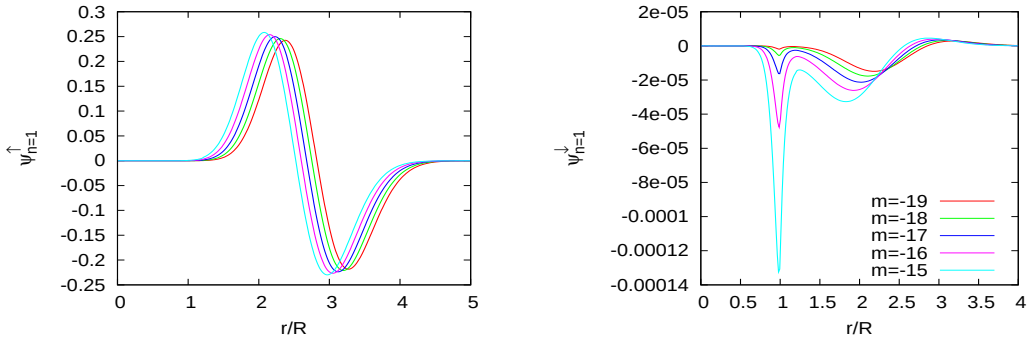

Figure 3-12: The spin up and spin down components of the eigenstates with $n = 1$ for various large $|m|$, when $g_{\text{eff}} = 40$, $z/R = 0.004$, and $m^* = 0.5m_e$, and $B_a/B_0 = 1.25$.

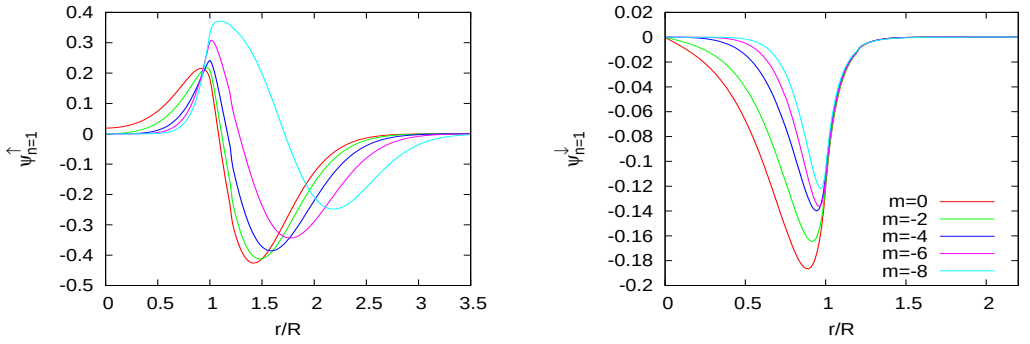

Figure 3-13: The spin up and spin down components of the eigenstates with $n = 1$ for various small $|m|$, when $g_{\text{eff}} = 40$, $z/R = 0.004$, and $m^* = 0.5m_e$, and $B_a/B_0 = 1.25$.

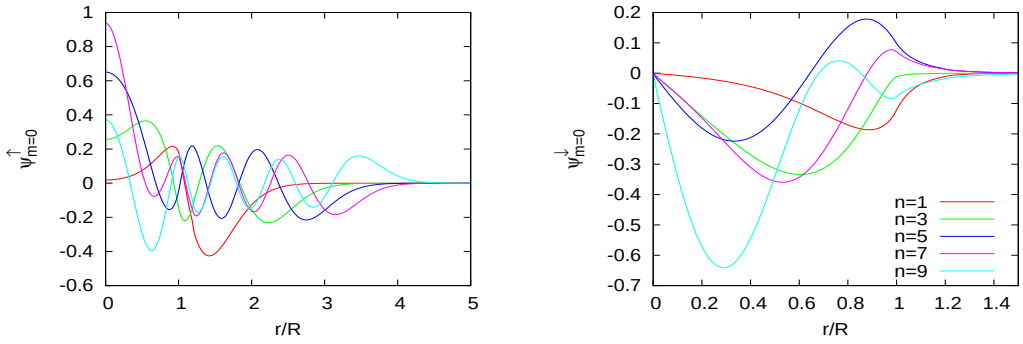

Figure 3-14: The spin up and spin down components of the eigenstates with $m = 0$ for various n, when $g_{\text{eff}} = 40$, $z/R = 0.004$, and $m^* = 0.5m_e$, and $B_a/B_0 = 1.25$. The eigenenergies $E(n, m)$ of the states are $E(1, 0)$=-35.79E_0, $E(3, 0)$=-10.94E_0, $E(5, 0)$=7.35E_0, $E(7, 0)$=23.51E_0, and $E(9, 0)$=37.69E_0.

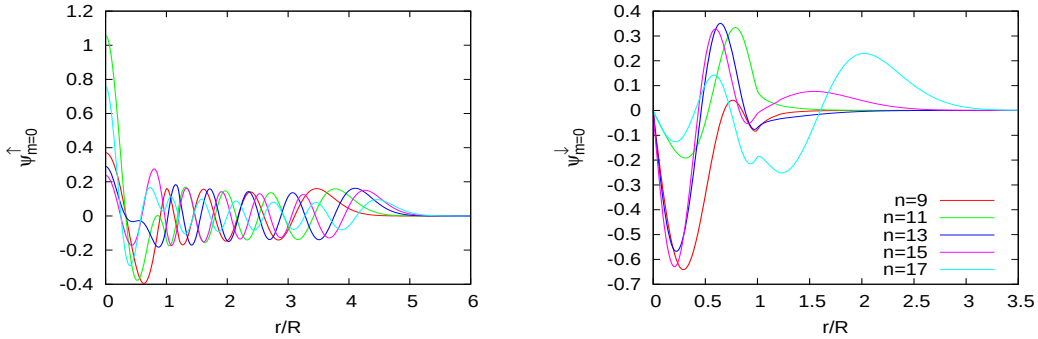

Figure 3-15: The spin up and spin down components of the eigenstates with $m = 0$ for various n, when $g_{\text{eff}} = 40$, $z/R = 0.004$, and $m^* = 0.5m_e$, and $B_a/B_0 = 1.25$. The eigenenergies $E(n, m)$ of the states are $E(9, 0)$=37.69E_0, $E(11, 0)$=52.42E_0, $E(13, 0)$=69.58E_0, $E(15, 0)$=78.40E_0, and $E(17, 0)$=89.75E_0.

Chapter 4

The effect of Abrikosov vortices

We have seen that due to the giant Zeeman effect, a relatively small inhomogeneous magnetic field due to a Meissner state of a superconductor can trap electron states and manipulate the spin texture of the states in an adjacent DMS. Another option is to use a magnetic field due to a vortex state of a type-II superconductor [6]. It is well known that a sufficiently strong uniform external magnetic field can penetrate into type-II superconductors in the form of periodic lattice of vortices as shown in figure 4-1 (a). In a nearby DMS, one benefit of using the field due to superconducting vortices is that the periodicity can be varied by varying the external magnetic field; as an applied field increases, the distance between vortices will decrease. As a result, spin and charge transport properties in hybrid superconductors/DMS systems are expected to be controlled by the external modulating field, enabling novel electronic devices.

In this Chapter, the hybrid illustrated in figure 4-1 (b) consisting of a type-II superconducting film on top of a DMS layer will be discussed. The energy spectrum and wave functions of bound states due to an isolated vortex and the vortex lattice are investigated numerically. This work substantially confirms the findings of Rappoport *et al* [6], but with some differences that are confirmed by developing and applying a tight-binding model to describe the energy bands

4.1 An isolated vortex

In this section, the free carriers inside the DMS quantum well, in the presence of the magnetic field from a single vortex, will be investigated. We start with

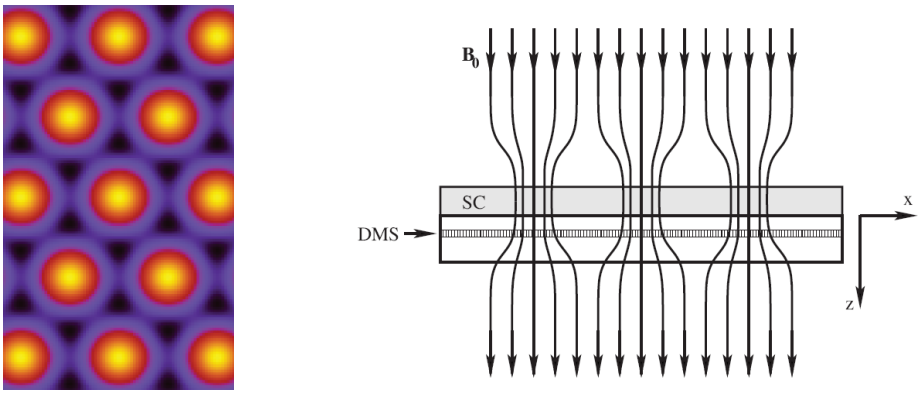

(a) (b)

Figure 4-1: (a) The periodic lattice of vortices in the vortex state of type-II superconductors (b) The hybrid system of a type-II superconducting film and a DMS layer [6]

the fundamental idea of superconducting vortices [16, 60, 61]. On the one hand, type-I superconductors can expel an applied magnetic field, $\vec{B}_a$, out of them by screening currents that flow around the edges of the samples; the screening currents generate a magnetic field in the direction opposite to that of the applied field in order to maintain zero field inside. This phenomenon is the well known Meissner effect. On the other hand, the applied field can penetrate into type-II superconductors, when $B_{C1} < B_a < B_{C2}$, where B_{C1} and B_{C2} are the lower and upper critical field. In this state, the screening currents generate a magnetic field that helps $\vec{B}_a$ pass through type-II superconductors inside the vortex cores. As a result, the external field is converged when it enters a type-II superconductor, and diverged after it passes through (see figure 4-1 (b)). This state is sometimes called the vortex state or mixed state because the central cores are actually normal states, while the other regions are superconducting states. However, the vortices will not enter if $B_a < B_{C1}$. In this phase, type-II superconductors are in the Meissner state similar to type-I superconductors. For a thick superconducting film, the radial and transverse components of the magnetic field from a single vortex in a DMS quantum well have been calculated and are given by [62, 63]:

$$B_r^v(r,z) = B_{\max} \int_0^\infty k\mathrm{d}k \frac{J_1(kr)\exp(-kz - \frac{1}{2}\xi^2 k^2)}{\tau(k+\tau)}, \tag{4.1}$$

$$B_z^v(r,z) = B_{\max}\int_0^\infty k\mathrm{d}k\frac{J_0(kr)\exp(-kz-\frac{1}{2}\xi^2k^2)}{\tau(k+\tau)}, \tag{4.2}$$

where r is the radical distance from the vortex core, z is the distance between the superconducting film and the DMS, $B_{\max} = \frac{\Phi_0}{4\pi\lambda^2} = \frac{\hbar}{2e\lambda^2}$ is the maximum value of the field, $\Phi_0 = h/e$ is the flux quantum, λ and ξ are the penetration depth and the coherence length of the superconductor, $\tau = \sqrt{k^2+\lambda^{-2}}$, and $J_\nu(r)$ is a Bessel function of order ν. Numerically, the exponential terms determine the

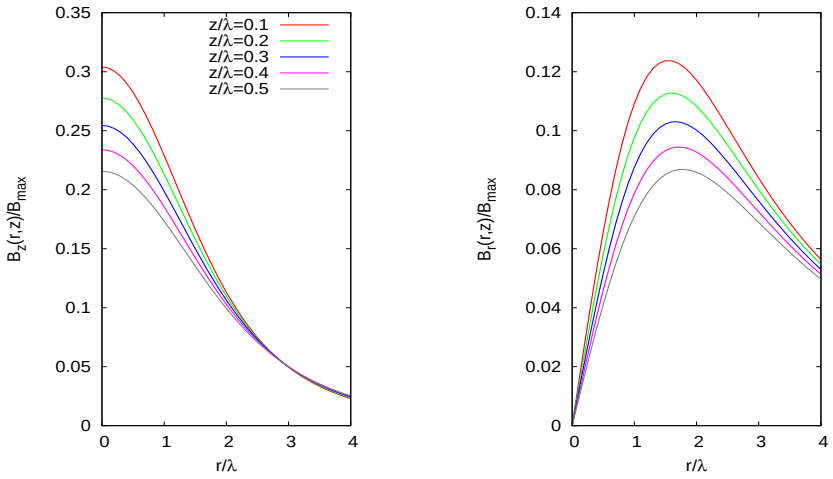

Figure 4-2: The distribution of transverse and radial components of the magnetic field due to a single vortex in Nb: λ=40 nm, ξ=35 nm, for various ratios of z/λ.

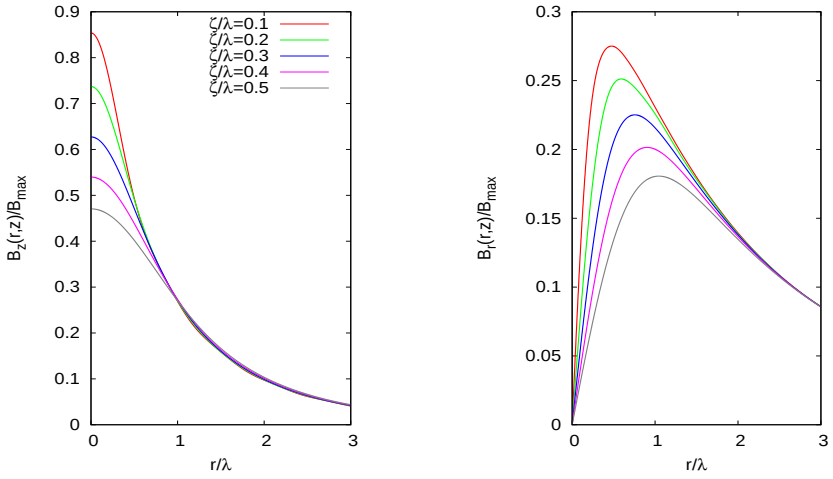

Figure 4-3: The distribution of transverse and radial components of the magnetic field due to a single vortex at $z/\lambda = 0.1$, for various ratios of ξ/λ.

range of integration. Figures 4-2 and 4-3 show the distribution of the calculated magnetic field induced by a superconducting vortex for various ratios of z/λ and ξ/λ respectively. It is clear that for fixed λ, as the ratio z/λ increases B_z and B_r decrease, while B_z and B_r rise when the ratio ξ/λ declines. In the following calculations, we will focus on the parameters corresponding to Nb: λ=40 nm, ξ=35 nm.

4.1.1 Numerical calculation of confined states

Electrons in a DMS underneath an isolated vortex are trapped by the concentrated magnetic field $\vec{B}^v$. We again use the effective mass approximation to describe the electrons, using the Hamiltonian

$$\widehat{H} = \frac{1}{2m^*}\left(\hat{p} + e\vec{A}^v(r;z)\right)^2 - \frac{1}{2}g_{\text{eff}}\mu_B\vec{\sigma}\cdot\vec{B}^v(r;z), \tag{4.3}$$

where z, the distance between the type-II superconducting film and the DMS layer, is just a parameter indicating the magnitude of magnetic field as seen in figure 4-2. The symmetry of the Hamiltonian is similar to that in equation (3.7), so we can deduce that the eigenfunctions also have the from

$$\Psi_m(r,\phi) = \exp(im\phi)\begin{pmatrix}\psi_m^{\uparrow}(r)\\ \psi_{m+1}^{\downarrow}(r)\exp(i\phi)\end{pmatrix}. \tag{4.4}$$

When the Zeeman term is sufficiently large ($g_{\text{eff}} > 500$), we may assume that $\vec{A}^v$ is negligible and rewrite the Hamiltonian in terms of dimensionless parameters to obtain the Schrödinger equation, $\tilde{H}\Psi_m = \varepsilon\Psi_m$, where

$$\tilde{H} = -\tilde{\nabla}^2 - \tilde{g}\vec{\sigma}\cdot\vec{b}^v. \tag{4.5}$$

Here, $r = \tilde{r}\lambda$, $\varepsilon = \frac{E}{E_0}$, $E_0 = \frac{\hbar^2}{2m^*\lambda^2}$, $\vec{b}^v = \vec{B}^v\frac{\Phi_0}{4\pi\lambda^2}$, $\tilde{g} = \frac{g_{\text{eff}}m^*}{4m_e}$, and $\tilde{\nabla} = \frac{1}{\tilde{r}}\frac{\partial}{\partial\tilde{r}}\left(\tilde{r}\frac{\partial}{\partial\tilde{r}}\right) + \frac{1}{\tilde{r}^2}\frac{\partial^2}{\partial\phi^2}$. In the following, it is convenient to drop tilde in the expression of $\tilde{r}$. The general form of eigenfunctions in (4.4) can be rewritten as

$$\Psi_m(r,\phi) = \Psi^{\mu}(r,\phi) = \sum_{\sigma=\pm\frac{1}{2}}\psi_{\mu-\sigma}^{\sigma}(r)e^{i(\mu-\sigma)\phi}\chi_\sigma, \tag{4.6}$$

where $m = \mu - \frac{1}{2}$; $\mu = \pm\frac{1}{2}, \pm\frac{3}{2}, \pm\frac{5}{2}$, etc., and $\chi_\sigma = \binom{1}{0}$ and $\binom{0}{1}$ for $\sigma = \frac{1}{2}$ and $-\frac{1}{2}$ respectively. We then use the basis set methods to turn the Schrödinger equation into a matrix problem as discussed in section 3.2.1. Because the solutions of the field free problem ($\vec{B}^v = 0$) in cylindrical coordinates are Bessel functions, it is convenient to expand $\psi^\sigma_{\mu-\sigma}(r)$ in the complete set of Bessel functions as

$$\psi^\sigma_{\mu-\sigma}(r) = \sum_j a^{\mu\sigma}_j J_{\mu-\sigma}(k_{\mu-\sigma,j} r). \tag{4.7}$$

The Bessel functions vanish at $r = d$, that is, $J_{\mu-\sigma}(k_{\mu-\sigma,j} d) = 0$ or $k_{\mu-\sigma,j} = \alpha_{\mu-\sigma,j}/d$, where $\alpha_{\mu-\sigma,j}$ are the zeros of Bessel functions, so j refers to the order of zero of the Bessel function. Now, $\Psi^\mu(r,\phi)$ can be written as

$$\Psi^\mu(r,\phi) = \sum_j \sum_\sigma a^{\mu\sigma}_j J_{\mu-\sigma}(k_{\mu-\sigma,j} r) e^{i(\mu-\sigma)\phi} \chi_\sigma, \tag{4.8}$$

Numerically, the j summation is truncated at $j_{\max}$ and the distance d is chosen to be the distance beyond the point at which the eigenstates are negligible. After substituting (4.8) into the Schrödinger equation, multiplying from the left by $r J_{\mu-\sigma'}(k_{\mu-\sigma',j'} r) e^{-i(\mu-\sigma')\phi} \chi^\dagger_{\sigma'}$, and integrating from $r = 0$ to $r = d$ and from $\phi = 0$ to $\phi = 2\pi$, for each j' and σ', we obtain

$$\sum_j \sum_\sigma \tilde{H}_{j'\sigma',j\sigma} a^{\mu\sigma}_j = \varepsilon \sum_j \sum_\sigma O_{j'\sigma',j\sigma} a^{\mu\sigma}_j, \tag{4.9}$$

where

$$\begin{aligned} O_{j'\sigma',j\sigma} &= \delta_{\sigma\sigma'} 2\pi \int_0^d r J_{\mu-\sigma'}(k_{\mu-\sigma',j'} r) J_{\mu-\sigma}(k_{\mu-\sigma,j} r) \mathrm{d}r \\ &= \delta_{jj'} \delta_{\sigma\sigma'} \pi d^2 J^2_{\mu-\sigma+1}(k_{\mu-\sigma,j} d), \end{aligned} \tag{4.10}$$

$$\begin{aligned} H_{j'\sigma',j\sigma} &= \delta_{jj'}\delta_{\sigma\sigma'} \pi k^2_{\mu-\sigma,j} d^2 J^2_{\mu-\sigma+1}(k_{\mu-\sigma,j} d) \\ &\quad - 2\sigma\delta_{\sigma\sigma'} \cdot 2\pi\tilde{g} \int_0^d r J_{\mu-\sigma'}(k_{\mu-\sigma',j'} r) b_z(r) J_{\mu-\sigma}(k_{\mu-\sigma,j} r) \mathrm{d}r \\ &\quad - (1-\delta_{\sigma\sigma'}) \cdot 2\pi\tilde{g} \int_0^d r J_{\mu-\sigma'}(k_{\mu-\sigma',j'} r) b_r(r) J_{\mu-\sigma}(k_{\mu-\sigma,j} r) \mathrm{d}r. \end{aligned} \tag{4.11}$$

Note that in order to get (4.10) and (4.11), we use the relations [64]

$$-\nabla^2 J_m(k_{m,j}r)e^{im\varphi} = k_{m,j}^2 J_m(k_{m,j}r)e^{im\varphi} \tag{4.12}$$

and

$$\int_0^1 [J_m(\alpha_{m,j}t)]^2 t\mathrm{d}t = \frac{1}{2}[J_{m+1}(\alpha_{m,j})]^2. \tag{4.13}$$

Equation (4.9) is actually a generalised eigenvalue problem $\tilde{H}a = \varepsilon O a$, where $\tilde{H}$ and O are $2 \times j_{\max}$ dimensional matrices, ε is the eigenvalue, and a, a vector of coefficients $a_j^{\mu\sigma}$, is the eigenvector.

4.1.2 Zeeman-bound states and energies

In this section, we will present the numerical solutions of Schrödinger equation describing the particle in the magnetic field of an isolated vortex, using the numerical method outlined in the previous section. After solving the generalised eigenvalue problem in (4.9) numerically, and using the normalisation condition $\int |\psi_m^{\uparrow}(r)|^2 + |\psi_{m+1}^{\downarrow}(r)|^2 r\mathrm{d}r = 1$, we get Zeeman-bound states and energies as shown in the following figures. In this calculation, we set $z = 0.1\lambda$, $m^* = 0.5m_e$, $g_{\text{eff}} = 500$, and use superconducting parameters corresponding to Nb: $\lambda = 40$ nm and $\xi = 35$ nm. In figure 4-4, the energies E/E_0, converged to six places of decimals, are plotted for various ratios of ξ/λ and z/λ. These require typically 40 basis functions and the distance $d = 10\lambda$. It is clear that the energy becomes increasingly negative as the ratios of ξ/λ and z/λ decrease because Zeeman potential well deepens when ξ/λ and z/λ decrease (see figure 4-2 and 4-3). Figure 4-5 shows the radial components $\psi_m^{\uparrow}(r)$ and $\psi_{m+1}^{\downarrow}(r)$ of the lowest energy states with $m = 0, -1$, and 1. It is found that $\psi_m^{\uparrow}(r)$ is greater than $\psi_{m+1}^{\downarrow}(r)$ for every m because of the huge Zeeman interaction. In figure 4-6, the wavefunctions for the lowest three states ($n = 0, 1, 2$) with $m = 0$ are illustrated. These results indicate the spatial extent of the Zeeman potential well. Moreover, the density of charge $\rho(r)$, the transversal spin density $s_z(r)$, and the radial spin density $s_r(r)$ for the $m = 0, -1$, and 1 states are shown in figure 4-7. Although the basis functions that we use are different from Rappoport [6] who use cubic B splines, the results are similar.

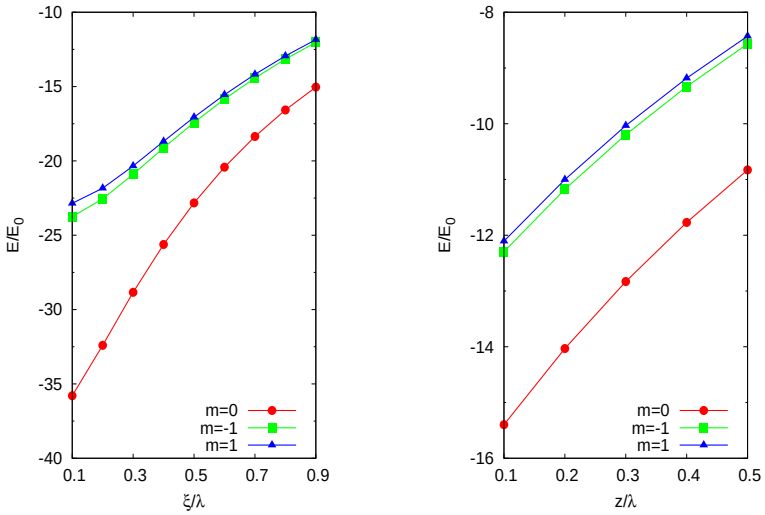

Figure 4-4: Left: The lowest energies E/E_0 for different angular momentum m as a function of ξ/λ, when $z = 0.1\lambda$. Right: The lowest energies E/E_0 for different angular momentum m as a function of z/λ, when $\xi/\lambda = 35/40$.

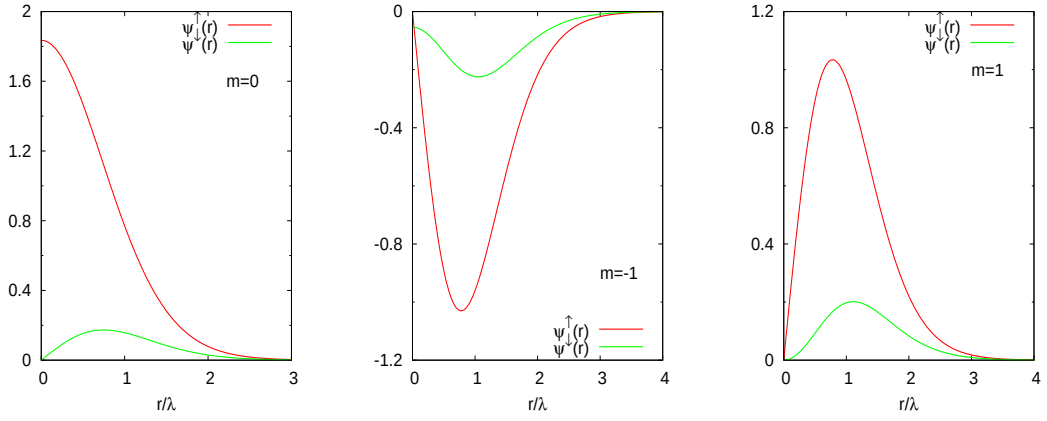

Figure 4-5: The radial components $\psi_m^{\uparrow}(r)$ and $\psi_{m+1}^{\downarrow}(r)$ of the lowest energy states with angular momentum $m = 0$ (left), -1 (center), and 1 (right).

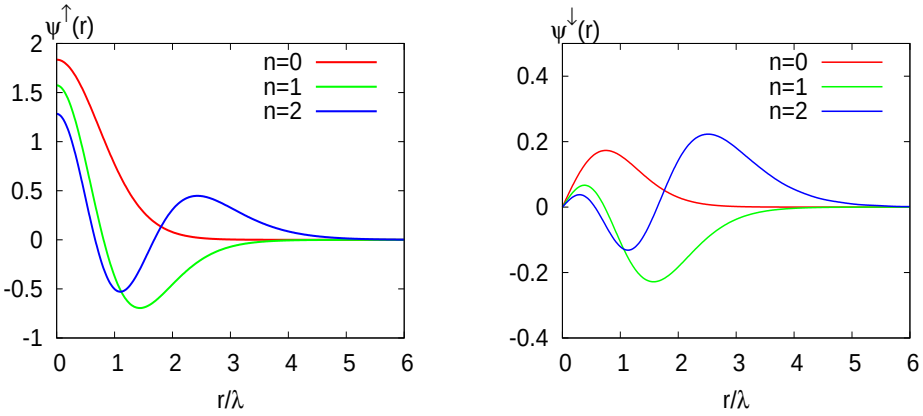

Figure 4-6: The spin up and spin down wavefunctions for the three lowest energy states $(n = 0, 1, 2)$ with $m = 0$.

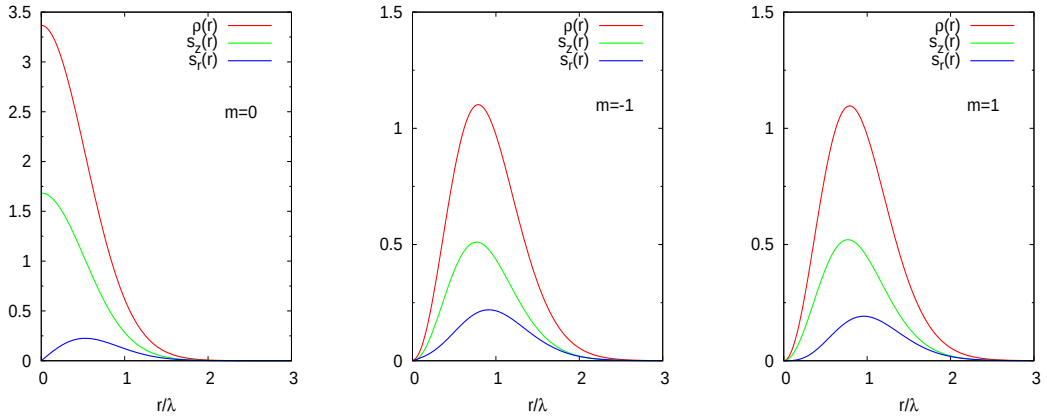

Figure 4-7: The density of charge $\rho(r) = |\psi^{\uparrow}_{m}(r)|^2 + |\psi^{\downarrow}_{m+1}(r)|^2$, the transversal spin density $s_z(r) = \frac{1}{2}(|\psi^{\uparrow}_{m}(r)|^2 - |\psi^{\downarrow}_{m+1}(r)|^2)$, and the radial spin density $s_r(r) = \mathrm{Re}[\psi^{\uparrow}_{m^*}(r)\psi^{\downarrow}_{m+1}(r)]$ of the lowest energy states with $m = 0$ (left), -1 (center), and 1 (right).

4.2 Two dimensional vortex lattice

In the previous section, it was shown that the magnetic field due to an isolated vortex can create spin polarised bound states in a DMS. Here, we consider a periodic array of vortices. We expect the bound states will in general interact and result in a band structure. This system has been previously investigated by Rappoport *et al.* [6].

4.2.1 Vortex lattice

As mentioned before, a type-II superconductor can fully expel an external magnetic field if its strength is less than B_{c1}. Nevertheless, when its value is between B_{c1} and B_{c2}, the superconductor will generate superconducting vortices. In 1957, Abrikosov found that the exact solution of this state is a periodic lattice of vortices, called the Abrikosov vortex phase [12]. In addition, the vortex lattice is actually a triangular lattice as shown in figure 4-8. The primitive translation vectors are $\vec{a} = (a, 0)$ and $\vec{b} = \frac{a}{2}(1, \sqrt{3})$ and the lattice vectors are $\vec{R} = n\vec{a} + m\vec{b}$; n, m are integer. It is generally agreed that the circulating currents flowing around a vortex core serve to screen out the external magnetic field; as a result, each vortex carries a fixed unit of magnetic flux, $\frac{\Phi_0}{2} = h/2e$. If N_v is the number of vortices in superconducting area, A, then the average magnetic field is given by

$$B = \frac{N_v \Phi_0}{2A} = \frac{N_v h}{2eA}. \tag{4.14}$$

The average magnetic field, B, is equal to the external uniform magnetic field, B_a, and there is a vortex per unit cell; therefore, we have

$$B_a = \frac{\Phi_0}{2A_{cell}} = \frac{\Phi_0}{a^2\sqrt{3}}. \tag{4.15}$$

Here, $A_{cell} = a^2\sqrt{3}/2$. Consequently, the external magnetic field , B_a, can control the distance between vortices, a, as shown in figure 4-9. As the field increases, the distance between vortices decreases. Due to the distribution of the magnetic field of each vortex, it appears that the value of this field at the centre of each vortex in figure 4-9 (d) is bigger than others.

The Hamiltonian describing electrons in a DMS in the magnetic field due to

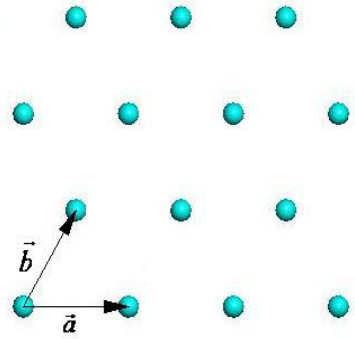

Figure 4-8: A triangular lattice with the primitive translation vectors $\vec{a}$ and $\vec{b}$.

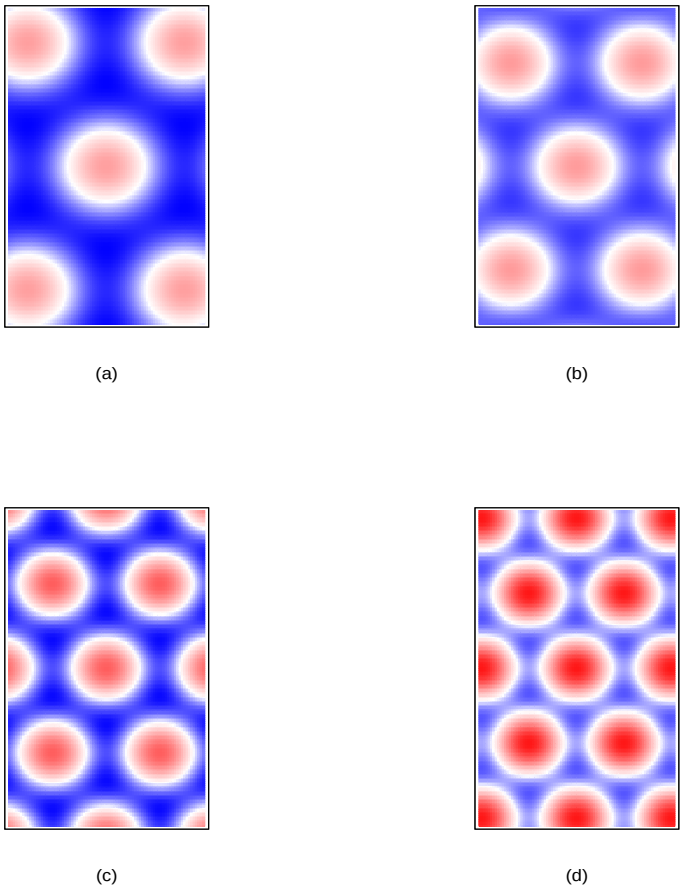

Figure 4-9: The transverse component of the magnetic field from the periodic lattice of vortices for external field B_a of (a) 0.07T, (b) 0.10T, (c) 0.15T, (d) 0.19T of 240×415.69 nm^2

the presence of a periodic lattice of vortices is

$$\widehat{H} = \frac{1}{2m^*}[\hat{p} + e\vec{A}_L(\vec{r};z)]^2 - \frac{1}{2}g_{\text{eff}}\mu_B\vec{\sigma}\cdot\vec{B}_L(\vec{r};z), \tag{4.16}$$

where the carriers are assumed to be electrons, whose charge is $-e$, and $\vec{B}_L$ is the magnetic field from the vortex lattice. We assume this is the summation of the fields for periodically distributed single vortices. Using Fourier analysis, we can write

$$\vec{B}_L(\vec{r};z) = \sum_{\vec{R}} \vec{B}^v(\vec{r}-\vec{R};z) = B_a\hat{z} + \sum_{\vec{G}\neq 0} e^{i\vec{G}\cdot\vec{r}}\vec{B}_{\vec{G}}(z), \tag{4.17}$$

where $\vec{G}$ denotes a reciprocal lattice vector. Similarly, the vector potential of $\vec{B}_L$ can be written as

$$\vec{A}_L(\vec{r}) = \vec{A}_a(\vec{r}) + \sum_{\vec{G}\neq 0} e^{i\vec{G}\cdot\vec{r}}\vec{A}_{\vec{G}}, \tag{4.18}$$

where $\vec{A}_a(\vec{r}) = (0, B_a x, 0)$ in the Landau gauge. However, we will not show $\vec{A}_L$ and $\vec{B}_L$ explicitly in this section. In order to construct the solution of the Hamiltonian (4.16), we will use a superposition method, choosing solutions of the Hamiltonian with the homogeneous field as basis functions. Accordingly, the concept of Landau levels will be discussed in the next section.

4.2.2 Landau levels

The energy levels of a particle in a uniform magnetic field are the "Landau levels" [49] named after L.D. Landau. The Hamiltonian of a free charged particle with charge $-e$ in a DMS in a constant uniform magnetic field is given by

$$\widehat{H} = \frac{(\hat{p} + e\vec{A}_a)^2}{2m^*} - \frac{1}{2}g_{\text{eff}}\mu_B\vec{\sigma}\cdot\vec{B}_a. \tag{4.19}$$

This problem was considered in section 2.1 using the symmetric gauge, appropriate for a system with rotational symmetry. Here, we choose the Landau gauge $\vec{A}_a = (0, B_a x, 0)$ to calculate particle properties in two dimension. Then, the eigenvalue problem becomes

$$\left[\frac{(\hat{p}_y + eB_a x)^2}{2m^*} + \frac{\hat{p}_x^2}{2m^*} - \frac{1}{2}g_{\text{eff}}\mu_B\sigma_z B_a\right]\phi = E\phi. \tag{4.20}$$

There is only the z component of $\vec{\sigma}$ in the Hamiltonian so that $[\widehat{H}, \sigma_z] = 0$. Therefore, the Hamiltonian and $\hat{s}_z$ have simultaneous eigenfunctions which can be written as

$$\phi = \psi(x, y)\chi_\sigma, \tag{4.21}$$

where the eigenstates of σ_z are $\chi_\sigma = \binom{1}{0}$ and $\binom{0}{1}$ for spin up and spin down respectively. Moreover, it is clear that there is no coordinate y in the Hamiltonian so that $\hat{p}_y$ commutes with the Hamiltonian: $\psi(x, y)$ is also an eigenfunction of $\hat{p}_y$. Thus,

$$\psi(x, y) = e^{ik_y y} f(x). \tag{4.22}$$

Inserting (4.22) and (4.21) in (4.20), we obtain

$$\left[\frac{\hat{p}_y^2}{2m^*} + \frac{eB_a x\hat{p}_y}{m^*} + \frac{(eB_a x)^2}{2m^*} + \frac{\hat{p}_x^2}{2m^*} - \frac{1}{2}g_{\text{eff}}\mu_B\sigma_z B_a - E\right] e^{ik_y y} f(x)\chi_\sigma = 0 \tag{4.23}$$

which becomes

$$f''(x)\chi_\sigma + \frac{2m^*}{\hbar^2}\left[-\frac{1}{2}m^*\omega_c^2(x - x_0)^2 + g_{\text{eff}}\mu_B\sigma B_a + E\right] f(x)\chi_\sigma = 0, \tag{4.24}$$

where $\omega_c = \frac{eB_a}{m^*}$, $x_0 = -\hbar k_y/eB_a$, and $\sigma_z\chi_\sigma = 2\sigma\chi_\sigma, \sigma = \pm 1/2$. Compared with the harmonic oscillator, equation (4.24) is similar to the Schrödinger equation for a linear oscillator oscillating with frequency ω_c; hence, energy levels and eigenstates are given by [6]

$$E_{N,\sigma} = (N + \frac{1}{2})\hbar\omega_c - \sigma g_{\text{eff}}\mu_B B_a, \tag{4.25}$$

$$\phi_{N,k_y,\sigma}(x, y) = \frac{1}{\sqrt{N_y b 2^N \ell_B N!\sqrt{\pi}}} e^{ik_y y} e^{-\frac{1}{2}(\frac{x}{\ell_B} + k_y\ell_B)^2} H_N(\frac{x}{\ell_B} + k_y\ell_B)\chi_\sigma, \tag{4.26}$$

where $H_N(x)$ is a Hermite polynomial of N$^{\text{th}}$ degree, $\ell_B = \sqrt{\hbar/eB_a}$ is the magnetic length, N_y is the number of magnetic unit cell in the y direction, and $(N_y b 2^N \ell_B N!\sqrt{\pi})^{-\frac{1}{2}}$ is a normalisation factor.

4.2.3 Magnetic translation operator

If a Hamiltonian consists of a kinetic energy operator and a periodic potential, its eigenstates will satisfy Bloch's theorem [65]. In the following, this theorem

will be discussed briefly. Then, we will return to our particular system, which needs to be described by a specific Bloch's theorem. Eventually, the magnetic translation operator will be introduced to search for eigenfunctions of a periodic potential with a magnetic field.

Consider the Hamiltonian $\widehat{H} = \frac{\hat{p}^2}{2m^*} + V(\vec{r})$, where the potential does not change if $\vec{r}$ is displaced by any lattice translation vector $\vec{R}_i$: $V(\vec{r}) = V(\vec{r} + \vec{R}_i)$. It is convenient to introduce a translation operator $\widehat{T}$ which has the property,

$$\widehat{T}(\vec{R}_i) f(\vec{r}) = f(\vec{r} + \vec{R}_i) \tag{4.27}$$

and it follows that successive application of translation operators satisfies

$$\widehat{T}(\vec{R}_i)\widehat{T}(\vec{R}_j) = \widehat{T}(\vec{R}_j)\widehat{T}(\vec{R}_i) = \widehat{T}(\vec{R}_i + \vec{R}_j). \tag{4.28}$$

Since the Hamiltonian is periodic, it is said to commute with the translation operator

$$\widehat{T}\widehat{H} = \widehat{H}\widehat{T}. \tag{4.29}$$

Accordingly, the eigenstates of the Hamiltonian can be chosen to be simultaneous eigenstates of $\widehat{T}$.

$$\widehat{H}\psi = \varepsilon\psi \tag{4.30}$$

$$\widehat{T}(\vec{R}_i)\psi = c(\vec{R}_i)\psi, \tag{4.31}$$

where c is an eigenvalue. This eigenvalue can be derived straightforwardly:

$$\widehat{T}(\vec{R}_i)\widehat{T}(\vec{R}_j)\psi = c(\vec{R}_j)\widehat{T}(\vec{R}_i)\psi = c(\vec{R}_j)c(\vec{R}_i)\psi$$

$$\widehat{T}(\vec{R}_i)\widehat{T}(\vec{R}_j)\psi = \widehat{T}(\vec{R}_i + \vec{R}_j)\psi = c(\vec{R}_j + \vec{R}_i)\psi$$

$$\therefore \qquad c(\vec{R}_j)c(\vec{R}_i) = c(\vec{R}_j + \vec{R}_i). \tag{4.32}$$

Consequently, we can deduce that

$$c(\vec{R}_i) = e^{i\vec{k}\cdot\vec{R}_i}. \tag{4.33}$$

To summarise, we have reviewed Bloch's theorem, in which eigenstates of a periodic Hamiltonian satisfy

$$\widehat{T}(\vec{R}_i)\psi(\vec{r}) = \psi(\vec{r}+\vec{R}_i) = e^{i\vec{k}\cdot\vec{R}_i}\psi(\vec{r}). \tag{4.34}$$

Now, we consider our system in which the Hamiltonian consists of kinetic energy with a vector potential and a periodic potential as shown in (4.16). It is easy to show that the ordinary translation operators do not commute with the Hamiltonian because in the kinetic term, we have the nonperiodic vector potential, $\vec{A}_a$, which changes after displacement by lattice translation vectors;

$$\widehat{T}(\vec{R}_i)\vec{A}_a(\vec{r}) = \vec{A}_a(\vec{r}+\vec{R}) \neq \vec{A}_a(\vec{r}). \tag{4.35}$$

Accordingly, we need to search for new translation operators that do commute with the Hamiltonian for systems containing a magnetic field. These are called "magnetic translation operators". There are several theoretical works [67, 68, 69] that discuss the problem of two-dimensional Bloch electrons in the presence of an electrostatic, periodic field and a uniform magnetic field. These investigate the magnetic translation operator in various gauges of the magnetic field; however, only the Landau gauge will be presented here. We start to find magnetic translation operators with the Schrödinger equation of a particle without spin.

$$\widehat{H}(\vec{r})\psi(\vec{r}) = \varepsilon\psi(\vec{r}), \tag{4.36}$$

where $\widehat{H}(\vec{r}) = \frac{1}{2m^*}(\hat{p} - Q\vec{A}(\vec{r}))^2$; Q is the charge of a particle. Then, operating $\widehat{T}(\vec{R})$ to both sides of (4.36) to obtain

$$\frac{1}{2m^*}[\hat{p} - Q\vec{A}(\vec{r}+\vec{R})]^2\psi(\vec{r}+\vec{R}) = \varepsilon\psi(\vec{r}+\vec{R}), \tag{4.37}$$

or

$$\frac{1}{2m^*}[\hat{p} - Q\vec{A}'(\vec{r})]^2\psi'(\vec{r}) = \varepsilon\psi'(\vec{r}), \tag{4.38}$$

where $\vec{A}'(\vec{r}) = \vec{A}(\vec{r}+\vec{R})$ and $\psi'(\vec{r}) = \psi(\vec{r}+\vec{R})$. Note that the translation operator does not change the energy. From gauge transformation [66], $\vec{A}'(\vec{r})$ and $\psi'(\vec{r})$ are related to $\vec{A}(\vec{r})$ and $\psi(\vec{r})$ respectively by (see Appendix D)

$$\vec{A}'(\vec{r}) = \vec{A}(\vec{r}+\vec{R}) = \vec{A}(\vec{r}) + \vec{\nabla}\chi(\vec{r},\vec{R}), \tag{4.39}$$

$$\vec{\psi}'(\vec{r}) = \vec{\psi}(\vec{r}+\vec{R}) = \vec{\psi}(\vec{r})\exp\left[i\xi\chi(\vec{r},\vec{R})\right]. \tag{4.40}$$

where $\xi = Q/\hbar$. Then, operating $e^{-i\xi\chi}\widehat{T}(\vec{R})$ to both sides of (4.36) and deriving in the following way:

$$\begin{aligned} e^{-i\xi\chi}\widehat{T}(\vec{R})\widehat{H}\psi &= \varepsilon e^{-i\xi\chi}\widehat{T}(\vec{R})\psi \\ e^{-i\xi\chi}\widehat{T}(\vec{R})\widehat{H}\psi &= \varepsilon\psi \\ e^{-i\xi\chi}\widehat{T}(\vec{R})\widehat{H}\psi &= \widehat{H}\psi \\ e^{-i\xi\chi}\widehat{T}(\vec{R})\widehat{H}\psi &= \widehat{H}e^{-i\xi\chi}\widehat{T}(\vec{R})\psi \end{aligned}$$

$$\therefore \qquad \left[\widehat{H}, e^{-i\xi\chi}\widehat{T}(\vec{R})\right] = 0. \tag{4.41}$$

Now, we have two operators $\widehat{H}$ and $e^{-i\xi\chi}\widehat{T}(\vec{R})$, which commute with each other. The latter is the magnetic translation operator.

$$\widehat{T}_M(\vec{R}) = e^{-i\xi\chi(\vec{r},\vec{R})}\widehat{T}(\vec{R}) \quad ;\xi = Q/\hbar. \tag{4.42}$$

In the Landau gauge, where $\vec{A} = B_a x\hat{j}$, we see from (4.39) that $\chi(\vec{r},\vec{R}) = B_a R_x y$, so we get

$$\widehat{T}_M(\vec{R}) = e^{-i\xi B_a R_x y}\widehat{T}(\vec{R}). \tag{4.43}$$

Then, two magnetic translation operators which act successively give

$$\begin{aligned} \widehat{T}_M(\vec{R})\widehat{T}_M(\vec{R}') &= e^{-i\xi B_a R_x y}\widehat{T}(\vec{R})e^{-i\xi B_a R'_x y}\widehat{T}(\vec{R}') \\ &= e^{-i\xi B_a R_x y}e^{-i\xi B_a R'_x (y+R_y)}\widehat{T}(\vec{R}+\vec{R}') \\ &= e^{-i\xi B_a R'_x R_y}e^{-i\xi B_a y(R_x+R'_x)}\widehat{T}(\vec{R}+\vec{R}') \\ &= e^{-i\xi B_a R'_x R_y}\widehat{T}_M(\vec{R}+\vec{R}') \end{aligned} \tag{4.44}$$

If the exponential term in (4.44) is equal to one, we can calculate the eigenvalue of $\widehat{T}_M$ as we did in the ordinary translation operator case. However, the exponential term is not always one, and in the case of the hexagonal lattice in figure 4-8, we must define a new unit cell for this to be the case. This magnetic unit cell is double the size of the original one, with $\vec{a} = (a, 0)$ and $\vec{b} = (0, b)$ the new primitive translation vectors (see figure 4-10) and $\vec{R} = n\vec{a} + m\vec{b}$ the new lattice vectors, where $b = a\sqrt{3}$. Accordingly, there are two vortices in the unit cell, the first at the origin and the second at the center, $(\frac{\vec{a}+\vec{b}}{2})$. The magnetic

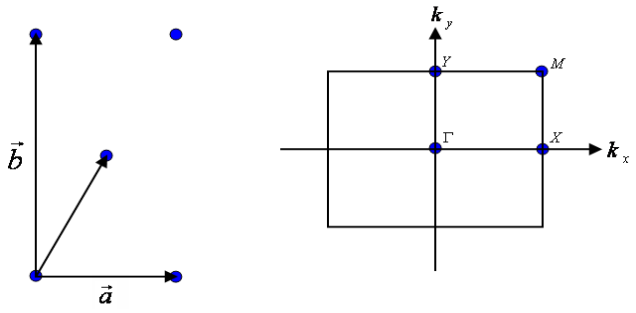

(a) (b)

Figure 4-10: (a) The magnetic unit cell which is twice the size of the previous one. (b) The magnetic Brillouin zone corresponding to (a)

Brillouin zone corresponding to this magnetic unit cell is illustrated in figure 4-10; $k_x \in (-\frac{\pi}{a}, \frac{\pi}{a}]$ and $k_y \in (-\frac{\pi}{b}, \frac{\pi}{b}]$. That is, the reciprocal magnetic lattice vectors are $\vec{G}_{n,m} = n\frac{2\pi}{a}\hat{x} + m\frac{2\pi}{b}\hat{y}$. After changing the unit cell, one can easily find the eigenvalue of the magnetic translation operator as

$$\widehat{T}_M(\vec{R})\psi_{\vec{k}}(\vec{r}) = e^{i(e/\hbar)B_a R_x y}\psi_{\vec{k}}(\vec{r}+\vec{R}) = e^{i\vec{k}\cdot\vec{R}}\psi_{\vec{k}}(\vec{r}). \tag{4.45}$$

Here, the charge of carriers is assumed to be $-e$ and the subscribed $\vec{k}$ is a good quantum number.

4.2.4 Calculation of energy spectrum using the Landau basis

Having understood the translational symmetry of our system, we now search for the eigenfunctions of the Hamiltonian which need to also be eigenstates of the magnetic translation operator. In other words, they must satisfy (4.45) which can be rewritten in terms of the magnetic length as

$$\psi_{\vec{k}}(\vec{r}+\vec{R}) = e^{i\vec{k}\cdot\vec{R}}e^{-iyR_x/\ell_B^2}\psi_{\vec{k}}(\vec{r}). \tag{4.46}$$

As mentioned before, we have changed the original unit cell to be the magnetic unit cell. It follows that we can also write the magnetic length as

$$\ell_B^2 = \frac{ab}{2\pi}. \tag{4.47}$$

In 1992, Pfannkuche and Gerhardts [70] suggested that the following linear combination of Landau level eigenstates satisfy (4.46):

$$\Psi_{N,\vec{k},\sigma}(\vec{r}) = \sum_{\lambda} e^{-ik_x\ell_B^2(k_y+\lambda\frac{2\pi}{b})}\phi_{N,k_y+\lambda\frac{2\pi}{b},\sigma}(\vec{r}). \tag{4.48}$$

Remember, these are solutions of the uniform field problem. Here, $\phi_{N,k_y,\sigma}(\vec{r})$ are the Landau level eigenstates; $\phi_{N,k_y,\sigma} = e^{ik_y y}\Phi_N(\frac{x}{\ell_B} + \ell_B k_y)\chi_\sigma$ (see equation (4.26)). In the following, the effect of translation $\Psi_{\vec{k}}(\vec{r})$ is shown explicitly. We displace $\vec{r}$ by a lattice translation vector $\vec{R}$:

$$\Psi_{N,\vec{k},\sigma}(\vec{r}+\vec{R}) = \sum_{\lambda} e^{-ik_x\ell_B^2(k_y+\lambda\frac{2\pi}{b})}e^{i(y+mb)(k_y+\lambda\frac{2\pi}{b})}\Phi_N\left(\frac{x+na}{\ell_B} + \ell_B(k_y+\lambda\frac{2\pi}{b})\right)\chi_\sigma, \tag{4.49}$$

where $\vec{R} = na\hat{i} + mb\hat{j}$. We note that $\frac{na}{\ell_B} = \ell_B(\frac{na}{\ell_B^2}) = \ell_B n\frac{2\pi}{b}$ and with $\lambda' = \lambda + n$, (4.49) becomes

$$\begin{aligned}
\Psi_{N,\vec{k},\sigma}(\vec{r}+\vec{R}) &= \sum_{\lambda'} e^{-ik_x\ell_B^2(k_y+(\lambda'-n)\frac{2\pi}{b})}e^{i(k_y+(\lambda'-n)\frac{2\pi}{b})(y+mb)} \\
&\quad \times \Phi_N(\frac{x}{\ell_B} + \ell_B(k_y+\lambda' G_y))\chi_\sigma \\
&= e^{ik_x na + ik_y mb - in\frac{2\pi}{b}y}\sum_{\lambda'} e^{-ik_x\ell_B^2(k_y+\lambda'\frac{2\pi}{b})}e^{i(k_y+\lambda'\frac{2\pi}{b})y} \\
&\quad \times \Phi_N(\frac{x}{\ell_B} + \ell_B(k_y+\lambda' G_y))\chi_\sigma \\
&= e^{i\vec{k}\cdot\vec{R}}e^{-iyR_x/\ell_B^2}\Psi_{N,\vec{k},\sigma}(\vec{r}).
\end{aligned} \tag{4.50}$$

As required, the wave functions $\Psi_{N,\vec{k},\sigma}(\vec{r})$ satisfy (4.46), and are therefore eigenstates of the magnetic translation operator. Multiplying by $\frac{1}{\sqrt{N_y}}$, these are orthonormal. Thus, we have

$$\Psi_{N,\vec{k},\sigma}(\vec{r}) = \frac{1}{\sqrt{N_y}}\sum_{\lambda} e^{-ik_x\ell_B^2(k_y+\lambda\frac{2\pi}{b})}\phi_{N,k_y+\lambda\frac{2\pi}{b},\sigma}(\vec{r}). \tag{4.51}$$

We now use these functions to expand the eigenfunctions $\psi_{\vec{k}}(\vec{r})$ of the Hamiltonian containing the non-uniform field:

$$\psi_{\vec{k}}(\vec{r}) = \sum_{N,\sigma} d_{N\sigma}(\vec{k})\Psi_{N,\vec{k},\sigma}(\vec{r}). \tag{4.52}$$

Here $d_{N\sigma}$ are coefficients which indicate the contribution of each Landau level state to the eigenstates, $\psi_{\vec{k}}$. It is obvious to see that the Hamiltonian does not commute with the spin operator $\hat{s}_z$. As a result, spin up and down wave functions need to be included in the sum because the Hamiltonian and $\hat{s}_z$ have no simultaneous eigenfunctions. Recall the Schrödinger equation is

$$\left(\frac{1}{2m^*}(\vec{p}+e\vec{A}_L)^2 - \frac{1}{2}g_{\text{eff}}\mu_B\vec{\sigma}\cdot\vec{B}_L\right)\psi_{\vec{k}'} = E_{\vec{k}'}\psi_{\vec{k}'}. \tag{4.53}$$

The periodic part of the vector potential, $\sum e^{i\vec{G}\cdot\vec{r}}\vec{A}_{\vec{G}}$ (see 4.18), is small when compared with the periodic term of the magnetic field due to the vortex lattice, $\sum e^{i\vec{G}\cdot\vec{r}}\vec{B}_{\vec{G}}(z)$ (see 4.17) because of the huge value of g_{eff}. For this reason, only the nonperiodic part, $\vec{A}_a$, will be included. This approximation gives us

$$-\frac{1}{2}g_{\text{eff}}\mu_B\vec{\sigma}\cdot(\vec{B}_L(\vec{r}) - B_a\hat{z})\psi_{\vec{k}'} = \sum_{N'\sigma'}(E_{\vec{k}'} - E_{N',\sigma'})\psi_{\vec{k}'}, \tag{4.54}$$

where $E_{N',\sigma'}$ are the Landau levels. Next, substituting (4.52) into (4.54), multiplying by $\Psi^{\dagger}_{N,\vec{k},\sigma}$and using the orthonormal property of $\Psi_{N,\vec{k},\sigma}$ gives

$$-\frac{1}{2}g_{\text{eff}}\mu_B\sum_{N'\sigma'}d_{N'\sigma'}(\vec{k})\int\Psi^{\dagger}_{N,\vec{k},\sigma}\vec{\sigma}\cdot(\vec{B_L}(\vec{r}) - B_a\hat{z})\Psi_{N',\vec{k}',\sigma'}\mathrm{d}\vec{r} = (E_{\vec{k}} - E_{N,\sigma})d_{N\sigma}(\vec{k}), \tag{4.55}$$

or

$$-\frac{1}{2}g_{\text{eff}}\mu_B\sum_{N'\sigma'}d_{N'\sigma'}(\vec{k})\vec{\sigma}_{\sigma\sigma'}\cdot\vec{b}_{N,N'} = (E_{\vec{k}} - E_{N,\sigma})d_{N\sigma}(\vec{k}), \tag{4.56}$$

where $\Psi_{N,\vec{k},\sigma} = \Psi_{N,\vec{k}}\chi_\sigma$, $\vec{b}_{N,N'} = \int\Psi^*_{N,\vec{k}}(\vec{B_L}(\vec{r}) - B_a\hat{z})\Psi_{N',\vec{k}'}\mathrm{d}\vec{r}$, and $\vec{\sigma}_{\sigma\sigma'} = \chi^{\dagger}_{\sigma}\vec{\sigma}\chi_{\sigma'}$. From the Fourier expansion in (4.17), $\vec{b}_{N,N'}$ can be written as

$$\vec{b}_{N,N'} = \sum_{\vec{G}\neq 0}\vec{B}_{\vec{G}}(z)\int\Psi^*_{N,\vec{k}}(\vec{r})e^{i\vec{G}\cdot\vec{r}}\Psi_{N',\vec{k}'}(\vec{r})\mathrm{d}\vec{r} \tag{4.57}$$

which gives

$$\vec{b}_{N,N'} = \frac{1}{N_y^2 b\ell_B\sqrt{\pi 2^{N+N'}N!N'!}}\sum_{\lambda\lambda'}\sum_{\vec{G}\neq 0} e^{ik_x\ell_B^2 k_y\lambda}e^{ik'_x\ell_B^2 k'_y\lambda'}\vec{B}_{\vec{G}}(z)\int f(x)\mathrm{d}x\int h(y)\mathrm{d}y, \tag{4.58}$$

where

$$\begin{aligned} h(y) &= e^{i(k'_y-k_y)y}e^{i[G_y+(\lambda'-\lambda)\frac{2\pi}{b}]y}, && (4.59)\\ f(x) &= e^{iG_x x}e^{-\frac{1}{2}(\frac{x}{\ell_B}+\ell_B k_y\lambda)^2}e^{-\frac{1}{2}(\frac{x}{\ell_B}+\ell_B k'_y\lambda')^2} \\ &\quad\times H_N(\frac{x}{\ell_B}+\ell_B k_y\lambda)H_{N'}(\frac{x}{\ell_B}+\ell_B k'_y\lambda'), && (4.60)\\ k_y\lambda &= k_y+\lambda\frac{2\pi}{b}. && (4.61)\end{aligned}$$

In Appendix E, we show that

$$\begin{aligned}\vec{b}_{N,N'} &= \delta_{\vec{k},\vec{k}'}\sqrt{\frac{T!}{S!}}\sum_{\vec{G}\neq 0}\vec{B}_{\vec{G}}(z)(i\sqrt{g})^{S-T}L_T^{S-T}(g)e^{-g/2}e^{i\pi nm}e^{i(k_xG_y-k_yG_x)\ell_B^2} \\ &\quad\times\left(\frac{G_x-iG_y}{G}\right)^{N-N'}, \end{aligned}\tag{4.62}$$

where $\vec{G}=(n\frac{2\pi}{a},m\frac{2\pi}{b})$, $g=\ell_B^2G^2/2$, S (T) is the greatest (smallest) of N and N', and $L_n^m(x)$ are associated Laguerre polynomials. The Fourier components $\vec{B}_{\vec{G}}(z)$ of the magnetic field can be calculated by (4.1), (4.2), and (4.17). It is found that $\vec{B}_{\vec{G}_{nm}}(z)=0$ if $n+m$ is an odd number . Thus,

$$\vec{B}_{\vec{G}}(z)=(-iG_x,-iG_y,G)\frac{B_a e^{-G_z-G^2\xi^2/2}}{G\tau(G\lambda+\tau)}, \tag{4.63}$$

where $\tau=\sqrt{G^2\lambda^2+1}$. In the calculation described below, we will set $z=0.1\lambda$ and use superconducting parameter corresponding to Nb: $\lambda=40$ nm and $\xi=35$ nm. Next, the band structure for the electrons in our system for various values of $\vec{B}_a$ will be shown.

4.2.5 Band structure

After solving the system of linear equations in (4.56) numerically, we obtain the band structure for the electrons in our system for various values of $\vec{B}_a$ as shown in the following tables and figures. It is clear that only $\vec{k}$ is a good quantum number in this system. Thus, mixing of spin, reciprocal lattice vectors, and Landau levels have to be included. Firstly, we show explicitly that $E_{\vec{k}}$ in our calculation converges. Table 4.1, 4.2, and 4.3 show the energies at $\vec{k}$=0 of the lowest and the 15^{th} energy band E_0 and E_{15}, calculated down to eight places of decimals, in different cases. To converge $E_{\vec{k}}$ and $\psi_{\vec{k}}$, reciprocal lattice vectors $\vec{G}$ need to be summed in order to get the precise value of B_L (see (4.17)). In this calculation, we set the maximum magnitude of $\vec{G}$ as $G_{\max}$, so $\vec{G}$ whose magnitude is less than $G_{\max}$ will be summed. One can calculate the numbers of $\vec{G}$ summed as

$$N_G \approx \frac{\pi G_{\max}^2}{(2\pi)^2/ab} = \frac{\ell_B^2 G_{\max}^2}{2}. \tag{4.64}$$

In table 4.1, the distance between vortices is $a = 2.8\lambda$ and the large $G_{\max}$=0.18 nm^{-1} are used to ensure that $E_{\vec{k}}$ converge. This table shows E_{15} needs 100 Landau levels to converge the energy, while E_0 needs less because an excited state normally oscillates more than the ground state. In table 4.2, the distance between vortices is again $a = 2.8\lambda$ and the number of the Landau levels used is 100 which is large enough to converge energies. This table shows insufficient $G_{\max}$ affect both E_0 and E_{15} and they will converge if $G_{\max}$ is large enough ($G_{\max}$=0.13 nm^{-1}, corresponding to $N_G = 29$). Moreover, in table 4.3, the distance between vortices is increased to $a = 3.8\lambda$ and the number of Landau levels is 100. We see that insufficient $G_{\max}$ also affects both E_0 and E_{15}, but a large enough $G_{\max}$ here is 0.08 nm^{-1}, corresponding to $N_G = 30$. Thus, we imply that $N_G = 30$ is a sufficient number of $\vec{G}$ in order to get the precise value of B_L for every value of a. Therefore, at least 30 reciprocal lattice vectors around the origin are used in the calculation of all band structure in figure 4-11. We find $E_{\vec{k}}$ do not change (eight places of decimals) if the number of Landau levels is greater than 150 in figure 4-11 (a), and 50 in figure 4-11 (f).

Looking at the converged band structure, we can understand the results as following. The band structure in a large external magnetic field resembles Landau levels, and it requires fewer Landau levels to calculate it because of the weak

E_0 (meV)	E_{15} (meV)	Numbers of the Landau levels	$G_{\max}$ (nm^{-1})	N_G
−2.72999208	−2.10746389	50	0.18	56
−2.72999208	−2.10746401	70	0.18	56
−2.72999208	−2.10746402	100	0.18	56
−2.72999208	−2.10746402	120	0.18	56

Table 4.1: The lowest and the 15^{th} energy bands E_0 and E_{15} at $\vec{k}$=0 for $a = 2.8\lambda$ and various numbers of the Landau levels

E_0 (meV)	E_{15} (meV)	Numbers of the Landau levels	$G_{\max}$ (nm^{-1})	N_G
−2.72999136	−2.10746362	100	0.11	20
−2.72999206	−2.10746369	100	0.12	24
−2.72999208	−2.10746402	100	0.13	29
−2.72999208	−2.10746402	100	0.14	33

Table 4.2: The lowest and the 15^{th} energy bands E_0 and E_{15} at $\vec{k}$=0 for $a = 2.8\lambda$ and various values of $G_{\max}$ (nm^{-1})

E_0 (meV)	E_{15} (meV)	Numbers of the Landau levels	$G_{\max}$ (nm^{-1})	N_G
−1.15917300	−0.77512977	100	0.06	16
−1.16547699	−0.77624703	100	0.07	23
−1.16836234	−0.77634860	100	0.08	30
−1.16836234	−0.77634860	100	0.09	38

Table 4.3: The lowest and the 15^{th} energy bands E_0 and E_{15} at $\vec{k}$=0 for $a = 3.8\lambda$ and various values of $G_{\max}$ (nm^{-1})

periodic potential. Conversely, the band structure in low external magnetic field resembles the energy levels of Zeeman bound states in section 4.1.2 because a is large. In this state, one can imagine that electrons are trapped in the isolated Zeeman quantum wells because of the the small interaction between them. On the other hand, $\hat{s}_z$ is not a good quantum number. As a consequence, each band consists of mixing of spin; however, due to the large Zeeman interaction, one could expect wave functions in each band to be mostly spin up. Considering all energy bands, we see that one can control the electronic band structure in DMS/type-II superconductors heterostructure by changing the magnitude of external magnetic field, $\vec{B}_a$.

Although these results appear sensible, they are different from those reported by Rappoport [6]. That is because the basis functions in (4.48) are different. The basis functions used in [6] are

$$\Psi_{N,\vec{k},\sigma}(\vec{r}) = \sum_{\lambda} e^{ik_x \lambda a} \phi_{N,k_y+\lambda\frac{2\pi}{b},\sigma}(\vec{r}). \tag{4.65}$$

We cannot show that the basis functions of Rappoport *et al.* are the eigenstates of magnetic translation operators. Thus, we use the basis functions from Pfannkuche and Gerhardts [70] which have been shown to be the eigenstates of magnetic translation operators explicitly. Moreover, $\vec{b}_{N,N'}$ in (E.9) are also different. In their work, there is no $e^{i\pi nm}$ in $\vec{b}_{N,N'}$. Nevertheless, we can obtain the same energy bands as Rappoport *et al.* if we calculate them without $e^{i\pi nm}$ in $\vec{b}_{N,N'}$. It seems that this term is the origin of the differences in results. Therefore, in the next section we will use an independent method to calculate the band structure and to verify whether our energy bands are correct or not.

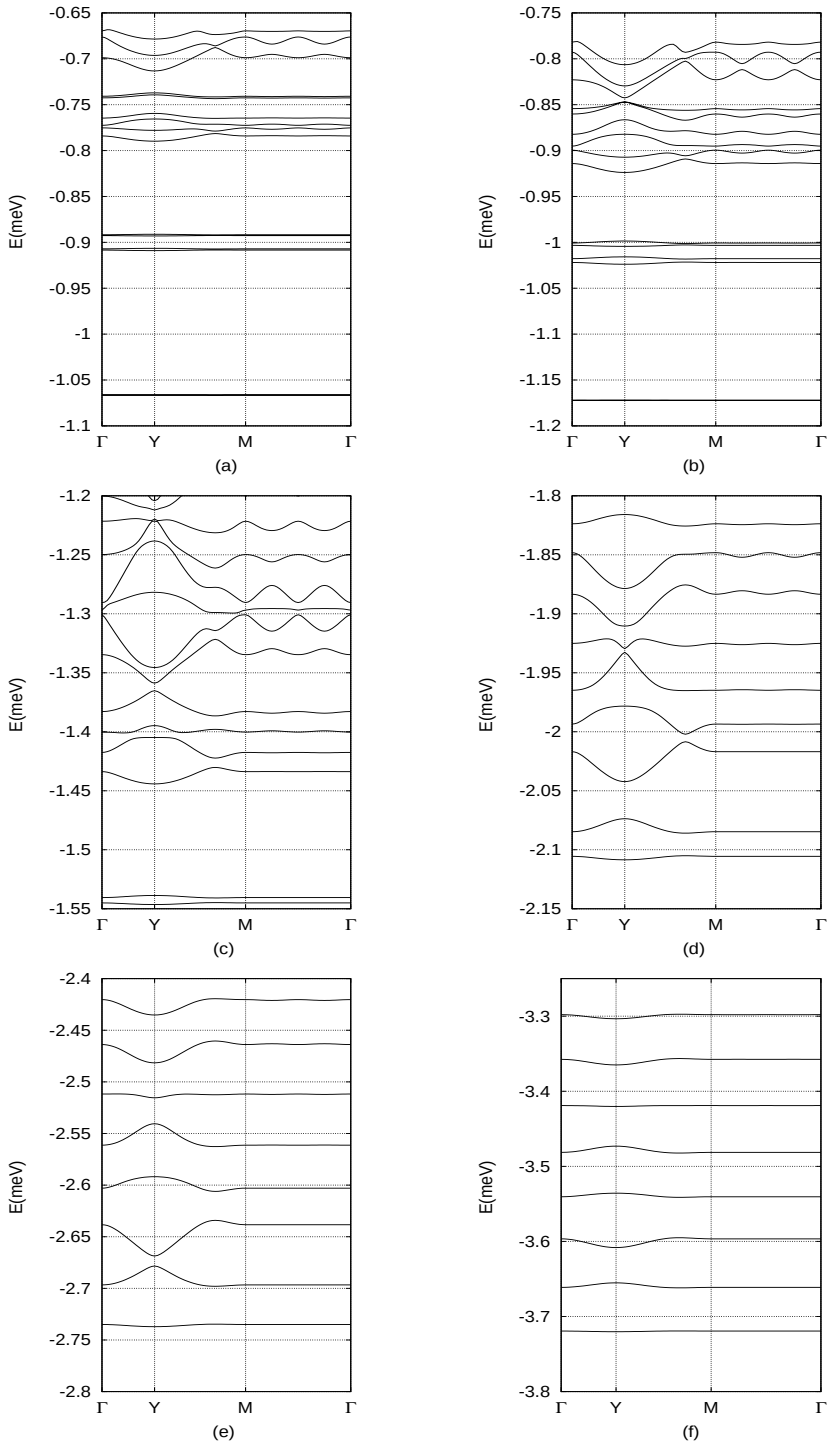

Figure 4-11: Electronic band structure for electrons in a DMS for vortex lattice parameter a of (a) 5.0λ, (b) 4.6λ, (c) 3.8λ, (d) 3.2λ, (e) 2.8λ, and (f) 2.4λ corresponding to applied field $\vec{B}_a$ of (a) 0.06T, (b) 0.07T, (c) 0.10T, (d) 0.15T, (e) 0.19T, and (f) 0.26T.

4.3 Tight-binding model for hybrid superconductor/DMS systems

To confirm our results in the previous section, the tight-binding method [72, 73] is used here to calculate the band structure as section 4.2.5. The concept of this method is that we assume that electrons spend most time bound to a Zeeman potential well. In other words, they slightly tunnel from a Zeeman potential well to others, so that the overlap of an electron state of one Zeeman potential well with that of its neighbours is relatively small. For these reasons, the tight-binding model well describe electron states, when the distance between vortices is large and electrons are in a quite deep quantum well, such as the three lowest states ($m = 0, -1$, and 1). In this section, the tight binding Hamiltonian is derived. For large vortex separation, the eigenvalues are obtained analytically at special values of $\vec{k}$, and used to determine the Hamiltonian matrix elements; these are then used to obtain the energy bands for all $\vec{k}$.

4.3.1 The Hamiltonian matrix elements

We express the wavefunction of electrons in a presence of a vortex lattice as a linear combination of isolated vortex states,

$$\psi(\vec{r}) = \sum_{\vec{R},\tau,m} a_{m\tau\vec{R}} \Psi_m(\vec{r} - \vec{R} - \vec{r_\tau}), \tag{4.66}$$

where $\vec{R} = (na, mb)$ are the magnetic translation vectors, and $\vec{r_\tau} = \tau\left(\frac{a}{2}, \frac{b}{2}\right)$; $\tau = 0$ or 1. In the following, we will use Dirac notation so that (4.66) can be written as

$$|\psi\rangle = \sum_{\vec{R},\tau,m} a_{m\tau\vec{R}} |m, \tau, \vec{R}\rangle. \tag{4.67}$$

In 1994, Graf and Vogl [74] proposed the tight-binding Hamiltonian matrix elements that take into account a magnetic field are

$$\langle \vec{R}'|\widehat{H}^A(\vec{r}, \hat{p} + e\vec{A})|\vec{R}\rangle = \exp\left[\frac{-ie}{\hbar}\int_{\vec{R}}^{\vec{R}'} \vec{A}(\vec{r}) \cdot \mathrm{d}\vec{r}\right] \langle \vec{R}'|\widehat{H}^0(\vec{r}, \hat{p})|\vec{R}\rangle, \tag{4.68}$$

where $\widehat{H}^A$ and $\widehat{H}^0$ are the Hamiltonians with and without a vector potential respectively. Here, we still use the Landau gauge, $\vec{A}_a(\vec{r}) = B_a x\hat{j}$ for the calculation as we did in the previous section, so (4.68) can be written as

$$\langle \vec{R}'|\widehat{H}^A(\vec{r},\hat{p}+e\vec{A})|\vec{R}\rangle = \exp\left[\frac{-ie}{2\hbar}(\vec{R}'-\vec{R})\cdot(\vec{A}_a(\vec{R}')+\vec{A}_a(\vec{R}))\right]\langle \vec{R}'|\widehat{H}^0(\vec{r},\hat{p})|\vec{R}\rangle. \tag{4.69}$$

In our system, electron states are characterised by m, τ, and $\vec{R}$; hence, our Hamiltonian with a vector potential in (4.16) can be written in the form,

$$\begin{aligned}\widehat{H}^A &= \sum_{\vec{R}',\tau',m'}\sum_{\vec{R},\tau,m}|m,\tau,\vec{R}\rangle\exp\left[\frac{-ie}{2\hbar}(\vec{R}_\tau-\vec{R}'_{\tau'})\cdot(\vec{A}_a(\vec{R}_\tau)+\vec{A}_a(\vec{R}'_{\tau'}))\right]\\ &\quad\times\langle m,\tau,\vec{R}|\widehat{H}^0|m',\tau',\vec{R}'\rangle\langle m',\tau',\vec{R}'|,\end{aligned} \tag{4.70}$$

where $\vec{R}_\tau = \vec{R}+\vec{r}_\tau$ and $\widehat{H}^0 = \frac{1}{2m^*}[\hat{p}^2 - \frac{1}{2}g_{\text{eff}}\mu_B\vec{\sigma}\cdot\vec{B}_L]$. As discussed in Section 4.2.3, the ordinary translators $\widehat{T}(\vec{R})$ do not commute with the Hamiltonian with a vector potential, whereas magnetic translation operators $\widehat{T}_M(\vec{R})$ do. In this section, we define magnetic translation operators as

$$\widehat{T}_M(\vec{L}) = \sum_{\vec{R},\tau,m}|m,\tau,\vec{R}\rangle e^{\frac{-ie}{\hbar}\vec{R}_\tau\cdot\vec{A}(\vec{L})}\langle m,\tau,\vec{R}-\vec{L}|, \tag{4.71}$$

where $\vec{L}$ are any magnetic translation vectors. Similar to Section 4.2.3, we can verify explicitly that magnetic translation operators in (4.71) do commute with the Hamiltonian (4.70) and also have the property : $\widehat{T}_M(\vec{L})\widehat{T}_M(\vec{L}') = \widehat{T}_M(\vec{L}+\vec{L}')$. Therefore, we can imply that their eigenvalues are $e^{i\vec{k}\cdot\vec{L}}$. In Appendix F, we show the wavefunctions of electrons in the presence of the field due to a vortex lattice are of the form,

$$|\vec{k}\rangle = \sum_{\tau,m}a_{m,\tau}|m,\tau,\vec{k}\rangle, \tag{4.72}$$

where $|m,\tau,\vec{k}\rangle = \dfrac{1}{\sqrt{N}}\displaystyle\sum_{\vec{R}}e^{-i\vec{k}\cdot\vec{R}}e^{-i\frac{e}{\hbar}\vec{r}_\tau\cdot\vec{A}_a(\vec{R})}|m,\tau,\vec{R}\rangle$; N is the number of unit cells.

Therefore, the Schrödinger equation is

$$\widehat{H}^A|\vec{k}'\rangle = E_{\vec{k}'}|\vec{k}'\rangle. \tag{4.73}$$

Multiplying from the left by $\langle m,\tau,\vec{k}|$ gives

$$\begin{aligned}\sum_{\tau',m'} a_{m'\tau'}\langle m,\tau,\vec{k}|\widehat{H}^A|m',\tau',\vec{k}'\rangle &= E_{\vec{k}'}\sum_{\tau',m'} a_{m'\tau'}\langle m,\tau,\vec{k}|m',\tau',\vec{k}'\rangle \\ &= E_{\vec{k}}a_{m\tau}\delta_{\vec{k}\vec{k}'}. \end{aligned} \tag{4.74}$$

Now, (4.74) can be turned into a generalised eigenvalue problem; however, the matrix elements $\langle m',\tau',\vec{k}'|\widehat{H}^A|m,\tau,\vec{k}\rangle$ are need to be determined. Instead of (4.72), we will use

$$|m,\tau,\vec{k}\rangle = \frac{1}{\sqrt{N}}\sum_{\vec{R}} e^{-i\vec{k}\cdot\vec{R}_\tau}e^{-\frac{ie}{\hbar}\vec{r}_\tau\cdot\vec{A}_a(\vec{R})}|m,\tau,\vec{R}\rangle. \tag{4.75}$$

We ensure that $|m,\tau,\vec{k}\rangle$ in (4.75) are the eigenstates of $\widehat{T}_M(\vec{L})$ and are also orthonormal as $|m,\tau,\vec{k}\rangle$ in (4.72). From (4.70) and (4.75), the matrix elements are

$$\begin{aligned}\langle m,\tau,\vec{k}|\widehat{H}^A|m',\tau',\vec{k}'\rangle &= \frac{1}{N}\sum_{\vec{R}\vec{R}'} e^{i\vec{k}\cdot\vec{R}_\tau}e^{\frac{ie}{\hbar}\vec{r}_\tau\cdot\vec{A}_a(\vec{R})}e^{-i\vec{k}'\cdot\vec{R}'_{\tau'}}e^{-\frac{ie}{\hbar}\vec{r}_{\tau'}\cdot\vec{A}_a(\vec{R}')} \\ &\quad\times\langle m,\tau,\vec{R}|\widehat{H}^A|m',\tau',\vec{R}'\rangle \\ &= \frac{1}{N}\sum_{\vec{R}\vec{R}'} e^{i\vec{k}\cdot\vec{R}_\tau}e^{-i\vec{k}'\cdot\vec{R}'_{\tau'}}e^{\frac{ie}{\hbar}(\vec{r}_\tau\cdot\vec{A}_a(\vec{R})-\vec{r}_{\tau'}\cdot\vec{A}_a(\vec{R}'))} \\ &\quad\times e^{-\frac{ie}{2\hbar}(\vec{R}_\tau-\vec{R}_{\tau'})\cdot[\vec{A}_a(\vec{R}_\tau)+\vec{A}_a(\vec{R}'_{\tau'})]} \\ &\quad\times\langle m,\tau,\vec{R}-\vec{R}',|\widehat{H}^0|m',\tau',0\rangle. \end{aligned} \tag{4.76}$$

Note that $\langle m,\tau,\vec{R}|\widehat{H}^0|m',\tau',\vec{R}'\rangle = \langle m,\tau,\vec{R}-\vec{R}'|\widehat{H}^0|m',\tau',0\rangle$ because of the symmetry of the Hamiltonian without $\vec{A}$: $\widehat{H}^0(\vec{r}-\vec{R}) = \widehat{H}^0(\vec{r})$. Then, using the relations $e^{-\frac{ie}{\hbar}\vec{R}\cdot\vec{A}_a(\vec{R})} = e^{-\frac{ie}{\hbar}B_a abmn} = e^{i2\pi mn} = 1$ and $\sum_{\vec{R}} e^{i(\vec{k}'-\vec{k})\cdot\vec{R}} = N\delta_{k\vec{k}'}$, we obtain

$$\begin{aligned}\langle m,\tau,\vec{k}|\widehat{H}^A|m',\tau',\vec{k}'\rangle &= \delta_{\vec{k}\vec{k}'}\sum_{\vec{R}} e^{i(\vec{k}\cdot\vec{R}_\tau-\vec{k}\cdot\vec{r}_{\tau'}+\frac{e}{\hbar}\vec{r}_\tau\cdot\vec{A}_a(\vec{R}))}e^{-\frac{ie}{2\hbar}(\vec{R}_\tau-\vec{r}_{\tau'})\cdot[\vec{A}_a(\vec{R}_\tau)+\vec{A}_a(\vec{r}_{\tau'})]} \\ &\quad\times\langle m,\tau-\tau',\vec{R}|\widehat{H}^0|m',0,0\rangle. \end{aligned} \tag{4.77}$$

In the spirit of the nearest neighbour approximation, we will calculate the matrix elements from the nearest electron states localised around the origin. For the

vortex lattice arranged in a triangular lattice, each vortex is surrounded by 6 nearest neighbour vortices. As a result, $\Psi_m(\vec{r})$ and $\Psi_m(\vec{r}-\vec{s}_n)$ are included in the calculation of matrix elements, where $\vec{s}_n = a(\cos\phi_n, \sin\phi_n)$ with n an integer from 0 to 5 and $\phi_n = \frac{n\pi}{3}$. When $\Psi_m(\vec{r})$ are calculated, $\vec{R}+\vec{r}_\tau-\vec{r}_{\tau'}=0$. Therefore, $\langle m,\tau-\tau',\vec{R}|\widehat{H}^0|m',0,0\rangle$ in (4.77) can be written as

$$\begin{aligned}\langle m,0,0|\widehat{H}^0|m',0,0\rangle &= \langle m,0,0|\widehat{H}^{iso}|m',0,0\rangle + \langle m,0,0|\Delta\widehat{H}|m',0,0\rangle \\ &= E_m + dE_m = \bar{E}_m, \end{aligned} \tag{4.78}$$

where $\widehat{H}^{iso}$ is the Hamiltonian without $\vec{A}^v$ of isolated vortex states in (4.3), E_m are the energies of the isolated vortex states calculated in section 4.1.2, and $dE_m = \langle m,0,0|\Delta H|m',0,0\rangle$. On the other hand, when $\Psi_m(\vec{r}-\vec{s}_n)$ are calculated, $\vec{R}+\vec{r}_\tau-\vec{r}_{\tau'}=\vec{s}_n$. We have

$$\begin{aligned}\langle m,\tau-\tau',\vec{R}|\widehat{H}^0|m',0,0\rangle &= \langle m,\vec{s}_n|\widehat{H}^0|m',0,0\rangle \\ &= \langle m,\vec{s}_n|\widehat{H}_{iso}|m',0,0\rangle + \langle m,\vec{s}_n|\Delta H|m',0,0\rangle \\ &= E_{m'}\langle m,\vec{s}_n|m',0,0\rangle + t^n_{mm'} \\ &= E_{m'}S^n_{mm'} + t^n_{mm'} \approx t^n_{mm'}, \end{aligned} \tag{4.79}$$

where $S^n_{mm'}$ known as the overlap integrals indicate the overlap between electron states and $t^n_{mm'}$ known as transfer integrals indicate how easy an electron transfers from one vortex to another one. In Appendix F, we assumed that $S^n_{mm'}=0$, so (4.79) may be approximate as $t^n_{mm'}$.

4.3.2 The transfer integrals

In this section, the transfer integrals will be investigated in order to find the relations between $t^n_{mm'}$, $t^0_{mm'}$, and $t^n_{m'm}$. These relations are important for constructing the tight-binding Hamiltonian both analytically and numerically. We start with relation between $t^n_{mm'}$ and $t^0_{mm'}$.

$$\begin{aligned} t^n_{mm'} &= \langle m,\vec{s}_n|\Delta H|m',0,0\rangle \\ &= -\frac{1}{2}g_{\text{eff}}\mu_B\langle m,\vec{s}_n|\vec{\sigma}\cdot\Delta\vec{B}(\vec{r})|m',0,0\rangle, \end{aligned} \tag{4.80}$$

where $\Delta\vec{B}(\vec{r}) = \vec{B}_L(\vec{r}) - \vec{B}^v(\vec{r})$. Because $\vec{\sigma}\cdot\Delta\vec{B}(\vec{r}) = \sigma_x\Delta B_x + \sigma_y\Delta B_y + \sigma_z\Delta B_z$, we can write

$$t^n_{mm'} = -\frac{1}{2}g_{\text{eff}}\mu_B(\Delta\mathfrak{H}^n_z + \Delta\mathfrak{H}^n_{xy}), \tag{4.81}$$

where $\Delta\mathfrak{H}^n_z = \langle m, \vec{s}_n|\sigma_z\Delta B_z|m', 0, 0\rangle$ and $\Delta\mathfrak{H}^n_{xy} = \langle m, \vec{s}_n|\sigma_x\Delta B_x + \sigma_y\Delta B_y|m', 0, 0\rangle$. $|m, \vec{s}_n\rangle$ and $|m', 0, 0\rangle$ are actually the isolated vortex states localised at $\vec{s}_n$ and the origin respectively, so $\Delta\mathfrak{H}^n_z$ can be written as

$$\begin{aligned}
\Delta\mathfrak{H}^n_z &= \int \Psi^\dagger_m(\vec{r} - \vec{s}_n)\begin{pmatrix}\Delta B_z & 0\\ 0 & -\Delta B_z\end{pmatrix}\Psi_{m'}(\vec{r})\mathrm{d}\vec{r} \\
&= \int e^{-im\phi_{\vec{r}-\vec{s}_n}}e^{im'\phi_{\vec{r}}}[\psi^\uparrow_m(|\vec{r} - \vec{s}_n|)]^*\Delta B_z(\vec{r})\psi^\uparrow_{m'}(r)\mathrm{d}\vec{r} \\
&\quad - \int e^{-im\phi_{\vec{r}-\vec{s}_n}}e^{im'\phi_{\vec{r}}}[\psi^\downarrow_{m+1}(|\vec{r} - \vec{s}_n|)]^*\Delta B_z(\vec{r})\psi^\downarrow_{m'+1}(r)e^{-i\phi_{\vec{r}-\vec{s}_n}}e^{i\phi_{\vec{r}}}\mathrm{d}\vec{r}.
\end{aligned} \tag{4.82}$$

Next, we set $\phi_{\vec{r}} = \phi_{\vec{r}'} + \phi_n$ and $\vec{r} = \hat{R}_n\vec{r}'$, where $\hat{R}_n$ is the rotation operator which rotates any vectors by ϕ_n. Then, we have $e^{-im\phi_{\vec{r}-\vec{s}_n}} = e^{-im\phi_{\vec{r}'-\vec{s}_0}}e^{-im\phi_n}$, $|\vec{r} - \vec{s}_n| = |\vec{r}' - \vec{s}_0|$, and $\Delta B_z(\vec{r}) = \Delta B_z(\vec{r}')$. Now (4.82) becomes

$$\Delta\mathfrak{H}^n_z = e^{i\phi_n(m'-m)}\Delta\mathfrak{H}^0_z. \tag{4.83}$$

Similarly, we also get

$$\Delta\mathfrak{H}^n_{xy} = e^{i\phi_n(m'-m)}\Delta\mathfrak{H}^0_{xy}. \tag{4.84}$$

Thus,

$$\begin{aligned}
t^n_{mm'} &= -\frac{1}{2}g_{\text{eff}}\mu_B e^{i\phi_n(m'-m)}(\Delta\mathfrak{H}^0_z + \Delta\mathfrak{H}^0_{xy}) \\
&= e^{i\phi_n(m'-m)}t^0_{mm'}.
\end{aligned} \tag{4.85}$$

We find (4.85) shows the relation between $t^0_{mm'}$ and $t^n_{mm'}$. Moreover, we also establish that $t^0_{mm'}$ are always real and $t^n_{mm'}$ are also real if $m = m'$. Next, we will find the relationship between $t^n_{mm'}$ and $t^n_{m'n}$ by using the assumption which was discussed in Appendix F. That is, the overlap between electron states is

negligible ($s^n_{mm'} \approx 0$).

$$\begin{aligned} t^n_{mm'} &= \int \Psi^\dagger_m(\vec{r}-\vec{s}_n)\Delta H(\vec{r})\Psi_{m'}(\vec{r})\mathrm{d}\vec{r} \\ &= \int \Psi^\dagger_m(\vec{r}-\vec{s}_n)\widehat{H}^0(\vec{r})\Psi_{m'}(\vec{r})\mathrm{d}\vec{r} - \int \Psi^\dagger_m(\vec{r}-\vec{s}_n)\widehat{H}_{iso}\Psi_{m'}(\vec{r})\mathrm{d}\vec{r} \end{aligned} \quad (4.86)$$

Changing $\vec{r}$ to $\vec{r}+\vec{s}_n$ and using the symmetry of the Hamiltonian : $\widehat{H}^0(\vec{r}+\vec{s}_n) = \widehat{H}^0(\vec{r})$ gives

$$\begin{aligned} t^n_{mm'} &= \int \Psi^\dagger_m(\vec{r})\widehat{H}^0(\vec{r})\Psi_{m'}(\vec{r}+\vec{s}_n)\mathrm{d}\vec{r} \\ &= \left[\int \Psi^\dagger_{m'}(\vec{r}+\vec{s}_n)(\widehat{H}_{iso}+\Delta H)\Psi_m(\vec{r})\mathrm{d}\vec{r}\right]^* \\ &= \left[t^{n+3}_{m'm}\right]^*. \end{aligned} \quad (4.87)$$

Inserting (4.85) into (4.87) gives

$$\begin{aligned} t^n_{mm'} &= \left[e^{i\phi_{n+3}(m-m')}t^0_{m'm}\right]^* \\ &= (-1)^{m-m'}\left[t^n_{m'm}\right]^*. \end{aligned} \quad (4.88)$$

The relations in equations (4.85) and (4.88) will be used to construct the Hamiltonian matrix in the next section.

4.3.3 The tight-binding Hamiltonian

As discussed in Section 4.2.5, when the distance between vortices is large, the band structure tends to the energy level of the states trapped in an isolated Zeeman potential well, especially the three lowest energy bands in figure 4-11 (a). For this reason, we expect that the tight-binding model can describe these three lowest bands because of the small overlap between electron states. In isolated vortex states, the three lowest energies are the energies of the ground state ($m = 0$) and the first two excited trapped states ($m = \pm 1$). Thus, the lowest band in figure 4-11 (a) is probably obtained by the isolated vortex states $m = 0$, while the other two bands (we will call them the second and the third energy bands) should be obtained by the isolated vortex states $m = \pm 1$. However, from our previous analysis, m is not a good quantum number. In other words, we

cannot calculate electron states and energies by only using a single value of m. In the tight-binding method, the distance between vortices is assumed to be large so that ΔH, which is proportional to $\sum_{\tau\neq 0}\sum_{\vec{R}\neq 0}\vec{B}^v(\vec{r}-\vec{r}_\tau-\vec{R})$, is small because of the small distribution of the magnetic field from vortices. Thus ΔH could be considered to be the perturbing Hamiltonian. From perturbation theory, we have

$$\widehat{H}_{iso}\Psi_m = E_m\Psi_m$$

$$(\widehat{H}_{iso}+\Delta H)\Psi'_m = E'_m\Psi'_m$$

$$E'_m = E_m + \langle\Psi_m|\Delta H|\Psi_m\rangle + \sum_{n\neq m}\frac{\langle\Psi_m|\Delta H|\Psi_n\rangle\langle\Psi_n|\Delta H|\Psi_m\rangle}{E_m-E_n}. \tag{4.89}$$

Equation (4.89) suggests that if $E_m - E_n$ is large, Ψ_n can be neglected in the calculation of E'_m. For this reason, although m is not a good quantum number, the isolated vortex states, $m = 0$, can be used to calculate the lowest band in figure 4-11 (a) because there is a large gap between energy bands ($E_0 - E_{\pm 1}$ is large). Moreover, $E_{\pm 1} - E_{\pm 2}$ is large so that the isolated vortex states, $m = \pm 1$, can be used to calculate the second and the third energy bands. Nevertheless, either the states $m = 1$ or $m = -1$ cannot describe those two energy bands because $E_{+1} - E_{-1}$ is small. In fact, each band in these three lowest energy bands consists of two nearly degenerate bands which we cannot see clearly in figure 4-11 (a). However, they can be seen obviously when we focus on these energy bands in the next section.

In the follow, the concept to construct the electronic energy structure will be shown. We divide the concept into two cases: The lowest energy band case, and the second and third energy band case.

Case I: the lowest energy band

We start by finding the Hamiltonian for a fixed value of $\vec{k}$. In this calculation, we choose $\vec{k} = 0$ for convenience. Because this energy band can be calculated by the isolated vortex states $m = 0$, one could expect that the Hamiltonian is a two dimensional matrix. From the matrix elements (4.77) and the relation (4.85), we derive it straightforwardly:

$$\widehat{H} = \begin{pmatrix} \bar{E}_0 + 2t^0_{00} & 0 \\ 0 & \bar{E}_0 - 2t^0_{00} \end{pmatrix} \tag{4.90}$$

and its eigenvalues are

$$E = \bar{E}_0 \pm 2t^0_{00}. \tag{4.91}$$

Remember that this energy band actually consists of two nearly degenerate bands, so we get two eigenvalue at $\vec{k} = 0$. Next, we set these eigenvalues to be equal to the energies at $\vec{k} = 0$ obtained by Landau basis in section 4.2.5 or obtained by experiments. Then, solve the equation system in order to get $\bar{E}_0$ and t^0_{00}. Suppose E_1 and E_2 are the energies obtained by Landau basis, where $E_2 > E_1$. Because t^0_{00} is negative, $\bar{E}_0$ and t^0_{00} can be written as

$$\bar{E}_0 = (E_1 + E_2)/2 \tag{4.92}$$

$$t^0_{00} = (E_1 - E_2)/4. \tag{4.93}$$

After that, we use $\bar{E}_0$ and t^0_{00} from (4.92) and (4.93) to construct numerically the Hamiltonian for various values of $\vec{k}$ and obtain the lowest energy bands which will be discussed in the next section.

Case II : the second and the third energy bands

Similar to case I, we start by finding the Hamiltonian with $\vec{k} = 0$. Because these energy bands can be calculated by the isolated vortex states $m = \pm 1$, one could expect that the Hamiltonian is a four dimensional matrix. From the matrix elements (4.77) and the relation (4.85) and (4.88), we derive it straightforwardly:

$$\widehat{H} = \begin{pmatrix} \bar{E}_{-1} + 2t^0_{-1-1} & 0 & 2t^0_{-1+1} & 0 \\ 0 & \bar{E}_{-1} - 2t^0_{-1-1} & 0 & -2t^0_{-1+1} \\ 2t^0_{-1+1} & 0 & \bar{E}_1 + 2t^0_{11} & 0 \\ 0 & -2t^0_{-1+1} & 0 & \bar{E}_1 - 2t^0_{11} \end{pmatrix} \tag{4.94}$$

This Hamiltonian has four eigenvalues, but we have five parameters : $\bar{E}_{-1}, \bar{E}_1, t^0_{-1-1}$,t^0_{-1+1}, and t^0_{1+1}. That is, we need one more eigenvalue to be able to fit the parameters to experimental or theoretical data. Thus, we construct another Hamiltonian with $\vec{k} = \mathrm{X}$ (see figure 4-10 (b)), which is

$$\widehat{H} = \begin{pmatrix} \bar{E}_{-1} + 2t^0_{-1-1} & -4it^0_{-1-1}\sin\frac{\pi}{4} & -2t^0_{-1+1} & 4it^0_{-1+1}\sin\frac{5\pi}{12} \\ 4it^0_{-1-1}\sin\frac{\pi}{4} & \bar{E}_{-1} + 2t^0_{-1-1} & 4it^0_{-1+1}\sin\frac{\pi}{12} & 2t^0_{-1+1} \\ -2t^0_{-1+1} & -4it^0_{-1+1}\sin\frac{\pi}{12} & \bar{E}_1 - 2t^0_{11} & -4it^0_{11}\sin\frac{\pi}{4} \\ -4it^0_{-1+1}\sin\frac{5\pi}{12} & 2t^0_{-1+1} & 4i\sin t^0_{11}\sin\frac{\pi}{4} & \bar{E}_1 + 2t^0_{11} \end{pmatrix} \quad (4.95)$$

Now, we have five parameters and eight eigenvalues. After finding their eigenvalues, we set four eigenvalues of $\widehat{H}$ in (4.94) and the lowest eigenvalues of $\widehat{H}$ in (4.95) to be equal to four energies at $\vec{k} = 0$ obtained in the calculation using the Landau basis in section 4.2.5, and equal to the lowest energy at $\vec{k} = \mathrm{X}$. Now, we have the equation system consisting of five parameters and five equations. After that, we solve that equation system and obtain $\bar{E}_{-1}, \bar{E}_1, t^0_{-1-1}, t^0_{-1+1}$, and t^0_{1+1}. Then we use these five parameters to construct the Hamiltonian for various $\vec{k}$ and obtain the second and the third energy bands. Note that this procedure needs to be performed for each different value of a.

4.3.4 Energy bands by the tight-binding method.

Before plotting the energy bands by the tight-binding method, we firstly need to find $\bar{E}_m$ and $t^0_{mm'}$ for each value of a. For the lowest energy band, $\bar{E}_0$ and t^0_{00} are calculated, while $\bar{E}_{-1}, \bar{E}_1, t^0_{-1-1}, t^0_{-1+1}$, and t^0_{1+1} are calculated for the second and the third energy bands. All of them are shown in table 4.4 and table 4.5. We find that as a increases, the magnitudes of $t^0_{mm'}$ decrease. That is, it is more difficult for electrons to hop from a Zeeman potential well to other wells, when the distance between vortices increases. Then, we use these values for each value of a to construct the three lowest energy bands in figure 4-11 (a) by tight-binding method, comparing these with those bands using the Landau basis, as shown in figure 4-12 and figure 4-13. Both figures show that the tight-binding energy bands approach to those by Landau basis, when a is large enough. These results correspond to the basic concept of the tight-binding method. In our model, we assume that the overlap integral $S^n_{mm'}$ is negligible; thus, these results also confirm that our assumption can be used when a is large enough. From 4.92 and 4.93, we can predict that $\bar{E}_0$ is the average value between two energies at $\vec{k} = 0$ and t^0_{00} are related to the difference between them. This prediction can be seen in table 4.4

$a(\lambda)$	$\bar{E}_0$(meV)	t^0_{00}(meV)
3.4	-1.8715	-3.3850×10^{-3}
3.8	-1.5428	-1.1312×10^{-3}
4.2	-1.3229	-3.1756×10^{-4}
4.6	-1.1721	-8.2695×10^{-5}

Table 4.4: The values of $\bar{E}_0$ and t^0_{00} for constructing the tight-binding energy bands in figure 4-12.

$a(\lambda)$	$\bar{E}_{-1}$(meV)	$\bar{E}_1$(meV)	t^0_{-1-1}(meV)	t^0_{-1+1}(meV)	t^0_{1+1}(meV)
4.2	-1.1832	-1.1614	2.5268×10^{-3}	-1.7786×10^{-3}	1.6495×10^{-3}
4.4	-1.0936	-1.0743	1.6885×10^{-3}	-1.1665×10^{-3}	1.0167×10^{-3}
4.6	-1.0197	-1.0021	1.0375×10^{-3}	-7.4545×10^{-4}	6.3382×10^{-4}
5.0	-0.9077	-0.8921	3.4157×10^{-4}	-2.6724×10^{-4}	2.3312×10^{-4}

Table 4.5: The values of $\bar{E}_{-1}$, $\bar{E}_1$, t^0_{-1-1}, t^0_{-1+1}, and t^0_{1+1} for constructing the tight-binding energy bands in figure 4-13.

and figure 4-12. On the other hands, although the eigenvalues of $\widehat{H}$ in (4.94) and (4.95) are too complicate to analyse explicitly as was done in the previous case, we find that $\bar{E}_{-1}$ and $\bar{E}_1$ are also related to two lower and two upper energies at $\vec{k} = 0$ respectively.

Moreover, at a given a, the energy bands calculated by the isolated states $m = 0$ can be explained by tight-binding method better than those calculated by the isolated states $m = \pm 1$ because these electrons are more tightly trapped by the Zeeman quantum well. Finally, the agreement between the two sets of energy band calculations using the Landau basis and the tight binding method confirm that our results in the previous section are correct.

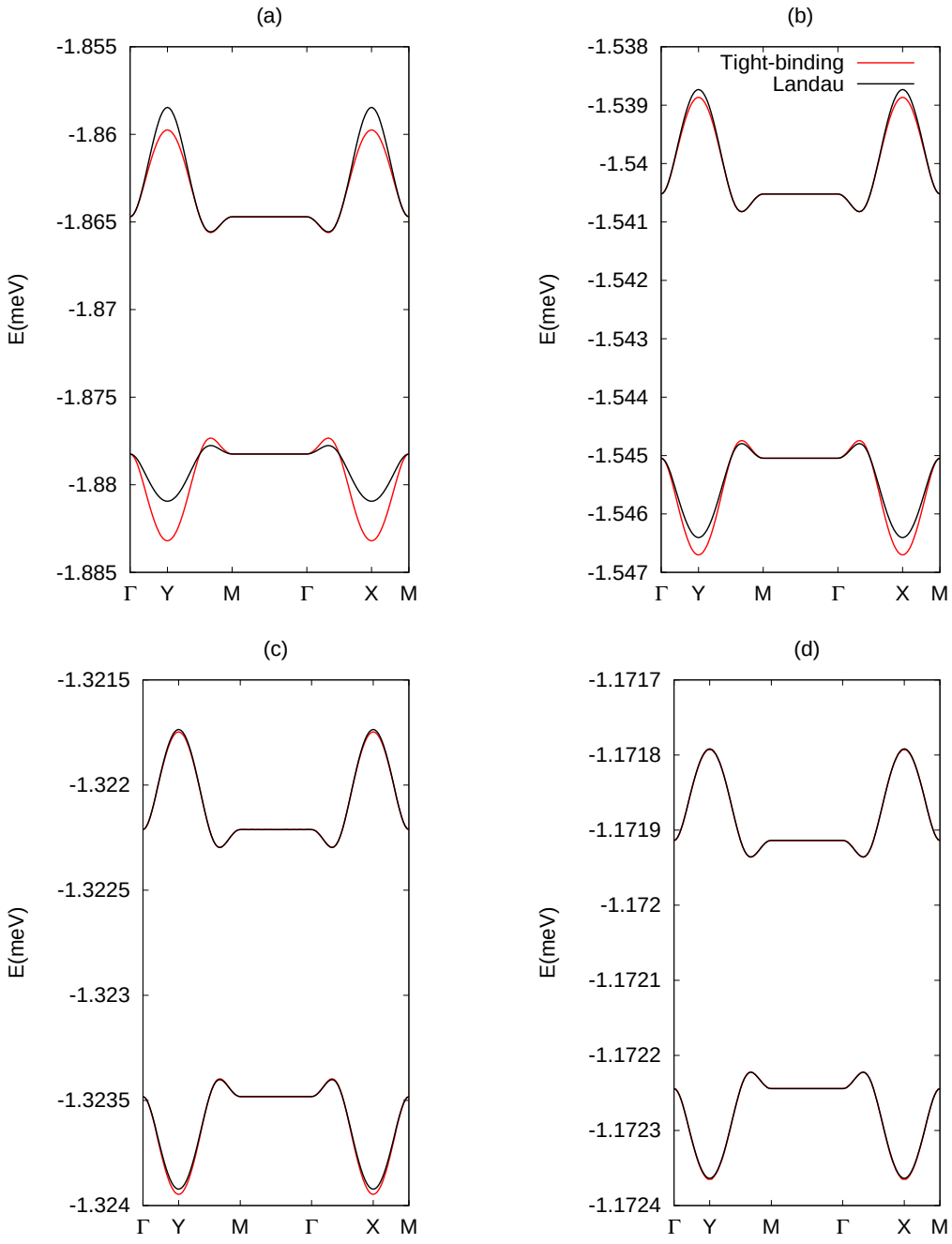

Figure 4-12: Comparison between the energy bands ($m = 0$) by tight-binding method and these by Landau basis for a/λ=3.4(a), 3.8(b), 4.2(c), 4.6(d).

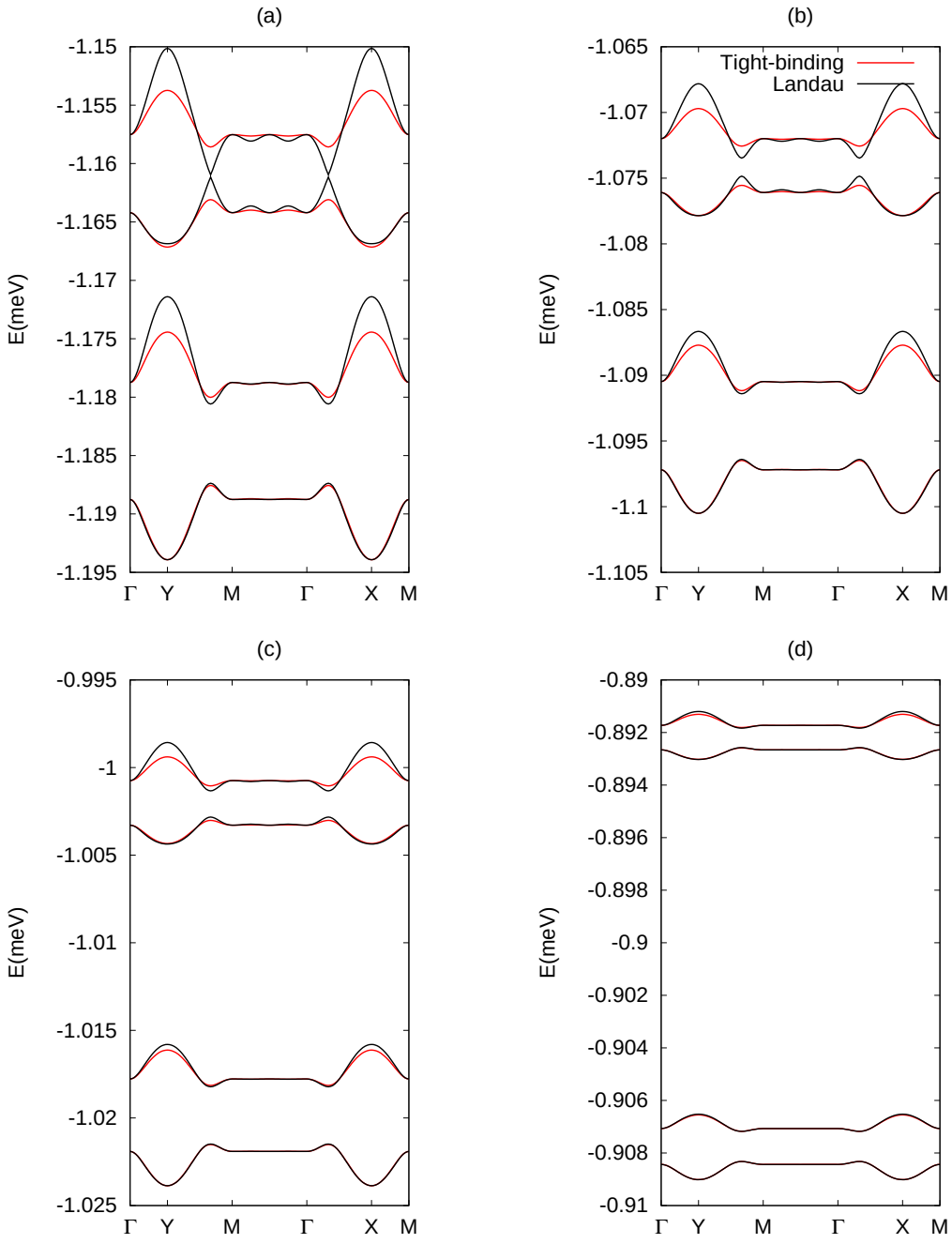

Figure 4-13: Comparison between the energy bands ($m = \pm 1$) by tight-binding method and these by Landau basis for a/λ=4.2(a), 4.4(b), 4.6(c), 5.0(d).

4.4 Summary

In this chapter, we have investigated the electronic structure of a DMS beneath a type-II superconducting film in the vortex state, repeating and extending the work of Rappoport *et al* [6]. First the Zeeman-confined states in a DMS, induced by an isolated vortex were considered, and it was found that they are nearly spin polarised. The effects of the magnetic field from a periodic lattice of vortices were then investigated numerically using the Landau basis. Due to the interaction between the Zeeman-confined states, the band structure of electrons in the DMS can be controlled by varying the applied magnetic field. The results obtained differ from those reported in Ref [6]. To confirm the corrections of the results reported here, a tight-binding model has been developed to describe the energy bands. The agreement between the lowest three bands given by the simple tight-binding model and the numerical Landau basis calculations confirms the validity of our results.

Chapter 5

Confined states associated with superconducting nanostructures

In a bulk superconductor, a sufficiently strong magnetic field can lead to the transition from a Meissner state to a vortex state where Abrikosov vortices are ideally arranged in a periodic triangular lattice. The number of vortices in the superconductor and the distance between them are influenced by an applied magnetic field. Recently, much theoretical, numerical, and experimental works have been devoted to the study of vortex states in thin superconducting nanostructures whose size is comparable to the coherence length ξ or the penetration depth λ [75, 76, 77, 78, 79, 80]. Many geometries of nanoscale superconductors have been investigated, including circles [81, 82, 83], squares [84], rings [85], and triangles [86]. It is found that the boundary of the superconductors plays a key role in determining the vortex distribution. Depending on the size and geometry of the superconductors, and the magnitude of applied magnetic field, the structure of vortices can be deviated from a triangular lattice, resulting in new superconducting states: a multivortex state and a giant vortex state. In a multivortex state, Abrikosov vortices are distorted by the boundary of the sample. There are still many individual vortices, where a magnetic field penetrates the superconductor, but their arrangement is not a triangular lattice. Examples of the density of Cooper-pairs $|\psi|^2$ in multivortex states are shown in figure 5-1 (a)-(d). A giant vortex state can be seen when two or more vortices overlap one another and become a single big vortex, illustrated in figure 5-1 (e) and (f). In this state, an applied field is concentrated at the centre of the giant vortex. The combination

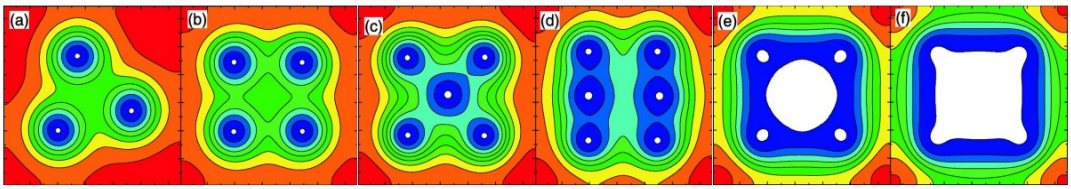

Figure 5-1: The average value of the Cooper-pair density over the thickness of a superconducting square with the width $W = 10\xi$ and the thickness $h = 0.1\xi$ at temperature $T = 0.4K$, obtained by the Ginzburg-Landau theory for vortex states with the vorticity L (the number of vortices) at the applied magnetic field B_a. (a) $L = 3$, $B_a = 0.305B_{c2}$, (b) $L = 4$, $B_a = 0.385B_{c2}$ (c), $L = 5$, $B_a = 0.4655B_{c2}$, (d) $L = 6$, $B_a = 0.525B_{c2}$, (e) $L = 8$, $B_a = 0.690B_{c2}$, and (d) $L = 10$, $B_a = 0.865B_{c2}$. From Ref. [84].

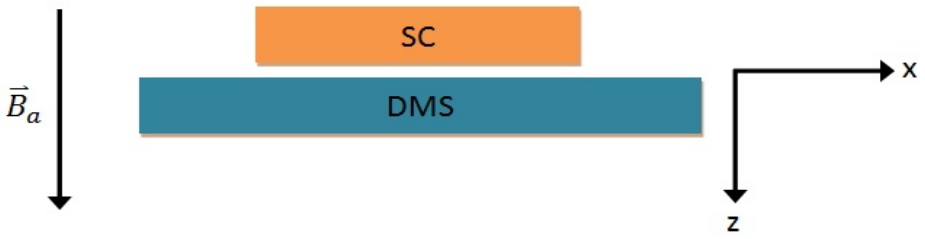

Figure 5-2: The hybrid system of a DMS and a superconducting square in an applied magnetic field $B_a\hat{z}$.

of a multivortex state and a giant vortex state is also possible as visible in figure 5-1 (e).

In this Chapter, we study the heterostructure of a square superconductor above a thin DMS, sketched in figure 5-2, to understand the effect of the magnetic field associated with the vortex phase of the superconductor on the electronic structure of electrons in the semiconductor. The focus is on the vortex configurations of both multivortex and giant vortex states, consisting of a small number of vortices. We expect the magnetic field due to a single vortex in this system will be able to confine electrons in a nearby DMS in a similar manner as an isolated vortex considered in the previous Chapter. As a result, in a multivortex state, it should be possible to create a group of spin polarised confined states. Depending upon the arrangement, these can be considered analogous to

artificial atomic levels, which may interact to form artificial molecular states. It is also interesting to explore confined states due to the field from a giant vortex, where further enhanced magnetic flux is concentrated at the centre of the vortex.

5.1 Numerical calculations of superconducting vortex states

In this section, we present the Ginzburg-Landau equations used to describe the vortex phase of a mesoscopic superconductor. These have been used extensively by Peeters group [81, 82, 83, 85] to investigate various superconducting geometries. As discussed in the Introduction, they govern the order parameter, magnetic field, and current density. The aim of this section is to determine the magnetic field produced by the supercurrent flowing inside a superconductor. We consider a thin superconducting square placed in the $x-y$ plane in an applied field $B_a\hat{z}$. Let us recall the Ginzburg-Landau equations and the Maxwell equation:

$$\alpha\psi + \beta\left|\psi\right|^2\psi + \frac{1}{2m^*}(-i\hbar\vec{\nabla} + 2e\vec{A})^2\psi = 0, \tag{5.1}$$

$$\vec{j}_s = \frac{i\hbar e}{m^*}(\psi^*\vec{\nabla}\psi - \psi\vec{\nabla}\psi^*) - \frac{4e^2}{m^*}\left|\psi\right|^2\vec{A}, \tag{5.2}$$

$$\vec{\nabla}\times\vec{\nabla}\times\vec{A}_s = \mu_0\vec{j}_s. \tag{5.3}$$

Note that e is the absolute value of the electron charge, $\vec{A}_s$ is the vector potential due to the supercurrent, and $\vec{A}$ in the Ginzburg-Landau equations is the vector potential due to the supercurrent and the external current that produces a uniform external field in which the superconductor is placed. In contrast to wavefunctions which are the solutions of the linear Schrödinger equation, the order parameter does not necessarily vanish at the boundary between the superconductor and vacuum (or insulator), but satisfies the boundary condition

$$\hat{n}_s\cdot(-i\hbar\vec{\nabla} + 2e\vec{A})\psi = 0. \tag{5.4}$$

If the thickness h of the superconductor is less than the coherence length ξ, the variation of the order parameter in the z direction is small [82]. As a result, one can solve the Ginzburg-Landau equations in two dimension, with ψ understood to

be the average value over the thickness h. We then measure all of the quantities in the following units: $\vec{\nabla} = \vec{\nabla}'/\xi$, $\vec{A} = \vec{A}'(\hbar/2e\xi)$, $\psi = \psi'\sqrt{-\alpha/\beta} = \psi'\psi_0$, $\vec{j} = \vec{j}'(2e\hbar\psi_0^2)/m^*\xi$, $\vec{B} = \vec{B}'(\hbar/2e\xi^2) = \vec{B}'B_{c2}$, and $\kappa = \lambda/\xi$. In the following, it is convenient to drop prime in the expressions. We then rewrite the above three equations (5.1)-(5.3) as

$$\left(-i\vec{\nabla}_{2D} + \vec{A}\right)^2 \psi = \psi\left(1 - |\psi|^2\right), \tag{5.5}$$

$$\vec{j}_s(x,y) = \frac{i}{2}\left(\psi^*\vec{\nabla}_{2D}\psi - \psi\vec{\nabla}_{2D}\psi^*\right) - |\psi|^2\vec{A}, \tag{5.6}$$

$$-\kappa^2\nabla_{3D}^2\vec{A}_s = \vec{j}_s(x,y)\,\Theta\left(\frac{h}{2} - |z|\right). \tag{5.7}$$

where 2D and 3D denote the dimension of the operators. In deriving (5.7), we choose the gauge $\vec{\nabla}\cdot\vec{A} = 0$.

To solve equation (5.5), we use relaxation methods [75, 76, 87] that transform the problem into a diffusion like equation. In particular

$$-\frac{\partial\psi}{\partial t} = \left(-i\vec{\nabla}_{2D} + \vec{A}\right)^2\psi - \psi\left(1 - |\psi|^2\right). \tag{5.8}$$

The steady states of this equation (as $t \to \infty$) when $\frac{\partial\psi}{\partial t} = 0$ correspond to solutions of equation (5.5). We discretise the order parameter on a uniform Cartesian grid, illustrated in figure 5-3, with ψ_j^n representing the order parameter at the grid point $\vec{r}_j$ and at time t_n; $t_n = n\Delta t$ where Δt is a fixed time step. Discretising the kinetic term gives [75, 76]

$$\left(-i\vec{\nabla}_{2D} + \vec{A}\right)^2\psi_j^n = \frac{1}{a^2}\left(-U_x^{kj}\psi_k^n - U_x^{ij}\psi_i^n - U_y^{mj}\psi_m^n - U_y^{gj}\psi_g^n + 4\psi_j^n\right), \tag{5.9}$$

where $U_\mu^{\vec{r}_1,\vec{r}_2} = \exp\left(i\int_{\vec{r}_2}^{\vec{r}_1}\vec{A}\mu\cdot d\vec{\mu}\right)$; $\mu = x$ or y and a is the distance between neighbouring grid points. Using a forward finite difference approximation for the time-derivative term, we have $\frac{\partial\psi_j^n}{\partial t} = \frac{\psi_j^{n+1} - \psi_j^n}{\Delta t}$. Therefore, the diffusion like equation (5.8) can be rewritten as

$$\begin{aligned}\psi_j^{n+1} &= \psi_j^n + \frac{\Delta t}{a^2}\left(U_x^{kj}\psi_k^n + U_x^{ij}\psi_i^n + U_y^{mj}\psi_m^n + U_y^{gj}\psi_g^n - 4\psi_j^n\right) \\ &\quad + \Delta t\psi_j^n\left(1 - \left|\psi_j^n\right|^2\right).\end{aligned} \tag{5.10}$$

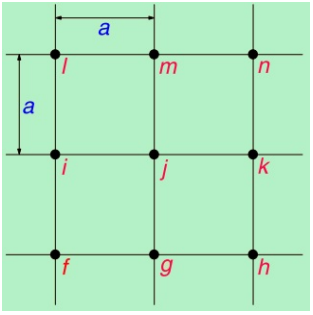

Figure 5-3: The uniform Cartesian grid and the lattice points f, g, h,..., and n on the grid (from Ref. [75]).

Jacobi methods [87] are applied starting from an initial estimate of the order parameter at time t_0, ψ^0 and approximating the initial vector potential to be that due to the uniform applied field which in the symmetric gauge is $\vec{A}_a = \frac{B_a}{2}(-y, x)$. We use typically grid spacing $a = 0.1$ and time interval $\Delta t = 0.001$. ψ^0 and $\vec{A}_a$ are used to find ψ^1, which is then used to find ψ^2. This procedure is used iteratively until the order parameter ψ^n is converged. Then, ψ^n is used in (5.6) to find the corresponding two dimensional supercurrent density $\vec{j}_s(x, y)$. To find the three dimensional vector potential, we expand $\vec{j}_s(x, y)$ over the thickness of the superconductor and solve the Maxwell equation (5.7) in three dimensions, applying the boundary condition that the vector potential produced by the superconducting current vanishes at large distances. Finally, we add $\vec{A}_a$ before returning to calculate the order parameter in (5.5) again. We solve these three equations self-consistently until both order parameter and vector potential are converged to obtain the total magnetic field $\vec{B}$ due to the superconducting vortices and the applied field B_a, $\vec{B} = \vec{\nabla} \times (\vec{A}_a + \vec{A}_s)$. The number of vortices and their arrangement are found to be sensitive to the applied field and the initial estimate of the order parameter ψ^0.

5.2 Numerical calculations of confined states in a DMS.

Having determined the local magnetic field due to a superconducting square in the vortex state, we now present the finite difference method to explore electron

states in an adjacent DMS plane beneath the superconductor. The general idea of the numerical method is to turn the differential equation into a linear algebra problem by discretising continuous functions into discrete values. We start with the Schrödinger equation of an electron with effective mass m^*, moving in the plane, given by

$$\widehat{H}\Psi(x,y) = \left[\frac{1}{2m^*}(-i\hbar\vec{\nabla} + e\vec{A})^2 - \frac{1}{2}g_{\text{eff}}\mu_B\vec{\sigma}\cdot\vec{B}\right]\Psi(x,y) = E\Psi(x,y), \quad (5.11)$$

where $\vec{B} = B_x(x,y)\hat{x} + B_y(x,y)\hat{y} + B_z(x,y)\hat{z}$. The equation is transformed with the following substitution: $\vec{\nabla} \to \vec{\nabla}'/\xi$, $\vec{A} \to \vec{A}'\,(\hbar/e\xi)$, $\vec{B} \to \vec{B}'\,(\hbar/e\xi^2)$, $E \to E'\,(\hbar^2/2m^*\xi^2) = E'E_0$, and $g_{\text{eff}}\,(m^*/2m_e) \to \tilde{g}$ with prime then dropped for clarity. The resulting units of $\vec{A}$ and $\vec{B}$ are different from those in the previous section since we want to use (5.9) when the kinetic term are discretised. Due to the x and y components of the magnetic field, spin is not a good quantum number. As a result, the eigenfunction $\Psi(x,y)$ has both spin up and spin down components and is expressed as $\binom{\psi^\uparrow}{\psi^\downarrow}$. This gives

$$\left(-i\vec{\nabla} + \vec{A}\right)^2 \begin{pmatrix} \psi^\uparrow \\ \psi^\downarrow \end{pmatrix} - \tilde{g}\begin{pmatrix} B_z\psi^\uparrow + (B_x - iB_y)\,\psi^\downarrow \\ (B_x + iB_y)\,\psi^\uparrow - B_z\psi^\downarrow \end{pmatrix} = E\begin{pmatrix} \psi^\uparrow \\ \psi^\downarrow \end{pmatrix}. \quad (5.12)$$

Discretising the variables in the equation above on the square grid in figure 5-3, containing N grid points gives $2N$ equations,

$$\begin{aligned}
\left(-i\vec{\nabla} + \vec{A}\right)^2 \psi_1^\uparrow - \tilde{g}\left[B_z^1\psi_1^\uparrow + \left(B_x^1 - iB_y^1\right)\psi_1^\downarrow\right] &= E\psi_1^\uparrow \\
\left(-i\vec{\nabla} + \vec{A}\right)^2 \psi_2^\uparrow - \tilde{g}\left[B_z^2\psi_1^\uparrow + \left(B_x^2 - iB_y^2\right)\psi_2^\downarrow\right] &= E\psi_2^\uparrow \\
&\vdots \\
\left(-i\vec{\nabla} + \vec{A}\right)^2 \psi_N^\uparrow - \tilde{g}\left[B_z^N\psi_1^\uparrow + \left(B_x^N - iB_y^N\right)\psi_N^\downarrow\right] &= E\psi_N^\uparrow \\
\left(-i\vec{\nabla} + \vec{A}\right)^2 \psi_1^\downarrow - \tilde{g}\left[\left(B_x^1 + iB_y^1\right)\psi_1^\uparrow - B_z^1\psi_1^\downarrow\right] &= E\psi_1^\downarrow \\
\left(-i\vec{\nabla} + \vec{A}\right)^2 \psi_2^\downarrow - \tilde{g}\left[\left(B_x^2 + iB_y^2\right)\psi_2^\uparrow - B_z^2\psi_1^\downarrow\right] &= E\psi_2^\downarrow \\
&\vdots \\
\left(-i\vec{\nabla} + \vec{A}\right)^2 \psi_N^\downarrow - \tilde{g}\left[\left(B_x^N + iB_y^N\right)\psi_N^\uparrow - B_z^N\psi_1^\downarrow\right] &= E\psi_N^\downarrow.
\end{aligned}$$

where $\psi_j^{\uparrow,\downarrow}$ and $B_{x,y,z}^j$ denote the eigenfunctions and the components of the magnetic field at position $\vec{r} = j$, and the kinetic term of each equation is discretised as equation (5.9). We ensure that the grid extends sufficiently so that $\psi_j^{\uparrow,\downarrow} = 0$ on its edges. The system of $2N$ equations has the form of the matrix eigenvalue problem, $H\psi = E\psi$, where H is a $2N \times 2N$ matrix, E is an eigenvalue, and ψ is a column vector containing the values of $\psi_j^{\uparrow}$ and $\psi_j^{\downarrow}$ on the N grid points.

5.3 A single vortex

Having outlined the numerical solution of the Ginzburg-Landau equations and the Schrödinger equation (5.11), we now present results for the magnetic field profile due to a superconducting square and the magnetically confined states in a DMS beneath the superconductor. We start with an investigation of a vortex phase containing a single vortex. In Chapter 4, an isolated vortex in an infinite superconductor was shown to induce Zeeman-trapped states in an adjacent DMS. The single vortex state of a nanoscale superconductor is expected to do the same. In the following we present results for this system and compare with those due to an isolated vortex.

5.3.1 The magnetic field profile due to a single vortex

In a vortex phase, where there is a mixing of a normal state and a superconducting state, the supercurrent $\vec{j}_s$ produces a magnetic field with two effects. As a Meissner state, the first is to screen the interior of a superconductor from the applied field to maintain superconductivity, and the second is to trap the field in the centre of a superconducting vortex. Depending upon the effects, the direction of the supercurrent density is illustrated in figure 5-4 (a). For a superconducting square in an applied field $B_a\hat{z}$ with a single vortex at the centre of the sample, the supercurrent density flows in a counterclockwise direction to generate a magnetic field opposing an applied field, clearly seen at the edge of the sample. On the other hand, the supercurrent density around a vortex circulates in a clockwise direction. The corresponding magnetic field is obtained form the Maxwell equation, $\vec{\nabla} \times (B_x^s\hat{x} + B_y^s\hat{y} + B_z^s\hat{z}) = \mu_0\vec{j}_s$. The z component of the field is shown in figure 5-4 (b). Although the geometry of the sample is a square, the magnetic

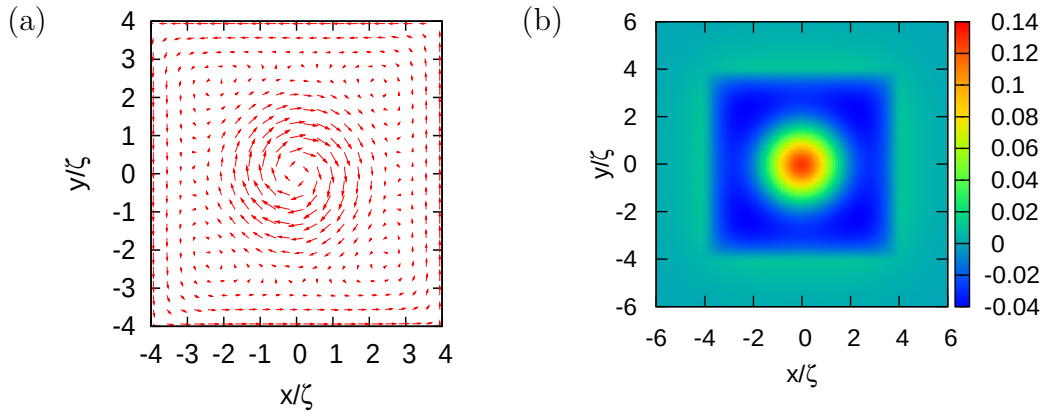

Figure 5-4: (a) The supercurrent density flowing in a superconducting square of width $W = 8.0\xi$, thickness $h = 0.8\xi$, and $\kappa = 1.0$ in a uniform magnetic field of $B_a = 0.22B_{c2}$. (b) The corresponding magnetic field in z direction, B_z^s, at a distance $z = 0.1\xi$ below the superconductor.

field due to a single vortex exhibits rotational symmetry as usual. We see the field opposing the applied field $B_a\hat{z}$ (negative field) exist over the superconducting space except for the area of the vortex.

Figure 5-5 (a) shows the effect of an applied field on the supercurrent. As B_a increases, we see the current changes only slightly in the vicinity of the single vortex, with large change at the edge of the sample. In figure 5-5 (b), the local magnetic field, $B_z = B_z^s + B_a$, due to a single vortex in a superconducting square for various B_a are compared with the field due to an isolated vortex in an infinitely large and very thick superconductor. Notice that the analytical expressions (4.1) and (4.2) describing the latter field show that the field scales as $\hbar/(2e\lambda^2)$ and is not a function of an applied field. It is convenient to compare these magnetic fields for the case $\lambda = \xi = 40$ nm (giving $\kappa = 1.0$) which are values of λ and ξ that correspond to superconducting niobium [88] (note that depending upon the purity of the material in an experiment, these values can vary [89]). Far from the centre of a vortex, the magnetic field will approach the applied field, while in the case of isolated vortex it will disappear because of the infinite size of the superconductor. When the applied field B_a increases, the local magnetic field B_z near the single vortex is raised, and the screening supercurrent leads to an increased magnetic field at the edge of the superconductor. This screening field does not exist in the case of the isolated vortex. Considering only the field that

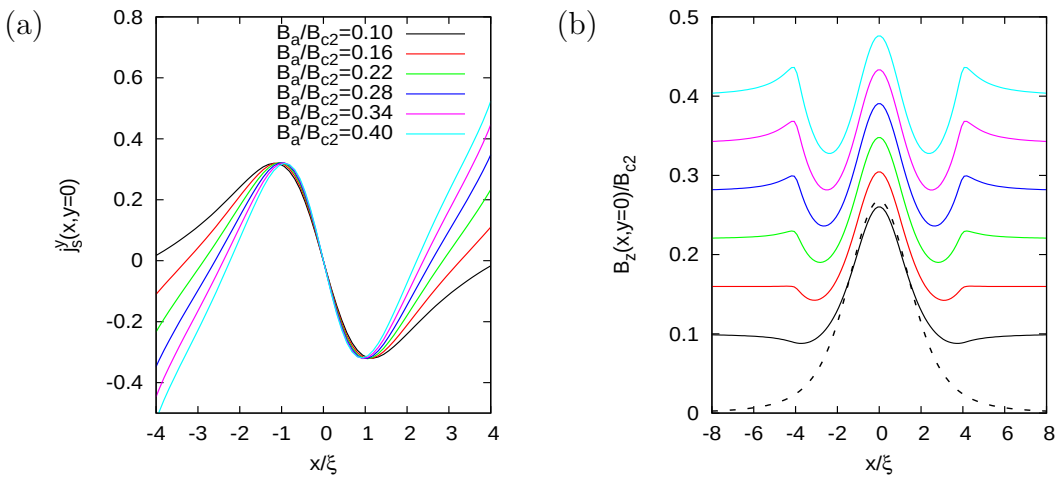

Figure 5-5: (a) The y component of the supercurrent density j_s^y plotted along the line $y = 0$ (see figure 5-4 (a)) in a superconducting square with the size of $8.0\xi \times 8.0\xi \times 0.8\xi$, and $\kappa = 1.0$ for various values of B_a. (b) The corresponding local magnetic field B_z along the line $y = 0$ at a distance $z = 0.1\xi$ below from the superconductor. The field due to an isolated vortex is presented by the dash line.

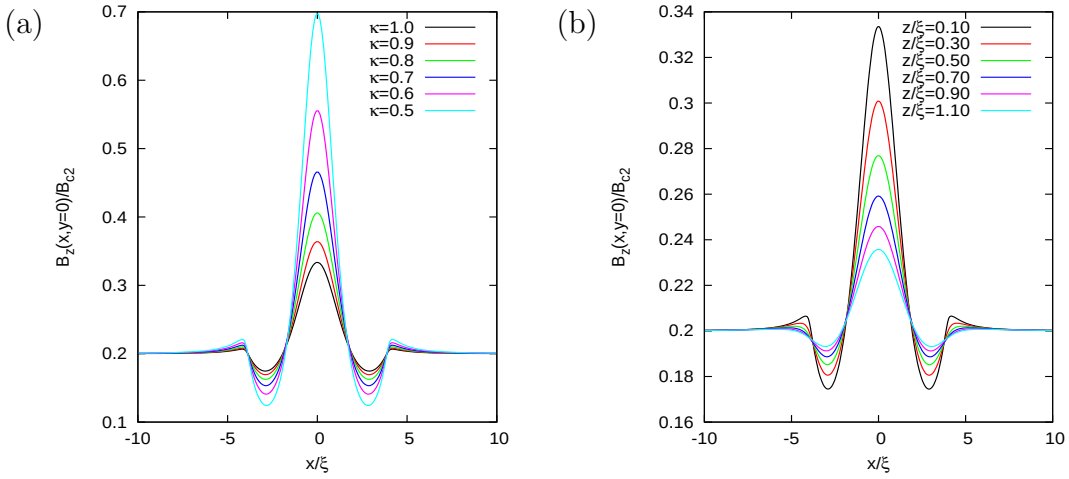

Figure 5-6: The local magnetic field B_z due to the superconducting square with the size of $8.0\xi \times 8.0\xi \times 0.8\xi$ in a uniform field of $B_a = 0.2B_{c2}$, plotted along the line $y = 0$ for (a) a separation $z = 0.1\xi$ and different values of κ, and (b) $\kappa = 1.0$ and various separations z.

is induced by the superconductor, B_z^s, we see that the field due to the isolated vortex is the strongest.

The variation of the local magnetic field due to the distance between the superconductor and the DMS plane, z, and the value of $\kappa = \lambda/\xi$ characterising the superconductor is also illustrated. Figure 5-6 (a) shows the field becomes stronger with decreasing value of κ, and 5-6 (b) shows the field increases as the separation of the superconductor and DMS decreases.

5.3.2 The energy spectrum and bound states

In the previous section, the modulation of the magnetic field that arises when a single vortex exists in a superconducting square has been reported. We have seen how the field varies with the variables B_a, z, and κ. Now, we investigate the solutions of the Schrödinger equation (5.11) which describe electron states in the plane of a DMS, confined by the inhomogeneous magnetic field due to the superconducting square. In the following calculations, we choose the superconducting square with dimensions $8.0\xi \times 8.0\xi \times 0.8\xi$, and $\lambda = \xi = 40$ nm. For the DMS, values of $g_{\text{eff}} = 500$, and $m^* = 0.5m_e$ are used. The distance between the superconductor and the DMS, z, is set to be $z = 0.1\xi = 4$ nm, which is experimentally reasonable and ensures a strong modulation of the field. Figure 5-7 (a) shows the energy spectrum of electrons in a uniform field (blue pluses), the magnetic field due to the superconducting square containing a single vortex (red dots), and the magnetic field due to an isolated vortex (black lines), plotted as a function of the applied field B_a.

In the absence of the superconductor, the energy spectrum is that of the Landau levels (2.8) (including the Zeeman energy) which is characterised by the quantum numbers n, m, σ, and the magnitude of the applied field B_a. As shown in figure (2-2), each Landau level is infinite-fold degenerate, with all states with negative m having the same energy. Therefore, each blue plus in figure 5-7 (a) represents the energy of infinite-fold degenerate Landau states. Examples of the corresponding wavefunctions are illustrated in figure 5-7 (b).

In the presence of the square superconductor, the degenerate Landau states are perturbed by the inhomogeneous field, in a manner that depends upon their spatial distribution. With a single vortex present the magnetic field is enhanced

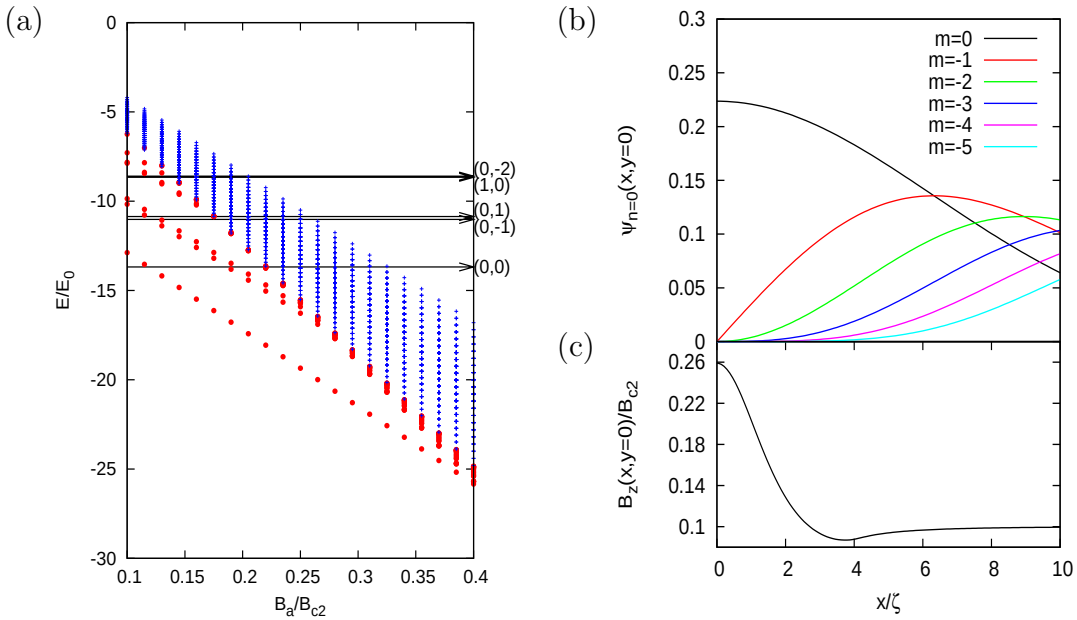

Figure 5-7: (a) The energy spectrum of electrons in a DMS. Blue pluses show the twenty lowest Landau levels (2.8) for different values of B_a. Red dots represent the spectrum in a presence of the magnetic field due to the superconducting square supporting a single vortex, showing those states that are lower than the lowest Landau levels. The black lines represent the lowest five energy levels in a presence of an isolated vortex, with the quantum numbers (n, m) of each level indicated to the right. (b) The radial wavefunctions of the degenerate lowest Landau states $\psi_{n=0,m,\sigma=1/2}$ in a uniform field of $B_a = 0.1B_{c2}$. (c) The local magnetic field B_z due to a single vortex in a uniform field of $B_a = 0.1B_{c2}$.

at the centre, and figure 5-7 (b) and (c) show that states with smaller $|m|$ will be perturbed most while the states with sufficiently large $|m|$ will be unperturbed. Therefore, the introduction of the superconductor will break the degeneracy of the energy levels, but there will be states existing close to the original energies since each level includes states with large negative quantum number m which are almost unaffected by the change of B_z. Hence, in figure 5-7 (a) we only plot those eigenvalues that exist in the presence of the superconducting square with a single vortex (red dots) which lie below the lowest Landau levels.

When the applied field is small, we observe the spectrum (red dots in figure 5-7 (a)) is similar to that found in the presence of an isolated vortex in an infinite superconductor. That is, the lowest energy level is clearly separated from others,

the first and the second excited levels form a doublet, and the forth and the fifth also. Unlike the case of the vortex in the finite superconducting square, the energies due to an isolated vortex are independent of an applied field.

Some examples of the spatial distribution of eigenstates that arise for a small applied field are shown in figure 5-8. The probability distribution $|\psi|^2$ have rotational symmetry, and the states are nearly spin polarised as was the case for those bound by the field due to an isolated vortex. These states are clearly associated with the vortex present in the square superconductor, so we call them "vortex-confined states". To further confirm the close connection between these states and those due to an isolated vortex, we consider the phase of the wavefunctions, defined by

$$\theta = \tan^{-1}\frac{\mathrm{Im}(\psi^{\uparrow,\downarrow})}{\mathrm{Re}(\psi^{\uparrow,\downarrow})}. \tag{5.13}$$

Figure 5-9 shows a close relation between the phase θ of the spin up component of these two kinds of states. For the lowest and the third excited state, the phase is approximately zero, corresponding to $m = 0$ like character. For the first and the second excited states, it changes from 0 to 2π in clockwise and anticlockwise directions respectively, corresponding to $m = \pm 1$ like character.

As the applied field increases, the energies decrease linearly, but at a slower rate than the Landau states, resulting in an increasingly different energy spectrum from that of the isolated vortex. For all fields in figure 5-7 (a) the lowest state is a vortex-confined state, but some of the excited states are not. These states distribute mostly outside the area of the superconducting square ($8.0\xi \times 8.0\xi \times 0.8\xi$) and seem to be influenced by the geometry of the superconductor as shown in figures 5-10, 5-11, and 5-12.

In order to understand the spectrum and the behaviour of the eigenstates, we consider the Zeeman energy arising from the normal component of th field, $-\frac{1}{2}g_{\mathrm{eff}}\mu_B\sigma_z B_z$. As discussed in Chapters 2 and 3, it can be considered as an effective potential for spin up wavefunctions which are dominant in all of the vortex-confined states. In figure 5-13, the Zeeman potential well and the spin up component of the lowest four bound states are illustrated with the same values of B_a used in figures 5-8, 5-10, 5-11, and 5-12. When $B_a = 0.1B_{c2}$, we obviously see the bound states are trapped by the magnetic field due to a single vortex. As B_a increases, the Zeeman potential is lowered, resulting in increasing negative

energy levels of all confined states as seen in figure 5-7 (a). At the same time, the depth of the Zeeman well decreases, so there are fewer vortex-confined states. Moreover, increasing B_a also leads to a larger magnetic field concentrated at the edge of the superconductor. This results in a new kind of state localised at the edge of the superconductor, which we refer to as "edge states". These states are found when B_a and the quantum number n are large enough. Compared to vortex-confined states, edge states extend over a larger area. This reduction in confinement is seen in their energies which are less well separated. As seen in figure 5-13 (c) and (d), the first, second, and third excited states are edge states whose energies are nearly degenerate.

To summarise, we have seen that a single vortex in a nanoscale superconductor can induce vortex-confined states in a adjacent DMS especially when an applied magnetic field B_a is small. In this case, we find that their behaviour and energy quantisation are similar to those due an isolated vortex in an infinite superconductor. As B_a increases, the energy quantisation begins to deviate from that due to an isolated vortex. Increasing B_a does not result in the vortex trapping additional states, but causes the magnetic concentration at the edge of the superconductor to induce edge states. We can roughly distinguish the vortex-confined states from edge states by considering the energy spectrum such as that shown in figure 5-7 (a). The energy levels of the former states are more widely separated in energy than those of the latter, as they are confined in a more narrow Zeeman quantum well.

5.4 Multivortex and giant vortex states

In the previous section, we have seen how the magnetic field due a superconducting square containing a single vortex can induce vortex confined states beneath the vortex and edge states near the boundary of the square in an adjacent DMS. We now extend the study to consider the magnetic field and confined states due to the vortex phase which contains more than one vortex in the sample, again solving the Ginzburg-Landau equations and the Schrödinger equation (5.11) numerically.

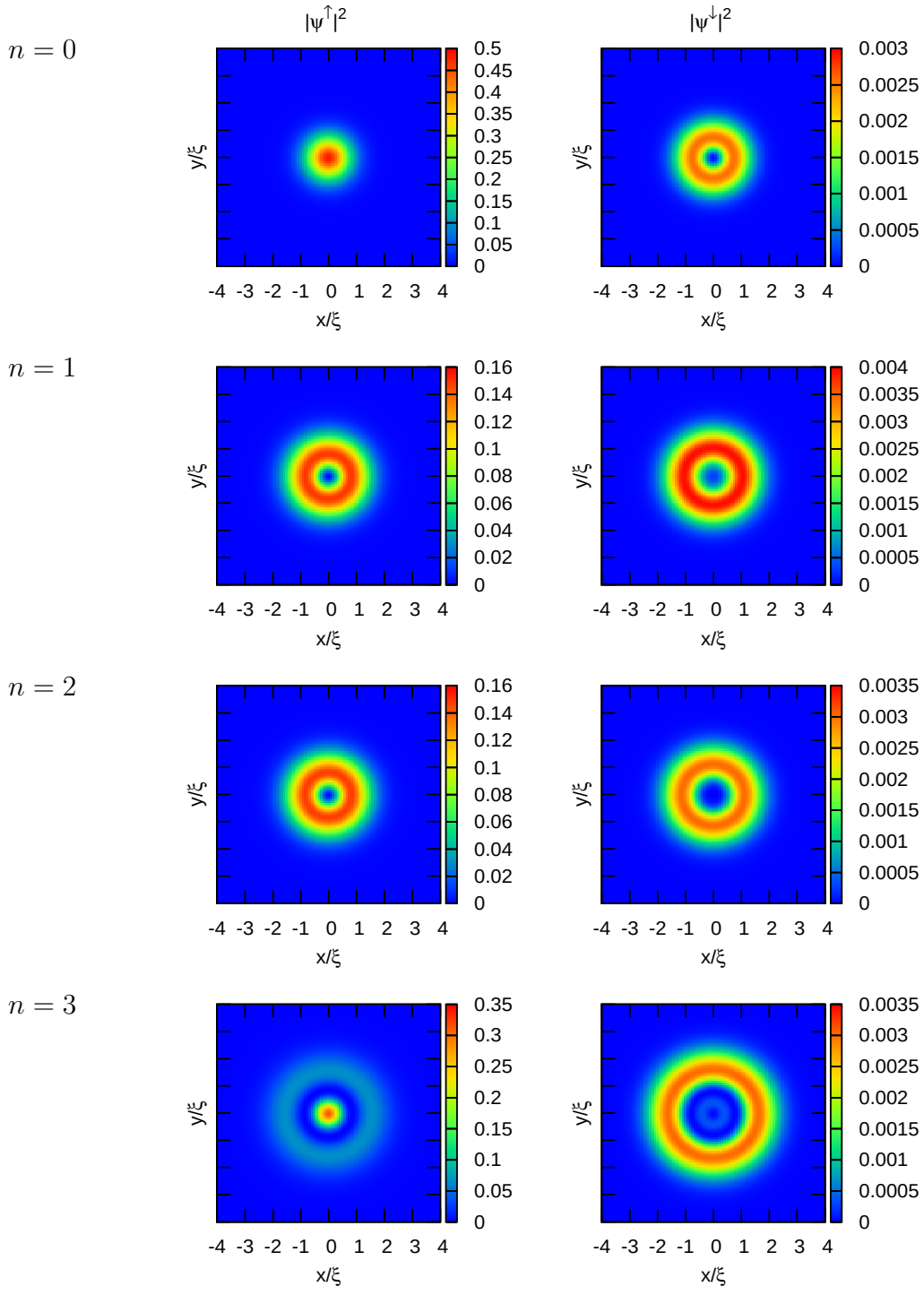

Figure 5-8: The square of spin up (on the left) and spin down (on the right) components of the lowest four eigenfunctions in the presence of a single vortex with $B_a = 0.10 B_{c2}$, plotted on the square area of a DMS plane.

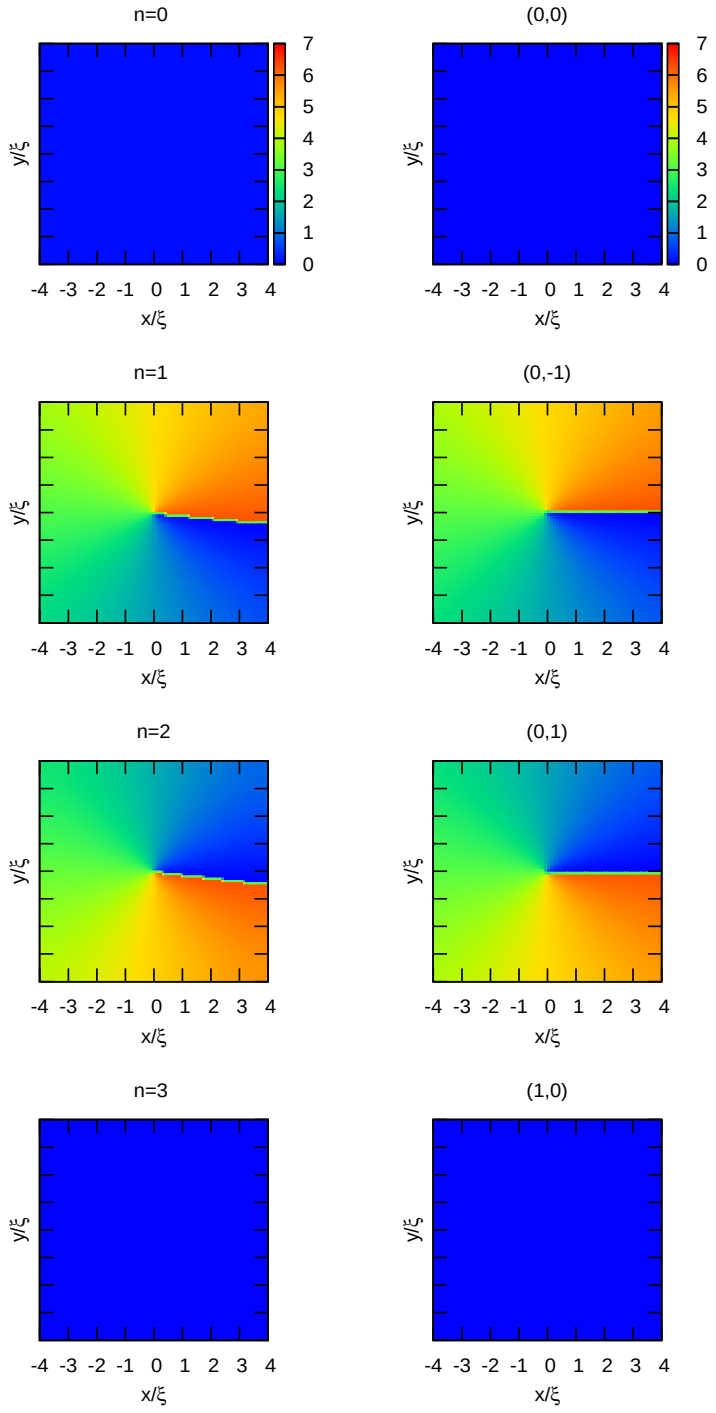

Figure 5-9: The phase θ of spin up component $\psi^{\uparrow}$ of the lowest four eigenstates in the presence of a single vortex with $B_a = 0.10B_{c2}$ (on the left), and an isolated vortex (on the right), plotted on the square area of a DMS plane. The quantum number n and (n, m) of each eigenstate are indicated on top of each figure.

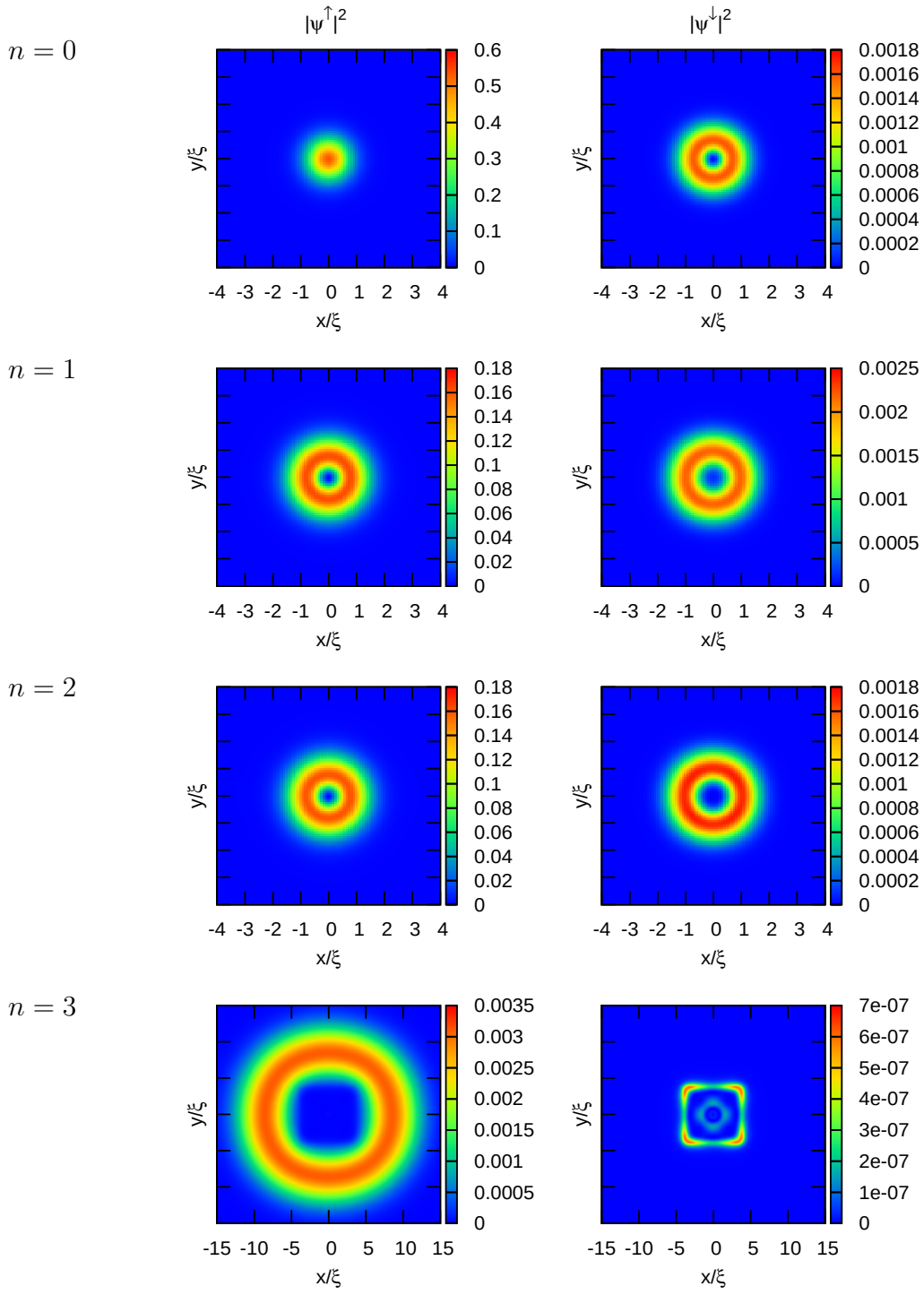

Figure 5-10: The square of spin up (on the left) and spin down (on the right) components of the lowest four eigenfunctions in the presence of a single vortex with $B_a = 0.19B_{c2}$, plotted on the square area of a DMS plane. Notice that the length scale for the state $n = 3$ is different.

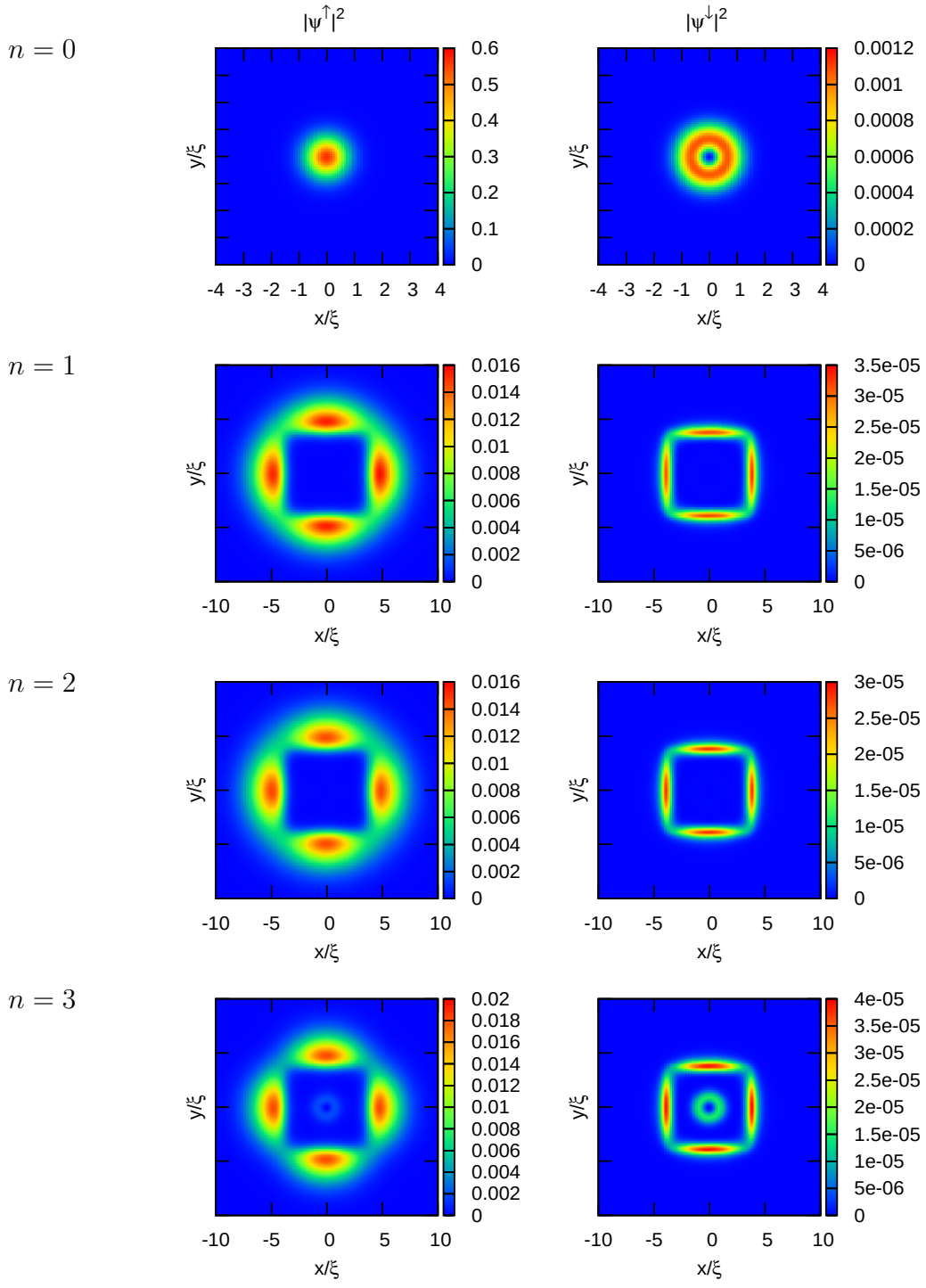

Figure 5-11: The square of spin up (on the left) and spin down (on the right) components of the lowest four eigenfunctions in the presence of a single vortex with $B_a = 0.28B_{c2}$, plotted on the square area of a DMS plane.

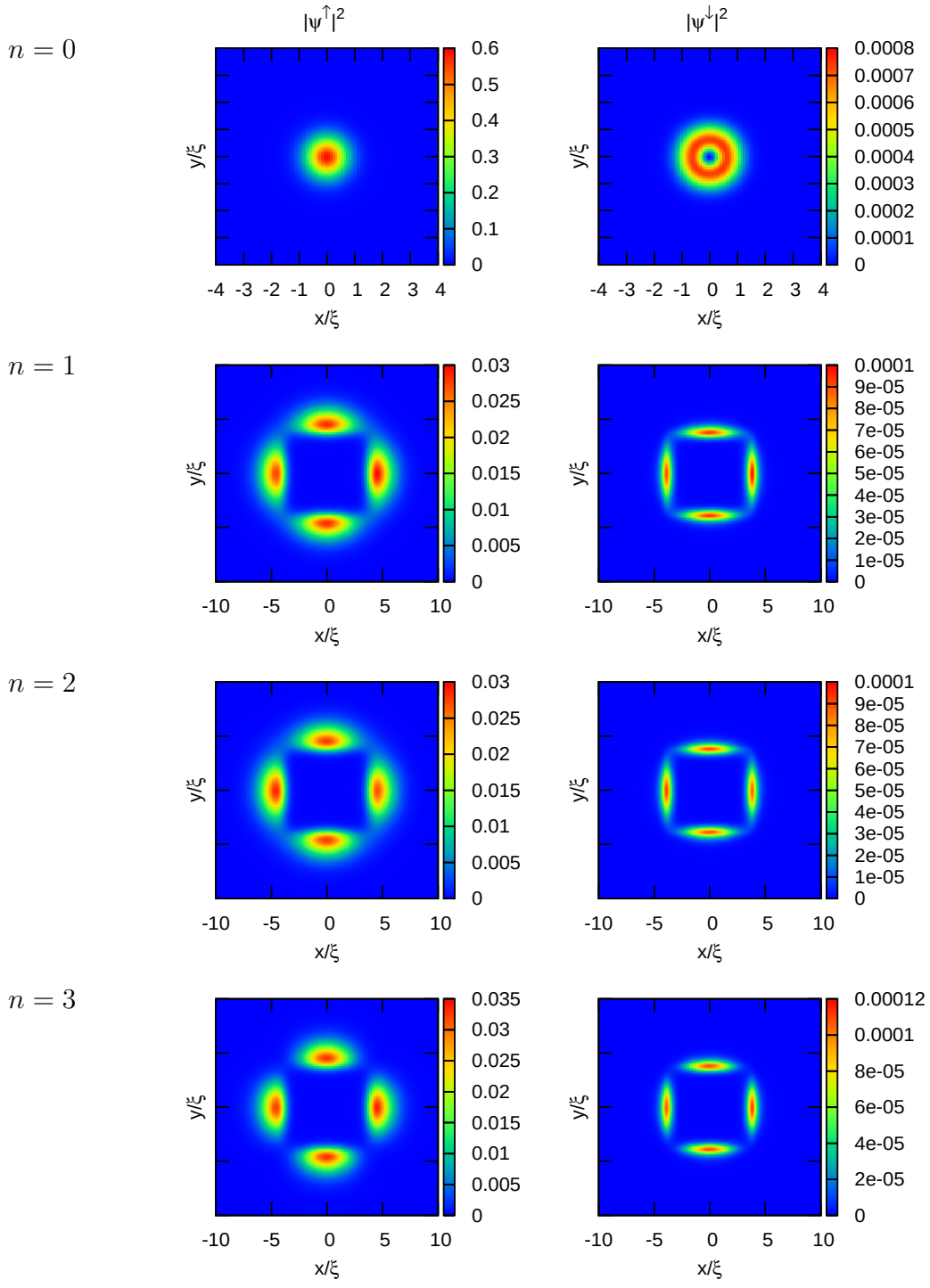

Figure 5-12: The square of spin up (on the left) and spin down (on the right) components of the lowest four eigenfunctions in the presence of a single vortex with $B_a = 0.37B_{c2}$, plotted on the square area of a DMS plane.

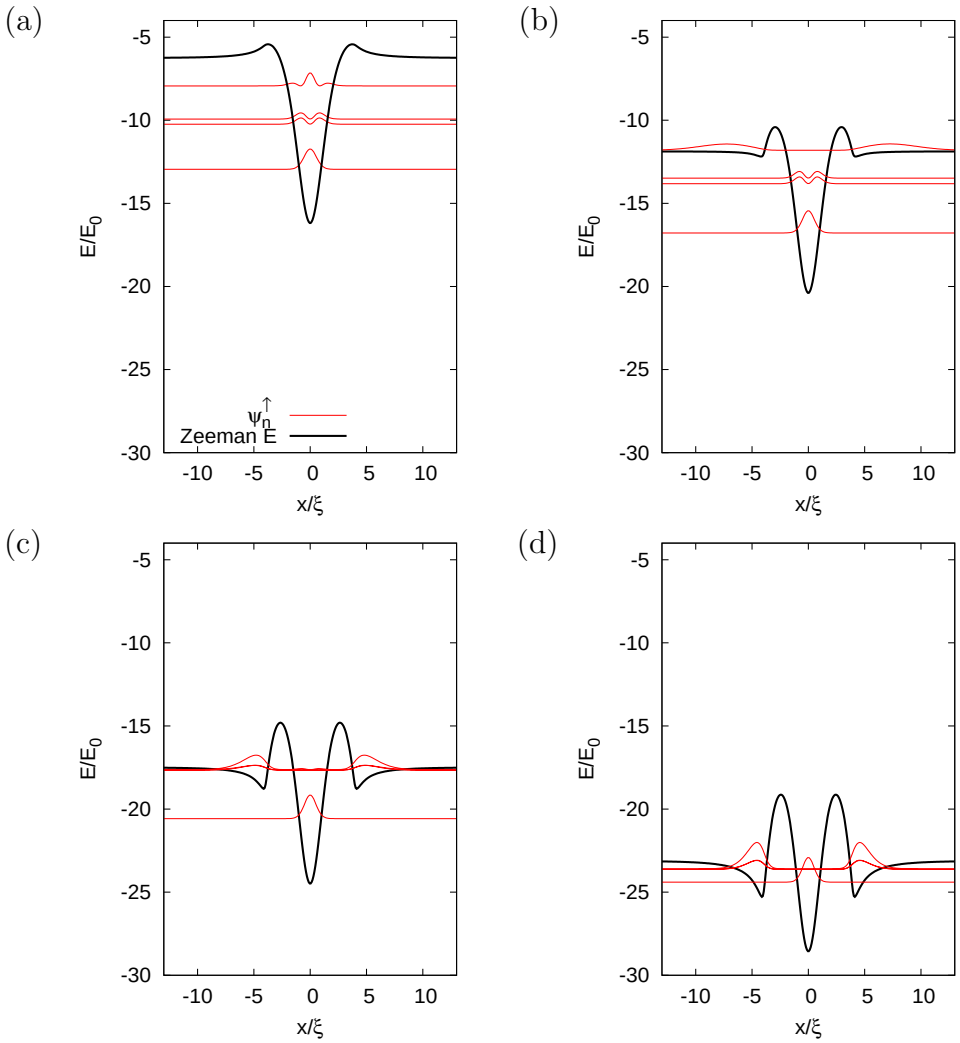

Figure 5-13: The z component of the Zeeman energy and the spin up component of the lowest four eigenstates, plotted along the line $y = 0$ in the presence of a single vortex with (a) $B_a = 0.10B_{c2}$, (b) $B_a = 0.19B_{c2}$, (c) $B_a = 0.28B_{c2}$, and (d) $B_a = 0.37B_{c2}$. The spin up wavefunctions are not normalised here in order to see them more clearly, but are offset vertically by an amount corresponding to their energies.

5.4.1 The magnetic field profile due to superconducting vortices

As previously discussed, the vortex phase of a nanoscale superconductor is different from that of a bulk superconductor. Abrikosov vortices are perturbed by the boundary of a sample and transformed into multivortex states or giant vortex states. In this section, we analyse the magnetic field due to these two superconducting states to understand the conditions where they exist.

For the vortex phase with vorticity $L = 2$, we find two vortices which occur along the diagonal of a superconducting square as shown in figure 5-14. Figure 5-15 shows the magnetic field B_z^s due to the state with $L = 2$. We see that for a given value of κ, multivortex states exist when B_a is small enough. The individual vortices approach one another with increasing field B_a, and become a giant vortex if B_a is sufficiently large. For a given value of B_a, we see multivortex states and giant vortex states exist when κ is sufficiently large and small respectively. Figure 5-15 also shows that the variations in the field B_z^s are stronger with decreasing of κ. That means that superconductors with small κ will be able to trap a greater number of vortex-confined states. Figure 5-16 shows the effect of the size of the sample. For a given applied field, giant vortex states can be destroyed by

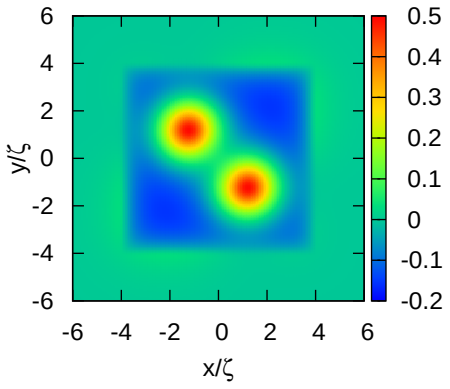

Figure 5-14: The magnetic field B_z^s due to the vortex state with $L = 2$ due to a superconducting square with the size $8.0\xi \times 8.0\xi \times 0.8\xi$, when $B_a = 0.3B_{c2}$, the distances $z = 0.05\xi$, and $\kappa = 0.5$.

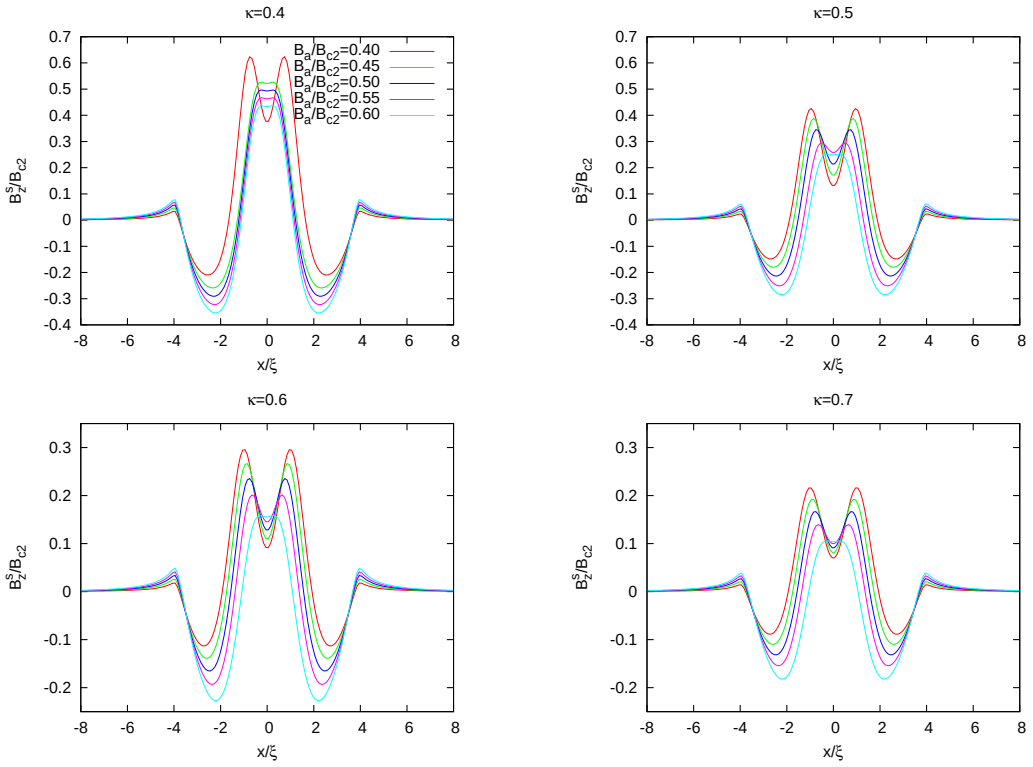

Figure 5-15: The magnetic field B_z^s due to the vortex state with $L = 2$ for different values of B_a and κ, plotted along the diagonal line passing through the centres of two vortices. The size of the superconductor is $8.0\xi \times 8.0\xi \times 0.8\xi$ and the field is calculated a distance $z = 0.05\xi$ beneath the superconductor

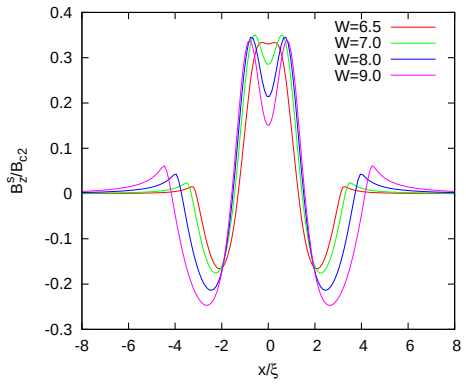

Figure 5-16: The magnetic field B_z^s due to the vortex state with $L = 2$ for different values of the width W of the square superconductor, plotted along the diagonal line passing through the centres of two vortices. Here, $B_a = 0.5B_{c2}$, $\kappa = 0.5$, $h = 0.8\xi$, and the field is calculated a distance $z = 0.05\xi$ beneath the superconductor.

increasing the dimensions of the superconductor.

Having considered the magnetic field due to multivortex and giant vortex states with vorticity $L = 2$, in the following we choose the superconductor to have size $8.0\xi \times 8.0\xi \times 0.8\xi$ and $\kappa = 0.5$ corresponding to Lead (Pb) [88], and study the states that occur with different values of L. This value of κ is relatively small, and so we expect to be able to use the field from this superconductor to trap a number of vortex-confined states in an adjacent DMS. The stability of superconducting vortex states is determined by the Gibbs free energy given by [82]

$$G = G_n + \int \left\{ (\vec{A} - \vec{A}_a) \cdot \vec{j}_s - \frac{1}{2}|\psi|^4 \right\} dV, \tag{5.14}$$

where G and G_n are the Gibbs free energy of the superconducting and the normal states respectively in units of $\mu_0 H_c^2 V/2$, where V is the volume of the sample; $V = W^2 h$, and H_c is the thermodynamic critical field; $H_c^2 = |\alpha|^2/\mu_0\beta$. $\vec{A}$, $\vec{j}_s$, and ψ are in the same units as presented in section 5.1. The difference $G - G_n$ as a function of B_a and the corresponding local magnetic fields B_z due to vortex states with $L = 2, 3$, and 4 are shown in figure 5-17 (a) and 5-18 respectively. Because the Ginzburg-Landau equations are nonlinear, for a given value of B_a, there are many possible solutions. However, stable states are ones that have the lowest energies for a given B_a. Figure 5-18 also provides the vortex configuration. It shows that giant vortex states occur when B_a is sufficiently large. In order to identify the occurrence of giant vortex states, the order parameter ψ at the centre of the superconducting square has been plotted as a function of B_a, using the idea proposed by Schweigert *et al.* [81] who found that $|\psi(0,0)|^2$ is zero when a giant vortex occurs in the superconductor. Figure 5-17 (b) shows that for the states $L = 2$ and 3, $|\psi(0,0)|^2$ decreases linearly until zero at a certain value of B_a, while it does not approach zero for the state $L = 4$. That is, giant vortex states do not occur in this size of a square superconductor with vorticity $L = 4$.

5.4.2 The energy spectrum and bound states

We have seen how an applied field B_a controls the vortex state of a nanoscale superconductor. For a given L, multivortex states and giant vortex states are usually found for low and high values of B_a respectively. We also see giant vortex states do not always exist for high B_a. Here, the energy spectrum and

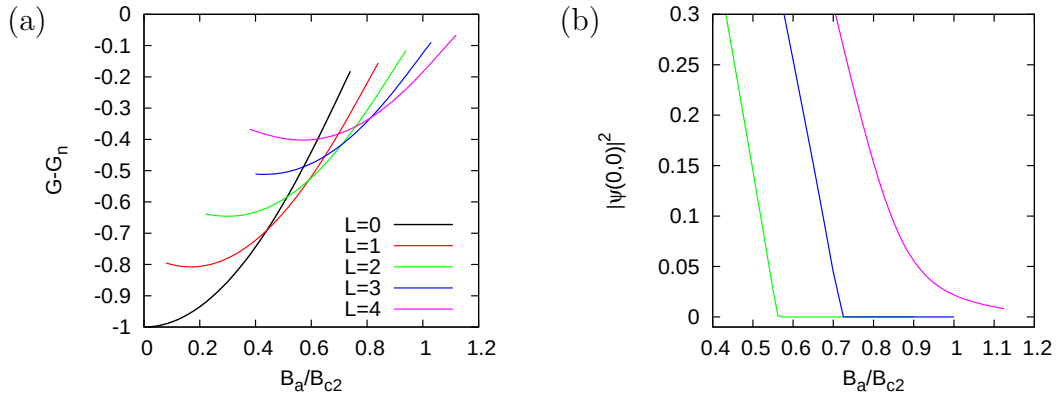

Figure 5-17: (a) The difference between superconducting and the normal state Gibbs free energy $G - G_n$ of a $8.0\xi \times 8.0\xi \times 0.8\xi$ superconductor for different vorticities L as a function of the uniform applied magnetic field B_a, (b) The square of the order parameter at the centre of the superconductor as a function of B_a for the vorticity $L = 2, 3$, and 4.

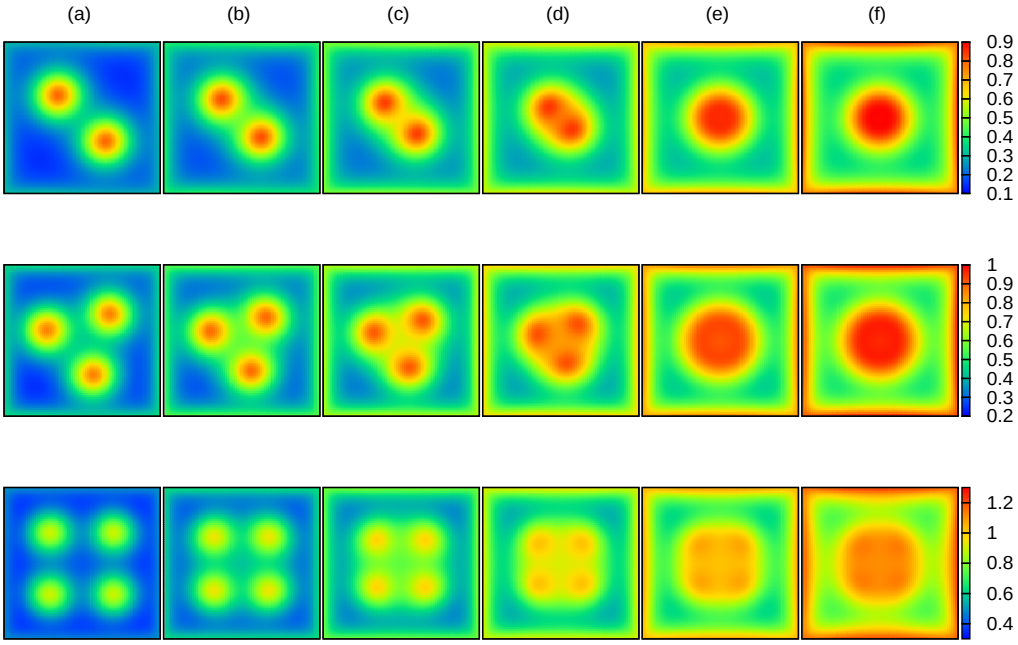

Figure 5-18: The local magnetic field B_z at a distances $z = 0.05\xi$, plotted over an area of $4\xi \times 4\xi$, due to the vortex state: $L = 2$ (top row) for applied fields B_a/B_{c2} = (a) 0.30, (b) 0.38, (c) 0.46, (d) 0.54, (e) 0.62, and (f) 0.70; $L = 3$ (middle row) for applied fields B_a/B_{c2} = (a) 0.45, (b) 0.53, (c) 0.61, (d) 0.69, (e) 0.77, and (f) 0.85; and $L = 4$ (bottom row) for applied fields B_a/B_{c2} = (a) 0.50, (b) 0.62, (c) 0.74, (d) 0.86, (e) 0.98, and (f) 1.10.

electron states in an adjacent DMS, induced by these inhomogeneous fields are considered. The following calculations consider a thin square superconductor with dimensions $8.0\xi \times 8.0\xi \times 0.8\xi$, and assume $\lambda = 40$ nm and $\xi = 80$ nm. These lengths correspond to Lead (Pb) [88]. For the DMS, the values $g_{\text{eff}} = 500$ and $m^* = 0.5m_e$ are assumed. The distance between the superconductor and the DMS is again set to the experimentally reasonable value, $z = 0.05\xi = 4$ nm, which ensures a strong modulation of the magnetic fields.

Figure 5-19 shows the calculated energy spectrum of the electrons in the DMS in the magnetic fields associated with different numbers of superconducting vortices, and some examples of the corresponding eigenstates are shown in figures 5-20, 5-21,...and 5-25. For the case where the vorticity $L = 1$, we find a spectrum that is reminiscent of that in figure 5-7, with both vortex-confined and edge states present. As expected, the superconductor with the smaller value of κ here is able to trap a greater number of vortex-confined states.

For the state with $L = 2$ in low applied fields B_a, we find that the energies are nearly two-fold degenerate (this is hard to discuss for figure 5-19 (b) as the splitting is smaller than the symbol size for low fields). The lowest two eigenstates found are shown in figure 5-20 where $B_a = 0.3B_{c2}$. They are strongly spin-polarised and correspond to almost identical spatial distribution. However, they can be distinguished by considering their phases. For each eigenstate, we see the most probability location of the electrons is in the region beneath the vortices. Considering the z component of the Zeeman energy acting as the effective potential when $B_a = 0.3B_{c2}$ in figure 5-26, we see that both the separation and the barrier between the two Zeeman potential wells are large, so we can infer that there is only a small interaction between wavefunctions localised to each quantum well.

With increasing applied field B_a, the vortices approach one another (see figure 5-18) with the result that the doubly degenerate levels decrease linearly in energy and exhibit an increasing splitting for fields up to $B_a = 0.59B_{c2}$. Figure 5-26 shows that the separation and the barrier between Zeeman potential wells are small by the time that $B_a = 0.5B_{c2}$. The effect on the interaction between wavefunctions are visible in figure 5-21. Similar to as occurs in the problem of a double quantum well [90], the lowest and the first excited state form a bonding and an antibonding state respectively, and the levels split in energy.

If B_a is greater than the critical value $B_a = 0.59B_{c2}$, the $L = 2$ multivortex state becomes a giant vortex state. An example of the effective potential that exists due to giant vortex states is shown in figure 5-26 for $B_a = 0.7B_{c2}$, where it is seen that the two quantum wells have merged to form a wider quantum well. The associated eigenstates and their phases illustrated in figure 5-22 for $B_a = 0.62B_{c2}$ resemble those trapped by a single vortex, exhibiting approximately rotational symmetry, but their spatial extent is larger. From now on, we will refer to states such as these as "giant vortex-confined states".

As B_a increases beyond $0.59B_{c2}$, the energy levels of the giant vortex-confined states decrease linearly with similar slope to those of the weakly coupled single vortex-confined states. The decrease in the depth of the effective Zeeman well, and evolution of the field at the edge of the superconductor result in progressively fewer giant vortex-confined states and more edge states. As shown in figure 5-23, when $B_a = 0.7$ there is only one giant vortex-confined state, the lowest level. For high B_a, the majority of the states whose energies are less than the lowest Landau levels are edge states whose phases clearly deviate from those exhibiting rotational symmetry.

For case when the vorticity $L = 3$ and 4, nearly degenerate states are also found when B_a is small and these can again be described by the Zeeman potential well as before. They are almost three-fold and four-fold degenerate for $L = 3$ and 4 respectively. Increasing B_a leads to a reduced distance between the vortices, an increased interaction between the wavefunctions of states associated with the separated vortices, and the energy splitting into three and four clearly distinguishable energy levels as shown in figure 5-19. The eigenstates that result from these interactions are shown in figure 5-24 and 5-25 respectively. They show differing degree of bonding in accordance with their relative energies.

If B_a is increased further, giant vortex-confined states occur for $L = 3$ when $B_a > 0.72B_{c2}$, but no such states arise for $L = 4$ as a giant vortex does not exist. Similar to the case of $L = 2$, when B_a is sufficiently large, most of the states whose energies are less than the lowest Landau levels are edge states.

Although the Zeeman potential well picture can describe the general occurrence and behaviour of the confined states, they cannot be used to explain the detailed energy splitting of degenerate states and the phases of the states which seem to be related to the degree of bonding of wavefunctions associated with

the separated vortices. In the next section, a tight-binding model is used to describe the splitting of energies seen in figure 5-19 and the interaction between the wavefunctions.

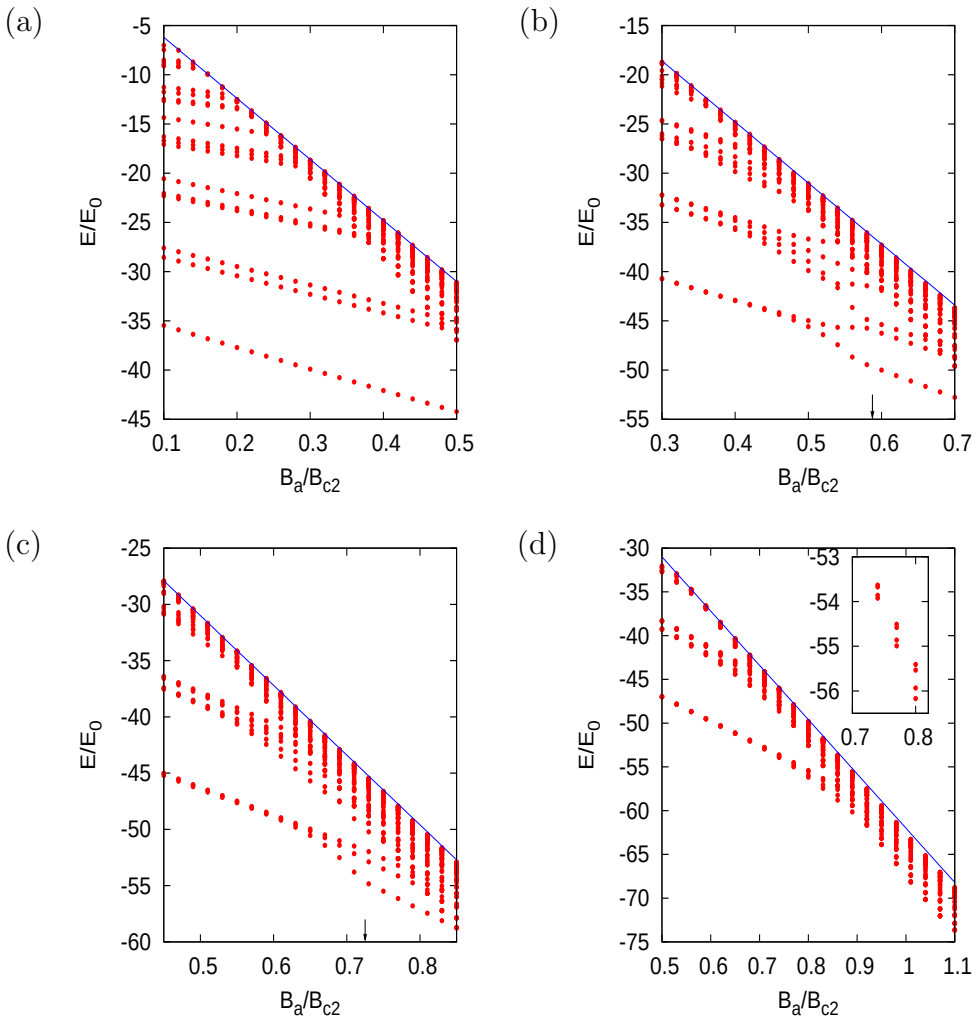

Figure 5-19: The energy spectrum of electrons in a DMS. Blue lines represent the lowest Landau level (2.8) for different values of B_a. Red dots give the spectrum of states lower in energy than the lowest Landau level in a presence of the inhomogeneous field associated with a superconducting order parameter with vorticity $L = 1$ (a), 2 (b), 3 (c), and 4 (d). The black arrows marking the horizontal axis indicate the critical magnetic field where multivortex states transform to giant vortex states. The inset in (d) focuses on the energy splitting of the lowest four energies.

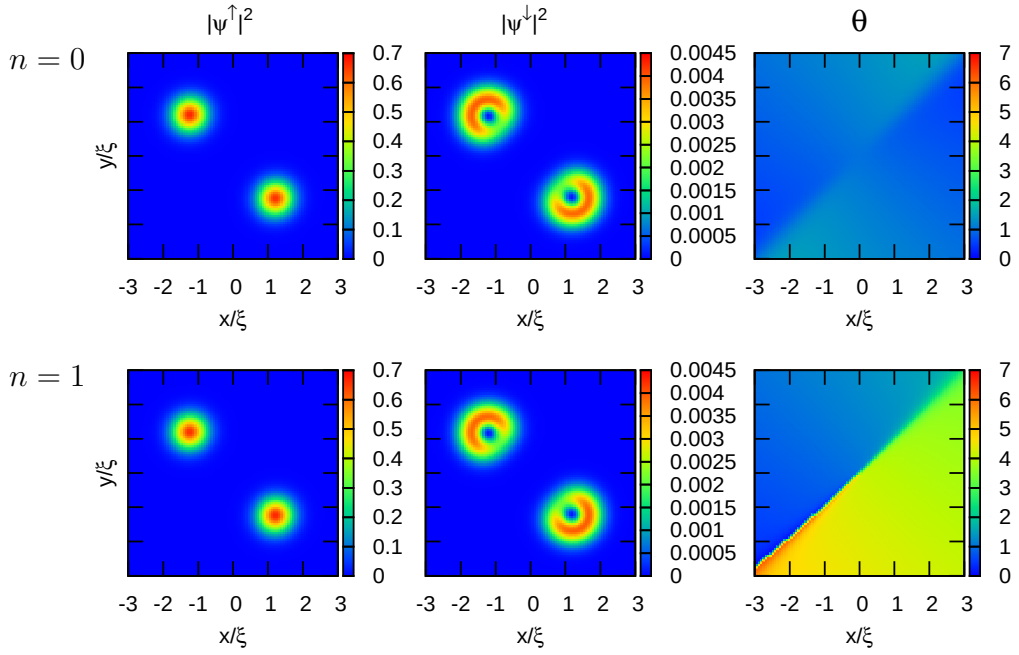

Figure 5-20: The square of spin up (left) and spin down (middle) components of the lowest two eigenfunctions in the presence of the vortex state with $L = 2$ and $B_a = 0.30B_{c2}$, plotted over the area of $6\xi \times 6\xi$ on a DMS plane beneath the square superconductor and the corresponding phase θ (right) of the spin up component.

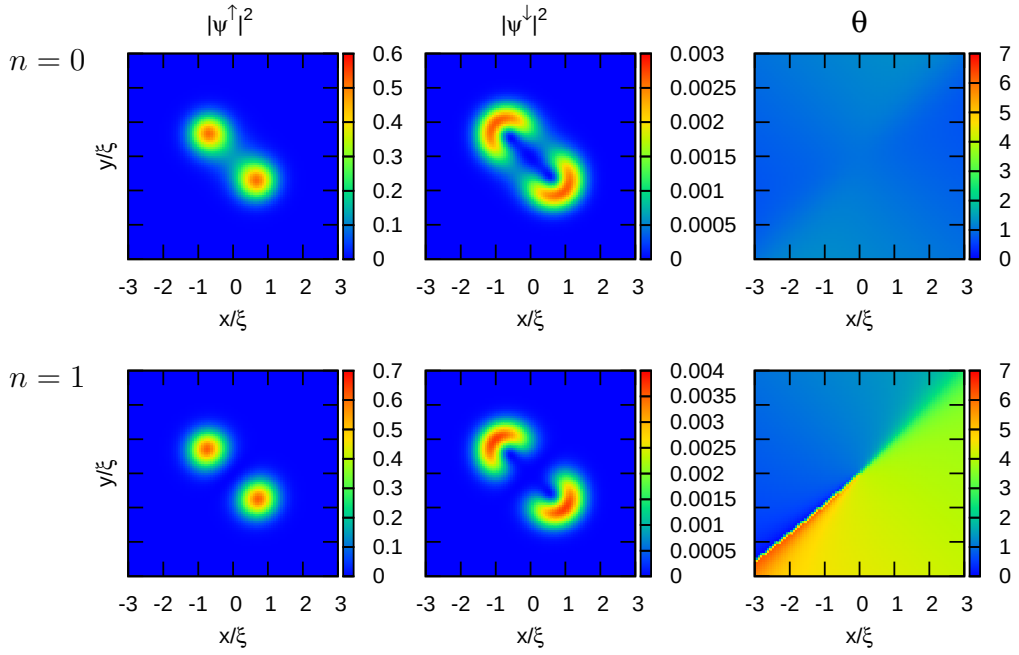

Figure 5-21: As figure 5-20 but when applied field $B_a = 0.50B_{c2}$.

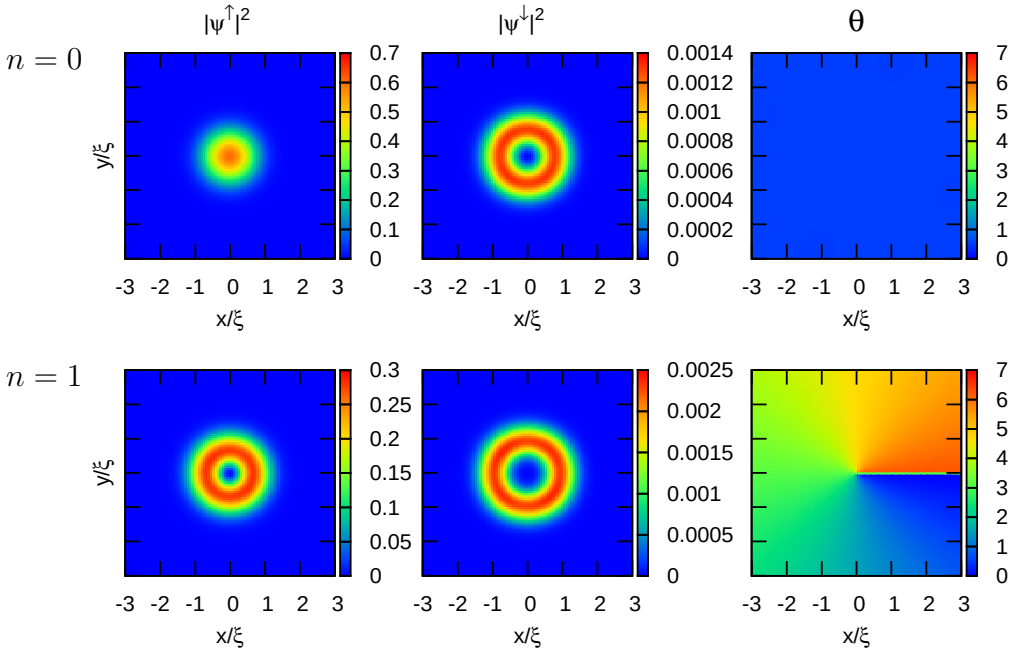

Figure 5-22: As figure 5-20 but when applied field $B_a = 0.62B_{c2}$.

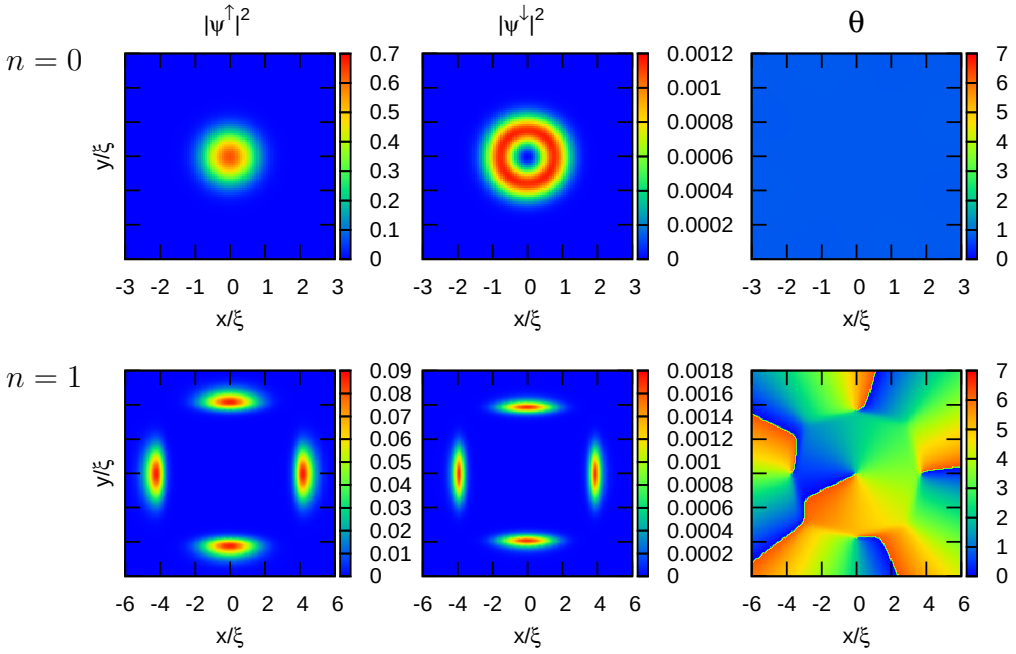

Figure 5-23: As figure 5-20 but when applied field $B_a = 0.70B_{c2}$. Notice that the length scale for the state $n = 1$ is different.

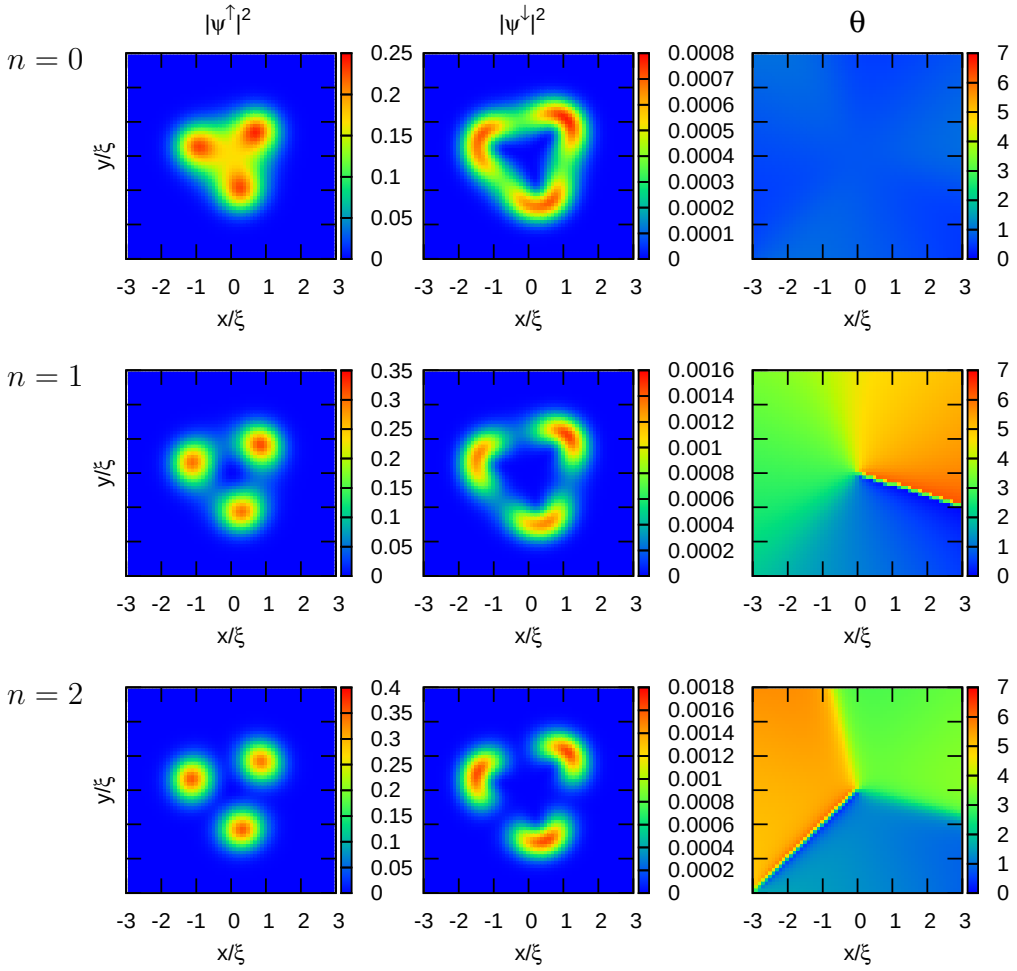

Figure 5-24: As figure 5-20 but for the lowest three eigenfunctions in the presence of vortex state $L = 3$ when applied field $B_a = 0.690 B_{c2}$.

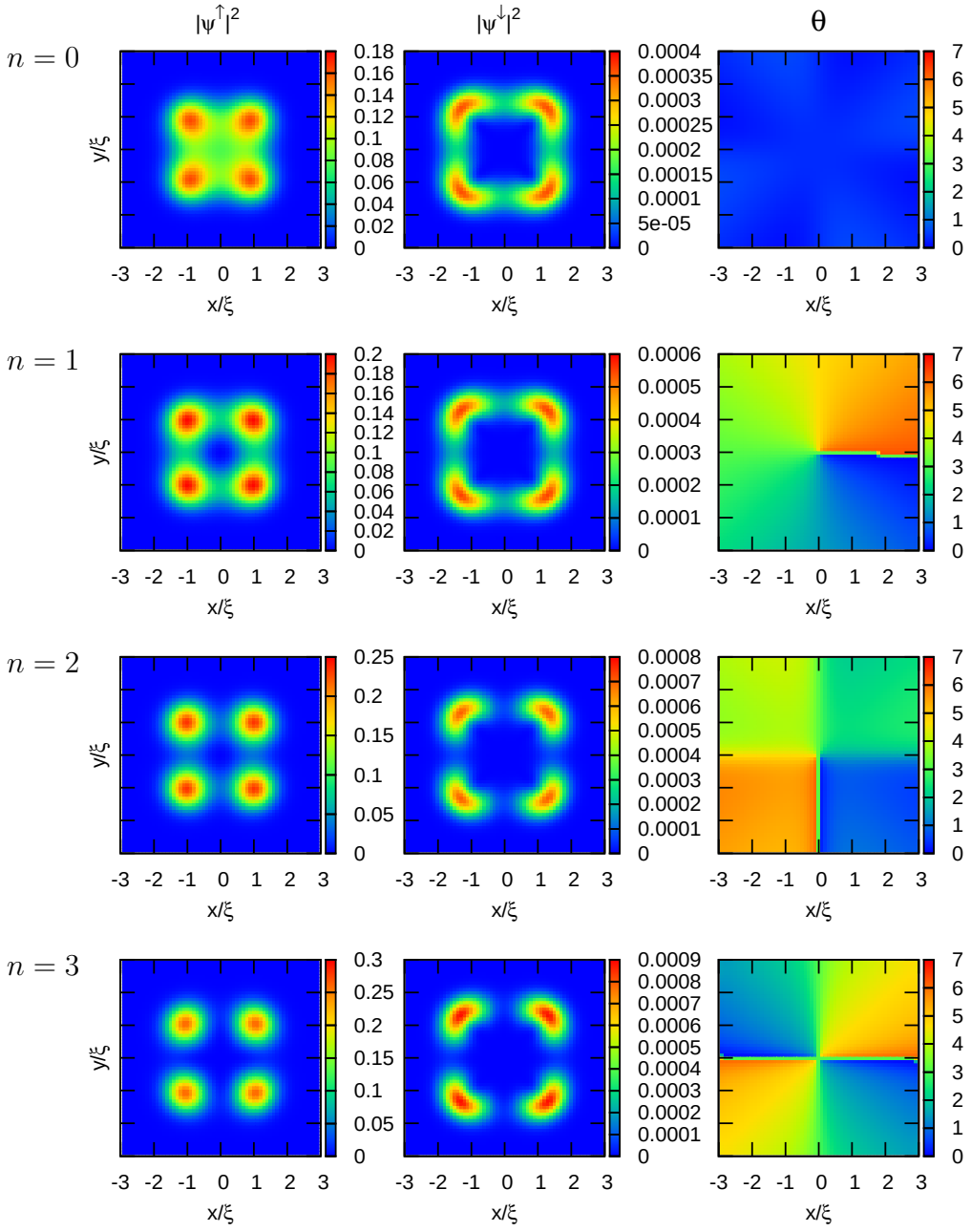

Figure 5-25: As figure 5-20 but for the lowest four eigenfunctions in the presence of vortex state $L = 4$ when applied field $B_a = 0.860 B_{c2}$.

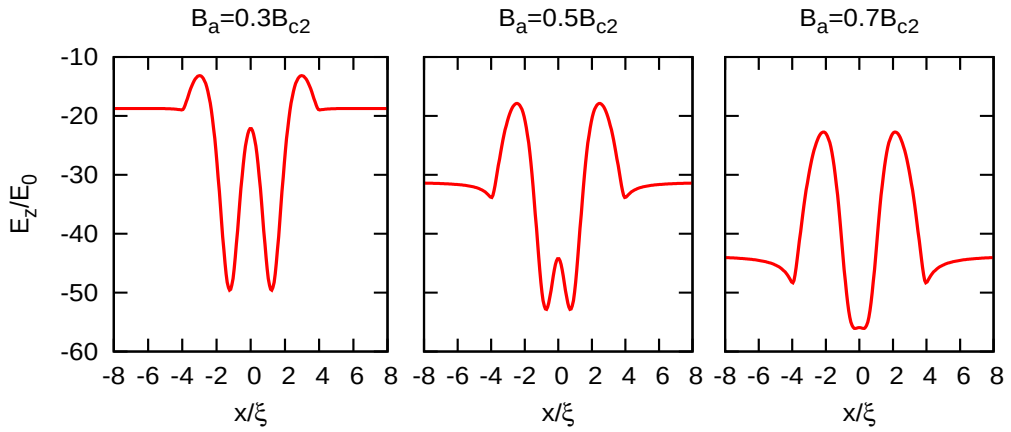

Figure 5-26: The z component of the Zeeman energy, $-\frac{1}{2}g_{\rm eff}\mu_B\sigma_z B_z$, associated with the magnetic field due to the vortex state with $L = 2$ for different values of the applied field B_a, displayed along the diagonal line passing through the centres of two vortices.

5.4.3 Tight-binding description of molecular vortex-confined states

When an applied magnetic field is small, we have seen in the previous section that individual vortices within a nanoscale square superconductor are widely separated, and the electron states in the adjacent DMS are mostly localised beneath the vortices. As the applied field increases the vortices move towards one another, and we expect that the tight-binding model [91] will be able to describe the interaction between them, especially the lowest state trapped in the deep Zeeman potential wells.

We start with the Hamiltonian that describes electrons in a DMS in a magnetic field of multivortex states with N vortices, which is

$$\widehat{H} = \frac{(\hat{p} + e\vec{A})^2}{2m^*} - \frac{1}{2}g_{\rm eff}\mu_B\vec{\sigma}\cdot\vec{B}, \tag{5.15}$$

where $\vec{B}(\vec{r}) = \sum_{n=1}^{N}\vec{B}^v(\vec{r} - \vec{R}_n)$, $\vec{B}^v(\vec{r})$ describing to the magnetic field due to a single vortex at the origin and $\vec{R}_n$ giving the vortex position. We first consider the Hamiltonian without the vector potential, which we denote $\widehat{H}^0$.

Because the results in the previous section show the lowest energy eigenstates are overwhelmingly spin up in character, we neglect the spin down component and express the eigenstates in the system of molecular vortices as

$$|\psi\rangle = \sum_n c_n \left|\psi_n^{\uparrow}\right\rangle, \tag{5.16}$$

Here, $\left|\psi_n^{\uparrow}\right\rangle$ is the spin up component of the lowest eigenstate associated with an isolated vortex at site $\vec{R}_n$, normalised as $\langle\psi_n^{\uparrow}|\psi_n^{\uparrow}\rangle = 1$. Only the lowest state corresponding to $m = 0$ is considered (we expect the theory can be extend to other m with appropriate complication), so we have $\left\langle\vec{r}\middle|\psi_n^{\uparrow}\right\rangle = \psi(|\vec{r} - \vec{R}_n|)\chi_{\uparrow}$, where ψ is assumed to be real. Multiplying from the left of the Schrödinger equation by $\langle\psi_m^{\uparrow}|$ gives

$$\langle\psi_m^{\uparrow}|\widehat{H}^0|\psi\rangle = \sum_n c_n \left\langle\psi_m^{\uparrow}\right| \widehat{H}^0 \left|\psi_n^{\uparrow}\right\rangle = E\langle\psi_m^{\uparrow}|\psi\rangle \tag{5.17}$$

or

$$c_n E_0 - c_{n+1}t - c_{n-1}t = Ec_n, \tag{5.18}$$

where we introduce $\langle\psi_n^{\uparrow}|\widehat{H}^0|\psi_n^{\uparrow}\rangle = E_0$, and $\langle\psi_m^{\uparrow}|\widehat{H}^0|\psi_n^{\uparrow}\rangle = -t$. In this calculation, the overlap between isolated vortex states on different vortices is assumed to vanish: $\left\langle\psi_m^{\uparrow}\middle|\psi_n^{\uparrow}\right\rangle = \delta_{nm}$. In a system with n-fold rotational symmetry, we have the coefficient $c_n = e^{i\phi n}$ (which can be shown in a similar manner to the Bloch condition in section 4.2.3). Continuity requires $c_{N+1} = c_1$, so straightforwardly we get the allowed values of ϕ to be $\phi_j = 2\pi j/N$; $j = 1, 2, 3, ...N$. Now, equation (5.18) and (5.16) can be rewritten as

$$E_j = E_0 - 2t\cos\phi_j. \tag{5.19}$$

$$|\psi_j\rangle = \sum_n e^{i\phi_j n}\left|\psi_n^{\uparrow}\right\rangle. \tag{5.20}$$

The above equation shows that if the number of the vortices N is 2, the energy level E_0 will split into 2 levels; $E_1 = E_0 + 2t$ and $E_2 = E_0 - 2t$ in agreement with figure 5-19 (b) for applied fields up to $\sim 0.59\ B_{c2}$ when the giant vortex forms. When $N = 3$, (5.19) predicts that the interaction between vortices will result in E_0 splitting into 2 levels $E_1 = E_2 = E_0 + t$ (two-fold degenerate) and

$E_3 = E_0 - 2t$. When $N = 4$, E_0 will split into 3 levels $E_2 = E_0 + 2t$, $E_1 = E_3 = E_0$ (two-fold degenerate) and $E_4 = E_0 - 2t$. These splitting are not those seen in figure 5-19 (c) and (d). The reason is that we have so far neglected the vector potential $\vec{A}$.

To include the vector potential $\vec{A}$, we introduce the Peierls substitution [92]

$$\psi(\vec{r} - \vec{R}_m) = \exp\left[\frac{-ie}{\hbar}\int_{\vec{R}_n}^{\vec{R}_m} \vec{A}\cdot d\vec{r}\right] \exp\left[\frac{i\hat{p}\cdot(\vec{R}_m - \vec{R}_n)}{\hbar}\right] \psi(\vec{r} - \vec{R}_n). \tag{5.21}$$

According to the n-fold rotational symmetry, if $m = n + 1$, we can use Stokes' theorem to calculate the integrals, as $\int_{\vec{R}_n}^{\vec{R}_m} \vec{A}\cdot d\vec{r} = \frac{1}{N}\oint \vec{A}\cdot d\vec{r} = \frac{1}{N}\int \vec{B}\cdot d\vec{S} = \Phi/N$, where Φ is the magnetic flux passing through the surface S which in this case is the polygon formed by vortices at the N vortices. We can therefore express the exponential term as

$$\exp\left[\frac{-ie}{\hbar}\int_{\vec{R}_n}^{\vec{R}_m} \vec{A}\cdot d\vec{r}\right] = \exp[-i2\pi\alpha/N], \tag{5.22}$$

where $\alpha = \Phi/\Phi_0$ with flux quantum $\Phi_0 = h/e$. The energy quantisation can be obtained by the same calculation as before, except in this case the Peierls substitution (5.21) gives the new condition: $c_{N+1} = c_1 \exp[-i2\pi\Phi/\Phi_0]$. If $c_n = e^{i\phi' n}$, the allowed values of ϕ' are $\phi'_j = 2\pi(j - \alpha)/N$; $j = 1, 2, 3, ...N$. Therefore, the energy quantisation and the eigenstates can be obtained by replacing ϕ_j in equations (5.19) and (5.20) by ϕ'_j,

$$E_j = E_0 - 2t\cos\phi'_j, \tag{5.23}$$

$$|\psi_j\rangle = \sum_n e^{i\phi'_j n} \left|\psi_n^{\uparrow}\right\rangle. \tag{5.24}$$

E_0 are the "on site energies of single vortex-confined states, which decrease linearly with increasing B_a. The hopping term t increases when B_a increases as the separation between the vortices decreases. The last term $\cos\phi'_j$ now depends upon both the number of vortices and the magnetic flux passing through the vortices, and determines the number of the distinct levels.

Reconsidering the spectrum in figure 5-19, we see the almost N-fold degenerate energies for low B_a are because in this limit the integrals t are very small. There is little interaction between wavefunctions associated with the separated vortices and therefore, the energy levels correspond to those of single vortex-confined states. As B_a slightly increases, the on site energy E_0 is still the dominant term and results in the almost N-fold degenerate levels declining linearly in the figure. A further increase in B_a results in the hopping t becoming large enough to reveal the splitting which is described by the trigonometric term. To explore only the splitting energies, we consider $E - E_0$ which is presented in figure 5-27. If $\alpha = 0$ when the vector potential $\vec{A} = 0$, there are two and three energy levels for $N = 3$ and 4 respectively as originally discussed. Variation of α results in additional splitting and a change in the number of levels. Figure 5-28 shows the values of α appropriate to the vortex configuration with 3 or 4 vortices, calculated by numerically integrating the flux over the approximated area within the plane of the DMS. The values obtained along with figure 5-28 show that for $N = 3$, the degenerate levels will split into 3 levels, with the gap between the lowest level and the first excited level wider than that between the first excited level and second excited level. For $N = 4$, the value of α indicates that the degenerate levels will split into 4, with a distribution corresponding to two pairs of relatively close levels separated by a more substantial interval. This is exactly the behaviour seen in the detailed calculation (see figure 5-19 (c) and the inset in (d)), and indicates that equation (5.23) derived from the tight-binding model can successfully describe the energy spectrum of the lowest energy wavefunctions, which are understood to be formed by electrons that are mostly bound underneath the individual vortices.

The eigenstates of the tight-binding model in (5.20) and (5.24) which are the combination of the isolated wavefunctions associated with individual vortices can be used to describe the phases of the eigenstates induced by the magnetic field due to multivortex states shown in figure 5-21, 5-24, and 5-25. Although the vector potential $\vec{A}$ changes the phases of the wavefunctions from ϕ to ϕ', we can roughly explore the phases by ignoring $\vec{A}$ for simplicity. It must be emphasised again that in this model we only consider the interaction between the lowest energy wavefunctions. When the number of vortices $N = 2$, two eigenstates that arise from the interaction between the lowest energy wavefunctions are

$$
\begin{aligned}
|\psi_1\rangle = &\quad e^{i\pi}\left|\psi_1^{\uparrow}\right\rangle + e^{i0}\left|\psi_2^{\uparrow}\right\rangle \qquad j=1\\
|\psi_2\rangle = &\quad e^{i0}\left|\psi_1^{\uparrow}\right\rangle + e^{i0}\left|\psi_2^{\uparrow}\right\rangle \qquad j=2.
\end{aligned}
$$

As discussed before, the lowest energy state is that with $j = 2$. The phase of each single-vortex wavefunction is zero. That means, these wavefunctions are in phase and can interact to form a bonding state, corresponding to that with $n = 0$ in figure 5-21. If $j = 1$, the phases of the wavefunctions are 0 and π, resulting in an antibonding state as seen in the figure for $n = 1$.

When $N = 3$, there are three isolated wavefunctions interacting one another to form three eigenstates,

$$
\begin{aligned}
|\psi_1\rangle = &\quad e^{i\frac{2\pi}{3}}\left|\psi_1^{\uparrow}\right\rangle + e^{i\frac{4\pi}{3}}\left|\psi_2^{\uparrow}\right\rangle + e^{i0}\left|\psi_3^{\uparrow}\right\rangle \qquad j=1\\
|\psi_2\rangle = &\quad e^{i\frac{4\pi}{3}}\left|\psi_1^{\uparrow}\right\rangle + e^{i\frac{2\pi}{3}}\left|\psi_2^{\uparrow}\right\rangle + e^{i0}\left|\psi_3^{\uparrow}\right\rangle \qquad j=2\\
|\psi_3\rangle = &\quad e^{i0}\left|\psi_1^{\uparrow}\right\rangle + e^{i0}\left|\psi_2^{\uparrow}\right\rangle + e^{i0}\left|\psi_3^{\uparrow}\right\rangle \qquad j=3
\end{aligned}
$$

For $j = 3$, all of the phases are 0 and consequently lead to the bonding state in figure 5-24 when $n = 0$. For $j = 1$ and 2 (degenerate states), the phases change as the sequence $0 \rightarrow 2\pi/3 \rightarrow 4\pi/3$ in clockwise and anticlockwise directions respectively (assume that sites are labelled in clockwise sense). The change of phases correspond to the states $n = 1$ and 2 in the figure. Notice that difference between the phases of the neighbouring wavefunctions is $2\pi/3$ for the degenerate states with $j = 1$ and 2. This illustrates the degree of bonding which is between bonding and antibonding states found when $N = 2$.

When $N = 4$, four isolated wavefunctions interact one another to form four eigenstates,

$$
\begin{aligned}
|\psi_1\rangle = &\quad e^{i\frac{\pi}{2}}\left|\psi_1^{\uparrow}\right\rangle + e^{i\pi}\left|\psi_2^{\uparrow}\right\rangle + e^{i\frac{3\pi}{2}}\left|\psi_3^{\uparrow}\right\rangle + e^{i0}\left|\psi_4^{\uparrow}\right\rangle \qquad j=1\\
|\psi_2\rangle = &\quad e^{i\pi}\left|\psi_1^{\uparrow}\right\rangle + e^{i0}\left|\psi_2^{\uparrow}\right\rangle + e^{i\pi}\left|\psi_3^{\uparrow}\right\rangle + e^{i0}\left|\psi_4^{\uparrow}\right\rangle \qquad j=2\\
|\psi_3\rangle = &\quad e^{i\frac{3\pi}{2}}\left|\psi_1^{\uparrow}\right\rangle + e^{i\pi}\left|\psi_2^{\uparrow}\right\rangle + e^{i\frac{\pi}{2}}\left|\psi_3^{\uparrow}\right\rangle + e^{i0}\left|\psi_4^{\uparrow}\right\rangle \qquad j=3\\
|\psi_4\rangle = &\quad e^{i0}\left|\psi_1^{\uparrow}\right\rangle + e^{i0}\left|\psi_2^{\uparrow}\right\rangle + e^{i0}\left|\psi_3^{\uparrow}\right\rangle + e^{i0}\left|\psi_4^{\uparrow}\right\rangle \qquad j=4
\end{aligned}
$$

Again, when $j = N$ (4 here), they always form a bonding state corresponding to the lowest state shown in figure 5-25. If $j = 1$ and 3 (degenerate states), the phases change as the sequence $0 \rightarrow \pi/2 \rightarrow \pi \rightarrow 3\pi/2$ in clockwise and anticlockwise directions respectively (phase difference between neighbouring wavefunction is $\pi/2$), corresponding to the states with $n = 1$ and 2 in the figure. Finally, when $j = 2$, the difference between the phase of the neighbouring wavefunctions is π similar to the antibonding state in the case of $N = 2$. This phase distribution correspond to the state with $n = 3$ in the figure.

We have seen the phases of wavefunctions associated with separated vortices determine the interaction between them and the energy level of the resulting eigenstates. When the difference between the phases of neighbouring single-vortex wavefunctions is small, the interaction between them resembles that in bonding states, resulting in a low energy eigenstate. On the other hand, when the difference is close to π, the interaction between them resembles that in antibonding states, resulting in a high energy eigenstate. If the vector potential $\vec{A}$ is not zero as assumed in the phase discussion above, the phases of the wavefunctions will change from ϕ to ϕ'. This does not substantially change the interpretation of the phase diagrams in figures 5-21, 5-24, and 5-25, but does modify the interactions and causes the splitting of degenerate states as discussed previously.

In this section, the energy spectrum of electrons in the presence of the magnetic field associated with a square superconductor containing a small number of vortices has been investigated. For a given value of the vorticity L, we find almost degenerate states at low applied fields B_a, which split as B_a increases. Giant vortex-confined states are found when B_a is large enough to transform the superconductor into a giant vortex state, which resemble a single vortex-confined states, but with a greater spatial extent. Edge states, which are usually found in high applied fields B_a, can exist if the magnetic field concentrated at the edge of the finite superconductor is sufficiently strong. Unlike the vortex-confined states, their energies are less widely separated. To get further insights, we have applied a tight-binding method to describe the energy splitting of degenerate states which is not well explained by a picture based only upon effective Zeeman potential wells. This can successfully explain the distribution of levels as the applied field is varied and the interaction between the wavefunctions associated with individual vortices.

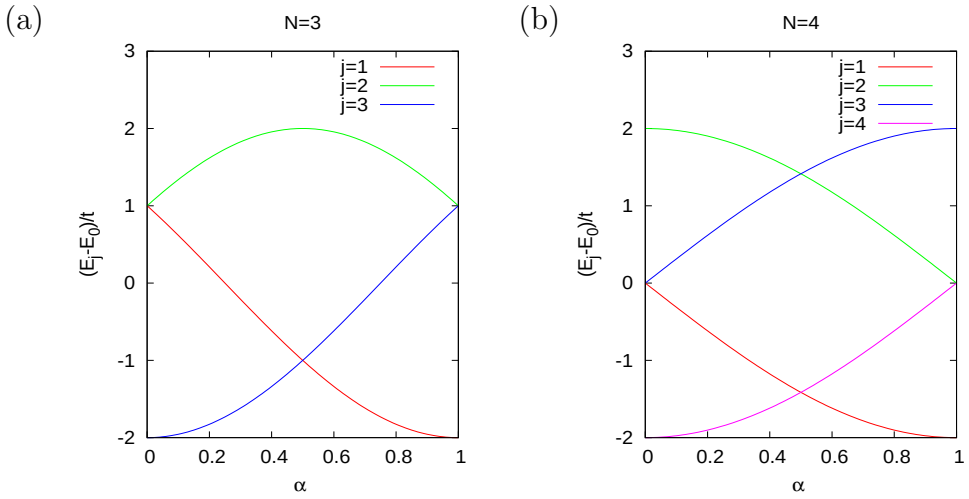

Figure 5-27: The splitting energies as a function of α for $N = 3$ and 4 predicted by the tight-binding model.

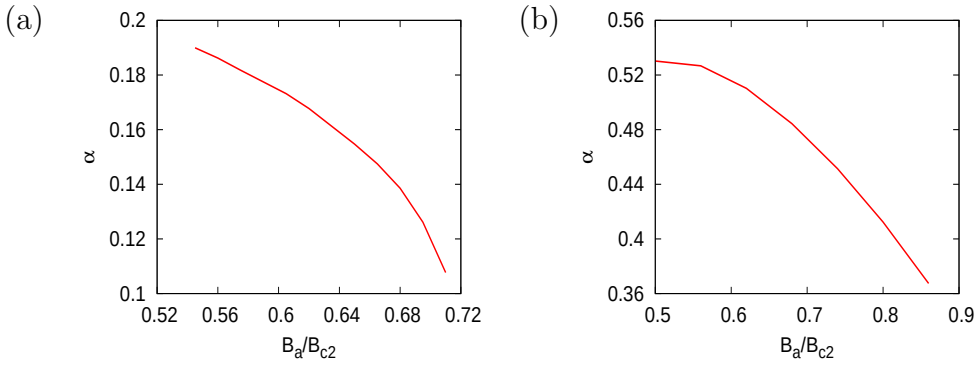

Figure 5-28: The variation of the magnetic flux parameter α associated with (a) 3 and (b) 4 vortex configurations, calculated in the plane of the DMS as a function of applied field B_a.

5.5 Summary

In this Chapter, we have considered the system consisting of the heterostructure of a square superconductor above a planar dilute magnetic semiconductor, focusing on the effects of the inhomogeneous magnetic field due to the vortex phase of the superconductor on the electronic structure of electrons in the semiconductor. We observe many kinds of electron states created in the DMS. We first verified that the magnetic field due to a single vortex is sufficiently strong to induce vortex-confined states, which are strongly spin-polarised in the DMS, similar to that due to an isolated vortex in an infinite superconductor. In the multivortex state, "molecular" vortex-confined states are found. In contrast to real molecules, here an applied magnetic field moves the positions of the vortices, which has the effect of controlling the interaction between vortex-confined states associated with neighbouring vortices. A tight-binding model has been successfully applied to describe the effect of this interaction. If the field is strong enough to transform the multivortex superconducting states to giant vortex state, the artificial molecules transform continuously into giant vortex-confined states which resemble single vortex-confined states, but with a greater spatial extent. Finally, edge states are identified that are localised at the edge of the superconductor, induced by the concentration of magnetic field that arises there.

Chapter 6

Conclusion and further work

In this thesis we have investigated the effect of inhomogeneous magnetic fields associated with superconductors on the electronic structure of electrons in a nearby DMS plane where the giant Zeeman effect exists. Unlike, a conventional semiconductor, the Zeeman interaction cannot be neglected, but can be considered as an additional potential which plays a key role in confining charge carriers and manipulating their spin degree of freedom. It can dramatically change the physics of the semiconductor in a magnetic field. Here, we have proposed many possibilities of using inhomogeneous magnetic fields due to superconductors.

Firstly, the inhomogeneous magnetic field due to a superconducting disk in a Meissner state was exploited. To understand the effects in this system, we began by approximating the magnetic field with a simple step-like model form, which only consists of the normal component of the field. The Zeeman energy due to the field has been clearly shown to be a spin dependent effective potential, resulting in spin dependent states of electrons in the adjacent DMS. Their spatial distribution was classified, and related to their energy. This model field also enabled the probability current densities of quantum states confined magnetically to be intuitively described by classical trajectories of electrons moving in cyclotron and skipping orbits. The weak point of this model field is an incorrect description of the energies of the quantum states that exist mostly far from the superconductor.

Next, we extended the study by using a more realistic magnetic field consisting of both normal and radial components. The corresponding energy spectrum of electrons in the DMS is found to be more complicated, but can be understood by considering the effect of each component of the field separately. The normal

component acts as a spin dependent attractive potential as before, while the radial component couples spin up and spin down wavefunctions together to form the eigenstates. The realistic field also induces edge states, which arise from the concentration of the magnetic field at the boundary of the superconductor, and which were absent in the simple step-like model field. The results make clear that the realistic field satisfying conservation of magnetic flux is more reliable as it correctly describes quantum states occurring far from the superconductor.

Another option is to use the inhomogeneous magnetic field due to a superconducting film in a vortex state in which an applied magnetic field is converged to the centre of a superconducting vortex. The concentrated field associated with an isolated vortex can induce nearly spin polarised electron states in the adjacent DMS. In the presence of an Abrikosov lattice of vortices, the bound states interact with one another, resulting in a band structure. Since each vortex carries a magnetic flux $\frac{\Phi_0}{2} = h/2e$, vortex separation can be controlled by the magnitude of the external field. Hence the applied field can control the band structure by moving vortices, illustrating one benefit of using a superconducting film. The results found for this system using a basis of Landau states are different from those previously reported by Rappoport *et al.* [6]. Therefore, to verify the corrections of our energy bands, a tight-binding theory has been developed to describe the bands when the interaction between the bound states is weak. This confirms our numerical findings.

Finally, we have explored the effects of the inhomogeneous field due to a square superconductor in a vortex state. In this case, each vortex in the superconductor interacts not only with neighbouring vortices, but also with the boundary, resulting in new kinds of superconducting vortex states; a multivortex and a giant vortex state. Calculations have been performed which show that the magnetic field due to a single vortex in a nanoscale square superconductor is strong enough to induce vortex-confined states in a nearby DMS. Similar to those due to an isolated vortex in an infinite superconductor, the electron states are spin polarised and exhibit rotational symmetry. In a multivortex state, we find molecular vortex-confined states in a DMS, due to interactions between single vortex-confined states underneath each of the vortices. The gradual transition from a multivortex state to a giant vortex state in the superconductor leads to a continuous transition from molecular vortex-confined states to giant-vortex

confined states, eventually exhibiting rotational symmetries, similar to those single vortex-confined states, but with a greater spatial distribution. Edge states which localised at the boundary of the superconductor are also found when the applied field is sufficiently strong. The physical picture of interacting single-vortex states has been confirmed by developing a description based upon the tight-binding method, which successfully describes the energy levels and the interaction between wavefunctions mostly localised underneath vortices when the superconductor is in a multivortex state.

For future work, it would be interesting to extend this study by exploiting different sources of inhomogeneous magnetic fields. For example, instead of an uniform external magnetic field, a magnetic dot with a dipole moment oriented perpendicular to the DMS plane could be placed on top of a superconducting film to generate a magnetic field for superconductor/DMS systems. There are both theoretical and experimental works [97, 98, 99, 100] investigating the configuration of the superconducting vortices in the presence of the magnetic field due to a magnetic dot. In this system, superconducting vortices exist beneath the dot region, while antivortices exist around the magnetic dot. The number of vortices, antivortices and their structure depend on the size and a magnetic moment of the magnetic dot. On the basis of the findings reported in this thesis, it would be expected that spin-up dominant states will be induced by the magnetic field due to vortices beneath the magnetic dot (in a nearby DMS) and spin-down dominant states induced by the magnetic field due to the antivortices localised around the dot. Therefore, it may be possible to see "molecular" electron states which consist of spin up and spin down bound states coupled via the in-plane component of the magnetic field at the boundary of the dot. The number of vortices and antivortices could be increased or decreased by varying the magnitude and direction of an additional external magnetic field, leading to controllable interaction between them. Both this system and those described in detail in this thesis could also be studied experimentally, probing the energy spectrum of the bound states in the DMS by measuring the longitudinal resistance of the Hall bar geometry consisting of the superconductor on top of a DMS Hall bar with the same width.

Appendix A

Analytical solution of Landau quantisation

In the following, we will solve the differential equation (2.6) analytically by investigating the behaviour of the wavefunction when ρ is close to 0 and infinity, and then find a suitable substitution for solving it. The idea is actually similar to the case of the hydrogen atom. Assuming ψ is a well behaved wavefunction, we first consider the limit $\rho \to \infty$ and find that (2.6) can be approximated by

$$\begin{aligned} \psi'' - \frac{\psi}{4} &= 0 \\ \therefore \quad \psi(\rho) &= c_1 e^{\frac{\rho}{2}} + c_2 e^{-\frac{\rho}{2}}. \end{aligned} \tag{A.1}$$

Because $\psi(\rho \to \infty)$ must be finite, $c_1 = 0$. For the limit $\rho \to 0$, ψ is expanded in power series:

$$\begin{aligned} \psi &= \rho^\alpha (1 + a\rho + b\rho^2 + \ldots) \approx \rho^\alpha \\ \psi' &= \alpha \rho^{\alpha-1} \\ \psi'' &= \alpha(\alpha - 1)\rho^{\alpha-2}, \end{aligned}$$

and substituted into (2.6) to obtain

$$\begin{aligned} \alpha(\alpha-1)\rho^{\alpha-1} + \alpha\rho^{\alpha-1} + (-\frac{\rho}{4} + \beta - \frac{m^2}{4\rho})\rho^\alpha &= 0 \\ \alpha(\alpha-1)\rho^{\alpha-1} + \alpha\rho^{\alpha-1} - \frac{m^2}{4}\rho^{\alpha-1} &= 0, \end{aligned} \tag{A.2}$$

where in the second equation in (A.2), the higher-order terms which become negligible when $\rho \to 0$ are dropped. Now one can see the solution easily; $\alpha = \pm |m|/2$. Again, $\psi(\rho \to 0)$ must be finite, so that only $\alpha = +|m|/2$ can exist. Therefore, we can deduce that ψ can be written as

$$\psi(\rho) = e^{-\frac{\rho}{2}} \rho^{|m|/2} \omega(\rho), \tag{A.3}$$

whose first and second derivatives are

$$\psi' = e^{-\frac{\rho}{2}} \rho^{|m|/2} \left[\omega' + \left(\frac{|m|}{2\rho} - \frac{1}{2} \right) \omega \right] \tag{A.4}$$

$$\psi'' = e^{-\frac{\rho}{2}} \rho^{|m|/2} \left[\omega'' + \left(\frac{|m|}{\rho} - 1 \right) \omega' + \left(\frac{|m|}{2\rho^2} + \frac{|m|^2}{4\rho^2} - \frac{|m|}{2\rho} + \frac{1}{4} \right) \omega \right]. \tag{A.5}$$

Substituting (A.4) and (A.5) into (2.6), one get

$$\rho\omega'' + (|m| + 1 - \rho)\omega' - (-\beta + \frac{|m|}{2} + \frac{1}{2})\omega = 0. \tag{A.6}$$

This is Kummer's equation, whose solution is [93]

$$\omega(\rho) = AM(-\beta + \frac{|m|}{2} + \frac{1}{2}, |m| + 1; \rho) + BU(-\beta + \frac{|m|}{2} + \frac{1}{2}, |m| + 1; \rho), \tag{A.7}$$

where $M(a, b; \rho)$ and $U(a, b; \rho)$ the a Kummer-M function and Kummer-U function respectively. A and B are arbitrary constants. When b is an integer, $U(a, b; \rho)$ is not finite at $\rho = 0$, so B must be 0. In general, as $\rho \to \infty$, $M(a, b; \rho)$ is proportional to $e^{\rho}\rho^{a-b}$ [93]. That is, in this limit, the wavefunction $\psi(\rho)$ is not finite at $\rho \to \infty$. However, as noted by Landau [49], when a is a nonpositive integer, $M(a, b; \rho)$ becomes a polynomial in ρ, making the wavefunction $\psi(\rho)$ regular everywhere. Therefore, we get the analytical solution

$$\psi(\rho) = e^{-\frac{\rho}{2}} \rho^{|m|/2} M(-n, |m| + 1; \rho), \tag{A.8}$$

where $n = \beta - \frac{|m|}{2} - \frac{1}{2}$ is a nonnegative integer. Finally, we rewrite the wavefunction $\psi(\rho)$ as a function of r and normalise the wavefunction $\psi(r)$ by requiring

the condition: $\int_0^\infty |\psi|^2 \, r dr = 1$ to obtain

$$\psi^\sigma_{nm}(r) = \frac{1}{\ell_B |m|!} \left[\frac{(|m|+n)!}{2^{|m|} n!} \right]^{\frac{1}{2}} \exp\left(\frac{-r^2}{4\ell_B^2} \right) \left(\frac{r}{\ell_B} \right)^{|m|} M(-n, |m|+1, r^2/2\ell_B^2), \tag{A.9}$$

where $\ell_B = \sqrt{\hbar/eB} = \sqrt{\hbar/m^*\omega_c}$ is the magnetic length. The normalisation factor is obtained by using the relation between the associated Laguerre function $L_n^m(\rho)$ and Kummer-M function, and its orthonormality [64]:

$$M(-n, m+1, \rho) = \frac{n!m!}{(m+n)!} L_n^m(\rho), \tag{A.10}$$

$$\int_0^\infty e^{-\rho} \rho^m L_n^m(\rho) L_{n'}^m(\rho) d\rho = \frac{(m+n)!}{n!} \delta_{nn'}. \tag{A.11}$$

Appendix B

The general form of the eigenfunction

Without approximation, we express the eigenfunctions of the Hamiltonian (3.7) as

$$\Psi(r,\phi) = \begin{pmatrix} \psi^{\uparrow}(r,\phi) \\ \psi^{\downarrow}(r,\phi) \end{pmatrix} = \sum_m \sum_p \begin{pmatrix} \psi_m^{\uparrow}(r)\exp(im\phi) \\ \psi_p^{\downarrow}(r)\exp(ip\phi) \end{pmatrix}. \tag{B.1}$$

Considering the Hamiltonian $\widehat{H}$, note that the vector potential does not change the symmetry, so we can study the eigenfunctions of $\widehat{H}$ by ignoring the vector potential. Next, for convenience we write the Hamiltonian as

$$-\frac{\hbar^2}{2m}\nabla^2 - \frac{1}{2}g_{\text{eff}}\mu_B \begin{pmatrix} B_z & B_r e^{-i\phi} \\ B_r e^{i\phi} & -B_z \end{pmatrix}, \tag{B.2}$$

where B_z and B_r are the transverse and radial components of the magnetic field $\vec{B}$. Then, the Schrödinger equation is

$$-\frac{\hbar^2}{2m}\begin{pmatrix} \nabla^2\psi^{\uparrow} \\ \nabla^2\psi^{\downarrow} \end{pmatrix} - \frac{1}{2}g_{\text{eff}}\mu_B \begin{pmatrix} B_z\psi^{\uparrow} & B_r e^{-i\phi}\psi^{\downarrow} \\ B_r e^{i\phi}\psi^{\uparrow} & -B_z\psi^{\downarrow} \end{pmatrix} = E\begin{pmatrix} \psi^{\uparrow} \\ \psi^{\downarrow} \end{pmatrix}. \tag{B.3}$$

We separate (B.3) into two equations. The first equation is

$$\begin{aligned} E\sum_m \psi_m^{\uparrow}(r)e^{im\phi} &= \sum_m -\frac{\hbar^2}{2m}\left(\frac{1}{r}\frac{\mathrm{d}}{\mathrm{d}r}\left(r\frac{\mathrm{d}}{\mathrm{d}r}\right)-\frac{m^2}{r^2}\right)\psi_m^{\uparrow}(r)e^{im\phi} \\ &\quad -\frac{1}{2}g_{\mathrm{eff}}\mu_B\sum_{m,p}\left(B_z\psi_m^{\uparrow}(r)e^{im\phi}+B_r\psi_p^{\downarrow}(r)e^{i(p-1)\phi}\right), \end{aligned} \tag{B.4}$$

and the second one is

$$\begin{aligned} E\sum_p \psi_p^{\downarrow}(r)e^{ip\phi} &= \sum_p -\frac{\hbar^2}{2m}\left(\frac{1}{r}\frac{\mathrm{d}}{\mathrm{d}r}\left(r\frac{\mathrm{d}}{\mathrm{d}r}\right)-\frac{p^2}{r^2}\right)\psi_p^{\downarrow}(r)e^{ip\phi} \\ &\quad -\frac{1}{2}g_{\mathrm{eff}}\mu_B\sum_{m,p}\left(B_r\psi_m^{\uparrow}(r)e^{i(m+1)\phi}-B_z\psi_p^{\downarrow}(r)e^{ip\phi}\right). \end{aligned} \tag{B.5}$$

Multiplying (B.4) by $\exp(-il\phi)/2\pi$ and integrating the ϕ coordinate from 0 to 2π, we obtain

$$-\frac{\hbar^2}{2m}\left(\frac{1}{r}\frac{\mathrm{d}}{\mathrm{d}r}\left(r\frac{\mathrm{d}}{\mathrm{d}r}\right)-\frac{l^2}{r^2}\right)\psi_l^{\uparrow}(r)-\frac{1}{2}g_{\mathrm{eff}}\mu_B(B_z\psi_l^{\uparrow}(r)+B_r\psi_{l+1}^{\downarrow})=E\psi_l^{\uparrow}(r). \tag{B.6}$$

Next, multiplying (B.5) by $\exp(-i(l+1)\phi)/2\pi$ and integrating over ϕ from 0 to 2π, we obtain

$$\begin{aligned} -\frac{\hbar^2}{2m}\left(\frac{1}{r}\frac{\mathrm{d}}{\mathrm{d}r}\left(r\frac{\mathrm{d}}{\mathrm{d}r}\right)-\left(\frac{l+1}{r}\right)^2\right)\psi_{l+1}^{\downarrow}(r) & \\ -\frac{1}{2}g_{\mathrm{eff}}\mu_B(B_r\psi_l^{\uparrow}(r)-B_z\psi_{l+1}^{\downarrow}(r)) &= E\psi_{l+1}^{\downarrow}(r). \end{aligned} \tag{B.7}$$

Then, multiplying (B.6) by $e^{il\phi}$ and (B.7) by $e^{i(l+1)\phi}$ gives

$$-\frac{\hbar^2}{2m}\nabla^2\psi_l^{\uparrow}(r)e^{il\phi}-\frac{1}{2}g_{\mathrm{eff}}\mu_B(B_z\psi_l^{\uparrow}(r)+B_r\psi_{l+1}^{\downarrow})e^{il\phi}=E\psi_l^{\uparrow}(r)e^{il\phi}, \tag{B.8}$$

$$-\frac{\hbar^2}{2m}\nabla^2\psi_{l+1}^{\downarrow}(r)e^{i(l+1)\phi}-\frac{1}{2}g_{\mathrm{eff}}\mu_B(B_r\psi_l^{\uparrow}(r)-B_z\psi_{l+1}^{\downarrow}(r))e^{i(l+1)\phi}=E\psi_{l+1}^{\downarrow}(r)e^{i(l+1)\phi}. \tag{B.9}$$

Equations (B.8) and (B.9) can be combined as.

$$\left[-\frac{\hbar^2}{2m}\nabla^2 - \frac{1}{2}g_{\text{eff}}\mu_B \begin{pmatrix} B_z & B_r e^{-i\phi} \\ B_r e^{i\phi} & -B_z \end{pmatrix}\right] e^{il\phi}\begin{pmatrix} \psi_l^{\uparrow}(r) \\ \psi_{l+1}^{\downarrow}(r)e^{i\phi} \end{pmatrix} = Ee^{il\phi}\begin{pmatrix} \psi_l^{\uparrow}(r) \\ \psi_{l+1}^{\downarrow}(r)e^{i\phi} \end{pmatrix}$$

or

$$\widehat{H}e^{il\phi}\begin{pmatrix} \psi_l^{\uparrow}(r) \\ \psi_{l+1}^{\downarrow}(r)e^{i\phi} \end{pmatrix} = Ee^{il\phi}\begin{pmatrix} \psi_l^{\uparrow}(r) \\ \psi_{l+1}^{\downarrow}(r)e^{i\phi} \end{pmatrix}. \tag{B.10}$$

This demonstrates that $\psi_l^{\uparrow}e^{il\phi}$ is only coupled to $\psi_{l+1}^{\downarrow}e^{i(l+1)\phi}$, so that the eigenstates of $\widehat{H}$ have the general from,

$$\Psi_m(r,\phi) = e^{im\phi}\begin{pmatrix} \psi_m^{\uparrow}(r) \\ e^{i\phi}\psi_{m+1}^{\downarrow}(r) \end{pmatrix}. \tag{B.11}$$

It is also straightforwardly to see the orthogonality of the eigenstates:

$$\int \Psi_m^{\dagger}(r,\phi)\Psi_{m'}(r,\phi)d^2\vec{r} \propto \delta_{mm'}. \tag{B.12}$$

Appendix C

B-splines

B-splines are piecewise polynomials that can be used for approximating arbitrary functions. In computational atomic physics, B-splines basis sets [94, 95, 96, 8] have been used widely to solve the Schrödinger equation and explore atomic structure. In this Appendix, we will introduce B-splines briefly, describe their behaviour, and show why we use them.

In this calculation, we will approximate a wavefunction $\psi(x)$ extending over an interval $[s_1, s_2]$ by using a set of n B-splines of order k. The interval is divided into segments described by the knot sequence $\{t_i\}, i = 1, 2, 3, ..., n + k$, where $s_1 = t_1 \leq t_2 \leq t_3 ... \leq t_{n+k} = s_2$. If the wavefunction $\psi(x)$ does not vanish at s_1 and s_2, we need to choose the multiplicity of the knot at the endpoints, s_1 and s_2, being k. For example, when k is 3, $s_1 = t_1 = t_2 = t_3 < t_4 < t_5 ... < t_n < t_{n+1} = t_{n+2} = t_{n+3} = s_2$. The B-splines of order k, $B_{i,k}(x)$, and their first derivatives, $DB_{i,k}(x)$, are defined by the recursive relation:

$$B_{i,1}(x) = \begin{cases} 1 & t_i \leq x < t_{i+1} \\ 0 & \text{otherwise,} \end{cases} \tag{C.1}$$

$$B_{i,k}(x) = \frac{x - t_i}{t_{i+k-1} - t_i} B_{i,k-1}(x) + \frac{t_{i+k} - x}{t_{i+k} - t_{i+1}} B_{i+1,k-1}(x), \tag{C.2}$$

and

$$DB_{i,k}(x) = \frac{k-1}{t_{i+k-1} - t_i} B_{i,k-1}(x) + \frac{k-1}{t_{i+k} - t_{i+1}} B_{i+1,k-1}(x). \tag{C.3}$$

The first order B-splines are clearly step functions and the higher order B-splines,

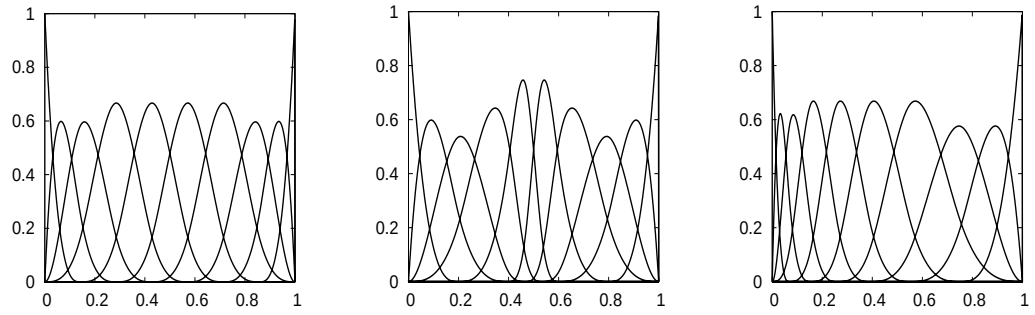

(a) (b) (c)

Figure C-1: 10 B-splines of order 4, $B_{i,4}(r)$, over the interval $[0, 1]$ distribute on (a) a uniform, (b) a concentrated, and (c) an exponential scale.

$B_{i,k}(x)$ are piecewise polynomials of degree $k-1$, existing inside the segment $[t_i < t_{i+k})$. Because the Schrödinger equation is a second order differential equation, we choose B-splines of order 4 to approximate the eigenfunctions as their first and second derivatives are continuous. Then, the wavefunction $\psi(x)$ can be expanded in terms of B-splines:

$$\psi(x) = \sum_{i=1}^{n} b_i B_{i,4}(x), \tag{C.4}$$

where b_i are the coefficients of the expansion. The main reason we use B-splines is the flexible knot distribution. The distribution of knots influences how fast eigenenergies and eigenstates converged. The key idea used to choose the distribution is that the region where wave functions vary rapidly needs more knots than the region where wavefunctions vary slowly. Figure C-1 illustrates a set of 10 B-splines of order 4 over the interval $[0, 1]$, where the knots distribute on a uniform, concentrated, and exponential scale respectively. When first investigating the eigenstates, one has no idea how they oscillate, so the uniform scale is used to explore roughly their behaviour. Subsequently, one can choose a suitable distribution of knots to converge energies faster. The more concentrated scale in figure C-1 (b) is suitable for the eigenstates that vary rapidly at the centre of the interval $[0, 1]$. We choose the exponential scale if the eigenstates vary rapidly at the first endpoint $s_1 = 0$.

The B-splines in equation (C.2) are not ready to use. They need to be slightly

modified to satisfy the boundary conditions at the endpoints. All $B_{i,k}(x)$ have to satisfy the boundary conditions of $\psi(x)$. In our numerical calculation, the first boundary condition is that $\psi(x)$ is assumed to vanish at a certain distance s_2, so we delete the last B-spline from the summation, which does not disappear at s_2. The second one can be found by the integrals:

$$\begin{aligned} \int \vec{\nabla} \cdot (\psi^* \vec{\nabla} \psi) dV &= \int (\vec{\nabla} \psi^* \cdot \vec{\nabla} \psi) dV + \int \psi^* \nabla^2 \psi dV \\ &= \int (\psi^* \vec{\nabla} \psi) \cdot d\vec{S}. \end{aligned} \tag{C.5}$$

The left side of the equation is the volume integral over the volume V and the right side is the surface integral over the boundary of the volume V. If the volume is large enough, ψ will exist only inside the volume and we could approximate the left integral, $\int (\psi \vec{\bigtriangledown} \psi) \cdot d\vec{S}$, to be zero. Thus, we obtain

$$-\int \psi^* \nabla^2 \psi dV = \int (\vec{\nabla} \psi^* \cdot \vec{\nabla} \psi) dV. \tag{C.6}$$

Simplifying the expression in x coordinate and multiplying it by $\hbar^2/2m$ gives the kinetic energy:

$$-\frac{\hbar^2}{2m} \int_{s_1}^{s_2} \psi^* \frac{\partial^2}{\partial x^2} \psi dx = \frac{\hbar^2}{2m} \int_{s_1}^{s_2} (\frac{\partial}{\partial x} \psi^*)(\frac{\partial}{\partial x} \psi) dx. \tag{C.7}$$

The left integral can be integrated by parts to obtain

$$-\frac{\hbar^2}{2m} \int_{s_1}^{s_2} \psi^* \frac{\partial^2}{\partial x^2} \psi dx = -\frac{\hbar^2}{2m} \left\{ \left[\psi^* \frac{\partial}{\partial x} \psi \right]_{s_1}^{s_2} - \int_{s_1}^{s_2} (\frac{\partial}{\partial x} \psi^*)(\frac{\partial}{\partial x} \psi) dx \right\}. \tag{C.8}$$

According to (C.7) and (C.8), one can see easily the second boundary condition, $\left[\psi^* \frac{\partial}{\partial x} \psi\right]_{s_1}^{s_2} = 0$. $B_{1,4}(x)$ is the only basis function that does not satisfy the condition as $B_{1,4}(s_1)$ and $DB_{1,4}(s_1)$ are not zero (see figure C-1). Accordingly, we delete $B_{1,4}(x)$ from the summation. Now, we have

$$\psi(x) = \sum_{i=2}^{n-1} b_i B_{i,4}(x). \tag{C.9}$$

However, the set of basis functions above fails to describe the wavefunction that does not vanish at s_1, so we need to define a new B-spline $B'_{2,4}(x)$ and finally get the summation:

$$\psi(x) = b_2 B'_{2,4}(x) + \sum_{i=3}^{n-1} b_i B_{i,4}(x), \tag{C.10}$$

where $B'_{2,4}(x) = B_{1,4}(x) + B_{2,4}(x)$ satisfying both boundary conditions; $B'_{2,4}(s_1) \neq 0$, $DB'_{2,4}(s_1) = 0$, and $B'_{2,4}(s_2) = 0$. The expansion (C.10) is now ready to describe arbitrary wavefunctions, satisfying $\psi^* \frac{\partial}{\partial x}\psi = 0$ at s_1 and s_2.

Appendix D

Gauge transformation

The Hamiltonian describing a free charged particle in a magnetic field is given by

$$\widehat{H} = \frac{1}{2m^*}(\hat{p} - Q\vec{A}(\vec{r}))^2, \tag{D.1}$$

where Q is the charge of the particle. If the vector potential $\vec{A}$ is changed to $\vec{A}'$, where

$$\vec{A}'(\vec{r}) = \vec{A}(\vec{r}) + \vec{\nabla}\chi(\vec{r}). \tag{D.2}$$

The magnetic field does not change because of the identity $\vec{\nabla} \times \vec{\nabla}\chi = 0$. That is, $\vec{B} = \vec{\nabla} \times \vec{A}(\vec{r}) = \vec{\nabla} \times \vec{A}'(\vec{r})$. The Schrödinger equation (D.1) can be written as

$$\frac{1}{2m^*}(\hat{p} - Q\vec{A}' + Q\vec{\nabla}\chi)^2\psi = \varepsilon\psi. \tag{D.3}$$

After transforming, one would expect the new eigenstate of the new Hamiltonian to has the same energy as the original eigenstate, since the magnetic field $\vec{B}$ which influences the energy of the particle is unchanged. Therefore,

$$\frac{1}{2m^*}(\hat{p} - Q\vec{A}')^2\psi' = \varepsilon\psi', \tag{D.4}$$

or

$$\frac{1}{2m^*}(\hat{p} - Q\vec{A} - Q\vec{\nabla}\chi)^2\psi' = \varepsilon\psi'. \tag{D.5}$$

Let us try

$$\psi' = \exp(iQ\chi/\hbar)\psi, \tag{D.6}$$

satisfying

$$\begin{aligned} \hat{p}\psi' &= \exp(iQ\chi/\hbar)\hat{p}\psi + Q(\vec{\nabla}\chi)\exp(iQ\chi/\hbar)\psi \\ (\hat{p} - Q\vec{\nabla}\chi)\psi' &= \exp(iQ\chi/\hbar)\hat{p}\psi \\ &= \exp(iQ\chi/\hbar)\hat{p}\exp(-iQ\chi/\hbar)\psi' \end{aligned} \tag{D.7}$$

Next, we return to (D.5) and use (D.6) and (D.7) to derive

$$\begin{aligned} \frac{1}{2m^*}(\hat{p} - Q\vec{A} - Q\vec{\nabla}\chi)^2\psi' &= \frac{1}{2m^*}((\hat{p} - Q\vec{\nabla}\chi) - Q\vec{A})((\hat{p} - Q\vec{\nabla}\chi) - Q\vec{A})\psi' \\ &= \frac{1}{2m^*}((\hat{p} - Q\vec{\nabla}\chi) - Q\vec{A})\exp(iQ\chi/\hbar)(\hat{p} - Q\vec{A})\psi \\ &= \frac{1}{2m^*}[\exp(iQ\chi/\hbar)\hat{p}(\hat{p} - Q\vec{A})\psi \\ &\quad - \exp(iQ\chi/\hbar)Q\vec{A}(\hat{p} - Q\vec{A})\psi] \\ &= \frac{1}{2m^*}\exp(iQ\chi/\hbar)(\hat{p} - Q\vec{A})^2\psi \\ &= \exp(iQ\chi/\hbar)\varepsilon\psi. \end{aligned}$$

$$\therefore \qquad \frac{1}{2m^*}(\hat{p} - Q\vec{A})^2\psi = \varepsilon\psi. \tag{D.8}$$

Thus, the relation between ψ and ψ' is $\psi' = \exp(iQ\chi/\hbar)\psi$.

In short, if the vector potential is changed from $\vec{A}(\vec{r})$ to $\vec{A}'(\vec{r})$ where $\vec{A}'(\vec{r}) = \vec{A}(\vec{r}) + \vec{\nabla}\chi$, one could search for $\psi'(\vec{r})$, which has the same energy as $\psi(\vec{r})$, as $\psi' = \exp(iQ\chi/\hbar)\psi$.

Appendix E

Evaluation of $\vec{b}_{N,N'}$

In what follows, we will evaluate $\vec{b}_{N,N'}$ by firstly considering the integration of $h(y)$ (4.59) and $f(x)$ (4.60) separately. Firstly,

$$\begin{aligned}\int_0^{bN_y} h(y)\mathrm{d}y &= N_y b\delta_{k'_y\lambda'+G_y,k_y\lambda} \\ &= N_y b\delta_{k'_y,k_y}\delta_{\lambda'\frac{2\pi}{b}+G_y,\lambda\frac{2\pi}{b}} \end{aligned} \tag{E.1}$$

since k_y must be in the first magnetic Brillouin zone; $k_y \in (-\frac{\pi}{b}, \frac{\pi}{b}]$. Next,

$$\int_{-\alpha}^{+\alpha} f(x)\mathrm{d}x = \beta \int_{-\alpha}^{+\alpha} e^{-x^2} H_N(x + \ell_B k_y\lambda - \gamma)H_{N'}(x + \ell_B k'_y\lambda' - \gamma)\mathrm{d}x, \tag{E.2}$$

where $\beta = \ell_B e^{-\ell_B^2 G^2/4} e^{-i\ell_B^2 \frac{G_x}{2}(k_y\lambda - k'_y\lambda')}$ and $\gamma = \frac{\ell_B}{2}(k_y\lambda + k'_y\lambda' - iG_x)$. Now, we know that $k'_y\lambda' + G_y = k_y\lambda$ from the integration of $h(y)$ so that $\ell_B k_y\lambda - \gamma$ and $\ell_B k'_y\lambda' - \gamma$ could be written as,

$$\ell_B k_y\lambda - \gamma = \frac{\ell_B}{2}(G_y + iG_x) = \tilde{x}_N, \tag{E.3}$$

$$\ell_B k'_y\lambda' - \gamma = \frac{\ell_B}{2}(-G_y + iG_x) = \tilde{x}_{N'}. \tag{E.4}$$

From the formula 7.377 in integral tables [71] , we obtain

$$\int_{-\alpha}^{+\alpha} f(x)\mathrm{d}x = \beta 2^S \sqrt{\pi} T! \tilde{x}_S^{S-T} L_T^{S-T}(\ell_B^2 G^2/2), \tag{E.5}$$

where S is the greatest of N and N', and T is the smallest. In addition, $L_n^m(x)$ are associated Laguerre polynomials. Inserting (E.5) and (E.1) in (4.58), we obtain

$$\begin{aligned}\vec{b}_{N,N'} &= \frac{1}{N_y^2 b\ell_B\sqrt{\pi 2^{S+T}S!T!}}\sum_{\vec{G}\neq 0}\sum_{\lambda}\vec{B}_{\vec{G}}(z)\beta 2^S\sqrt{\pi}T!\tilde{x}_S^{S-T}L_T^{S-T}(\ell_B^2G^2/2)\\ &\quad\times N_y b e^{ik_x\ell_B^2k_y\lambda}e^{-ik'_x\ell_B^2(k_y\lambda-G_y)}\delta_{k_yk'_y},\end{aligned}\tag{E.6}$$

where $\beta = \ell_B e^{-\ell_B^2G^2/4}e^{-i\ell_B^2\frac{G_x}{2}(2k_y\lambda-G_y)}$. Next $\vec{b}_{N,N'}$ can be derived straightforwardly by using the standard identity [65] $\sum e^{i\lambda a(k_x-k'_x)} = N_y\delta_{k_xk'_x}$.

$$\begin{aligned}\vec{b}_{N,N'} &= \delta_{\vec{k},\vec{k}'}\sqrt{2^{S-T}}\sqrt{\frac{T!}{S!}}\sum_{\vec{G}\neq 0}\vec{B}_{\vec{G}}(z)\tilde{x}_S^{S-T}L_T^{S-T}(\ell_B^2G^2/2)\\ &\quad\times e^{-\ell_B^2G^2/4}e^{i\pi nm}e^{i(k_xG_y-k_yG_x)\ell_B^2},\end{aligned}\tag{E.7}$$

where $\vec{G} = (n\frac{2\pi}{a}, m\frac{2\pi}{b})$. It does not matter whether N or N' is greater, we can evaluate

$$\tilde{x}_S^{S-T} = \left(i\sqrt{\frac{g}{2}}\right)^{S-T}\left(\frac{G_x-iG_y}{G}\right)^{N-N'},\tag{E.8}$$

where $g = \ell_B^2G^2/2$. Hence, (E.7) becomes

$$\begin{aligned}\vec{b}_{N,N'} &= \delta_{\vec{k},\vec{k}'}\sqrt{\frac{T!}{S!}}\sum_{\vec{G}\neq 0}\vec{B}_{\vec{G}}(z)(i\sqrt{g})^{S-T}L_T^{S-T}(g)e^{-g/2}e^{i\pi nm}e^{i(k_xG_y-k_yG_x)\ell_B^2}\\ &\quad\times\left(\frac{G_x-iG_y}{G}\right)^{N-N'}.\end{aligned}\tag{E.9}$$

Appendix F

Eigenstates of magnetic translation operators

Because $e^{i\vec{k}\cdot\vec{L}}$ are the eigenvalues of magnetic translation operators, which commute with the Hamiltonian, it is said that $\vec{k}$ is a good quantum number. For this reason, the wavefunction of electrons in the presence of the magnetic field due to vortex lattice $|\psi\rangle$ can be label by $|\vec{k}\rangle$. Now, we have

$$\widehat{T}_M(\vec{L})|\vec{k}\rangle = e^{i\vec{k}\cdot\vec{L}}|\vec{k}\rangle, \tag{F.1}$$

where $|\vec{k}\rangle \equiv |\psi\rangle = \sum a_{m\tau\vec{R}}|m,\tau,\vec{R}\rangle$ (see 4.67). From the definition of $\widehat{T}_M(\vec{L})$ in (4.71), (F.1) can be written as

$$\left(\sum_{m',\tau',\vec{R}'} |m',\tau',\vec{R}'\rangle e^{-\frac{ie}{\hbar}\vec{R}'_{\tau'}\cdot\vec{A}(\vec{L})}\langle m',\tau',\vec{R}'-\vec{L}|\right)\left(\sum_{m,\tau,\vec{R},} a_{m\tau\vec{R}}|m,\tau,\vec{R}\rangle\right)$$

$$= e^{i\vec{k}\cdot\vec{L}}\sum_{m,\tau,\vec{R}} a_{m\tau\vec{R}}|m,\tau,\vec{R}\rangle. \tag{F.2}$$

Multiplying from the left by $\langle m'',\tau'',\vec{R}''|$ gives

$$e^{-\frac{ie}{\hbar}\vec{R}''_{\tau''}\cdot\vec{A}(\vec{L})}a_{m''\tau''\vec{R}''-\vec{L}} = e^{i\vec{k}\cdot\vec{L}}a_{m''\tau''\vec{R}''}. \tag{F.3}$$

Changing τ'', $\vec{R}''$, $\vec{L}$, $\vec{A}(-\vec{L})$, and m'' to τ, $\vec{R}$, $-\vec{L}$, $-\vec{A}(\vec{L})$, and m respectively gives

$$e^{\frac{ie}{\hbar}\vec{R}_\tau\cdot\vec{A}(\vec{L})}a_{m\tau\vec{R}+\vec{L}} = e^{-i\vec{k}\cdot\vec{L}}a_{m\tau\vec{R}}. \tag{F.4}$$

If $\vec{R}=0$, we have

$$a_{m\tau\vec{L}} = e^{-i\vec{k}\cdot\vec{L}}e^{-\frac{ie}{\hbar}\vec{r}_\tau\cdot\vec{A}(\vec{L})}a_{m\tau 0}. \tag{F.5}$$

To normalise the wavefunction, let $a_{m\tau 0} = \frac{1}{\sqrt{N}}a_{m\tau}$ and change $\vec{L}$ to $\vec{R}$; thus, we have

$$a_{m\tau\vec{R}} = \frac{1}{\sqrt{N}}e^{-i\vec{k}\cdot\vec{R}}e^{-\frac{ie}{\hbar}\vec{r}_\tau\cdot\vec{A}(\vec{R})}a_{m\tau}. \tag{F.6}$$

Therefore, $|\vec{k}\rangle$ can be written as

$$\begin{aligned} |\vec{k}\rangle &= \sum_{m,\tau,\vec{R}}\frac{1}{\sqrt{N}}e^{-i\vec{k}\cdot\vec{R}}e^{-\frac{ie}{\hbar}\vec{r}_\tau\cdot\vec{A}(\vec{R})}a_{m\tau}|m,\tau,\vec{R}\rangle \\ &= \sum_{m,\tau}a_{m\tau}|m,\tau,\vec{k}\rangle, \end{aligned} \tag{F.7}$$

where $|m,\tau,\vec{k}\rangle = \frac{1}{\sqrt{N}}\sum_{\vec{R}}e^{-i\vec{k}\cdot\vec{R}}e^{-\frac{ie}{\hbar}\vec{r}_\tau\cdot\vec{A}(\vec{R})}|m,\tau,\vec{R}\rangle$ are orthonormal wavefunctions as shown below.

$$\langle m',\tau',\vec{k}'|m,\tau,\vec{k}\rangle = \frac{1}{N}\sum_{\vec{R},\vec{R}'}e^{i\vec{k}'\cdot\vec{R}'}e^{\frac{ie}{\hbar}\vec{r}_{\tau'}\cdot\vec{A}(\vec{R}')}e^{-i\vec{k}\cdot\vec{R}}e^{-\frac{ie}{\hbar}\vec{r}_\tau\cdot\vec{A}(\vec{R})}\langle m',\tau',\vec{R}'|m,\tau,\vec{R}\rangle. \tag{F.8}$$

We assume (tight binding) that there is no the overlap of an electron state of one Zeeman potential well with that of its neighbours when the distance between vortices is large enough. That is, $\langle m',\tau',\vec{R}'|m,\tau,\vec{R}\rangle = \delta_{mm'}\delta_{\vec{R}_\tau,\vec{R}'_{\tau'}}$. Therefore, (F.8) becomes

$$\begin{aligned} \langle m',\tau',\vec{k}'|m,\tau,\vec{k}\rangle &= \frac{1}{N}\delta_{mm'}\delta_{\vec{R}_\tau,\vec{R}'_{\tau'}}\sum_{\vec{R}}e^{i(\vec{k}'-\vec{k})\cdot\vec{R}} \\ &= \delta_{mm'}\delta_{\vec{R}_\tau,\vec{R}'_{\tau'}}\delta_{\vec{k},\vec{k}'}, \end{aligned} \tag{F.9}$$

using $\sum_{\vec{R}}e^{i(\vec{k}'-\vec{k})\cdot\vec{R}} = N\delta_{\vec{k},\vec{k}'}$. [65]

Bibliography

[1] J. K. Furdyna, J. Appl. Phys. **64**, R29 (1988).

[2] J. K. Furdyna, J. Appl. Phys. **53**, 7637 (1982).

[3] T. Dietl, M. Sawicki, M. Dahl, D. Heiman, E. D. Isaacs, M. J. Graf, S. I. Gubarev, and D. L. Alov, Phys. Rev. B **43**, 3154 (1991).

[4] M. Berciu, T.G. Rappoport, and B. Jankó, Nature 435, 71 (2005).

[5] M. Berciu and B. Jankó, Phys. Rev. Lett. 90, 246804 (2003).

[6] T.G. Rappoport *et al*, Phys. Rev. B **74**, 094502 (2006).

[7] P. Redliński, T. Wojtowicz, T. G. Rappoport, A. Libál, J. K. Furdyna, and B. Jankó, Phys. Rev. B **72**, 085209 (2005).

[8] S.-H. Lin, T. G. Rappoport, M. Berciu, and B. Jankó, J. Appl. Phys. **107**, 034307 (2010).

[9] X. L. Wang, C. T. Lin, B. Liang, S. Yu, S. Ooi, K. Hirata, S. Y. Ding, D. Q. Shi, S. X. Dou, Z. W. Lin, J. Appl. Phys. **107**, 09G116 (2007).

[10] A. Fert, Rev. Mod. Phys. **80**, 1517 (2008).

[11] Igor Žutić, Jaroslav Fabian, and S. Das Sarma, Rev. Mod. Phys. **76**, 323 (2004).

[12] A. A. Abrikosov, Sov, Phys. JETP **5**, 1174 (1957).

[13] H. Kamerlingh Onnes, Commun. Phys. Lab. **12**, 120 (1911).

[14] W. Buckel, *Superconductivity: Fundamentals and Applications*, (VCH, Weinheim, 1991).

[15] V. L. Ginzburg and L. D. Landau, Zh. Eksperim.i. Theory. Fiz **20**, 1064 (1950).

[16] J. F. Annett, *Superconductivity, Superfluids, and Condensates*, (Oxford University Press, Oxford, 2005).

[17] V. V. Schmidt, P. Müller, and A. V. Ustinov, *The physics of Superconductors: Introduction to Fundamentals and Applications*, (Springer-Verlag, Berlin Heidelberg, 1997).

[18] D. Saint-James, G. Sarma and E. J. Thomas, *Type II Superconductivity Pergamon* (Oxford 1969).

[19] D. R. Tilley and J. Tilley, *Superfluidity and Superconductivity*, 3rd ed. (IOP Publishing Ltd, Bristol ,1990).

[20] U. Essmann and H. Trauble, Phys. Lett. **24A**, 526 (1967).

[21] P. L. Gammel *et al.,* Phys. Rev. Lett. **59**, 2592 (1987).

[22] H. F. Hess *et al.,* Phys. Rev. Lett. **62**, 214 (1989).

[23] C. A. Bolle *et al.,* Phys. Rev. Lett. **66**, 112 (1991).

[24] B. H. Bransden and C. J. Joachain, *Physics of Atoms and Molecules*, (Longman, London and New York, 1980).

[25] Kossut, Acta Phys. Pol. A **100**, 111 (2001).

[26] R. K. Zheng, M. P. Moody, B. Gault, Z. W. Liu, H. Liu, and S. P. Ringer, J. Magn. Magn. Mater. **321**, 935 (2009).

[27] K. Sato *et al.,* Rev. Mod. Phys. **82**, 1633 (2010).

[28] A. V. Komarov, S. M. Ryabchenko, O. V. Terletskii, I. I. Zheru, and R. D. Ivanchuk, Zh. Eksp. Teor. Fiz. **73**, 608 (1977).

[29] A. V. Komarov, S. M. Ryabchenko, Yu. G. Semyonov, B. D. Shanina, and N. I. Vitrihovskii, Zh. ksp. Teor. Fiz. **79**, 1554 (1980) [Sov. Phys. JETP **52**, 783 (1980)].

[30] R. B. Bylsma, W. M. Becker, J. Kossut, and U. Debska, Phys. Rev. B **33**, 8207 (1986).

[31] H.C. Mertin, H.E. Gumlich, and Ch. Jung, Semicond. Sci. Technol. **8**, 1634 (1993).

[32] L. Li *et al.,* Phys. Rev. B **85**, 174430 (2012).

[33] J. Blinowski and P. Kacman, Phys. Rev. B **67**, 121204(R) (2003).

[34] J. Wang, C. Sun, J. Kono, A. Oiwa, H. Munekata, L. Cywinski, and L. J. Sham, Phys. Rev. Lett. **95**, 167401 (2005)

[35] H. Y. Jung *et al.,* Nature Mater. **9**, 47 (2009).

[36] I. Zutic, J. Fabian, and S.D. Sarma, Rev. Mod. Phys. **76**, 323 (2004).

[37] P Kacman, Semicond. Sci. Technol. **16**, R25 (2001).

[38] S. A. Wolf *et al.,* Science **294**, 1488 (2001).

[39] K. Chang and F. M. Peeters, Solid State Commun. **120**, 181 (2001).

[40] P. Krstajic and F. M. Peeters, Phys. Rev. B **72**, 125350 (2005).

[41] G. Papp, S. Borza, and F. M. Peeters, Phys. stat. sol. (b) **243**, 1956 (2006).

[42] P. Olbrich *et al.,* Phys. Rev. B **86**, 085310 (2012).

[43] L. Solimany and B. Kramer, Solid State Commun. **96**, 471 (1995).

[44] H. S. Sim, K. H. Ahn, K. J. Chang, G. Ihm, N. Kim, and S. J. Lee, Phys. Rev. Lett. **80**, 1501 (1998).

[45] J. Reijniers, F. M. Peeters, and A. Matulis, Phys. Rev. B **59**, 2817 (1999).

[46] S. J. Lee, S. Souma, G. Ihm, and K. J. Chang, Phys. Rep. **394**, 1 (2004).

[47] B. Kocsis, G. Palla, and J. Cserti, Phys. Rev. B **71**, 075331 (2005).

[48] Y. Song and Y. Guo, J. Appl. Phys. **108**, 064306 (2010).

[49] L. D. Landau and E. M. Lifshitz, *Quantum Mechanics (Non-relativistic Theory)*, 3rd ed. (BPC Wheatons Ltd, Exeter ,1977).

[50] J. Main and G. Wunner, Found. Phys. **31**, 447 (2001).

[51] S. M. Reimann, M. Brack, A. G. Magner, J. Blaschke, and M. V. N. Murthy, Phys. Rev. A **53**, 39 (1996).

[52] R. W. Robinett, Am. J. Phys. **64**, 440 (1996).

[53] C. S. Lent, Phys. Rev. B **43**, 4179 (1991).

[54] G. J. Mata and R. Medina Eur. J. Phys. **21**, 191 (2000).

[55] W. Greiner, *Quantum Mechanics-An Introduction*, 3rd ed. (Springer-Verlag, Berlin,1989).

[56] C. W. J. Beenakker, H. Vanhouten, and B. J. Vanwees, Superlattices Microstruct. **5**, 127 (1988).

[57] G. Montambaux, Eur. Phys. J. B **79**, 215 (2011).

[58] P.M. Morse and H. Feshbach, *Methods of Theoretical Physics*, (McGraw-Hill, New York, 1953).

[59] R. L. Liboff, *Introductory Quantum Mechanics*, 3rd ed. (Addison-Wesley, New York,1980).

[60] M. Rongchao and M. Yueteng, Physica C 468, 2384 (2008).

[61] R. P. Huebener *Magnetic Flux Structures in Superconductors*, 2nd ed.(Berlin, Springer, 1979).

[62] G. Carneiro and E. H. Brandt, Phys. Rev. B **61**, 6370 (1999).

[63] J. Pearl, Appl. Phys. Lett. **5**, 65 (1964).

[64] G. Arfken, *Mathematical methods for physicsts*, 3rd ed.(Academic press, London, 1985).

[65] N. W. Ashcroft and N. D. Mermin, *Solid State Physics*, (Butler and Tanner Ltd, Frome and London, 1976).

[66] C. Kittel, *Introduction to Solid Siate Physics*, 8th ed. (Wiley, 2005).

[67] E. Brown, Phys. Rev. **133**, A1038 (1964).

[68] A. Wal, Physica B **404**, 1040 (2008).

[69] W. Opechowski and W. G. Tam, Physica **42**, 529 (1969).

[70] D. Pfannkuche and R. R. Gerhardts, Phys. Rev. B **46**, 12606 (1992).

[71] I.S. Gradxshteyn and I.M. Ryzhik, *Table of Integrals, Series, and Products*, 5th ed. (Academic Press, London, 1965).

[72] J. C. Slater and G. F. Koster, Phys. Rev. **94**, 1498 (1954).

[73] G. Burns, *Solid State Physics*, (Academic Press, London, 1985).

[74] M. Graf and P. Vogl, Phys. Rev. B **51**, 4940 (1994).

[75] M. T. I. Rakib, *Vortex matter in a superconducting disk with magnetic coating*, Master thesis, Antwerpen University (2006).

[76] M. V. Milošević, *Vortex Matter in Mesoscopic Superconductor / Ferromagnet Heterosystems*, PhD thesis, Antwerpen University (2004).

[77] R. Kato, Y. Enomoto, and S. Maekawa, Phys. Rev. B **44**, 6916 (1991).

[78] R. Kato, Y. Enomoto, and S. Maekawa, Phys. Rev. B **47**, 8016 (1993).

[79] A. I. Buzdin and J. P. Brison, Phys. Lett. A **196**, 267 (1994).

[80] A. K. Geim *et al.*, Nature **390**, 259 (1997).

[81] V. A. Schweigert, F. M. Peeters, and P. S. Deo, Phys. Rev. Lett. **81**, 2783 (1998).

[82] V. A. Schweigert and F. M. Peeters, Phys. Rev. B **57**, 13817 (1998).

[83] B. J. Baelus, L. R. E. Cabral, and F. M. Peeters, Phys. Rev. B **69**, 064506 (2004).

[84] B.J. Baelus *et al.*, Phys. Rev. B **73**, 024514 (2006).

[85] J. Baelus, F. M. Peeters, and V. A. Schweigert, Phys. Rev. B **61**, 9734 (2000).

[86] L. R. E. Cabral and J. Albino Aguiar, Phys. Rev. B **80**, 214533 (2009).

[87] W. H. Press *et al.*, *Numerical recipes in FORTRAN 90 : the art of parallel scientific computing. Vol. 2*, 2nd ed. (Cambridge University Press, Cambridge, 1996).

[88] N. Mehta, *Textbook of engineering physics, Part II*, (PHI Learning Private Limited, New Delhi, 2009).

[89] B. W. Maxfield and W. L. McLean, Phys. Rev. **139**, A1515 (1965).

[90] P. Harrison, *Quantum Wells, Wires and Dots*, 2nd ed. (John Wiley and Sons Ltd, Chichester, 2009).

[91] J. G. Analytis, S. J. Blundell, and A. Ardavan, Am. J. Phys. **72**, 613 (2004).

[92] R.E. Peierls, *Quantum Theory of solids*, (Oxford University Press, Oxford, 1955).

[93] M. Abramowitz and I. A. Stegun, *Handbook of mathematical functions with formulas, graphs, and mathematical tables* (Dover Publications, New York, 1970).

[94] H. Bachau, E. Cormier, P. Decleva, J. E. Hansen, and F. Martin, Rep. Prog. Phys. **64**, 1815 (2001).

[95] J. Sapirstein and W. R. Johnson, J. Phys. B: At. Mol. Opt. Phys. **29**, 5213 (1996).

[96] B. W. Shore, J. Phys. B **6**, 1923 (1973).

[97] S. J. Bending *et al*, Physica C **468**, 518 (2008).

[98] D. J. Priour, Jr. and H. A. Fertig, Phys. Rev. Lett. **93**, 057003 (2004).

[99] M. V. Milosevic and F. M. Peeters, Phys. Rev. B **68**, 024509 (2003).

[100] M. V. Milosevic, G. R. Berdiyorov, and F. M. Peeters, Phys. Rev. B **75**, 052502 (2007).